# Over-the-Horizon Radar Array Calibration

by

ISHAN SAMJEVA DANIEL SOLOMON
B.ENG.(HONS), B.SC.

Thesis submitted for the degree of

**Doctor of Philosophy**

Department of Electrical and Electronic Engineering
Faculty of Engineering
The University of Adelaide
Adelaide, South Australia

April 1998

# Contents

# Abstract

Modern over-the-horizon radars are currently being developed which have arrays than can be erected quickly, with minimal site preparation. Due to the rapid deployment of these arrays, antenna/sensor position errors may be present. Further since the antennas have a simple and cost-effective design, mutual coupling may be present. These imperfections, which can degrade radar performance, form the basis for the work conducted in this thesis.

The effect of these model errors on radar performance is first analysed. The degradation in signal-to-noise ratio, array gain, bearing estimation and array sidelobe levels, are determined. The major degradation is observed in the array sidelobe levels, which in turn results in the clutter-to-noise ratio (and hence target detectability) being worsened in the presence of non-stationary interferences. For these reasons, array calibration is required to improve the array sidelobe levels.

New array calibration algorithms are then developed to correct for sensor position errors and mutual coupling, using sources in the radar environment. These algorithms are analysed using simulations, and are found to perform well. The Cramer-Rao lower bound is derived, for the problem scenarios considered, and the algorithms are shown to achieve the bound. Further the Cramer-Rao lower bound is analysed, to obtain useful insight into the array calibration problem and identifiability.

Scattered echoes from meteor trails are shown to be excellent sources of opportunity for over-the-horizon radar array calibration. These echoes are found in general to : have planar wavefronts, be present in large numbers, be sufficiently strong, and be of adequate duration for sufficient snapshots to be obtained for array calibration. It also is shown that meteor head echoes are good sources of opportunity, and their properties along with that of other sources, are determined.

Finally, the receiving array of the Jindalee over-the-horizon radar (located in central Australia) is calibrated using echoes from meteor trails. The results obtained are compared with standard calibration (for this radar), which involves the use of special calibration sources. Array calibration using meteor trail echoes is found to perform as well as the standard array calibration, indicating that echoes from meteor trails can perform good array calibration.

# Declaration

This work contains no material which has been accepted for the award of any other degree or diploma in any university or other tertiary institution and, to the best of my knowledge and belief, contains no material previously published or written by another person, except where due reference has been made in the text.

I give consent to this copy of my thesis, when deposited in the University Library, being available for loan and photocopying.

Signature ________________________

Date April, 1998

# Acknowledgments

I would like to first thank Professor Douglas Gray, my principal supervisor. His expertise in array processing, together with his general signal processing knowledge, enabled him to provide extremely useful criticism, analysis, and suggestions on my work. He also taught me a lot about presentations, both oral and written.

Dr. Stuart Anderson, my co-supervisor, suggested this problem and provided me with advice on matters relating to radars, both of skywave and surface-wave types. He also helped me significantly with the final phase of publications.

Professor Yuri Abramovich, while not officially a supervisor, was instrumental, from the formulation of the problem, to its conclusion. He provided me with several suggestions and criticism, on many wide ranging aspects of radar signal processing.

I would like to thank the Defence Science and Technology Organisation, for supporting me during the course of this research; I am especially grateful to Dr. Bruce Ward, Dr. Chris Coleman, Dr. Dan Meehan, Dr. Dick Thomas and Mrs. Elizabeth Ashforth. I also would like to thank the Cooperative Research Centre for Sensor Signal and Information Processing, for providing me with good facilities for conducting research.

I am also grateful to Professor Benjamin Friedlander, who provided me with good feedback when I contacted him in California, and Professor Kok Teo who provided some useful suggestions on my work.

I would like to thank the Lord for all things, and finally I would like to thank my parents for their support and sacrifices, over the years, and to them I dedicate this thesis.

# List of Figures

# List of Tables

# Glossary

## Abbreviations

| | |
|---|---|
| **ASL** | average sidelobe level |
| **C-TLS** | constrained total least squares |
| **CRLB** | Cramer-Rao lower bound |
| **DOAs** | directions-of-arrival |
| **ESPRIT** | estimation of signal parameters via rotational invariance techniques |
| **FIM** | Fisher information matrix |
| **ISLB** | integrated sidelobe level |
| **LS** | least squares |
| **ML** | maximum likelihood |
| **MUSIC** | multiple signal classification |
| **PSL** | peak sidelobe level |
| **SCV** | sub-clutter visibility |
| **SLB** | sidelobe |
| **SNR** | signal-to-noise ratio |
| **STD** | standard deviation |
| **TLS** | total least squares |

# Symbols

| | |
|---|---|
| $\mathbf{x}^T$, $\mathbf{X}^T$ | transpose |
| $\mathbf{x}^H$, $\mathbf{X}^H$ | conjugate transpose |
| $\hat{x}$, $\hat{\mathbf{x}}$, $\hat{\mathbf{X}}$ | estimates |
| $trace\{\mathbf{X}\}$ | trace of matrix $\mathbf{X}$ |
| $\Re\{x\}$ | real part of $x$ |
| $\Im\{x\}$ | imaginary part of $x$ |
| $conj(x)$, $x^*$ | conjugate of $x$ |
| $diag\{\mathbf{x}\}$, $\mathbf{D}_{\mathbf{x}}$ | diagonal matrix containing the elements of $\mathbf{x}$ along its main diagonal |
| $\lvert\mathbf{x}\rvert$ | vector norm of $\mathbf{x}$ |
| $\lVert\mathbf{X}\rVert_F$ | Frobenious norm of matrix $\mathbf{X}$ |
| $\frac{\partial Q}{\partial x}$ | partial derivative of $Q$ with respect to $x$ |
| $\dot{x}_y$ | first derivative of $x$ with respect to $y$ |
| $e^x$, $\exp(x)$ | exponential operator |
| $\delta(t_1, t_2)$ | one when $t_1 = t_2$, and zero otherwise |
| $(\mathbf{X})^+$ | generalised inverse of matrix $\mathbf{X}$ |
| $\odot$ | Hadamard product |
| $j$ | complex operator |
| $\mathbf{I}_M$ | $M$x$M$ identity matrix |
| $M$ | number of sensors / receivers |
| $t$ | time index |
| $T$ | number of snapshots/samples |
| $N$ | number of signals |
| $N_C$ | number of clusters |
| $N_T$ | total number of signals in all clusters |
| $N_{\tilde{Z}}$ | number of columns in matrix $\tilde{\mathbf{Z}}$ |
| $\theta$, $\phi$ | bearing (azimuth), direction-of-arrival |
| $\Phi$ | set of bearings not in main beamwidth |
| $(x_m, y_m)$ | actual position of $m$th sensor |
| $(x_m^o, y_m^o)$ | nominal position of $m$th sensor |
| $(\Delta x_m, \Delta y_m)$ | position error of $m$th sensor |
| $\lambda$ | radar wavelength |

| | |
|---|---|
| $f$ | radar frequency |
| $w$ | radar angular frequency |
| $v$ | speed of light |
| $\tau_{mn}$ | time delay for $n$th signal to arrive at $m$th sensor |
| $\mathbf{a}(\theta)$ | array steering vector |
| $\mathbf{a}_o(\theta)$ | nominal steering vector |
| $\mathbf{v}$ | actual steering vector (including the effects of mutual coupling) |
| $\mathbf{A}$ | matrix of array steering vectors |
| $\mathbf{D}(\theta)$, $\mathbf{D}_2(\theta)$ | diagonal matrices involved in the derivatives of $\mathbf{a}(\theta)$ |
| $s_n(t)$ | baseband waveform of the $n$th signal at time $t$ |
| $s_I(t)$ | baseband waveform of interference signal at time $t$ |
| $n_m(t)$ | receiver noise at time $t$ |
| $z_m(t)$ | output of $m$th sensor/receiver at time $t$ |
| $\mathbf{s}(t)$ | vector of baseband waveforms of signals, at time $t$ |
| $\mathbf{n}(t)$ | vector of noise outputs at time $t$ |
| $\mathbf{n}_T(t)$ | vector of total noise contribution (i.e. including interferers) at time $t$ |
| $\mathbf{z}(t)$ | vector of sensor outputs at time $t$ |
| $\mathbf{z}_C(t)$ | clutter signal at time $t$ |
| $\bar{\mathbf{z}}_m(t)$ | output of consecutive receivers starting at $m$th receiver, at time $t$ |
| $\tilde{\mathbf{Z}}$ | matrix with data from all clusters |
| $\check{\mathbf{z}}(t)$ | vector of sensor outputs for all sources, at time $t$ |
| $\tilde{z}_\theta(t)$ | beamformer output for a beam steered in direction $\theta$, at time $t$ |
| $\mathbf{w}(\theta)$ | beamformer weight vector |
| $B_\theta(\phi)$ | beampattern for steer direction $\theta$ |
| $ASL(\theta)$ | average sidelobe level for a beam steered in direction $\theta$ |
| $p(\theta)$ | beamformer power output in direction $\theta$ |
| $\sigma_S^2$, $\sigma_N^2$, $\sigma_I^2$ | signal, noise, and interferer powers |
| $\sigma_n^2$ | power of $n$th disjoint source |
| $s_n$, $\mathbf{s}$, $\mathbf{S}$ | complex parameters |
| $\mathbf{R}$ | spatial covariance matrix |
| $\mathbf{R}_n$ | spatial covariance matrix of $n$th disjoint source/cluster |
| $\mathbf{P}$ | signal covariance matrix |
| $\mathbf{P}_n$ | signal covariance matrix of $n$th disjoint cluster |

| | |
|---|---|
| $\mathbf{Q}$ | noise covariance matrix |
| $\mathbf{v}_m$, $\mathbf{V}$ | $m$th eigenvector and matrix of eigenvectors |
| $\lambda_m$ | $m$th eigenvalue |
| $\mathbf{E}$ | signal subspace |
| $\mathbf{U}$ | noise subspace |
| $\alpha_m$, $\psi_m$ | gain and phase error, for $m$th element |
| $\mathbf{\Gamma}$ | diagonal matrix of receiver gain/phase errors |
| $\sigma_a$ | standard deviation of amplitude errors |
| $\sigma_\psi$ | standard deviation of phase errors |
| $\mathbf{S}_C$ | scattering matrix |
| $\mathbf{C}$ | coupling matrix |
| $\mathbf{C}_o$ | nominal coupling matrix |
| $\mathbf{Z}_o$ | array impedance matrix |
| $Z_L$ | scalar load impedance |
| $Q$ | cost function |
| $\mathbf{H}$ | Hessian matrix |
| $\mathbf{r}$ | gradient vector |
| $\mathbf{\Psi}$ | unknowns to be estimated |
| $\mathbf{J}$ | Fisher information matrix |
| $\mathbf{CRLB}(\mathbf{\Psi})$ | Cramer-Rao lower bound for estimating $\mathbf{\Psi}$ |

Boldface lower case variables are column vectors.

Boldface upper case variables are matrices.

# Publications

The list of publications relating to this thesis are :

- I. S. D. Solomon, Yu. I. Abramovich, D. A. Gray and S. J. Anderson, "OTH radar antenna array calibration analysis", Fourth International Symposium on Signal Processing and its Applications, August 1996, Gold Coast, Australia, pp. 471-474.
- I. S. D. Solomon, D. A. Gray, Yu. I. Abramovich and S. J. Anderson, "Estimating of array mutual coupling and sensor positions for over-the-horizon radar", Digital Signal Processing Applications Conference (TENCON), November 1996, Perth, Australia, pp. 846-851.
- I. S. D. Solomon, D. A. Gray, Yu. I. Abramovich and S. J. Anderson, "Sources for OTH radar array calibration", IEEE Antennas and Propagation Symposium, July 1997, Montreal, Canada, pp. 306-309.
- I. S. D. Solomon, D. A. Gray, Yu. I. Abramovich and S. J. Anderson, "OTH radar array calibration using disparate sources", IEE Radar Conference, October 1997, Edinburgh, Scotland, pp. 176-180.
- I. S. D. Solomon, D. A. Gray, Yu. I. Abramovich and S. J. Anderson, "Over-the-horizon radar array calibration using echoes from ionised meteor trails", IEE Proceedings - Radar, Sonar and Navigation, June 1998, Vol. 145, No. 3, pp. 173-180 (to appear).
- I. S. D. Solomon, D. A. Gray, Yu. I. Abramovich and S. J. Anderson, "Array calibration of OTH radars using disparate sources", submitted to IEEE Transactions on Antennas and Propagation.
- I. S. D. Solomon, Yu. I. Abramovich, D. A. Gray and S. J. Anderson, "Performance of OTH radar array calibration", IEEE International Conference on Acoustics, Speech, and

Signal Processing (ICASSP), May 1998, Seattle, Washington, U.S.A., pp 2025-2028.

- I. S. D. Solomon, Yu. I. Abramovich, D. A. Gray and S. J. Anderson, "Mutual coupling estimation", International Radar Symposium, September 1998, Munich, Germany (to appear).

- I. S. D. Solomon, D. A. Gray, Yu. I. Abramovich and S. J. Anderson, "Meteor trail echoes for OTH radar array calibration", *in preparation for* Radio Science.

# CHAPTER 1

# Introduction

## 1.1 Problem Description

Over-the-horizon (OTH) radars are currently being developed for coastal and long range surveillance. These systems are to be used primarily for detecting targets (such as ships and aircraft) and for remote sensing the ocean surface. Unlike other radars these radars achieve over-the-horizon propagation, by operating in the 3-30 MHz frequency band, called the High Frequency (HF) band.

Two main types of OTH radars exist : skywave and surface-wave radars. Skywave OTH radars [190, 103, 116], use the reflection of the ionosphere and the diffraction from the ground/sea, to get electromagnetic waves to propagate beyond the horizon. Long distance propagation is obtained for such systems, but the radar signals are often distorted by the ionosphere. Surface-wave OTH radars [9, 133, 110] work by coupling electromagnetic waves with the conducting surface of the ocean, obtaining propagation to ranges up to a few hundred kilometres around the earth. Surface-wave radars cover the close-in ranges that are not covered by skywave radars, and hence can often fill the surveillance gap. Surface-wave radar data is of higher quality, since ionospheric contamination of radar signals usually does not occur.

The work reported here is primarily for surface-wave radar systems, but is applicable for skywave radar systems as well. The surface-wave radar environment is illustrated in figure 1.1, although the diagram is not to scale. Surface-wave radars are located near the ocean surface, and exploit surface-wave propagation to detect targets. These radars usually contain well-separated (quasi-bistatic) transmit (Tx) and receive (Rx) subsystems. The transmit subsystem transmits energy in a particular direction, and backscattered energy is analysed by the receive subsystem. Interference signals (for example from radio stations) are from active sources, and

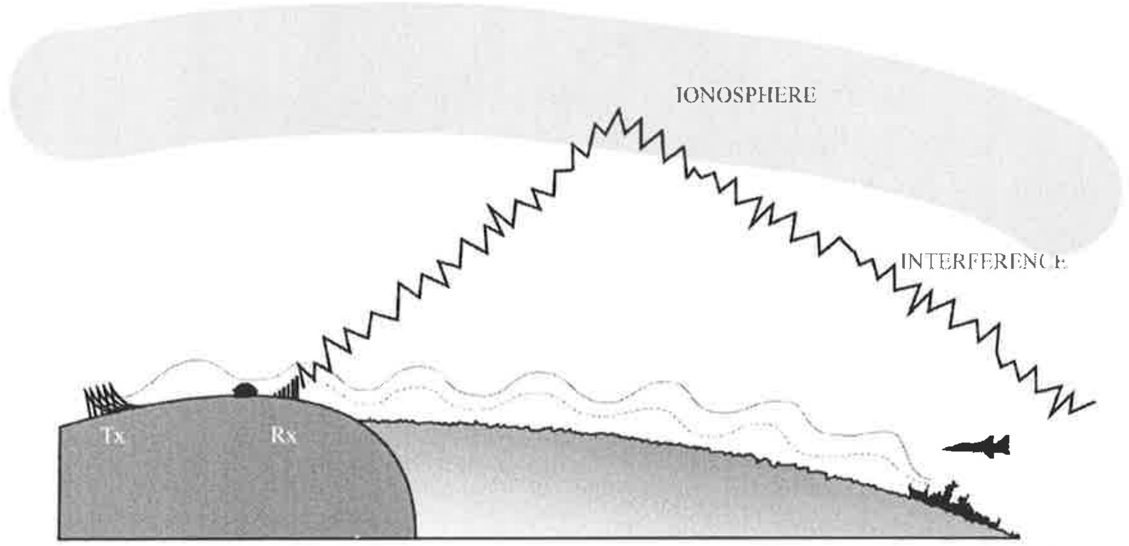

Figure 1.1: The surface-wave radar environment.

can reach the receive subsystem either via surface-wave or skywave propagation modes.

Typical OTH radar receive subsystems use an array of antenna elements, to obtain better target detectability and further to estimate the bearings of the targets. The electromagnetic waves scattered from targets, the ocean and land, together with interference signals, induce voltages on the antenna elements. These voltages are measured simultaneously using multiple receivers, with a single receiver connected to each antenna, to form the array output. Measurements made at discrete time instants, called snapshots, are then processed by the radar. Radar signal processing transforms the received signals over a period of time (called a dwell) into ARD (azimuth-range-Doppler) data, which expresses the received power as a function of bearing (usually azimuth), range (distance from the radar) and Doppler (or velocity). Target detection and remote sensing is then performed on the ARD data.

Figure 1.2 shows the received power (in dB) of a surface-wave radar [9], as a function of range bin and Doppler. Surface-wave returns are observed in range bins 80-100, while skywave returns are observed after about range bin 190 (the vertical lines over the other range bins are processing artifacts). The strong returns at 0 Hz (in range bins 90-100) are scattered returns from the ground; the very strong return near range bin 83 is energy received directly

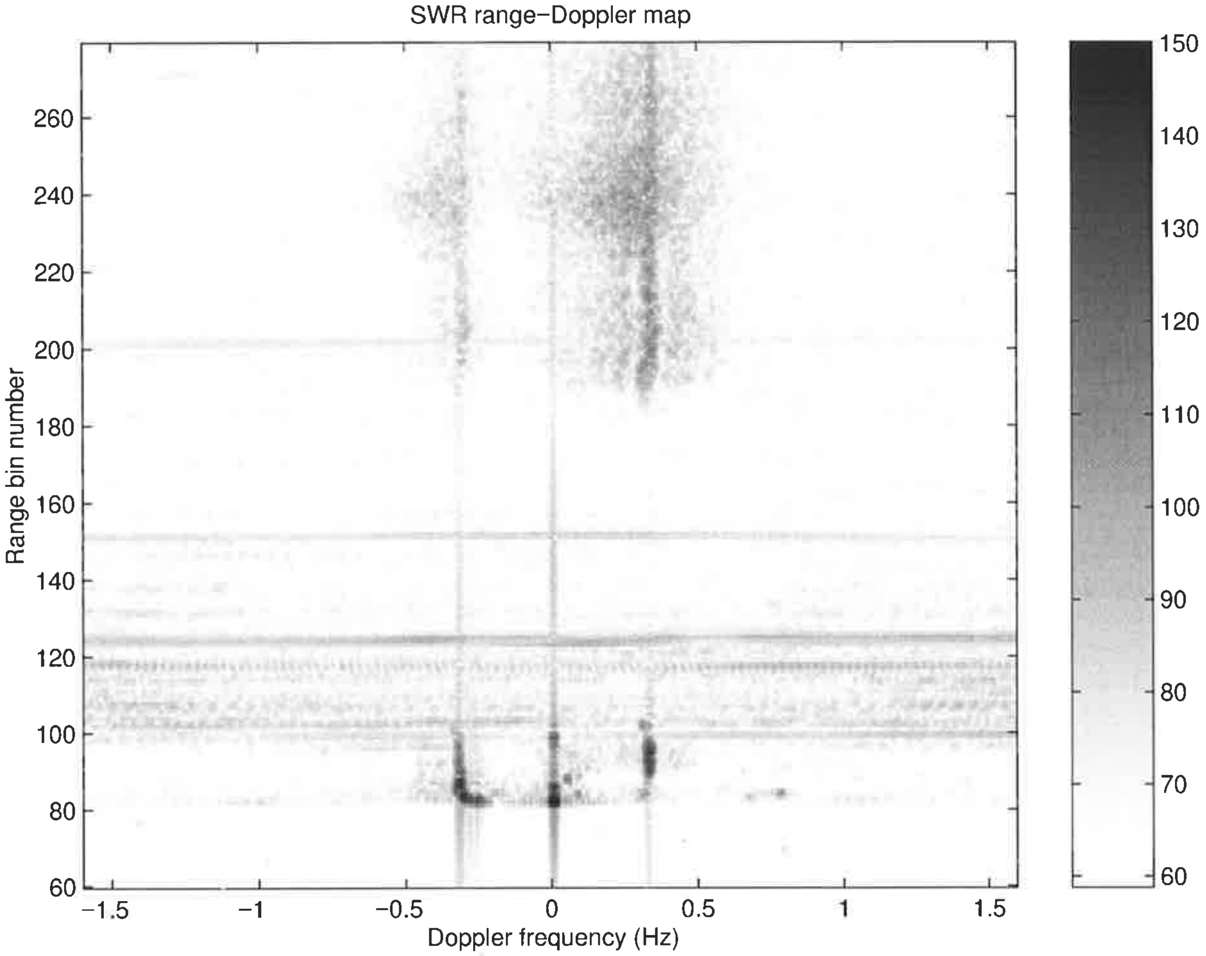

Figure 1.2: Example of surface-wave radar data.

from the transmitter. The pair of returns either side of the ground returns are sea-clutter returns (known as Bragg-lines). Both ground and sea-clutter returns appear in certain range bins (90-100) since both land and sea are present at these ranges, in the radar's coverage. Note the surface-wave returns are cleaner (less spread in Doppler) than the skywave returns. In figure 1.2 the horizontal lines in range bins 100-125, 152 and 202, are scattered returns from meteor trails, which are highly Doppler-spread.

The surface-wave radars currently being proposed have receiving antenna arrays that can be erected quickly, with minimal site preparation, and are designed to be easily relocated. Due to rapid deployment of these receiving arrays, individual antennas in the array may not be in their exact designed locations, and hence antenna position errors may be present. Further due to the simple and cost-effective design of these antennas, mutual coupling between antenna elements is expected to be significant. These imperfections will effect signal processing for the new generation radar systems, and hence this issue must be studied. The effect of these imperfections on radar array processing and means for estimating/correcting these imperfections, known as array calibration, form the basis for the work described in this thesis.

The main issues that need to be addressed in this thesis are as follows :

- the effect of the imperfections (or model errors) on radar performance has to be determined. Radar performance measures which are most affected need to be identified;
- sources which are suitable for performing array calibration, have to be determined. The sources used could be either special sources or sources of opportunity, the latter sources being preferred. Characteristics of these calibration sources, which relate to array calibration, have to be determined;
- signal processing techniques for estimating (and correcting) the imperfections, using the calibration sources, have to be developed. The algorithms developed must exploit the characteristics of the sources, and the performance of the algorithms need to be established. The time duration for performing array calibration is not very important, since it will only need to be performed about once a day (when mutual coupling varies due to ground conditions varying).

## 1.2 Outline of Thesis and Main Contributions

In **chapter 2**, background material on array processing is presented, a description of areas of research which involve array calibration is given, and previous techniques used for array calibration which are relevant for OTH radars are outlined.

In **chapter 3** an analysis of the effect of gain/phase errors, sensor position errors and mutual coupling on radar performance, is conducted. The degradation in signal-to-noise ratio, bearing estimation and sidelobe levels, are given directly in terms of the standard deviation of these errors. Further, the effect of these model errors on array processing in a non-stationary interference environment, is investigated. **The main contributions were : (a) obtaining the performance degradations in terms of the model error standard deviations; (b) showing that model errors could degrade target detectability in the HF radar scenario.**

In **chapter 4** an array calibration algorithm is developed for estimating sensor position errors and mutual coupling using *disjoint* (single-mode) sources. In this thesis, *disjoint* sources refers to those which do not occupy both the same time snapshots and the same radar range cells; meteor trail echoes being a typical example of such sources (see chapter 7). The performance of the algorithm developed is investigated in detail using simulations. **The main contribution was developing an array calibration algorithm, for utilising echoes from meteor trails, to estimate sensor position errors and mutual coupling.**

In **chapter 5** an array calibration algorithm is developed for estimating sensor position errors and mutual coupling, using *disparate* sources. The concept of *cluster* is used in this chapter, to denote any collection of sources which all occupy both the same time snapshots and the same radar range cells (i.e. are overlapped or non-disjoint). The algorithm developed in this chapter can use the sources, present in different disjoint clusters, to estimate the unknown parameters (note the problem considered in chapter 4 is a special case of that considered here). This algorithm can use the following *disparate* sources : multimode and near-field sources (in addition to single-mode sources), and sources with either time-varying or time-invariant bearings; the bearing of each source being either known or unknown. The algorithm's performance is investigated in detail using simulations. **The main contribution was the development of an array calibration algorithm, for using disparate sources, to estimate sensor position errors and mutual coupling.**

In **chapter 6** theoretical performance bounds for the array calibration problems considered in both chapter 4 and 5 are determined, and the algorithms' performances are compared to the bounds. The bounds are also analysed to investigate their variation with signal-to-noise ratio, number of snapshots, number of sources, etc. **The main contribution was the determination of the Cramer-Rao lower bounds for the array calibration problems considered in chapter 4 and 5.**

In **chapter 7** sources present in the HF environment, and their applicability for array calibration, is discussed. It will be shown that echoes from meteors could be used as planewave sources of opportunity, for OTH radar array calibration. The properties of these echoes, investigated using the Jindalee OTH radar array, are discussed (note while the temporal properties of meteor echoes have been investigated in the past, the spatial properties have essentially not been studied). Also in this chapter, array calibration is performed on the Jindalee radar array, using echoes from meteors; results obtained being presented to illustrate the success achieved. **The main contributions were showing that the spatial properties of meteor head and trail echoes allow them to be used for OTH radar array calibration, and demonstrating that meteor trail echoes can be used to calibrate the amplitude and phase errors in the Jindalee radar's receiving array.**

In the **appendices**, array weighting required to obtain minimum sidelobe levels, a theoretical analysis of the Cramer-Rao lower bound for the mutual coupling estimation problem, and error surface theoretical expressions, are given. **The main contributions were obtaining both the identifiability conditions and theoretical Cramer-Rao lower bound variance expressions, in the mutual coupling only estimation problem.**

# CHAPTER 2

# Background Array Processing and Array Calibration

In this chapter some background material is presented for the chapters that follow. In section 2.1 array processing theory, relevant to OTH radars and array calibration algorithms, is presented. To motivate the reader, in section 2.2 a description of areas where array calibration has been performed is given. In section 2.3 existing array calibration techniques that relate to OTH radar array calibration are reviewed. The chapter ends with a discussion in section 2.4.

## 2.1 Array Processing Background

Array processing involves the use of sampled data from an array of sensors for the detection and localisation of targets. In the case of radars, a signal is transmitted and scattered returns/signals received by an antenna array, are processed.

The output of the $m$th sensor (antenna), when $N$ signals impinge the radar receiving array, is

$$z_m(t) = \sum_{n=1}^{N} s_n(t - \tau_{mn}) + n_m(t) \tag{2.1}$$

where $s_n(t)$ is the baseband waveform of the $n$th signal received, and the additive noise $n_m(t)$ is either receiver noise or noise external to the array. The time delay $\tau_{mn}$, in the case of a two-dimensional planar (or nominally linear) array, for planewave signals is

$$\tau_{mn} = (x_m \sin\theta_n + y_m \cos\theta_n)/v \tag{2.2}$$

where $x_m$ and $y_m$ are the $x$ and $y$ coordinates of the $m$th sensor, and $v$ is the speed of light

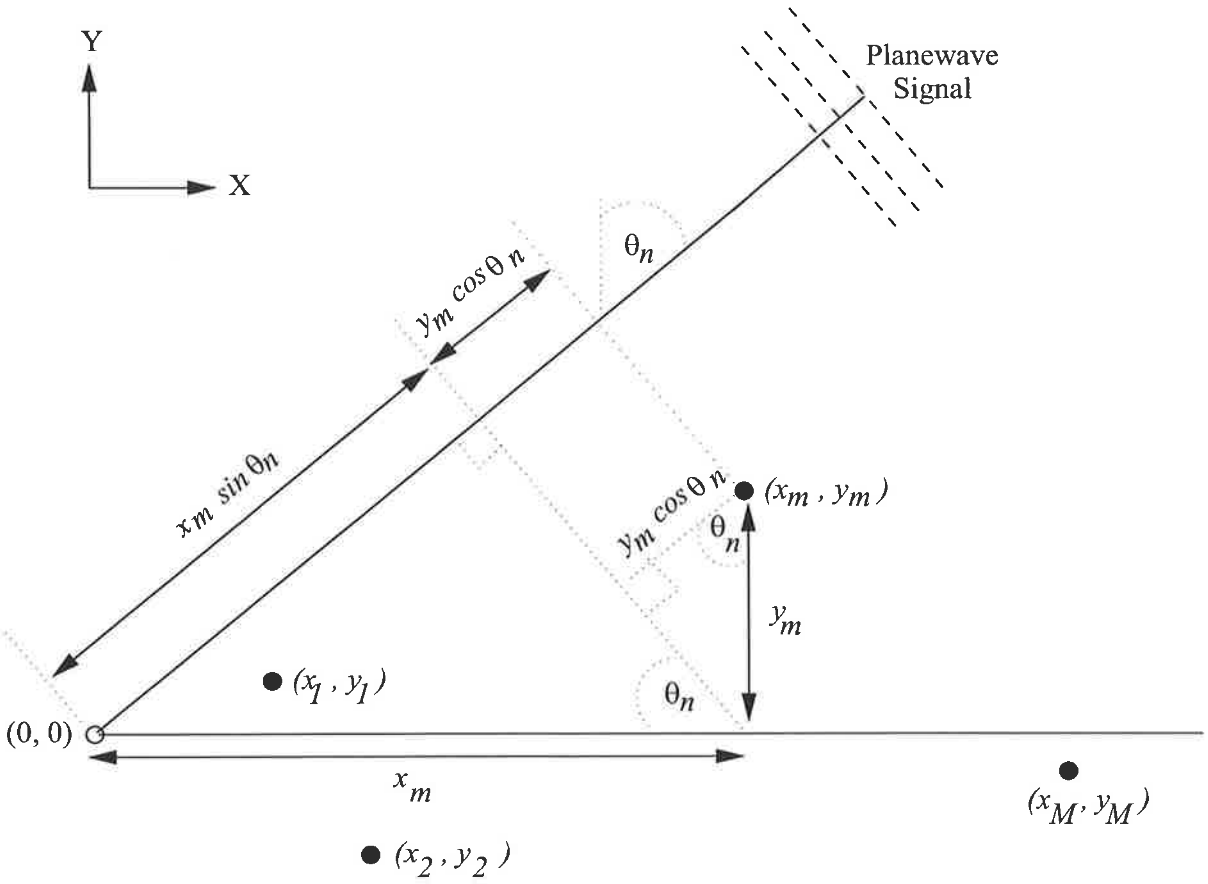

Figure 2.1: Planewave signal impinging an array of sensors.

in free space. The parameter $\theta_n$ is the bearing of the $n$th signal, and is often called the signal's direction-of-arrival (DOA) or azimuth (the elevation angle is assumed to be small and is hence ignored). Here $\theta_n$ is specified with respect to broadside (i.e. the direction orthogonal to the array), and end-fire directions (i.e. both the directions along the array) correspond to $\theta_n = \pm 90^\circ$. Note $\tau_{mn}$ contains sensor location information, and $\tau_{mn}$ is defined as the time delay with respect to the position $(x, y) = (0, 0)$ as shown in figure 2.1.

Now consider narrowband signals. In array processing a narrowband signal is defined as a signal which has a bandwidth much smaller than the reciprocal of the propagation time for the signal wavefront to travel across the array. For the case of narrowband signals, the output of the $m$th sensor is

$$z_m(t) = \sum_{n=1}^{N} s_n(t) e^{jw\tau_{mn}} + n_m(t) \tag{2.3}$$

where $w$ is the radar's operating frequency and $j$ is the complex operator.

Now consider an array of $M$ identical sensors. The vector of $M$ sensor outputs is

$$\mathbf{z}(t) = \sum_{n=1}^{N} \mathbf{a}(\theta_n) s_n(t) + \mathbf{n}(t) \tag{2.4}$$

where $\mathbf{z}(t) = [z_1(t), z_2(t), ..., z_M(t)]^T$, $\mathbf{n}(t) = [n_1(t), n_2(t), ..., n_M(t)]^T$, and the array steering vector

$$\mathbf{a}(\theta_n) = [e^{jw\tau_{1n}}, e^{jw\tau_{2n}}, ..., e^{jw\tau_{Mn}}]^T \tag{2.5}$$

Equation (2.4) can be written compactly as

$$\mathbf{z}(t) = \mathbf{A}\mathbf{s}(t) + \mathbf{n}(t) \tag{2.6}$$

where $\mathbf{A} = [\mathbf{a}(\theta_1), \mathbf{a}(\theta_2), ..., \mathbf{a}(\theta_N)]$ and $\mathbf{s}(t) = [s_1(t), s_2(t), ..., s_N(t)]^T$. The "array manifold" is the locus of $\{\mathbf{a}(\theta) : \forall\theta\}$, which is a closed curve for a linear array but in general is a surface.

Array processing for Gaussian signals usually involves the second order statistics of the received data, which is obtained by determining the spatial covariance matrix of the received signals. (Note the spatial covariance matrix is often referred to as the cross-spectral matrix, since for narrowband signals they are effectively equivalent). The spatial covariance matrix of the received data, assuming zero mean noise, is

$$\begin{aligned} \mathbf{R} &= E\{\mathbf{z}(t)\mathbf{z}^H(t)\} && (2.7) \\ &= \mathbf{A}E\{\mathbf{s}(t)\mathbf{s}^H(t)\}\mathbf{A}^H + E\{\mathbf{n}(t)\mathbf{n}^H(t)\} && (2.8) \\ &= \mathbf{APA}^H + \mathbf{Q} && (2.9) \end{aligned}$$

where $E\{\}$ is the statistical expectation operator. It has been assumed here that the signals are uncorrelated with the noise, and so $E\{\mathbf{n}(t)\mathbf{s}^H(t)\} = 0$. The $M$x$M$ spatial covariance matrix is Hermitian (i.e. $\mathbf{R}^H = \mathbf{R}$), and for the case of a uniformly spaced linear array (and diagonal $\mathbf{P}$) $\mathbf{R}$ is Toeplitz (all elements along any diagonal are equal). The signal covariance matrix $\mathbf{P}$ and the noise covariance matrix $\mathbf{Q}$ are

$$\begin{aligned} \mathbf{P} &= E\{\mathbf{s}(t)\mathbf{s}^H(t)\} && (2.10) \\ \mathbf{Q} &= E\{\mathbf{n}(t)\mathbf{n}^H(t)\} && (2.11) \end{aligned}$$

The signal covariance matrix is diagonal when all the signals are uncorrelated, and is non-diagonal when correlated (multipath) signals are present. In the case of some/all signal(s) being coherent (fully correlated) with other signal(s), matrix $\mathbf{P}$ is rank-deficient and hence singular.

When the noise is only made up of receiver noise, it is usually assumed that the noise is complex Gaussian distributed, stationary, uncorrelated between receivers ($E\{n_m(t)n_k^*(t)\} = 0$ for $m \neq k$) and has common variance $\sigma_N^2$. This is referred to as spatially white noise, and for this case the noise covariance matrix is

$$\mathbf{Q} = \sigma_N^2 \mathbf{I}_M \tag{2.12}$$

For external noise signals, the noise may not be spatially white, and hence the data is usually "prewhitened"; that is the vector of receiver outputs is multiplied by $\mathbf{Q}^{-1/2}$ before any array processing is performed.

Array processing often involves the "eigendecomposition" of the spatial covariance matrix, where the spatial covariance matrix is expressed as

$$\mathbf{R} = \mathbf{A}\mathbf{P}\mathbf{A}^H + \sigma_N^2 \mathbf{I}_M = \mathbf{V}\mathbf{\Lambda}_\lambda \mathbf{V}^H = \sum_{m=1}^{M} \lambda_m \mathbf{v}_m \mathbf{v}_m^H \tag{2.13}$$

where $\mathbf{V}$ is a $M$x$M$ unitary matrix of linearly independent columns, with each column $\mathbf{v}_m$ (a unit norm vector) called an "eigenvector" of $\mathbf{R}$. The $M$x$M$ diagonal matrix $\mathbf{\Lambda}_\lambda = diag\{\lambda_1, \lambda_2, ..., \lambda_M\}$ contains the real "eigenvalues" of the covariance matrix, and are ordered so that $\lambda_1 \geq \lambda_2 \geq ... \geq \lambda_M \geq 0$. The smallest $M - N$ eigenvalues, called "noise eigenvalues", are equal to $\sigma_N^2$; their corresponding $M - N$ eigenvectors are called "noise eigenvectors". The $N$ largest eigenvalues are called "signal eigenvalues", and their corresponding $N$ eigenvectors are called "signal eigenvectors". The signal eigenvectors span the range space of $\mathbf{A}$, while the noise eigenvectors are orthogonal to $\mathbf{A}$ and so span the nullspace of $\mathbf{A}$. The vector $\mathbf{v}_1$ is referred to as the principal eigenvector of $\mathbf{R}$.

The spatial covariance matrix is sometimes expressed as

$$\mathbf{R} = \mathbf{E}\mathbf{\Lambda}_{\lambda_s}\mathbf{E}^H + \mathbf{U}\mathbf{\Lambda}_{\lambda_n}\mathbf{U}^H \tag{2.14}$$

where the "signal subspace" $\mathbf{E} = [\mathbf{v}_1, \mathbf{v}_2, ..., \mathbf{v}_N]$, and the so called "noise subspace" $\mathbf{U} = [\mathbf{v}_{N+1}, \mathbf{v}_{N+2}, ..., \mathbf{v}_M]$. The diagonal matrix $\mathbf{\Lambda}_{\lambda_s}$ contains the signal eigenvalues, and the diagonal matrix $\mathbf{\Lambda}_{\lambda_n}$ contains the noise eigenvalues.

Thus far it has been assumed that the exact covariance matrix can be estimated via an infinite number of array snapshots. In practice the covariance matrix must be estimated from a finite number of snapshots $T$, and is usually estimated as

$$\hat{\mathbf{R}} = \frac{1}{T}\sum_{t=1}^{T} \mathbf{z}(t)\mathbf{z}^{H}(t) \tag{2.15}$$

where $\hat{\mathbf{R}}$ is called the sample covariance matrix. The eigendecomposition of $\hat{\mathbf{R}}$ gives

$$\hat{\mathbf{R}} = \hat{\mathbf{E}}\hat{\mathbf{\Lambda}}_{\lambda_s}\hat{\mathbf{E}}^{H} + \hat{\mathbf{U}}\hat{\mathbf{\Lambda}}_{\lambda_n}\hat{\mathbf{U}}^{H} \tag{2.16}$$

where $\hat{\mathbf{E}}$ and $\hat{\mathbf{U}}$ are the estimated subspaces, and the diagonal matrices $\hat{\mathbf{\Lambda}}_{\lambda_s}$ and $\hat{\mathbf{\Lambda}}_{\lambda_n}$ contain the estimated signal and noise eigenvalues respectively.

Note the number of signals $N$ has often to be known before localisation of targets can be performed. Techniques for estimating $N$ exist in the literature (see for example [6, 245, 239, 247, 242]). The number of signals must be less than the number of sensors $M$.

Now some of the methods used for bearing estimation are outlined. These methods were developed for passive sonar array processing, and while they are not necessarily applicable (especially subspace methods) for OTH radar target detection/localisation, they are described here since they have been (and can be) exploited in array calibration methods for sonars, radars, etc. First the maximum likelihood method, which is the “optimal” method, is described. Then beamforming methods and subspace methods, which are computationally more attractive techniques, are discussed. Note the spatial covariance matrix contains information about the signal bearings, and these methods use the covariance matrix in different ways to estimate the signal bearings. For convenience, hereafter the spatial covariance matrix will be simply referred to as the “covariance matrix”.

### *2.1.1 Maximum Likelihood Method*

The Maximum Likelihood (ML) method [212, 214] is derived from the likelihood function of the observation data probability density function, and is an optimal method for bearing estimation. The deterministic maximum likelihood (DML) method assumes the signals are deterministic and unknown, while the stochastic maximum likelihood (SML) method models the signals as Gaussian random processes. The DML method’s estimates of the signal bearings are obtained at the minimum of

$$p_{dml}(\theta) = trace\{[\mathbf{I} - \mathbf{A}(\mathbf{A}^H\mathbf{A})^{-1}\mathbf{A}^H]\hat{\mathbf{R}}\} \tag{2.17}$$

where $trace\{\}$ is the trace operator. Optimisation techniques for obtaining the minimum have been proposed in [21, 54, 278, 187], but are computationally expensive and do not guarantee global convergence. Since the ML methods require computationally expensive optimisation procedures, they have not been used widely, and suboptimal methods have instead been used. Instead of the ML methods, which require an $N$-dimensional search, methods which use a one-dimensional search have been often employed.

### 2.1.2 Beamformers

Beamforming involves the "steering" of a beam, to obtain a spatial spectrum from which the signal bearings can be estimated. The direction(s) in which the power output of a beamformer are at a maximum, are interpreted as the signal bearings. The beamformer's output is

$$\tilde{z}_\theta(t) = \mathbf{w}^H(\theta)\mathbf{z}(t) \tag{2.18}$$

where $\theta$ is known as the steer direction and $\mathbf{w}(\theta)$ is the processor's weights for forming a beam in direction $\theta$. The output power of the beamformer is

$$p(\theta) = \frac{1}{T}\sum_{t=1}^{T} \|\tilde{z}_\theta(t)\|^2 = \frac{1}{T}\sum_{t=1}^{T} \mathbf{w}^H(\theta)\mathbf{z}(t)\mathbf{z}^H(t)\mathbf{w}(\theta) = \mathbf{w}^H(\theta)\,\hat{\mathbf{R}}\,\mathbf{w}(\theta) \tag{2.19}$$

assuming $\mathbf{w}(\theta)$ is the same for $t = 1, 2, ..., T$.

The array beampattern for the steer direction $\theta$, is the power output of the beamformer for a unit amplitude signal in direction $\phi$. It is defined as

$$B_\theta(\phi) = \|\mathbf{w}^H(\theta)\mathbf{a}(\phi)\|^2 = \mathbf{w}^H(\theta)\mathbf{a}(\phi)\mathbf{a}^H(\phi)\mathbf{w}(\theta) \tag{2.20}$$

The beampattern is usually displayed as a function of $\phi$, and illustrates the relative contributions equal magnitude signals from different directions make.

The conventional (Bartlett) beamformer/processor is analogous to the classical Fourier-based spectrum estimator for time-series data. This beamformer maximises the output power in the steer direction. This processor's data-independent weights are

$$\mathbf{w}(\theta) = \frac{\mathbf{a}(\theta)}{M} \tag{2.21}$$

The beamformer output is then

$$p_{con}(\theta) = \frac{\mathbf{a}^H(\theta)\,\hat{\mathbf{R}}\,\mathbf{a}(\theta)}{M^2} \tag{2.22}$$

If the signals are well separated, $p_{con}(\theta)$ will have peaks close to the signal bearings. This beamformer has the same resolution limitation as the Fourier-based estimator for time series data, and is not able to resolve closely spaced signals. This beamformer cannot resolve signals closer than $2\pi/M$ radians.

The minimum variance distorsionless response (MVDR) processor [25], also called the Capon processor and the adaptive processor, provides better resolution. This beamformer minimises the output power, while fixing the output in the steer direction using the linear constraint

$$\mathbf{w}^H(\theta)\mathbf{a}(\theta) = 1 \tag{2.23}$$

The data-dependent weights for this processor can be obtained using Lagrange multipliers, and are

$$\mathbf{w}(\theta) = \frac{\hat{\mathbf{R}}^{-1}\,\mathbf{a}(\theta)}{\mathbf{a}^H(\theta)\hat{\mathbf{R}}^{-1}\,\mathbf{a}(\theta)} \tag{2.24}$$

The beamformer output is then

$$p_{mvdr}(\theta) = \frac{1}{\mathbf{a}^H(\theta)\hat{\mathbf{R}}^{-1}\mathbf{a}(\theta)} \tag{2.25}$$

When noise-only data can be measured, different weights for this processor can be obtained by using the estimated noise-only covariance matrix $\hat{\mathbf{Q}}$ in equation (2.24), instead of $\hat{\mathbf{R}}$. The bearing estimates of the MVDR processor, unlike the ML method, do not converge to the true signal bearings when the number of snapshots alone approach infinity.

The MVDR processor has been widely used in array processing, and is the most appropriate for OTH radar array processing. This processor is capable of rejecting interference signals, estimated in $\hat{\mathbf{R}}$ or $\hat{\mathbf{Q}}$, by using the data specific (adaptive) weights. While the resolution of the MVDR processor may not be as good as the ML method and subspace methods (to be described next), bearing resolution is not of great importance for OTH radars; since multiple targets can often be separated by their different Doppler and/or range. The MVDR processor is more robust than the ML methods to model errors.

### 2.1.3 Subspace Methods

Subspace methods, also called eigenstructure methods and high-resolution methods, use the eigenstructure of the covariance matrix and its properties, to estimate the bearings of the signals. These methods are based on the fact that the signal subspace and the array manifold intersect at locations corresponding to the bearings of the signals. Subspace methods have resolution that is not limited by the aperture of the array, or in principal by the signal-to-noise ratio, when the number of snapshots or signal-to-noise ratio are large. Subspace methods originated from Pisarenko's method [158].

The MUltiple SIgnal Classification (MUSIC) algorithm [178, 179, 19] uses the property that the noise subspace $\mathbf{U}$ is orthogonal to the array manifold at the true signal bearings (for uncorrelated signals) and uses an orthogonality measure to determine the signal bearings. The MUSIC algorithm (inverse of orthogonality measure) is

$$p_{music}(\theta) = \frac{1}{||\hat{\mathbf{U}}^H \mathbf{a}(\theta)||^2} = \frac{1}{\mathbf{a}^H(\theta)\hat{\mathbf{U}}\hat{\mathbf{U}}^H \mathbf{a}(\theta)} \tag{2.26}$$

where bearings corresponding to the peaks are the signal bearings. The peak values of the MUSIC algorithm are not the signal powers, and hence after the signal bearings have been estimated other techniques have to be used to determine the signal powers. The MUSIC algorithm has been shown to perform like the ML method (i.e. "optimally") when the number of snapshots (and signal-to-noise ratio) are large and the signals are uncorrelated [212].

While the MUSIC algorithm provides better resolution than beamforming methods, it fails to resolve closely spaced signals when the number of snapshots and the signal-to-noise ratio are small. Further, the resolving ability of the MUSIC algorithm is seriously affected when signals are highly correlated [212]. Note when the signals are coherent, the noise subspace is not orthogonal to the array manifold at the true bearings, and hence MUSIC provides peaks at incorrect bearings. Spatial smoothing techniques have been proposed in the literature [50, 186, 255, 157, 44, 246] for overcoming this signal correlation problem, but they are only applicable for certain array configurations.

The Weighted MUSIC algorithm is a modification of the standard MUSIC algorithm, proposed as an improvement over MUSIC. The algorithm involves the maximisation of

$$p_{wmusic}(\theta) = \frac{1}{\mathbf{a}^H(\theta)\hat{\mathbf{U}}\mathbf{W}\hat{\mathbf{U}}^H\mathbf{a}(\theta)} \tag{2.27}$$

where $\mathbf{W}$ is a weighting matrix which is used to weight the relative contributions of the eigenvectors. Note if $\mathbf{W} = \mathbf{I}$, the algorithm simplifies to the MUSIC algorithm. While the best asymptotic properties have been shown to occur for $\mathbf{W} = \mathbf{I}$ (i.e. MUSIC), alternate weighting may result in better performance when the number of snapshots is small and when the signals are highly correlated [214]. The Minimum Norm method [164, 114] is an example of Weighted MUSIC.

The Root-MUSIC algorithm involves the solution of polynomial equations, to obtain estimates for the signal bearings [17]. These polynomial equations are in terms of the noise eigenvectors, and are only applicable for uniform linear arrays. The Root-MUSIC algorithm has the same asymptotic properties as the MUSIC algorithm, but performs better than MUSIC when only a limited number of snapshots are available [113].

The Estimation of Signal Parameters via Rotational Invariance Techniques (ESPRIT) algorithm, is valid for an array with two identical subarrays which are physically displaced by a known displacement [154, 174]. ESPRIT estimates the displacement matrix relating the subspaces of the subarrays, and then the signal bearings are determined from this displacement matrix. LS-ESPRIT estimates the displacement matrix using least-squares, while TLS-ESPRIT uses total least squares. LS-ESPRIT and TLS-ESPRIT have the same asymptotic properties, but TLS-ESPRIT performs better for limited number of snapshots [113]. ESPRIT is computationally more efficient than the MUSIC algorithm.

While beamformers and subspace methods discussed above provide computationally efficient estimates of the signal bearings, as mentioned earlier, they do not perform adequately when the number of snapshots is small or when the signals are highly correlated or coherent. Parametric subspace methods have recently been proposed which have the same statistical performance as the ML method (and work with limited snapshots and coherent signals), while being computationally more efficient than the ML method. These methods are called “subspace fitting” methods.

One of these methods, known as the Weighted Subspace Fitting (WSF) method [227, 228, 229], estimates the signal bearings by minimising

$$p_{wsf}(\theta) = trace\{[\mathbf{I} - \mathbf{A}(\mathbf{A}^H\mathbf{A})^{-1}\mathbf{A}^H]\hat{\mathbf{E}}\mathbf{W}\hat{\mathbf{E}}\} \tag{2.28}$$

where $\mathbf{W} = (\hat{\mathbf{\Lambda}}_{\lambda_s} - \hat{\sigma}_N^2 I)^2 \hat{\mathbf{\Lambda}}_{\lambda_s}^{-1}$, and $\hat{\sigma}_N^2$ may be obtained by averaging the noise eigenvalues. Another parametric subspace method is the Method Of Direction Estimation (MODE) algorithm, developed in [215, 216]. Its performance is at least as good as the ML method for both uncorrelated and correlated signals [216, 213].

## 2.2 Array Calibration Application Areas

The problem of array calibration, for improving the detection of targets or for the enhancement of images, has been considered in a number of different fields. Array calibration has been considered for telescope imaging, microwave radars, airborne radars, synthetic aperture radars, passive sonar towed arrays, synthetic aperture sonar imaging systems, multiple camera systems, ultrasound arrays and microphone arrays. In this section, to motivate the reader, application areas of array calibration will be outlined, while in the next section specific array calibration methods in the literature which are relevant to this thesis are reviewed.

### *2.2.1 Telescope Images*

The quality of telescope images are limited primarily by atmospheric distortion, which is mainly due to random phase variations of incoming light over the aperture of the telescope. The effect of this phase variation, or wavefront distortion, is to worsen the resolution of the telescope images, and hence limit the detail in the image.

Muller and Buffington proposed a technique [135] which uses an optical phase shifter to shift the effective phase of the light by varying amounts along the aperture of the telescope. Their technique determines the required phase shifts from the light of the actual reference object being observed, rather than from other close by objects. By defining image sharpness measures, and maximising one of these measures, they were able to determine appropriate phase corrections for removing image distortion.

Post-processing techniques on the image, and hybrid techniques which use both post-processing and pre-correction optics, have also been proposed in the literature. For example techniques using wavefront sensor measurements to determine the aberration, and then correcting in real-time the atmospheric distortion with adaptive optics have been used [172, 188]

Closure phase, which is a measured number that is independent of instrumental (phase) errors, has been exploited by automatic methods (called self-calibration) to obtain high-resolution images [33]. Atmospheric distortion is also overcome by these methods.

Radio telescope array outputs are also affected by atmospheric distortion and need phase compensation [48, 123]. For these systems phase compensation is performed digitally.

### 2.2.2 General Antenna Arrays

Antenna array performance are affected by non-identical antenna patterns, receiver mismatch, errors in antenna positions, mutual coupling, etc. Antenna arrays have been calibrated via many methods :

- internal calibration has been used in [207, 155] to calibrate amplitude and phase variations using calibration loops;
- calibration has been achieved by using measured antenna patterns in [14];
- external sources have been used for array calibration in [40, 41];
- external sources of opportunity were used in [152] to calibrate receiver phase errors. A radio star was used as the source of known position, which progresses through the radar's beams as the earth rotates.

Ground-based microwave radar arrays have been used for high resolution aircraft imaging [208], where the high resolution images need to be of sufficient quality for aircraft target recognition. Imperfections, such as antenna placement errors and receiver mismatch, degrade the images, and hence diffraction-limited image quality is not achieved. Calibration techniques for improving the image quality, using point sources in the form of reflectors (passive sources) or beacons (active sources), have been discussed in [210] to overcome distorted arrays. Techniques using multiple scatterers have been discussed in [106], while clutter returns have been used for calibrating narrow beamwidth microwave radars in [11].

### 2.2.3 Airborne Radar

Airborne antennas (in an array) may have different patterns, so calibration is required to enable high-resolution localisation of targets in space-time adaptive processing (STAP) systems. In [112, 167] a method has been proposed which uses the ground clutter to perform this calibration. The method is based on the fact that the ground returns in different Doppler bins, are from distinct azimuths. Hence the array spatial information at each azimuth can be obtained independently from that of other azimuths.

Antenna arrays mounted on the belly of aircraft, used for communication, have been considered in [130, 88]. These direction-finding arrays, usually calibrated in special calibration flights, have antenna gain and phase mismatches, antenna position errors, and are in the presence of near-field scatterers which effect performance. In [130] a method is proposed for calibrating such arrays over multiple elevation angles simultaneously using geographically separated multiple cooperative, co-channel sources.

### 2.2.4 *Synthetic Aperture Radar*

Synthetic Aperture Radar (SAR) is used for remote sensing and reconnaissance, providing high resolution images by synthesising an increased aperture (synthetic aperture). The increased effective aperture is obtained by processing data, coherently received at equally spaced intervals, as the aircraft travels in a straight line at a uniform speed. In practice however the aircraft deviates from a straight line path (vertically and laterally) and may have non-uniform speed, hence the SAR images are degraded. Further, atmospheric propagation can also degrade the images. Various methods have been proposed to improve SAR images [145].

Motion compensation techniques have been developed to measure sensor platform motion, using accelerometer and inertial units, and then the received signals phase corrected to give higher quality images [134].

Post-processing of images using autofocusing techniques have also been used widely. Techniques such as map drift, contrast optimisation, and shift-and-correlate have been used for SAR image enhancement [36, 47]. Both point and extended objects have been used for performing autofocusing. These techniques not only overcome the image degradation due to aircraft path deviation, but also that due to atmospheric propagation.

For quantitative interpretation of SAR images, airborne SAR are often calibrated using corner reflectors [176] while spaceborne SAR are calibrated using active radar calibration units [102] (in addition to corner reflectors).

Inverse synthetic aperture radar (ISAR), which uses the motion of the target being imaged to synthesise an aperture, requires precise motion compensation to obtain high quality images of manoeuvering targets. Autofocusing techniques for ISAR, using single or multiple scatterers to calibrate phase errors, have been proposed [248].

### 2.2.5 *Passive Sonar Towed Arrays*

Passive sonar hydrophone arrays are used to detect acoustic sources in underwater environments. These flexible arrays are often deformed due to course fluctuations, underwater currents, swells, etc. When the array shape deviates, the performance of the sonar degrades, and array shape estimation is required in order to limit the performance degradation.

Techniques which use data only from the hyrophones for shape estimation have been proposed in [149, 82, 58, 235, 196], while techniques which use non-acoustic sensors (compasses, depth sensors) for shape estimation have been been proposed in [150, 95, 84].

### 2.2.6 Sonar Imaging Systems

Sonar imaging systems contain a transducer array which both transmits and receives acoustic energy in an ocean. A pulse is transmitted, and surface reverberation scatters some energy back to be received by the transducer which then converts the pressure waves into electrical signals.

Sources of calibration errors in sonar imaging systems are the non-ideal response of the receivers (range dependent magnitude and phase errors), array misalignment, reflections from the hull and other reflectors, etc. Calibration is performed using cross correlation [42] or using a calibrated transducer [75], for example.

### 2.2.7 Synthetic Aperture Sonar Imaging Systems

Synthetic Aperture Sonar (SAS) imaging systems use SAR techniques to increase the effective aperture of the sonar array, hence obtaining better cross-range resolution. Coherent data is collected as the sonar moves along a straight path, resulting in the increased effective aperture.

However since a towed array may not follow a straight path, motion compensation must be performed. Often data from inertial navigation systems are not sufficiently accurate for motion compensation, and so cross-correlation based techniques have been proposed [43]. Also, autofocusing algorithms, originally developed for SAR, have been considered for motion compensation and medium-induced phase fluctuation compensation [100, 61].

### 2.2.8 Computer Vision

Calibration is of key importance in computer vision. Calibration of a moving camera has been considered in [127]. For every displacement, correspondences between at least seven points have to be established, and camera position, orientation and image parameters then calibrated. This method does not require any special object/pattern to perform calibration.

Multi-sensor calibration has been considered for non-moving imagery in vision systems

[62]. Here sensor (camera) orientation, object coordinates and other calibration parameters, are estimated without any knowledge of the object. Multi-sensor calibration of moving imagery, for enabling a mobile robot to navigate in a complex environment, has been considered in [35].

### 2.2.9 Ultrasound Arrays

Ultrasound arrays have been used for imaging patients so cancer diagnosis may be performed. These arrays have had only limited success in detecting low contrast lesions, due to aberrations in tissues (resulting in different acoustic speeds), sensor position errors, etc. An aberration correction method has been proposed in [144], which uses cross-correlation of reflected ultrasound signals. This method works for point reflectors and also diffuse reflectors. Methods using the mean speckle brightness as a measure for reducing phase errors, has been studied [275]. Techniques which compensate for amplitude errors in phase-compensated data, have also been considered [276, 277].

### 2.2.10 Microphone Arrays

Microphone arrays are used for audio, teleconference, hearing aid and voice recognition applications, to enhance the signal-to-noise ratio in noisy environments. A beam is steered towards the source of interest, while background noise and interferers are rejected. Gain/delay mismatches in the array, however reduce performance substantially, and hence must be calibrated [237].

## 2.3 Previous Array Calibration Methods

Array calibration methods that have been proposed in the literature, which are relevant for OTH radars, are now reviewed.

The general assumptions made by array calibration methods are : (a) the signals and noise are stationary over the calibration interval; (b) the number of signals are known (or can be estimated), and have different directions-of-arrival; (c) the signals are not perfectly correlated; (d) the noise covariance matrix is known up to a multiplicative constant; (e) the sensors are not placed along a straight line; (f) there are more sensors than sources; (g) the location of one of the sensors and the direction to another sensor, are known. Further the nominal sensor position values are assumed to be known, and the sensor position errors are assumed to be small compared to the inter-element spacing. The nominal sensor position values are usually used as initial estimates to initiate the algorithms.

### 2.3.1 Methods for Estimating Sensor Positions

Array calibration methods can be divided into two broad categories, depending on the type of sources they use. “Passive” array calibration methods use sources in the data (“sources of opportunity”), and are also known as “self calibrating” methods; the source DOAs are usually unknown. “Active” array calibration methods need special sources with known parameters for array calibration; the source DOAs are usually known.

Array calibration methods usually use only disjoint sources, or only non-disjoint sources. Disjoint sources refer to sources which can all be separated in time or frequency, while non-disjoint sources are sources which are all overlapped in time and frequency (note in chapter 4 and subsequent chapters a different definition will be used for disjoint sources).

Rockah and Schultheiss studied the Cramer-Rao lower bound, for passive array calibration using disjoint sources, in [170, 171, 168]. They showed that when the location of one sensor and the direction to another sensor are known, three sources are sufficient to calibrate for sensor position errors; the calibration accuracy increasing with source strength and observation time. However if the later (direction to another sensor) is unknown, then only array shape can be estimated (angular rotation of the array is unknown and cannot be estimated). If further the location of none of the sensors is known, then not only is the angular rotation of the array unknown, but also an unknown translation of the array exists. The work in these papers are the basis for the assumptions (e) and (g) above. Identifiability issues have also been considered in [118, 122, 60, 80, 31, 194] for different scenarios (e.g. combination of known and unknown DOA sources, three-dimensional arrays, correlated signals, etc).

Ng and Nehorai have analysed the Cramer-Rao lower bound for active array calibration (using non-disjoint sources) in [138, 139]. They showed, for uncorrelated signals, to minimise the Cramer-Rao lower bound the bearing of the calibration sources must be uniformly distributed. The minimum value of the Cramer-Rao lower bound was shown to be inversely proportional to the number of signals and the number of snapshots. In these papers it was suggested that active array calibration is expected to provide better accuracy than passive array calibration. Further it was mentioned, that numerical examples indicated, that the use of uncorrelated calibration signals appear to provide better sensor position estimates, than using correlated signals.

### *Passive Methods*

Rockah and Schultheiss developed a procedure for estimating sensor positions [171], which differs slightly from the maximum likelihood method. A least squares procedure for successive approximations was used to derive an iterative algorithm. The results obtained were shown to be close to the Cramer-Rao lower bound. A minimum of three disjoint sources are required.

Weiss and Friedlander have developed a ML method for estimating sensor positions [250]. The method uses disjoint sources in the data, and is based on an iterative two step procedure. In the first step the signal DOAs of the sources are estimated, using the best available estimates of the sensor positions. In the second step the sensor positions are estimated, using the signal DOAs estimated in the first step. The cost function used is said to converge to either the global or local minimum, depending on how close the nominal sensor positions and initial signal DOAs are to their true values.

Weiss and Friedlander also developed an eigenstructure based method for estimating sensor positions, using non-disjoint sources in the data [251]. The method is based on the fact that the noise subspace (for an estimate of the covariance matrix) is almost orthogonal to the true signal steering vector; the cost function used being a minimum when the signal steering vector is almost orthogonal to the estimated noise subspace. The parameter values at this minimum are the estimated values. The algorithm iterates between two steps : (1) the MUSIC algorithm is used to estimate the signal DOAs, using the last estimate of the sensor positions; (2) a closed form solution that is related to the Gauss-Newton technique is used to estimate the sensor positions, using the last estimate of the signal DOAs. A necessary condition for uniqueness (for the narrowband case) is $2M - 3 + N \leq 2(M - N)N$. While the ML method [250] proposed by these authors provides a solution which is optimal in the maximum likelihood sense, it is expected to typically require more computation than this eigenstructure method.

Lo developed a technique for reducing the array calibration computation time of a ML estimator [120]. He noted that while ML estimators of signal DOAs remove the problem with eigenvector methods when the signal-to-noise ratio (SNR) and/or data record length are small, they require more computation. By the numerical solution of the nonlinear least-squares problem for the ML estimation being replaced by iterating a finite sequence of linear regression formula (known as "cyclic regression"), the computation time was reduced to be less than eigenvector methods. Existing sources in the data are used, and the sources do not have to be non-disjoint. This method also estimates sensor gains and phases, however if these quantities are known, then the steps for estimating them can be simply skipped.

Bucker [24], Ferguson [58] and Goris [80] have worked on methods known as "sharpness methods", for towed array shape estimation. Sharpness methods work on the principal that when the estimated positions of the sensors coincide with their actual positions, the sharpness measure is a maximum. The sharpness measure is calculated by summing, the product of the beam output power squared and the sine of the beamsteer angle, over all beamsteer directions. The shape of the array is synthesised using a harmonic series, which is calculated using Bucker's iterative algorithm [24]. (Note in [80], Goris has also presented least-squares methods for narrowband and broadband sources).

Ng proposed a method for estimating sensor positions in [141], which uses non-disjoint sources in the data. The cost function used is similar to that used by Weiss and Friedlander in [251], but is defined over "DOA regions" rather than at the estimated DOAs of the sources (as in [251]). The cost function is minimised using an exhaustive search over the region of sensor positional uncertainty; the estimated sensor positions being obtained at the minimum.

Hwang and Williams have developed a method for estimating sensor positions using a ML approach in [101]. Their method uses non-disjoint sources of unknown DOAs. The proposed iterative algorithm uses a total least squares (TLS) approach to estimate the source DOAs, and a constrained total least squares (C-TLS) approach to estimate the sensor positions. Hwang and Williams compared their TLS/C-TLS method with a least squares (LS) method, and concluded that generally TLS/C-TLS converges closer to the true values than do LS (but requires more computation).

### *Active Methods*

Dorny developed a method [40, 41] for using a few beacons, of known location, to determine the array sensor positions. The beacons are blinked consecutively (disjoint sources), and the phases of each signal at the sensors compared to a reference sensor. From the comparisons for each beacon, the sensor positions and the relative phase difference between sensors, are determined using a least-squares procedure.

The sensor positions, estimated by this method, were the positions which permit the best focussing of the array in the directions of the beacons. Dorny showed that if the beacons were distributed uniformly over the region of interest, the positions obtained should provide acceptable focussing throughout this region. The gain loss was small for pointing angles within the spread of the beacons, with the loss increasing near the edges of the beacon spread, and becomes large for angles outside the spread. Dorny also looked at the impact of beacon position errors and of phase measurement errors (owing to multipath).

Ng and Nehorai [138, 139] developed two approaches for estimating sensor positions using known DOA non-disjoint sources of known waveform. Iterative Newton-type algorithms for a ML estimator and an eigenstructure-based estimator were proposed. Both methods require at least two sources.

Seymour et. al. developed a method for using known DOA non-disjoint sources [185]. The method is based on minimising the sum of projections of the steering vector (computed using the estimated sensor positions) on the noise subspace for each calibration source. An iterative procedure is obtained using the gradient search algorithm. Results indicated that the final sensor position errors varied inversely with SNR of the calibration sources, and the number of snapshots. At least two sources are required.

Lo and Marple developed an eigenvector method [121] which requires at least two disjoint calibrating sources of known bearing. Covariance Differencing (or Despoking) is used, and it is assumed the signal and noise environment do not change during the calibration period. The principal eigenvector of the Covariance Differencing matrix is used to obtain the sensor positions.

Gray et. al. [82, 59] have developed a method for using the principal eigenvector of the cross-spectral matrix to estimate the sensor positions. A ML estimate of the signal vector is used to determine the phase of the signal at each hydrophone. Gray showed that while a single source of known DOA is insufficient to unambiguously determine the sensor positions, the ambiguities can be removed for towed arrays using constraints. The constraint that the spacing between adjacent sensors, in a towed array, should be equal to a fixed value ("chord" approach) is used. This results in two solutions for each sensor position; the solution which results in the minimum array distortion from the nominal shape is used to obtain the sensor location. Results show that the method works best when the source is at broadside direction and degrades when the source is moved towards end-fire. A computationally more efficient variant of this method has been proposed by Smith et. al. in [195, 196], where the sensors are partitioned into subarrays and the Gray et. al. method used on each subarray. (Note also the Gray et. al. method has been modified for broadband sources in [197]).

Zhang and Zhu have proposed two non-iterative (single-step) methods for estimating sensor positions [271, 272], using sources of known DOAs; the first method uses disjoint sources, while the second method uses non-disjoint sources. In [271] the principal eigenvectors, from each disjoint source's covariance matrix, together with a small perturbation expression are used to obtain equations from which the sensor position errors can be estimated. Three or more principal eigenvectors, and hence sources, are required. Sensor gain/phase errors can also be estimated using this method, after the sensor positions have been estimated, and is performed in a single step too.

In [272], Zhang and Zhu use an approach similar to the eigenstructure method proposed by Weiss and Friedlander in [251], for estimating the sensor positions. The key difference is that Zhang and Zhu use sources with known DOAs, and hence are able to obtain estimates in a single step. Three sources are required.

Yongkang et. al. proposed a method which effectively requires disjoint sources of known DOAs to estimate the sensor positions [267]. Using the phase difference between corresponding elements of each principal eigenvector (of the disjoint sources), equations are obtained for estimating the sensor positions. This non-iterative method requires three or more sources. Gain and phase uncertainties can also be estimated using this method (in a single step), and is performed after the sensor positions have been estimated. Yongkang et. al. mentioned that for an antenna array which rotates not only can a single source be used for obtaining multiple disjoint "effective" sources, but also the "real" source can have unknown DOA since the DOA separation between the "effective" sources can be determined from the platform's angular rotation.

### 2.3.2 Methods for Estimating Mutual Coupling

Weiss and Friedlander developed an eigenstructure based method for estimating a symmetric Toeplitz coupling matrix, using non-disjoint sources in the data [252, 66] (gain/phase errors are also estimated). This method (as in [251]) is based on the fact that the noise subspace (for an estimate of the covariance matrix) is almost orthogonal to the true signal steering vector; the cost function used being a minimum when the signal steering vector is almost orthogonal to the estimated noise subspace. The parameters values at this minimum are the estimated values. The algorithm iterates between three steps : (1) the MUSIC algorithm is used to estimate the signal DOAs, using the last estimate of the coupling matrix and gain/phase values; (2) the gain/phase values are estimated from a quadratic minimisation problem, using the last estimate of the signal DOAs and coupling matrix; (3) a symmetric Toeplitz coupling matrix is estimated from a quadratic minimisation problem, using the last estimates of the signal DOAs and gain/phase values. A necessary condition for uniqueness is that $4M + N \leq 2(M - N)N$. This method has slow convergence and has been shown to provide non-unique solutions for linear arrays [156].

Pierre and Kaveh have developed a method for estimating a non-Toeplitz calibration matrix (mutual coupling and gain/phase errors) using known DOA disjoint calibration sources [156]. The method is based on fitting the principal eigenvectors, of the calibration source covariance matrices, to the ideal steering vector using least-squares. The number of calibration sources required is equal to the number of sensors. A unique calibration matrix is expected from this method.

Zhang and Zhu have developed two eigenvector-based methods [270] for estimating a symmetric Toeplitz coupling matrix, using known DOA calibration sources in addition to the sources in the data. The first method can work with just one calibration source, but the source must be disjoint from the sources in the data. The second method requires at least two calibration sources, however these sources do not have to be disjoint from the sources in the data. Both methods are non-iterative, and provide analytic expressions for the coupling matrix being estimated.

Qiu and Zhu have developed an eigenvector-based method [160] for estimating a symmetric Toeplitz coupling matrix, using a single near-field calibration source with known DOA. The optimum position of the near-field calibration source was shown to be along the line of the array.

Hung has developed a method for estimating a non-Toeplitz coupling matrix [99]. The method uses a movable pilot source (which effectively means disjoint known DOA calibration sources) in the far-field of the array, which circles the array once providing 1440 snapshots (single snapshot every 0.25 degrees). The method is based on fitting the measured sensor outputs to the signal steering vectors, using the coupling matrix.

See generalised the method of Pierre and Kaveh (in [156]) to work with unequal length steering vectors [181]. Like Pierre and Kaveh's method this method is based on fitting the principal eigenvectors, of the calibration source covariance matrices, to the ideal steering vector using least-squares. A non-Toeplitz calibration matrix (mutual coupling and gain/phase errors) is estimated using known DOA disjoint calibration sources. The number of sources must be at least $(M^2)/(M-1)$.

### 2.3.3 Methods for Estimating Sensor Positions and Mutual Coupling

See et. al. in [182, 183, 140, 184] extended their method in [181], for estimating a non-Toeplitz calibration matrix, to estimate sensor positions as well. Array calibration is again performed using a set of measured steering vectors, which are obtained from disjoint calibration sources with known DOAs ([184] allows for a small amount of uncertainty in the DOAs). While an analytic expression is obtained for the calibration matrix, an iterative procedure is required for obtaining the sensor positions (Newton-type algorithm) and the scaling constants (note in [140] the scaling constants are assumed to be known, and hence are not estimated). A necessary condition for a unique solution is that the number of sources must be at least $(M^2 + M - 2)/(M - 2)$. Depending on the initial parameter estimates, it was stated that, the algorithm may converge to a local or global minimum.

### 2.3.4 Other Methods

In addition to the methods described above :

- methods for estimating sensor positions, which are specific to time-varying/towed arrays, have been considered in [93, 20, 125, 224, 15, 165, 234, 84, 162, 71, 259, 72, 73, 57, 78];
- methods which compensate for the effects of mutual coupling using measured array patterns, mutual coupling models or special hardware, have been proposed in [107, 151, 211, 70, 4, 5, 16, 173], while procedures for modifying beamformers/bearing-estimators to incorporate mutual coupling information have been given in [87, 266, 92, 37];
- the use of measured array steering vectors at given directions for beamforming has been considered in [180, 253];
- array calibration methods for estimating direction-independent gain/phase errors have been proposed in [153, 63, 74, 260, 261, 97, 98, 111, 142, 137, 257, 273, 274, 124, 128, 129, 169];
- array calibration methods for estimating direction-dependent gain/phase errors have been proposed in [22, 23, 7, 60];
- array calibration using higher than second-order cumulants, for non-Gaussian signals, have been considered in [39, 258, 244];
- in [27, 28] methods are proposed for bearing estimation using arrays with sensor position errors, but [27] is only applicable for nominally uniform linear arrays while [28] is only applicable for uniform planar arrays;
- robust beamforming methods for working in the presence of model errors have been proposed in [236, 147, 230, 231, 49, 94, 56, 225, 265, 163], as an alternative to performing array calibration.

## 2.4 Discussion

Array processing background, relevant to OTH radars and array calibration, has been presented in section 2.1. Application areas where array calibration has been performed have been outlined in section 2.2 to motivate the reader, while specific methods which are relevant to OTH radar array calibration have been reviewed in section 2.3.

The methods in section 2.3, however, are not suitable for the specific problem considered in this thesis, of estimating both sensor positions and mutual coupling. Only the methods by See et. al. in [182, 183, 140, 184] estimate sensor positions and mutual coupling; these methods however require a large number of far-field special sources (greater than 10 sources for a 8-element array), and thus are not really suitable for calibrating OTH radars. For OTH radar array calibration, it is highly desirable to use as many sources of opportunity, and as few special sources as possible.

In chapter 4 a method is developed for using disjoint sources of opportunity, which are present in the HF environment in the form of echoes from meteor trails, to estimate sensor positions and mutual coupling. This method generalises the work of Weiss and Friedlander in [251, 252, 66]. In chapter 5 a method is developed for using disparate sources, to estimate sensor positions and mutual coupling. This method can use special sources and sources of opportunity, and further can use sources with time-varying DOAs.

# CHAPTER 3

# Effect of Model Errors on Radar Array Processing

Surface-wave radars operate in environments (see figure 1.1) where the propagation conditions for the target/clutter signals (via surface-wave) and interference signals (via skywave), are very different. The interference signals are modulated by the ionosphere, which can result in the interference signals being spatially (and temporally) non-stationary over the radar's coherent integration time (dwell). To overcome this non-stationarity, and reject interferers, time-varying beamformer weights are often used (within the dwell); so the weights can adapt to the interferer's time-varying spatial properties. Time-varying beamformer weights however affect radar Doppler processing, which is performed after beamforming.

Doppler processing involves the processing of returns from several (coherent) radar transmissions, to obtain the Doppler of signals. Doppler can be used to discriminate between targets and clutter returns, the latter occuring near zero Doppler. Doppler processing enhances the target's signal-to-noise ratio and also the clutter-to-noise ratio (or sub-clutter visibility); both measures being indicators of how well the radar can perform in detecting targets.

While the effect of model errors on array processing has been studied for many sonar and radar configurations, the effect on surface-wave radars, especially for the problem described above, have not been considered. In section 3.1 previous work analysing the effect of model errors on array processing is briefly outlined, in section 3.2 the problem description is given, and then in sections 3.3 and 3.4 an analysis is conducted which is specific to surface-wave radars. Finally in section 3.5 the chapter is concluded.

## 3.1 Literature

McDonough analysed the effect of amplitude and phase errors in the data [131]. He considered both the conventional and adaptive processors, and looked at the effect on array power output. He showed that the conventional processor was the least sensitive to the model errors. The sensitivity of the adaptive Capon (MVDR) processor (using the signal-plus-noise covariance matrix) was related to the eigenvalue spread between the smallest and largest eigenvalue of the covariance matrix; the larger the eigenvalue spread, the larger the sensitivity.

In [34] Cox analysed the effect of steering vector mismatch on the performance of the conventional processor, adaptive MVDR processor using the noise-only covariance matrix, and the adaptive MVDR processor using the signal-plus-noise covariance matrix. Cox attributed the steering vector mismatch to amplitude/phase errors, sensor position errors, distortion of wavefront during propagation, sampling or quantisation. He indicated that the conventional processor is insensitive to small mismatch and the MVDR processor, using the noise-only covariance matrix, can be more sensitive (than the conventional processor) if the eigenvalue spread is large. The MVDR processor with the signal used in the covariance matrix was significantly more sensitive to mismatch than the MVDR processor with the noise-only covariance matrix, for large input SNR, due to the adaptivity causing signal suppression in the former processor. The signal suppression that occurs in this MVDR processor can result in less array gain obtained for a strong signal than a weak signal. Cox illustrated how the power output of this processor is less sensitive (than the array gain) to mismatch, since the increase in noise power output partially offsets the reduction in signal output power.

Farrier analysed the effect of amplitude and phase errors, in the array processor, on array gain [52, 53]. He obtained theoretical expressions for the array gain, and showed how the array gain degrades with increasing errors. The results obtained by Cox in [34] were shown to be valid only for small perturbations. Farrier considered both non-adaptive and adaptive (using the signal-plus-noise covariance matrix) beamformers.

Godara in [77] analysed the effect of errors in both the steering vector and the adaptive weights, on the performance of the MVDR processor. He obtained analytic expressions for the output signal power, output noise power and array gain. He found the output signal power and output noise power increase with the size of errors, while the array gain decreases. The array gain degradation of the MVDR processor, with the signal-plus-noise covariance matrix, due to steering vector errors was found to depend on the input signal power (as observed by Cox), but the array gain degradation due to weight vector errors was independent of the input signal power. For the MVDR processor with the noise-only covariance matrix, the array gain degradation was not dependent on the input signal power for both types of errors.

In addition to the above :

- Godara in [76] considered the effect of random phase errors in array phase shifters, and compared the results obtained with those for steering vector errors;
- Vural in [233] analysed the effects of system and medium perturbations on adaptive processors;
- Quazi in [161] analysed the effect of weight errors, phase errors, and antenna element failure;
- Gray in [81] looked at the effect of time-delay errors, in time-delay and sum beamformers, due to sampled receiver outputs;
- Nitzberg in [143] considered the effect of weight computation precision;
- the impact of model errors on average sidelobe levels has been considered in detail by Ruze in [175], while the impact on peak sidelobe levels has been considered by Hsiao in [96]. The impact on sidelobe levels has also been studied in [209, 51, 105, 13];
- the effect of steering vector errors on the signal to interference-plus-noise ratio of the adaptive processor has been considered in [32, 243], while the affect on maximum rejection of interferences has been analysed in [117];
- the effect of sensor position errors on the array pattern has been analysed in [29], while the effect of array platform motion has been investigated in [91];
- the performance of high-resolution DOA estimators in the presence of model errors, has been analysed in [64, 219, 68, 69, 254, 226, 249, 256, 218, 65, 89, 90, 263, 264, 67, 268].

While the above studies have considered a variety of model errors and array processors, none of them have studied the problem as it relates to surface-wave radar array processing, and so this is considered now. The effect of model errors on the performance of the adaptive MVDR processor, when the weights are obtained using the noise-only covariance matrix [1], is studied. Not only are the effects of gain/phase errors (due to receiver gain/phase mismatch) and sensor position errors considered, but also the effects of mutual coupling. Further, the MVDR processor's performance is obtained specifically in terms of the size (standard deviation) of the errors themselves. The effect of the model errors is considered on the following radar performance characteristics :

- array gain;

---

[1] it is assumed the noise-only covariance matrix can be estimated, by using quiet (transmitter off) intervals, or otherwise.

- signal-to-noise ratio (SNR);
- bearing estimation;
- sidelobe levels;
- sub-clutter visibility (clutter-to-noise ratio) for adaptive spatial anti-interference processing.

## 3.2 Description

Consider a receiving array which is affected by receiver gain/phase errors and sensor position errors. For $N$ narrowband signals impinging the $M$ element array, the vector of sensor outputs[2]

$$\mathbf{z}(t) = \mathbf{\Gamma A}\,\mathbf{s}(t) + \mathbf{n}(t) \tag{3.1}$$

where $\mathbf{A}$ contains the true sensor positions and is defined in section 2.1 along with $\mathbf{s}(t)$ and the spatially white receiver noise $\mathbf{n}(t)$. The diagonal matrix $\mathbf{\Gamma}$ is defined as

$$\mathbf{\Gamma} = diag\{(1+\alpha_1)e^{-j\psi_1}, (1+\alpha_2)e^{-j\psi_2}, ..., (1+\alpha_M)e^{-j\psi_M}\} \tag{3.2}$$

where $\alpha_m$ and $\psi_m$ are the receiver gain and phase errors respectively for the $m$th sensor. Now if the array is also affected by mutual coupling, the vector of sensor outputs become [87]

$$\mathbf{z}(t) = \mathbf{C}\,\mathbf{\Gamma A}\,\mathbf{s}(t) + \mathbf{n}(t) \tag{3.3}$$

where the coupling matrix $\mathbf{C} = (\mathbf{I}_M + \mathbf{Z}_o/Z_L)^{-1}$. The matrix $\mathbf{I}_M$ is the $M$x$M$ identity matrix and $\mathbf{Z}_o$ is the array impedance matrix. The scalar $Z_L$ is the load impedance.

In the presence of an interferer, the received signal is

$$\mathbf{z}(t) = \mathbf{C}\,\mathbf{\Gamma A}\,\mathbf{s}(t) + \mathbf{C}\,\mathbf{\Gamma}\,\mathbf{a}(\phi_I)\,s_I(t) + \mathbf{n}(t) \tag{3.4}$$

where $s_I(t)$ is the interfering signal and $\phi_I$ is its DOA.

The MVDR processor, using the noise-only covariance matrix for the estimation of the weights, is

$$\mathbf{w}(\theta) = \frac{\mathbf{Q}^{-1}\,\mathbf{a}_o(\theta)}{\mathbf{a}_o^H(\theta)\mathbf{Q}^{-1}\,\mathbf{a}_o(\theta)} \tag{3.5}$$

where $\mathbf{a}_o(\theta)$ is the nominal steering vector. The $m$th element of $\mathbf{a}_o(\theta)$ is $e^{jw(x_m^o \sin\theta + y_m^o \cos\theta)/v}$,

---

[2] assuming the receiver noise $\mathbf{n}(t)$ is unaffected by the gain/phase errors.

where $x_m^o$ and $y_m^o$ are the nominal sensor positions. The matrix $\mathbf{Q}$ is the noise-only covariance matrix, and is defined as [3]

$$\mathbf{Q} = E\{\mathbf{n}_T(t)\mathbf{n}_T(t)^H\} \tag{3.6}$$

where the total noise contribution is $\mathbf{n}_T(t) = \mathbf{C}\mathbf{\Gamma}\mathbf{a}(\phi_I)s_I(t) + \mathbf{n}(t)$.

The beampattern for the look direction $\theta$ is

$$B_\theta(\phi) = \mathbf{w}^H(\theta)\mathbf{C}\,\mathbf{\Gamma}\,\mathbf{a}(\phi)\,\mathbf{a}^H(\phi)\mathbf{\Gamma}^H\mathbf{C}^H\mathbf{w}(\theta) \tag{3.7}$$

## 3.3 Performance Measures

Simulations were conducted, to analyse the performance of this processor with array model errors, for typical OTH radar scenarios. A 16 element nominally uniform linear array with inter-element spacing ($d$) of $0.4\lambda$ was considered, with the signal-to-noise ratio equal to 0 dB and the signal-to-interference ratio -20 dB. The gain errors, phase errors and sensor position errors, were assumed to be zero mean Gaussian random variables. Gain errors of standard deviation $\{0.2,\ 0.4,\ 0.5\}$, phase errors of standard deviation $\{12^\circ,\ 24^\circ,\ 36^\circ\}$, and sensor position errors of standard deviation $\{0.1d,\ 0.2d,\ 0.3d\}$, were considered. Coupling matrices were obtained using "Antenna Wire Analysis Software" [38], for a uniform linear array of monopoles at 12 MHz with 10 m ($0.4\lambda$) inter-element spacing, as is typical for OTH radars. The height of the monopoles affects the amount of mutual coupling; coupling matrices for typical heights of $0.25\lambda$, $0.4\lambda$ and $0.5\lambda$, being used.

The signal direction ($\phi_s$) was fixed at broadside, and the interferer direction ($\phi_I$) was varied from end-fire to broadside. Fifty simulations were conducted for each interferer direction, and the mean and standard deviation of the performance measures calculated (only the mean values are presented here).

---

[3] note however, if the noise is non-stationary (as considered in section 3.4), then $\mathbf{Q}$ will be time dependent.

### 3.3.1 Signal-to-Noise Ratio and Array Gain

It can be shown that the signal-to-noise ratio of the array output, for a beam steered in direction $\phi_s$ and for a signal in direction $\phi_s$, is [4]

$$SNR = \frac{\sigma_S^2 B_{\phi_s}(\phi_s)}{\sigma_N^2 \mathbf{w}^H(\phi_s)\mathbf{w}(\phi_s) + \sigma_I^2 B_{\phi_s}(\phi_I)} \tag{3.8}$$

The array gain is

$$G = \frac{(\sigma_N^2 + \sigma_I^2)}{\sigma_S^2} SNR \tag{3.9}$$

The SNR as a function of signal-interferer separation, for the error standard deviations, is shown in figure 3.1. The logarithmic scale for the $x$-axis is to illustrate the behaviour for small separations. The solid curve is for no model errors, while the other curves are for the model errors specified. Note the conventional beamformer's beamwidth for the array considered is about 8° (the beamwidth is $\approx (0.88\lambda)/(Md)$ radians), so for separations less than this value the interferer is within the main beam, which results in SNR degradation even in the absence of model errors. The SNR (and hence array gain) degradations due to model errors (that is the degradations with respect to the solid curve), are clearly not large; the degradations observed being essentially independent of signal-interferer separation.

### 3.3.2 Beampointing Error

The beampointing error ($\phi_p$) is $|\phi_{max} - \phi_s|$, where $\phi_{max} = \{\xi : B_{\phi_s}(\xi) = \max(B_{\phi_s}(\phi))\}$. The variation of $\phi_p$ with signal-interferer separation, for different error standard deviations, is shown in figure 3.2. Again, the solid curve is for no model errors, while the other curves are for the model errors specified. Phase errors and position errors are seen to cause the largest beampointing errors. Except for small separations, where the interferer is within the main beam, the beampointing errors shown in figure 3.2 are never more than one degree (an eighth of the beamwidth).

Note a signal with finite SNR impinging an array (in the absence of model errors), will cause a beampointing error $\sigma_\theta = 1/(const\sqrt{SNR})$ [18], where $const = (\pi/\sqrt{3})M(d/\lambda)\cos(\theta)$. Hence the beampointing errors caused by model errors are significant, only when they exceed the beampointing error given by this formula. For beampointing errors due to finite SNR to be

---

[4] If the receiver noise $\mathbf{n}(t)$ is affected by receiver gain/phase errors, then the first term in the denominator of equation (3.8) becomes $\sigma_N^2 \mathbf{w}^H(\phi_s)\Gamma\Gamma^H\mathbf{w}(\phi_s)$, since $\mathbf{Q} = \sigma_N^2\Gamma\Gamma^H$. The results obtained in this case were found to be very similar to those presented here.

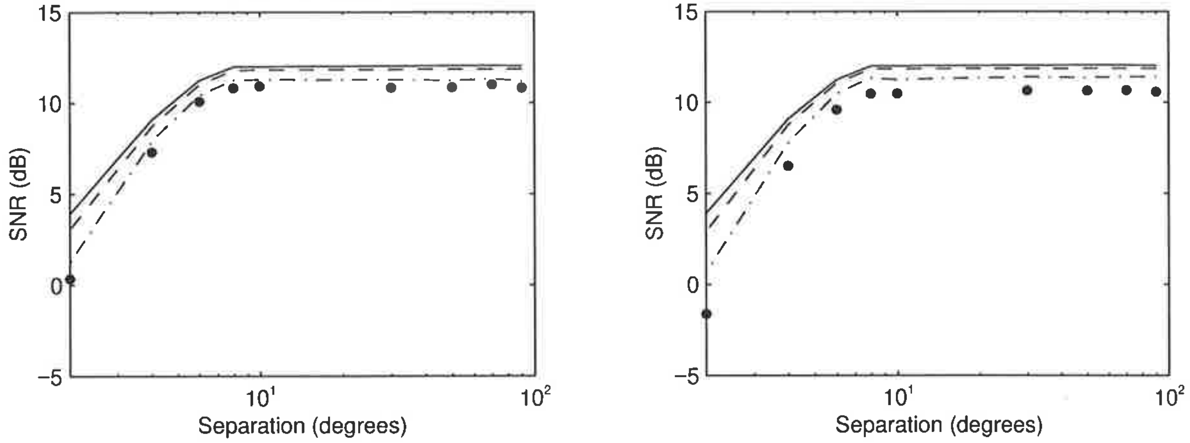
(a) Gain Errors

(b) Phase Errors

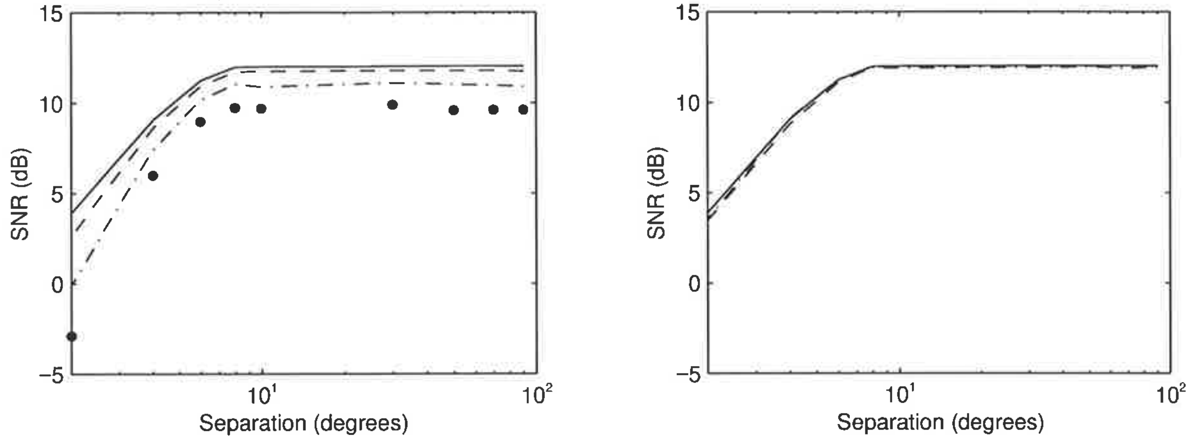
(c) Position Errors

(d) Mutual Coupling

Figure 3.1: Variation of signal-to-noise ratio with signal-interference separation, for the specified model error - (a) gain errors : $\sigma_{\alpha_m}$ = 0 (–), 0.2 (– –), 0.4 (–.–), 0.5 (...); (b) phase errors : $\sigma_{\psi_m}$ = 0° (–), 12° (– –), 24° (–.–), 36° (...); (c) sensor position errors : $\sigma_{x_m} = \sigma_{y_m}$ = 0 (–), 0.1$d$ (– –), 0.2$d$ (–.–), 0.3$d$ (...); (d) mutual coupling : element height ($h$) = 0.25$\lambda$ (–), 0.4$\lambda$ (–.–), 0.5$\lambda$ (– –).

less than that due to model errors (i.e. less than one degree say), would require the SNR of the signal to be at least 14 dB (for the scenario considered). Thus for signals with SNR less than 14 dB the beampointing errors due to model errors are not of concern, while for signals with SNR greater than or equal to 14 dB the beampointing errors due to model errors are significant.

### 3.3.3 Sidelobe Levels

To determine the affect on the sidelobe levels, a Hamming window was used with the weight vector. The modified weight vector is given as

$$\mathbf{w}(\theta) = \frac{\mathbf{Q}^{-1}\mathbf{D_W}\,\mathbf{a}_o(\theta)}{\mathbf{a}_o^H(\theta)\mathbf{Q}^{-1}\mathbf{D_W}\,\mathbf{a}_o(\theta)} \tag{3.10}$$

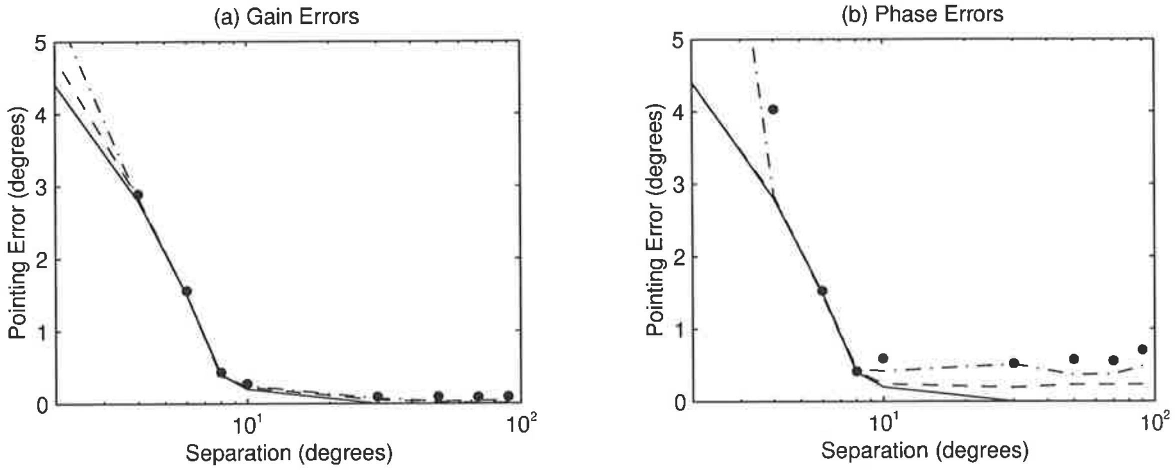
(a) Gain Errors

(b) Phase Errors

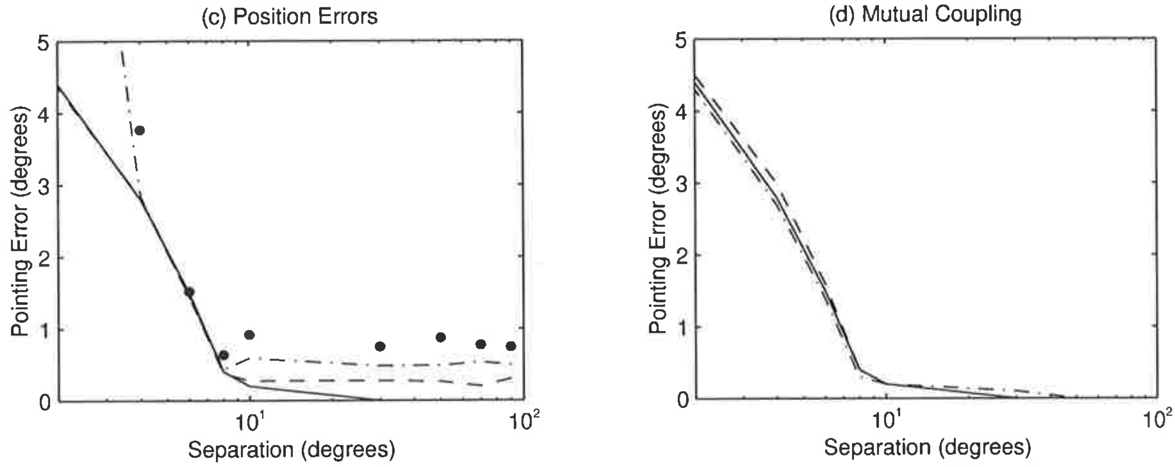
(c) Position Errors

(d) Mutual Coupling

Figure 3.2: Variation of pointing error with signal-interference separation, for the specified model error - (a) gain errors : $\sigma_{\alpha_m}$ = 0 (–), 0.2 (––), 0.4 (–.–), 0.5 (...); (b) phase errors : $\sigma_{\psi_m}$ = 0° (–), 12° (––), 24° (–.–), 36° (...); (c) sensor position errors : $\sigma_{x_m} = \sigma_{y_m} = 0$ (–), $0.1d$ (––), $0.2d$ (–.–), $0.3d$ (...); (d) mutual coupling : element height ($h$) = $0.25\lambda$ (–), $0.4\lambda$ (–.–), $0.5\lambda$ (––).

where $\mathbf{D_W}$ is a diagonal matrix containing the Hamming window weights.

The average sidelobe level (ASL) and the peak sidelobe level (PSL) are given as

$$ASL = \frac{\int_{\phi\epsilon\mathbf{\Phi}} B_{\phi_s}(\phi)\cos\phi\, d\phi}{B_{\phi_s}(\phi_s)} \tag{3.11}$$

$$PSL = \frac{\max_{\phi\epsilon\mathbf{\Phi}}\{B_{\phi_s}(\phi)\}}{B_{\phi_s}(\phi_s)} \tag{3.12}$$

where $\mathbf{\Phi}$ is the set of angles not in the main beamwidth, and the $\cos\phi$ in equation (3.11) is to obtain the correct contribution of powers (which would be obtained with a volumetric integration).

The ASL and PSL as a function of signal-interferer separation, for different error standard

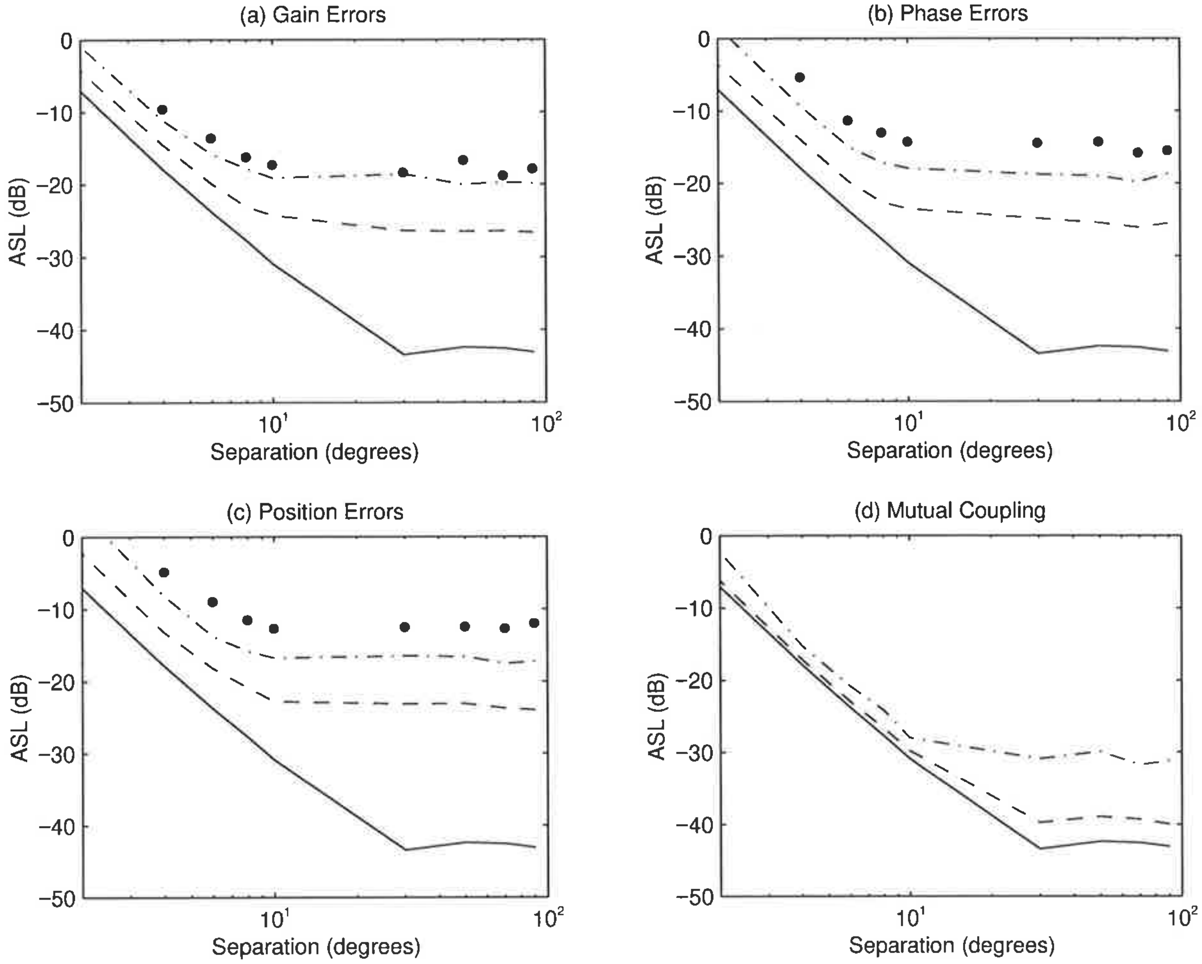

Figure 3.3: Variation of average sidelobe level with signal-interference separation, for the specified model error - (a) gain errors : $\sigma_{\alpha_m}$ = 0 (–), 0.2 (––), 0.4 (–.–), 0.5 (...); (b) phase errors : $\sigma_{\psi_m}$ = 0° (–), 12° (––), 24° (–.–), 36° (...); (c) sensor position errors : $\sigma_{x_m} = \sigma_{y_m}$ = 0 (–), 0.1$d$ (––), 0.2$d$ (–.–), 0.3$d$ (...); (d) mutual coupling : element height ($h$) = 0.25$\lambda$ (–), 0.4$\lambda$ (–.–), 0.5$\lambda$ (––).

deviations, are shown in figures 3.3 and 3.4 respectively. As can be clearly seen, the sidelobes are seriously affected by model errors; the sidelobes degrading with increasing model error standard deviations. Energy scattered through the array sidelobes could hence seriously degrade performance. The impact of these high sidelobes on OTH radars operating in a non-stationary interference environment, is demonstrated next.

## 3.4 Non-stationary Interferer Environment

OTH radars must be capable of operating in highly non-stationary interference environments, which frequently occur in the HF band. For the rejection of these interferers, time-varying weights are often used (e.g. [1]), which result in fluctuations of the beampattern as they adapt

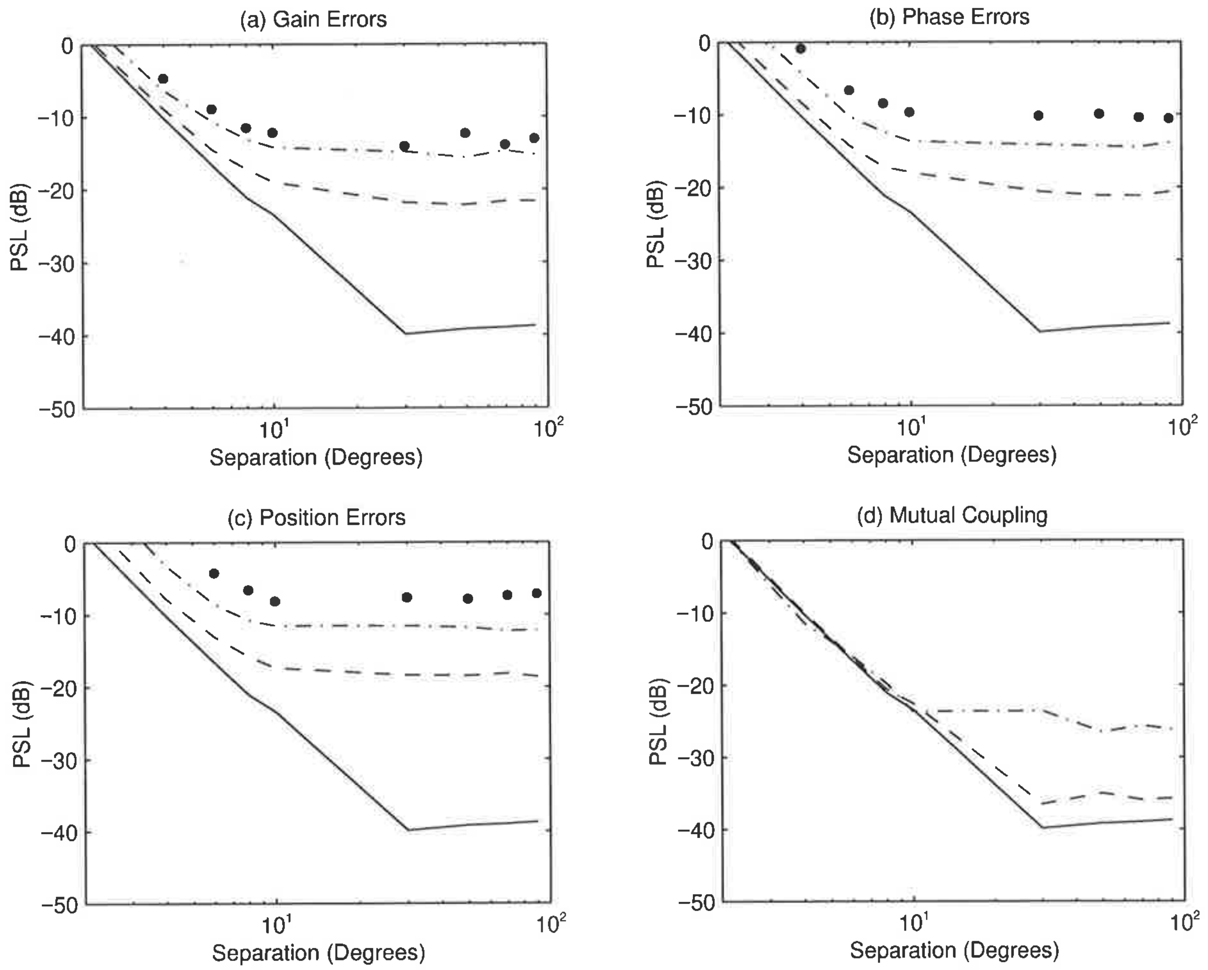

Figure 3.4: Variation of peak sidelobe level with signal-interference separation, for the specified model error - (a) gain errors : $\sigma_{\alpha_m}$ = 0 (–), 0.2 (– –), 0.4 (–.–), 0.5 (...); (b) phase errors : $\sigma_{\psi_m}$ = 0° (–), 12° (– –), 24° (–.–), 36° (...); (c) sensor position errors : $\sigma_{x_m} = \sigma_{y_m}$ = 0 (–), 0.1$d$ (– –), 0.2$d$ (–.–), 0.3$d$ (...); (d) mutual coupling : element height ($h$) = 0.25$\lambda$ (–), 0.4$\lambda$ (–.–), 0.5$\lambda$ (– –).

to the varying spatial properties of non-stationary interferers. High sidelobe levels, due to model errors, could hence affect the performance of these approaches.

It is now shown that the type of spatial non-stationarity of the interferer plays an important role in the implications of adaptive spatial processing for obtaining good sub-clutter visibility. Sub-clutter visibility, defined as the ratio of the peak clutter power (obtained after Doppler processing) to the mean noise power level, is a radar performance measure which indicates its capability in detecting targets; the larger the sub-clutter visibility the better the detection capability of the radar. Two models presented in [2], which reflect the spatial fluctuations of ionospherically-propagated interference signals, are analysed. The clutter model used in the analysis is also from [2].

### 3.4.1 *Fluctuating Interferer Wavefront Model*

For the first model, the spatial fluctuations are modelled as an autoregressive multivariate process, fluctuating around the mean plane-wave vector. The vector of sensor outputs for the total noise contribution, is given as

$$\mathbf{n}_T(t) = \sum_{r=1}^{R} \sigma_r \, \mathbf{D_a}(\phi_r) \, \mathbf{c}_r(t) \, s_I(t - \tau_r) \exp(j \Delta w_{gr} t) + \mathbf{n}(t) \tag{3.13}$$

where $R$ is the number of correlated (multipath) signals, or propagation modes, from the interferer. The root-mean-square power of the $r$th mode is $\sigma_r$, and the DOA information for the $r$th mode is given by the matrix $\mathbf{D_a}(\phi_r) = diag\{\mathbf{a}(\phi_r)\}$, where $\phi_r$ is the (mean) DOA of the interferer. The regular component of the ionospheric Doppler shift for the $r$th mode is $\Delta w_{gr}$, and $\tau_r$ is the corresponding group delay. The radiated interferer waveform is $s_I(t)$, and the additive receiver noise is $\mathbf{n}(t)$ as before. The vector $\mathbf{c}_r(t)$, introduced to model the spatio-temporal fluctuations, is a $N$-variate random process, described by a 2-dimensional Markov chain (spatio-temporal), as given below.

$$\mathbf{c}_r(t) = \rho_r(\Delta t)\mathbf{c}_r(t - \Delta t) + \sqrt{1 - |\rho_r(\Delta t)|^2} \, \boldsymbol{\epsilon}^r(t) \tag{3.14}$$

$$\epsilon^r_{k+1}(t) = \kappa(d_{k+1})\epsilon^r_k(t) + \sqrt{1 - |\kappa(d_{k+1})|^2} \, \gamma^r_{k+1}(t) \tag{3.15}$$

$$E[\gamma^r_{k+1}(t_1)\gamma^m_{l+1}(t_2)^*] = \delta^{rm}_{kl}(t_1, t_2) \tag{3.16}$$

where $d_{k+1}$ is an inter-element distance, both $\rho_r(\Delta t)$ and $\kappa(d_{k+1})$ are autoregressive coefficients, $\epsilon^r_{k+1}(t)$ is the $(k+1)$th element of the vector $\boldsymbol{\epsilon}^r(t)$ and $\epsilon^r_1(t) = \gamma^r_1(t)$. The behaviour of this interferer (for $R = 1$, $\phi_1 = 40^{\circ}$) is illustrated in figure 3.5(a), which shows the beamformed output of this interferer at different time snapshots. This figure indicates that the interferer has a crinkled wavefront, with the crinkling varying over time.

### 3.4.2 *Fluctuating Interferer DOA Model*

For the second model, the interferer wavefront of each propagation mode is represented by a classical plane-wave description with time varying DOA. The vector of sensor outputs for the total noise contribution, is given as

$$\mathbf{n}_T(t) = \sum_{r=1}^{R} \sigma_r \, \mathbf{a}(\phi_r(t)) \, s_I(t - \tau_r) \exp(j \Delta w_{gr} t) + \mathbf{n}(t) \tag{3.17}$$

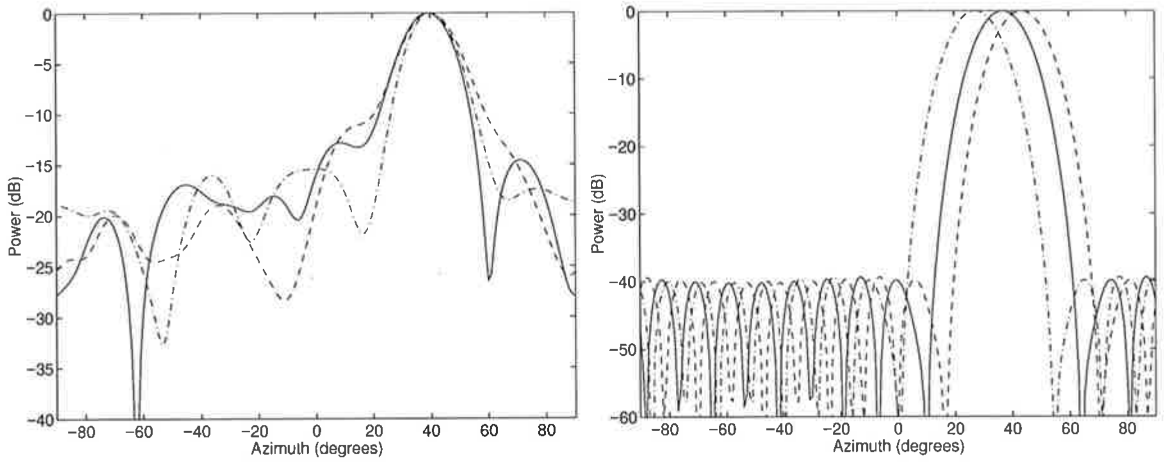

(a) fluctuating interferer wavefront model

(b) fluctuating interferer DOA model

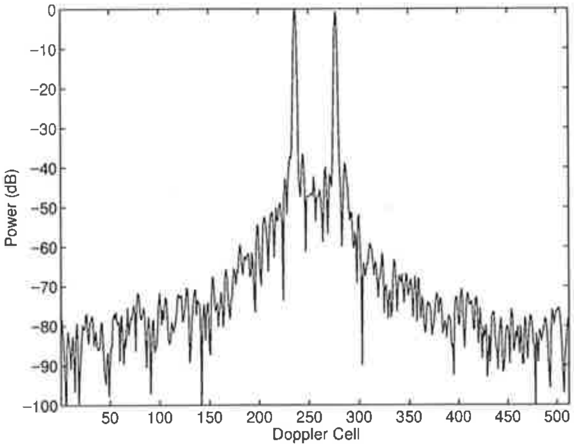

(c) sea clutter model

Figure 3.5: Examples illustrating the models used for non-stationary interference analysis.

The DOA at time $t$, for the $r$th mode, is defined as

$$\phi_r(t) = \phi_r^o + \Delta\phi_r\beta_r(t) \tag{3.18}$$

$$\beta_r(t) = \kappa(d_{k+1})\beta_r(t-\Delta t) + \sqrt{1-|\kappa(d_{k+1})|^2}\,\gamma_r(t) \tag{3.19}$$

The behaviour of this interferer (for $R = 1$, $\phi_1^o = 40^o$, $\Delta\phi_1 = 10^o$) is illustrated in figure 3.5(b), which shows the beamformed output of this interferer at different time snapshots. Figure 3.5(b) indicates that the interferer has a planar wavefront, with the DOA of the interferer varying over time.

### 3.4.3 Sea Clutter Model

For the clutter model $\mathbf{z}_C(t)$, a second-order autoregressive model is used. The vector of sensor outputs is given as

$$\mathbf{z}_C(t) = -\sum_{i=1}^{2} C_i^{cl}\, \mathbf{z}_C(t - i\tau) + \alpha^{cl}\, \boldsymbol{\epsilon}^{cl}(t) \tag{3.20}$$

where $\tau$ is the repetition period of the radar's waveform, and the spatial properties of the clutter are defined by the transmitter's antenna pattern :

$$\epsilon_k^{cl}(t) = \xi\, \epsilon_{k-1}^{cl}(t) + \sqrt{1 - |\xi^2|}\, \gamma_k^{cl}(t) \tag{3.21}$$

$$E[\gamma_k^{cl}(t_1)\, \gamma_l^{cl}(t_2)^*] = \delta_{kl}(t_1, t_2) \tag{3.22}$$

where $\xi$ is an autoregressive coefficient. Parameters for the clutter model have been chosen to reflect sea-surface scattering (see [2]) : $C_1^{cl} = -1.9359$; $C_2^{cl} = 0.998$; $\alpha^{cl} = 0.009675$.

The clutter Doppler spectrum, generated using this model with the above mentioned parameters, is shown in figure 3.5(c). The two peaks observed in this Doppler spectrum represent the sea clutter Bragg-lines.

### 3.4.4 Results

The time-varying vector of weights used for beamforming in a non-stationary interference environment, is

$$\mathbf{w}(\theta, t) = \frac{\mathbf{Q}^{-1}(t)\mathbf{D_W}\, \mathbf{a}_o(\theta)}{\mathbf{a}_o^H(\theta)\mathbf{Q}^{-1}(t)\mathbf{D_W}\, \mathbf{a}_o(\theta)} \tag{3.23}$$

where now the noise-only covariance matrix is time dependent, and is $\mathbf{Q}(t) = E\{\mathbf{n}_T(t)\, \mathbf{n}_T(t)^H\}$. The beamformed clutter signal is then given as

$$\tilde{z}_C(t) = \mathbf{w}^H(\theta, t)\, \mathbf{z}_C(t) \tag{3.24}$$

To reflect a typical OTH radar scenario, the following parameter values were chosen (see [2]) : $\xi = 0.5$; $\rho_r(\Delta t) = e^{-0.05}$ for $\Delta t = 0.1$ seconds; $\kappa(d_{k+1}) = 0.9$. An example of the effect of model errors on the clutter spectrum is shown in figure 3.6. Three clutter spectra are shown : (a) when no interferer exists and there are no model errors (−); (b) when an interferer with a fluctuating DOA exists and there are no model errors (−−); and (c) when an interferer with fluctuating DOA exists and there are model errors (−.−). In the case of model errors the sub-clutter visibility (SCV), defined as the ratio of the peak Bragg-line power to the mean noise

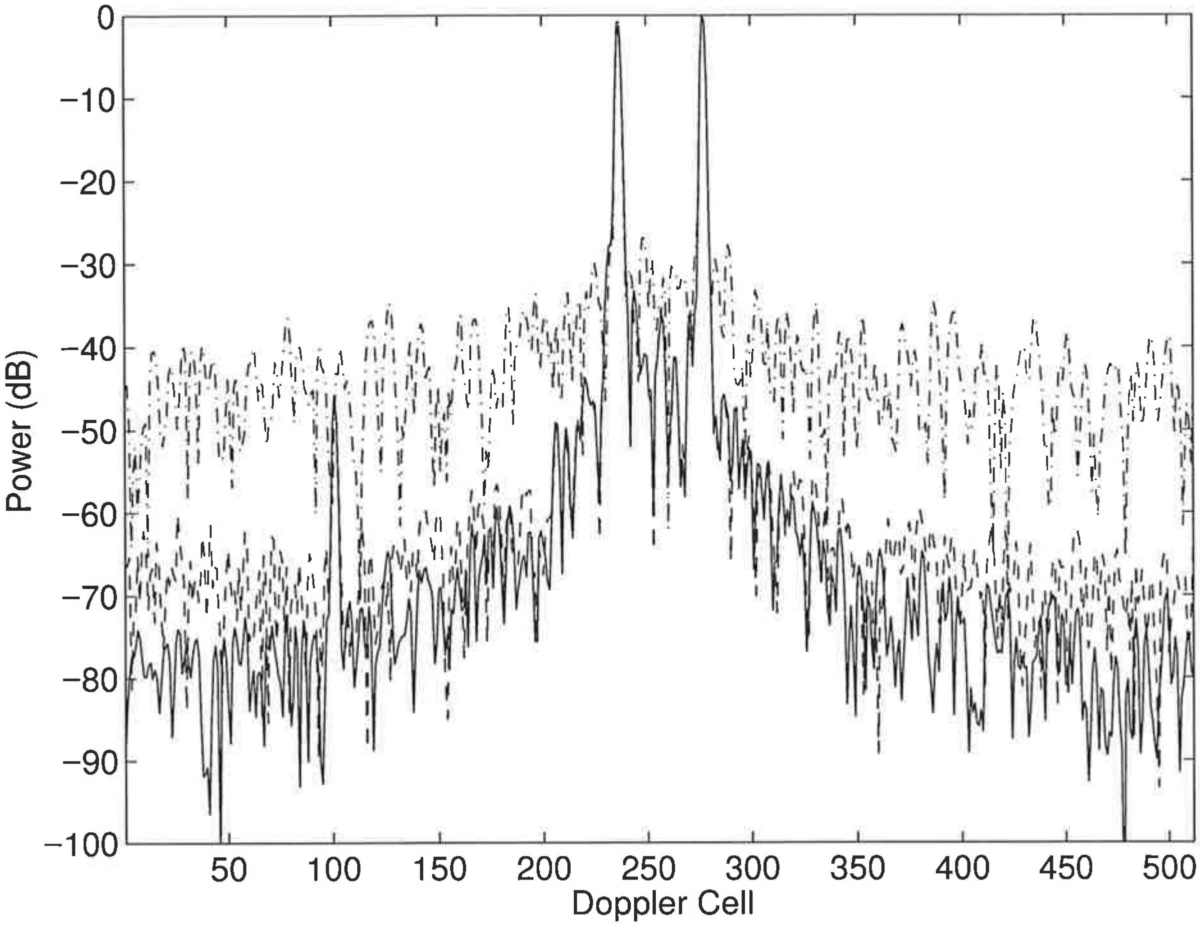

Figure 3.6: Example of SCV degradation. The clutter spectra shown are : (a) when no interferer exists and there are no model errors (−); (b) when an interferer exists and there are no model errors (−−); and (c) when an interferer exists and there are model errors (−.−). A target is present at Doppler cell 100.

power, is much less than in the absence of model errors. Note the target (located at Doppler cell 100) which is clearly visible in the absence of model errors, is not visible in the case of model errors. Thus the effect of model errors is to reduce the SCV, and hence target detectability. An explanation as to how model errors reduce the SCV is given later in this section.

The degradation in SCV as a function of errors in sensor positions is shown in figure 3.7(a), for both interferer models. The degradation displayed is relative to an environment with no interferers; the average results from 500 simulations being depicted. Clearly the model errors degrade the attainable SCV when the fluctuating interference DOA model is used. The degradation due to the model errors, when the fluctuating interference wavefront model is used, is not as large but is still significant. Similar results were obtained for the other model errors; the SCV degradation as a function of gain errors being displayed in figure 3.7(b).

An understanding of how increased sidelobe levels effect SCV, is obtained by considering

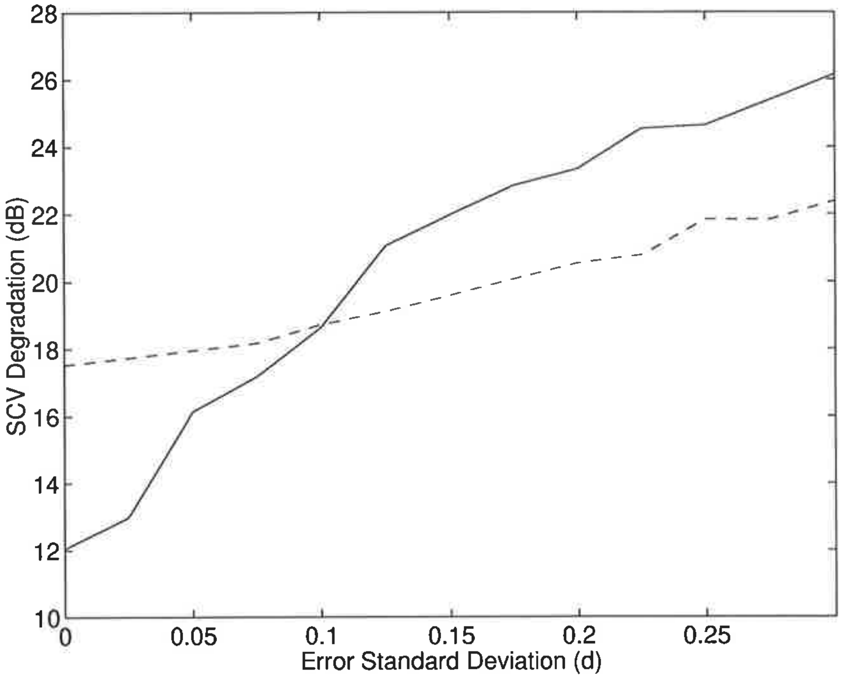

(a) sensor position errors

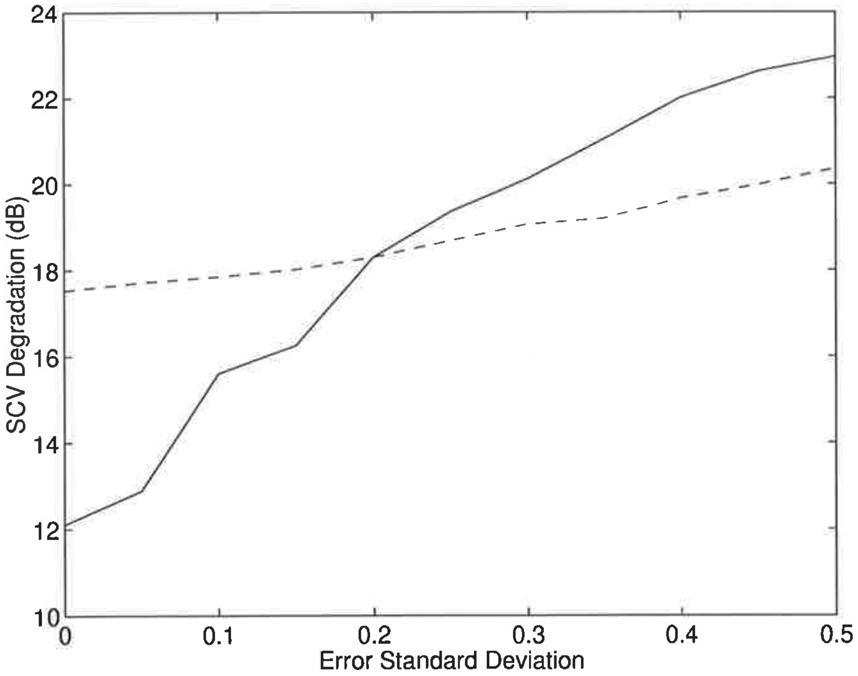

(b) gain errors

Figure 3.7: SCV degradation versus model error standard deviation, for a fluctuating interference DOA model (—) and a fluctuating interference wavefront model (– –).

the time-varying beampatterns shown in figure 3.8. In this figure, the main beam has been shifted to 90°, so that the sidelobes can be seen clearly. When no model errors exist, as in figure 3.8(a), the sidelobe levels are essentially constant over time with changes in the null position around 50° (for rejecting the interferer) apparent. When model errors exist however, as in figure 3.8(b), not only are the sidelobe levels higher (as seen in section 3.33) but the sidelobes vary substantially over time. Because of the high sidelobe levels, nulling the interferer results in more degradation on the beampattern, and since the spatial properties of the interferer changes with time, the null position and the degradation caused vary with time. Clutter processed by the beampatterns in figure 3.8(b) will clearly not be as coherent as that processed by the beampatterns in figure 3.8(a), since the clutter will in fact be modulated by the variation in the beampattern (or the adaptive weights) when it is beamformed. After beamforming the data is Doppler processed, which involves coherently processing radar returns over several radar transmissions. Since clutter processed by the beampatterns in figure 3.8(b) will not be as coherent as that processed by the beampatterns in figure 3.8(a), the clutter-to-noise ratio (or SCV) obtained after Doppler processing will be worse. Thus the SCV (and hence target detection) is worse when model errors exist.

## 3.5 Conclusion

The effect of receiver gain/phase errors, sensor position errors and mutual coupling, on OTH radar array processing, has been analysed for the case where the adaptive processor weights are obtained using the noise-only covariance matrix. While the array signal-to-noise ratio is somewhat degraded and the beampointing error may be up to an eighth of the beamwidth, the major performance degradation is the array sidelobe levels; energy received through these sidelobes could hence seriously degrade performance. Further it was shown, under non-stationary interference environments, the attainable SCV could be limited by these high sidelobe levels. Array calibration is thus necessary, so the array sidelobe levels can be improved.

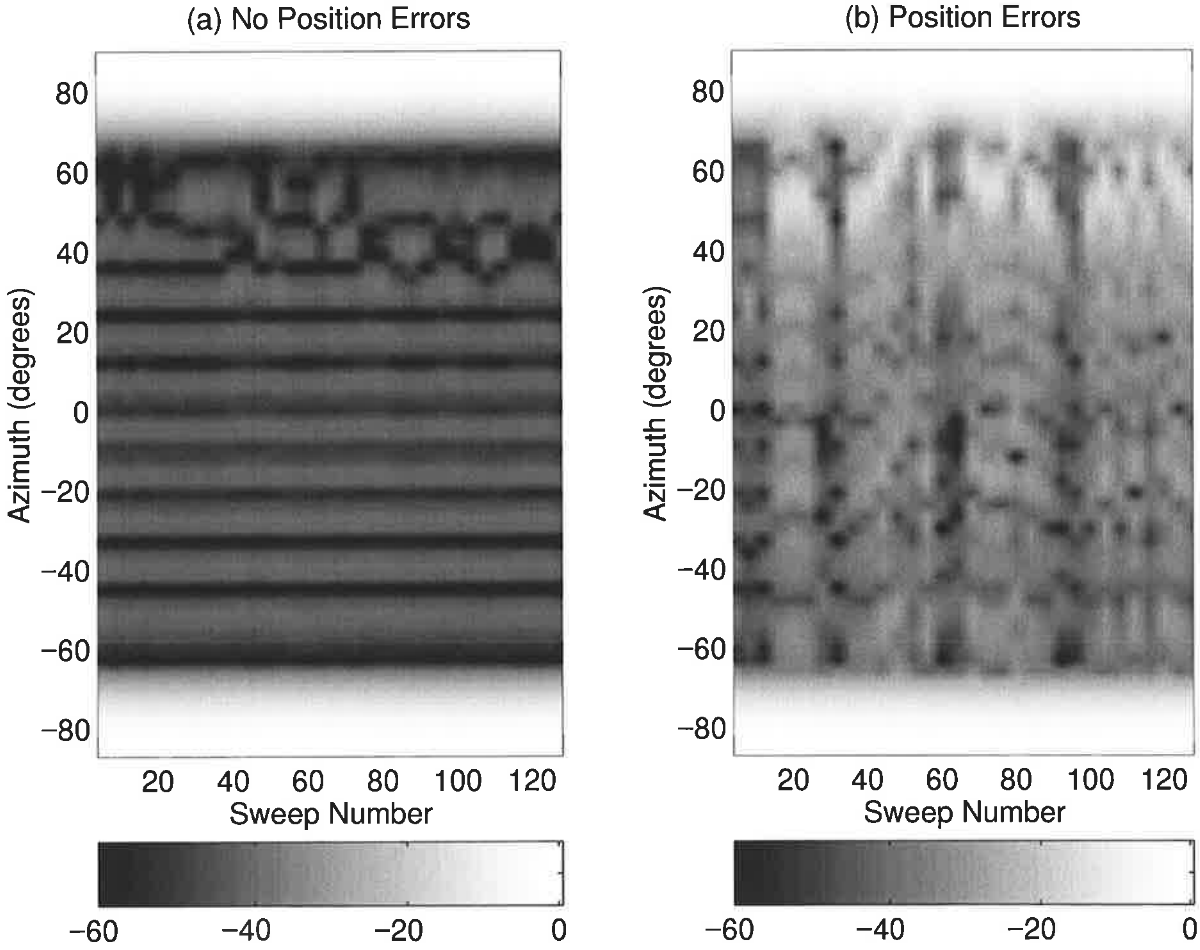

Figure 3.8: Beampatterns for the first 128 time samples (sweeps) - (a) position errors are not present; (b) position errors are present.

# CHAPTER 4

# Array Calibration using Disjoint Sources

In this chapter a method is developed for estimating the coupling matrix and sensor position errors; it is assumed that receiver gain/phase errors have been corrected, by injecting signals internally at the receiver inputs. The method proposed is for using (single-mode) meteor trail echoes, which are shown in chapter 7 to be disjoint sources of time-invariant DOA. This method was obtained by generalising and modifying the methods proposed by Weiss and Friedlander in [251, 252, 66]. First the Weiss-Friedlander methods are generalised, and the resulting algorithm analysed via simulations; the simulations are generated using a measured coupling matrix and this coupling matrix has to be estimated by the algorithm. The generalised method was found to perform poorly, for this and other experimentally-measured coupling matrices, since the Toeplitz coupling matrix model employed by the algorithms in [252, 66] are not suitable in these cases.

This generalised method is then modified, to (a) employ a more general model for the coupling matrix, and (b) so disjoint sources (in the form of meteor trail echoes) could be used for performing the array calibration. The later modification results in fewer sources being required for a given number of unknowns, while the former modification results in more unknown parameters. Experimentally-measured coupling matrices are again used in simulations to assess the performance of this modified method.

The layout of this chapter is as follows. Mutual coupling models are discussed in section 4.1, while in section 4.2 and 4.3 the generalised Weiss-Friedlander method is considered. In section 4.4 the modified method is presented, and the performance of the method is investigated in sections 4.5 and 4.6; an alternative sensor position estimator is proposed in section 4.7 for reducing the number of failures. In section 4.8 performance criteria for determining in practice if array calibration has been successful are proposed, in section 4.9 the mutual coupling estimation performance of the algorithm is investigated, and in section 4.10 the algorithm's error surface is analysed.

## 4.1 Mutual Coupling Models

Mutual coupling is caused by antenna elements receiving energy re-radiated by other antenna elements. The voltage received by an element is then the sum of the direct voltage due to a signal, plus the sum of all voltages due to the re-radiation by other elements in the array. Mutual coupling causes elements, in an array of identical elements, to have non-equal radiation patterns i.e. not all elements 'see' the same environment.

A detailed model of mutual coupling was presented by Manikas and Fistas in [126]. The coupling matrix was specified as

$$\mathbf{C} = \mathbf{K} \odot \mathbf{L} \odot e^{j\mathbf{\Psi}} \odot \mathbf{G} \odot e^{j\pi\mathbf{D}} \tag{4.1}$$

where [1] matrix $\mathbf{K}$ has the root-mean-square values of the direct and re-radiated signals, matrix $\mathbf{L}$ has the losses in free space propagation, matrix $\mathbf{\Psi}$ has the random phases of the re-radiated signals, matrix $\mathbf{G}$ has the gain and phases relating to the propagation of the re-radiated signals, and matrix $\mathbf{D}$ has the inter-element distances. These five matrices are given in equations (4.2)-(4.6) below.

$$\mathbf{K} = \begin{bmatrix} \sqrt{1-\alpha_1} & \sqrt{\alpha_2} & \cdots & \sqrt{\alpha_N} \\ \sqrt{\alpha_1} & \sqrt{1-\alpha_2} & \cdots & \sqrt{\alpha_N} \\ \vdots & \vdots & \vdots & \vdots \\ \sqrt{\alpha_1} & \sqrt{\alpha_2} & \cdots & \sqrt{1-\alpha_N} \end{bmatrix} \tag{4.2}$$

where $\alpha_k$ is the relative power of the signal that is re-radiated by element $k$ and is propagated to the other elements.

$$\mathbf{L} = \begin{bmatrix} 1 & \cdots & l_{1N} \\ \vdots & 1 & \vdots \\ l_{1N} & \cdots & 1 \end{bmatrix} \tag{4.3}$$

where $l_{mk}$ is a real number representing the propagation loss suffered by the spherically

---

[1] $\odot$ denotes the Hadamard product i.e. $[a_{mk}] \odot [b_{mk}] = [a_{mk}b_{mk}]$

propagated re-radiated signal, and equals $G_m/(2\pi d_{mk})$, where $G_m$ is referred to as the "power gain" of element $m$ and $d_{mk}$ is the distance (in wavelengths) between the $m$th and $k$th elements.

$$\mathbf{\Psi} = \begin{bmatrix} 0 & \psi_2 & \cdots & \psi_N \\ \psi_1 & 0 & \cdots & \psi_N \\ \vdots & \vdots & 0 & \vdots \\ \psi_1 & \psi_2 & \cdots & 0 \end{bmatrix} \tag{4.4}$$

where $\psi_m$ is the random phase introduced by the $m$th element to the re-radiated signal.

$$\mathbf{G} = \begin{bmatrix} 1 & \cdots & g_{1N} \\ \vdots & 1 & \vdots \\ g_{N1} & \cdots & 1 \end{bmatrix} \tag{4.5}$$

where $g_{mk}$ is a complex number, which is said to represent the gain and phase characteristics of both element $m$ and element $k$ in the propagation path between the elements i.e. it accounts for the differing gain/phase response of antennas and the ground between antenna pairs.

$$\mathbf{D} = \begin{bmatrix} 0 & \cdots & d_{1N} \\ \vdots & 0 & \vdots \\ d_{N1} & \cdots & 0 \end{bmatrix} \tag{4.6}$$

This coupling matrix model, while providing good insight into the physics of mutual coupling, has numerous unknowns. A commonly used coupling matrix model for uniform linear arrays is the symmetric Toeplitz coupling matrix (the analogous model for uniform circular arrays is the symmetric circulant coupling matrix). The symmetric Toeplitz coupling matrix is

$$\mathbf{C} = \begin{bmatrix} c_1 & c_2 & c_3 & \cdots & c_M \\ c_2 & c_1 & c_2 & \cdots & c_{M-1} \\ c_3 & c_2 & c_1 & \cdots & c_{M-2} \\ \vdots & \vdots & \vdots & \vdots & \vdots \\ c_M & c_{M-1} & c_{M-2} & \cdots & c_1 \end{bmatrix} \tag{4.7}$$

Such a model assumes equal coupling between any two equally spaced sensors in the array. Note for an "almost" uniform linear array, where the antenna position deviations from a uniform linear array are small, this model should still be applicable. In this chapter, this model is (initially) investigated for nominally uniform linear arrays, although it is not appropriate for arbitrary array geometries. Note coupling matrices are independent of incident signal powers and their directions.

## 4.2 Generalised Weiss-Friedlander Method

Weiss and Friedlander, as mentioned in chapter 2, have developed :

- a method for estimating sensor position errors, for an array with neither mutual coupling or gain/phase errors [251]; and
- a method for estimating a symmetric Toeplitz/circulant coupling matrix (and gain/phase errors) for a uniform linear/circular array with no sensor position errors [252, 66].

These methods are based on the fact that the noise subspace (for an estimate of the covariance matrix) is almost orthogonal to the true signal steering vector, the cost function used being a minimum when the signal steering vector is almost orthogonal to the estimated noise subspace. The parameter values at this minimum are the estimated values. The cost function used is based on the MUSIC algorithm, which is very sensitive to model errors. Hence for the exact covariance matrix, or for an estimated covariance matrix with sufficient number of integrations, this cost function is a good choice. These methods use single-mode (uncorrelated) non-disjoint sources of opportunity; where non-disjoint sources, from a radar perspective, means the sources occupy the same time snapshots and the same radar range cells. Note in section 4.4 the modified method proposes using disjoint sources.

The first contribution of this chapter is to generalise these two methods, to estimate both sensor position errors and a symmetric Toeplitz coupling matrix; the details of the resulting method is presented below. Initially the generalised method is considered, and tested for nominally uniform linear arrays. Note since only small sensor position errors (with respect to the inter-element spacing) are considered, it is expected that the sensor position errors will not effect the Toeplitz structure of the coupling matrix, considered by Weiss-Friedlander for uniform linear arrays.

The covariance matrix is first estimated for the $N$ non-disjoint sources, as follows

$$\hat{\mathbf{R}} = \frac{1}{T}\sum_{t=1}^{T}\mathbf{z}(t)\mathbf{z}^{H}(t) \tag{4.8}$$

where the data containing the $N$ sources (in the absence of gain/phase errors) is $\mathbf{z}(t) = \mathbf{C}\mathbf{A}\mathbf{s}(t) + \mathbf{n}(t)$.

The cost function for the generalised problem (and for a narrowband system) is

$$Q = \|\hat{\mathbf{U}}^H \mathbf{C}\mathbf{A}\|^2 = \sum_{n=1}^{N} \|\hat{\mathbf{U}}^H \mathbf{C}\mathbf{a}(\theta_n)\|^2 \tag{4.9}$$

where $\hat{\mathbf{U}}$ is the estimated noise subspace, obtained from the eigendecomposition of $\hat{\mathbf{R}}$. (Note the similarity between this cost function and the MUSIC algorithm in equation (2.26), which is used for estimating DOAs only). This cost function is a least squares formulation of $N(M-N)$ complex equations. There are $2M-3$ unknown sensor positions (see assumptions below), $N$ unknown directions-of-arrival, and $2M-2$ unknown coupling parameters (since $M$ complex parameters are being estimated and the symmetric Toeplitz matrix is estimated up to an arbitrary complex scalar). Hence a solution can exist only if $(2M-3)+N+(2M-2) \leq 2N(M-N)$ which implies $2N^2+(1-2M)N+(4M-5) \leq 0$; for example for a 16-element array $3 \leq N \leq 13$.

The iterative procedure for minimising the cost function in equation (4.9) consists of three steps; the order being obtained heuristically. The **first step** uses the best estimates of sensor positions and coupling values available, and estimates the $N$ signal DOAs, using the MUSIC algorithm as follows

$$p(\theta) = \frac{1}{\|\hat{\mathbf{U}}^H \mathbf{C}\mathbf{a}(\theta)\|^2} \tag{4.10}$$

The DOAs corresponding to peak values of $p(\theta)$ are the estimated DOAs of the $N$ signals.

In the **second step** the sensor positions are estimated [251] using a closed form solution that is related to the Gauss-Newton technique. The actual position of the $m$th sensor is

$$(x_m, y_m) = (x_m^o, y_m^o) + (\Delta x_m, \Delta y_m) \tag{4.11}$$

where $x_m^o$ and $y_m^o$ define the nominal (or last estimated) sensor position of the $m$th sensor, and $\Delta x_m$ and $\Delta y_m$ define the position error of the $m$th sensor. For sufficiently small position errors, matrix $\mathbf{A}$ can be approximated as

$$\mathbf{A} = \mathbf{A}_0 + \mathbf{\Lambda_x}\mathbf{A}_1 + \mathbf{\Lambda_y}\mathbf{A}_2 \tag{4.12}$$

where $\mathbf{A}_0$ is $\mathbf{A}$ with the sensor positions $(x_m^o, y_m^o)$, and

$$\mathbf{\Lambda_x} = diag\{\Delta x_1, \Delta x_2, ..., \Delta x_M\} \tag{4.13}$$

$$\begin{aligned}
\mathbf{\Lambda_y} &= diag\{\Delta y_1, \Delta y_2, ..., \Delta y_M\} && (4.14)\\
\mathbf{A}_1 &= j\mathbf{A}_0(w/v)\, diag\{\sin(\theta_1), \sin(\theta_2), ..., \sin(\theta_N)\} && (4.15)\\
\mathbf{A}_2 &= j\mathbf{A}_0(w/v)\, diag\{\cos(\theta_1), \cos(\theta_2), ..., \cos(\theta_N)\} && (4.16)
\end{aligned}$$

The cost function can then be written as

$$\begin{aligned}
Q &= ||\hat{\mathbf{U}}^H \mathbf{C}[\mathbf{A}_0 + \mathbf{\Lambda_x}\mathbf{A}_1 + \mathbf{\Lambda_y}\mathbf{A}_2]||^2 && (4.17)\\
&= \sum_{n=1}^{N} ||\hat{\mathbf{U}}^H \mathbf{C}[\mathbf{a}_0(\theta_n) + \mathbf{\Lambda_x}\mathbf{a}_1(\theta_n) + \mathbf{\Lambda_y}\mathbf{a}_2(\theta_n)]||^2 && (4.18)\\
&= \sum_{n=1}^{N} ||\hat{\mathbf{U}}^H \mathbf{C}[\mathbf{a}_0(\theta_n) + diag\{\mathbf{a}_1(\theta_n)\}\mathbf{v_x} + diag\{\mathbf{a}_2(\theta_n)\}\mathbf{v_y}]||^2 && (4.19)
\end{aligned}$$

where the vectors $\mathbf{a}_0(\theta_n)$, $\mathbf{a}_1(\theta_n)$ and $\mathbf{a}_2(\theta_n)$ are the $n$th column vectors of $\mathbf{A}_0$, $\mathbf{A}_1$ and $\mathbf{A}_2$ respectively, and $\mathbf{v_x}$ and $\mathbf{v_y}$ are vectors whose $m$th element is $\Delta x_m$ and $\Delta y_m$ respectively. Now define

$$\begin{aligned}
\mathbf{v_{xy}} &= [\mathbf{v_x}^T, \mathbf{v_y}^T]^T && (4.20)\\
\mathbf{B}(n) &= -[\hat{\mathbf{U}}^H \mathbf{C}\, diag\{\mathbf{a}_1(\theta_n)\}, \hat{\mathbf{U}}^H \mathbf{C}\, diag\{\mathbf{a}_2(\theta_n)\}] && (4.21)\\
\mathbf{Z}(n) &= \hat{\mathbf{U}}^H \mathbf{C}\, \mathbf{a}_0(\theta_n) && (4.22)
\end{aligned}$$

then the cost function becomes

$$Q = \sum_{n=1}^{N} ||\mathbf{Z}(n) - \mathbf{B}(n)\mathbf{v_{xy}}||^2 \tag{4.23}$$

The real vector $\mathbf{v_{xy}}$ that minimises $Q$ is

$$\mathbf{v_{xy}} = [Re\{\mathbf{B}^H\mathbf{B}\}]^{-1} Re\{\mathbf{B}^H\mathbf{Z}\} \tag{4.24}$$

where

$$\begin{aligned}
\mathbf{B} &= [\mathbf{B}^T(1), \mathbf{B}^T(2), ..., \mathbf{B}^T(N)]^T && (4.25)\\
\mathbf{Z} &= [\mathbf{Z}^T(1), \mathbf{Z}^T(2), ..., \mathbf{Z}^T(N)]^T && (4.26)
\end{aligned}$$

and $\Re\{\}$ is the real part. The DOAs estimated, and the best available values of the coupling parameters, are used in this second step to estimate the sensor position errors using equation

(4.24).

In the **third step** the symmetric Toeplitz coupling matrix is estimated [252, 66] by expressing $\mathbf{C}\mathbf{a}(\theta_n)$ as $\mathbf{W}(\theta_n)\mathbf{c}$ (i.e. by exploiting the Toeplitz structure the unknowns in $\mathbf{C}$ can be placed in the vector $\mathbf{c}$ and the known values in $\mathbf{a}(\theta_n)$ can be placed in the matrix $\mathbf{W}(\theta_n)$). The cost function in equation (4.9) can then be written as

$$\begin{aligned} Q &= \sum_{n=1}^{N} \mathbf{a}^H(\theta_n)\mathbf{C}^H\hat{\mathbf{U}}\hat{\mathbf{U}}^H\mathbf{C}\mathbf{a}(\theta_n) & (4.27) \\ &= \mathbf{c}^H \left\{ \sum_{n=1}^{N} \mathbf{W}^H(\theta_n)\hat{\mathbf{U}}\hat{\mathbf{U}}^H\mathbf{W}(\theta_n) \right\} \mathbf{c} & (4.28) \end{aligned}$$

The quadratic minimum for estimating $\mathbf{c}$, under the constraint $c_1 = 1$ (to exclude the trivial solution), is

$$\mathbf{c} = \frac{\mathbf{G}^{-1}\mathbf{u}}{\mathbf{u}^H\mathbf{G}^{-1}\mathbf{u}} \tag{4.29}$$

where $\mathbf{G} = \sum_{n=1}^{N} \mathbf{W}^H(\theta_n)\hat{\mathbf{U}}\hat{\mathbf{U}}^H\mathbf{W}(\theta_n)$ and $\mathbf{u} = [1, 0, ..., 0]^T$. For the symmetric Toeplitz coupling matrix model, the matrix $\mathbf{W}(\theta_n)$ is the sum of the two $M$x$M$ matrices [252, 66],

$$[\mathbf{W_1}]_{mk} = \begin{cases} a_{m+k-1} & m+n \leq M+1 \\ 0 & \text{otherwise} \end{cases} \tag{4.30}$$

$$[\mathbf{W_2}]_{mk} = \begin{cases} a_{m-k+1} & m \geq n \geq 2 \\ 0 & \text{otherwise} \end{cases} \tag{4.31}$$

Note since the cost function in equation (4.9) is multi-modal, this algorithm is only expected to provide a solution close to the global minimum when the initial parameter values are sufficiently close to the actual parameter values. Under such conditions, each of the three steps above decrease the cost function, and so convergence of the algorithm is expected.

The assumptions made are :

- the location of one sensor and the direction to another sensor (and so effectively one of its coordinates) are known [170, 171, 168];
- the actual array geometry is not linear [170, 156];
- the signals and noise are stationary over the interval the covariance matrix is estimated; and
- the noise covariance is known up to a multiplicative constant.

## 4.3 Performance of Generalised Method

The performance of this generalised method is now investigated, using an experimentally measured coupling matrix. This coupling matrix [136] was obtained by Netherway and Carson from the uniform linear Jindalee transmitting array. First the case where the coupling matrix is exactly Toeplitz is considered, by creating a symmetric Toeplitz matrix using the coupling values in the first row of the measured matrix. Then the algorithm's performance is considered when the full measured coupling matrix is used.

Three sources were considered, each with SNR of 30 dB, and with DOAs of $-45^o$, $0^o$ and $+45^o$. The covariance matrix was estimated from 500 snapshots of the sources. The simulations were performed for a nominally uniform linear array of 16 elements with inter-element spacing of $d = 0.4\lambda$. The actual sensor positions were $x_m = md + \Delta x_m$ and $y_m = \Delta y_m$, where $\Delta x_m$ and $\Delta y_m$ are zero mean Gaussian random variables with standard deviation of $0.1d$. The randomly generated sensor position errors are kept the same for both examples considered here.

The algorithm was initialised using the nominal sensor positions, and the identity matrix was used as the initial coupling matrix. The algorithm was terminated when the cost function Q changed in value by less than 0.1 percent.

The results obtained for the Toeplitz coupling matrix are shown in figure 4.1. Figure 4.1(a)-(b) show the amplitude, of the actual coupling matrix used and the estimated coupling matrix respectively, while figure 4.1(d)-(e) show the phase, of the actual coupling matrix used and the estimated coupling matrix respectively. The phase values of the coupling matrices have not been unwrapped to allow easy comparison. The root-mean-square coupling amplitude estimation error is 0.04, while the root-mean-square phase estimation error is 0.03 radians. Figure 4.1(c) and 4.1(f) show the sensor position errors for, the nominal sensor positions (o) and the estimated sensor positions ($*$). These results indicate the algorithm has performed very well. The coupling matrix estimated is very similar to the actual coupling matrix used, and the estimated sensor positions are very close to the true sensor positions. The DOAs estimated were $-45.3^o$, $-0.3^o$ and $+44.6^o$. A number of simulations were conducted, similarly good results being obtained in each case.

In chapter 3 the degradation caused by uncompensated mutual coupling and sensor position errors on radar performance was quantified; the main degradation being in the array sidelobe levels. Hence to further analyse the performance of the algorithm, it is necessary to compare the sidelobe levels obtained using the estimated parameters with those of the uncalibrated array.

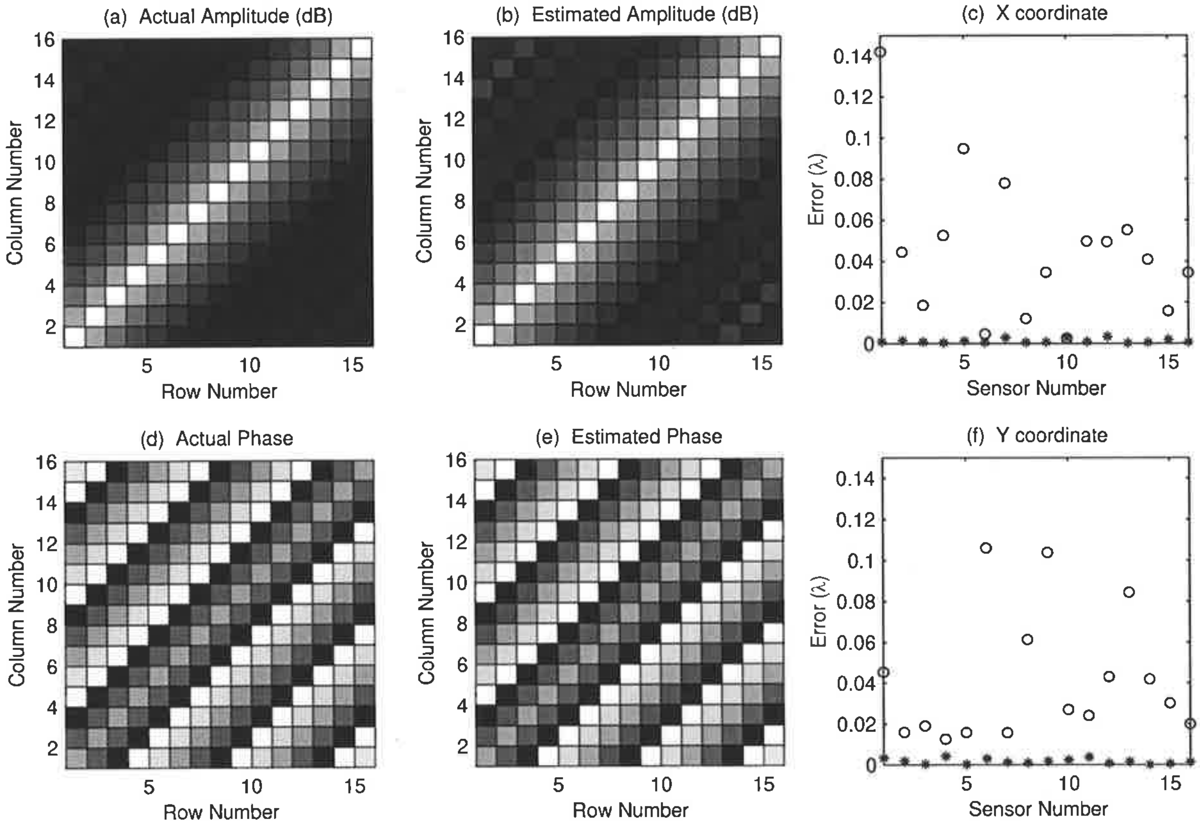

Figure 4.1: Generalised Weiss-Friedlander method's performance - Toeplitz coupling matrix.

Given the sensor positions and the coupling matrix, the weighting required to obtain minimum average sidelobes can be shown to be (see Appendix A equation (A.9))

$$\mathbf{w}(\theta_o) = \frac{(\hat{\mathbf{C}}^H)^{-1}\mathbf{K}^{-1}\hat{\mathbf{a}}(\theta_o)}{\hat{\mathbf{a}}^H(\theta_o)\mathbf{K}^{-1}\hat{\mathbf{a}}(\theta_o)} \tag{4.32}$$

where $\mathbf{K} = \int \hat{\mathbf{a}}(\phi)\hat{\mathbf{a}}^H(\phi)\cos\phi d\phi$, $\hat{\mathbf{a}}(\phi)$ is the steering vector formed using the estimated sensor positions, and $\hat{\mathbf{C}}$ is the estimated coupling matrix. The range of the integral for calculating $\mathbf{K}$ is over the sidelobe region (i.e. the region outside the main beam). The array beampattern is then obtained as

$$B_{\theta_o}(\phi) = \left\|\mathbf{w}^H(\theta_o)\mathbf{v}(\phi)\right\|^2 \tag{4.33}$$

where $\theta_o$ is the steer direction of the beam, $\phi$ is the signal bearing considered, $\mathbf{v}(\phi)$ is the actual steering vector including the effects of mutual coupling (i.e. $\mathbf{v}(\phi) = \mathbf{C}\mathbf{a}(\phi)$). The sidelobe levels can then be calculated.

To determine the sidelobe levels obtained using the parameters estimated above, the sidelobe region required to compute matrix $\mathbf{K}$ was chosen such that the resulting beam had the same

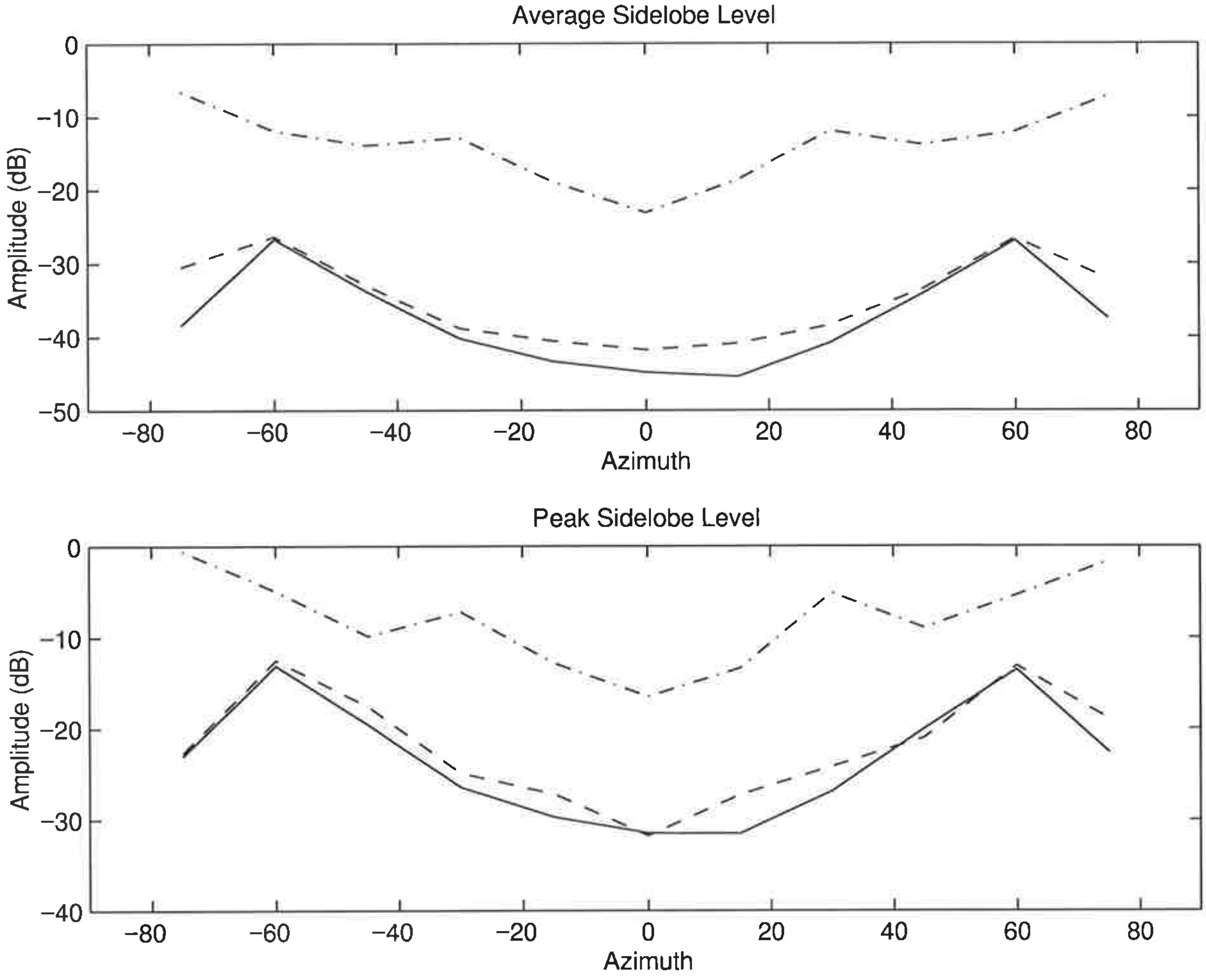

Figure 4.2: Average and peak sidelobe levels for parameters estimated in figure 4.1 - nominal parameters (—.—), estimated parameters (— —) and actual parameters (–).

beamwidth as that obtainable using the Hamming window. The average and peak sidelobe levels, obtained using equation (4.33), are shown in figure 4.2 as a function of look direction ($\theta_o$). The sidelobe levels using the estimated parameters (— —) are fairly close to the sidelobe levels for the actual parameters (–), and significantly better than those for the nominal parameters (—.—). Hence it can be concluded that the algorithm has performed quite well.

Next the performance of the algorithm with the full experimentally measured coupling matrix, is considered as discussed before. The results obtained are shown in figure 4.3. The results are clearly poor. The amplitude of the estimated coupling matrix is quite different from the amplitude of the actual matrix; the root-mean-square estimation error being 0.47. Large discrepancies are also observed in the phase values; the root-mean-square estimation error being 1.17 radians. The estimated sensor positions are not close to the true sensor positions, with the mean difference being about 0.015 wavelengths. The DOAs estimated were $-45.7^\circ$, $-0.5^\circ$ and $+45.2^\circ$.

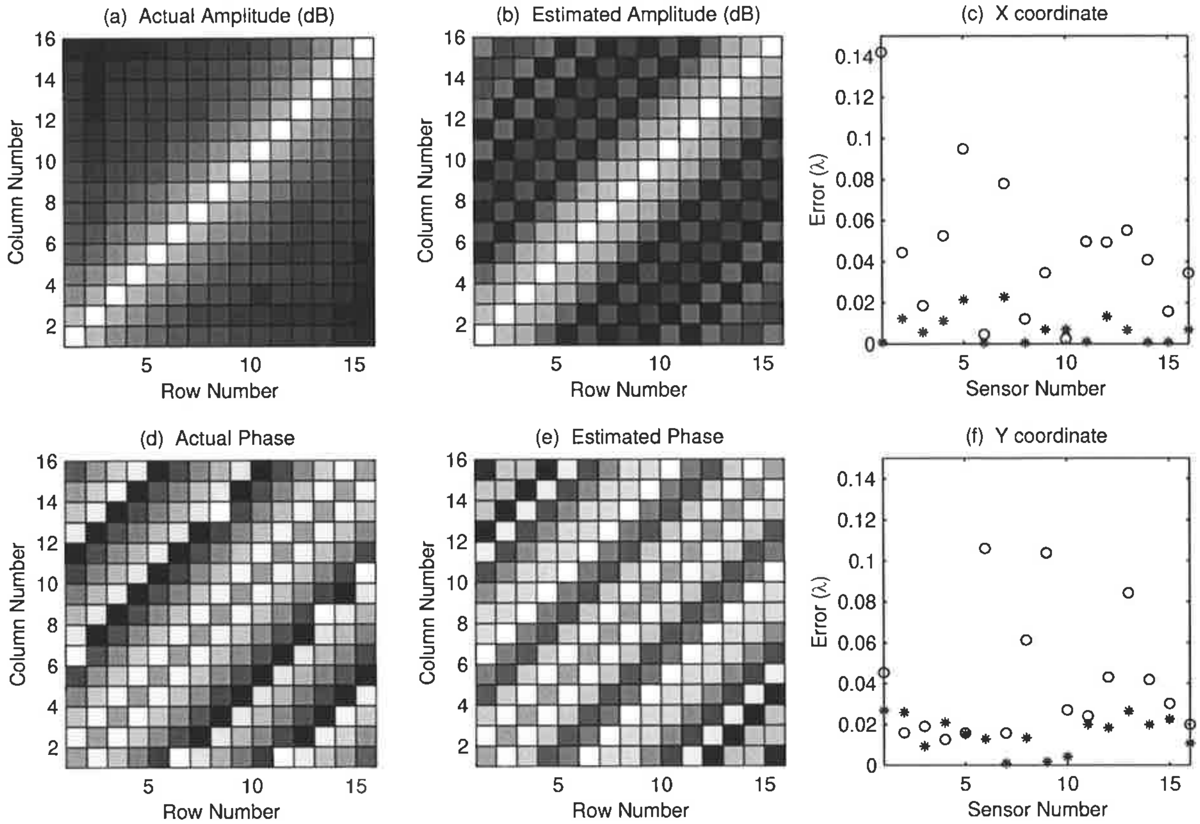

Figure 4.3: Generalised Weiss-Friedlander method's performance - full measured coupling matrix.

The sidelobe levels in this case are shown in figure 4.4. As expected the results are not as good as those in figure 4.2, with the sidelobe levels for the estimated parameters much worse than that for the actual parameters. Similar results were obtained for several simulations conducted, with different sensor position errors and coupling matrices. No significant improvement was observed when the number of sources used for array calibration was increased.

While this algorithm does well for Toeplitz coupling matrices, the algorithm is unsatisfactory for this experimentally measured coupling matrix. Hence an alternate model for the coupling matrix needs to be considered.

## 4.4 Modified Algorithm for OTH radars

Any coupling matrix $\mathbf{C}$ is equal to its transpose due to the 'reciprocity' theorem, which states that the energy received by element $k$ due to the re-radiation of element $m$ is equal to the energy received by element $m$ due to the re-radiation by element $k$. This was found to be valid in experimentally measured $\mathbf{C}$. Hence it was decided, for the array calibration algorithms developed in this thesis, to only restrict the coupling matrix to be symmetric. Note this model,

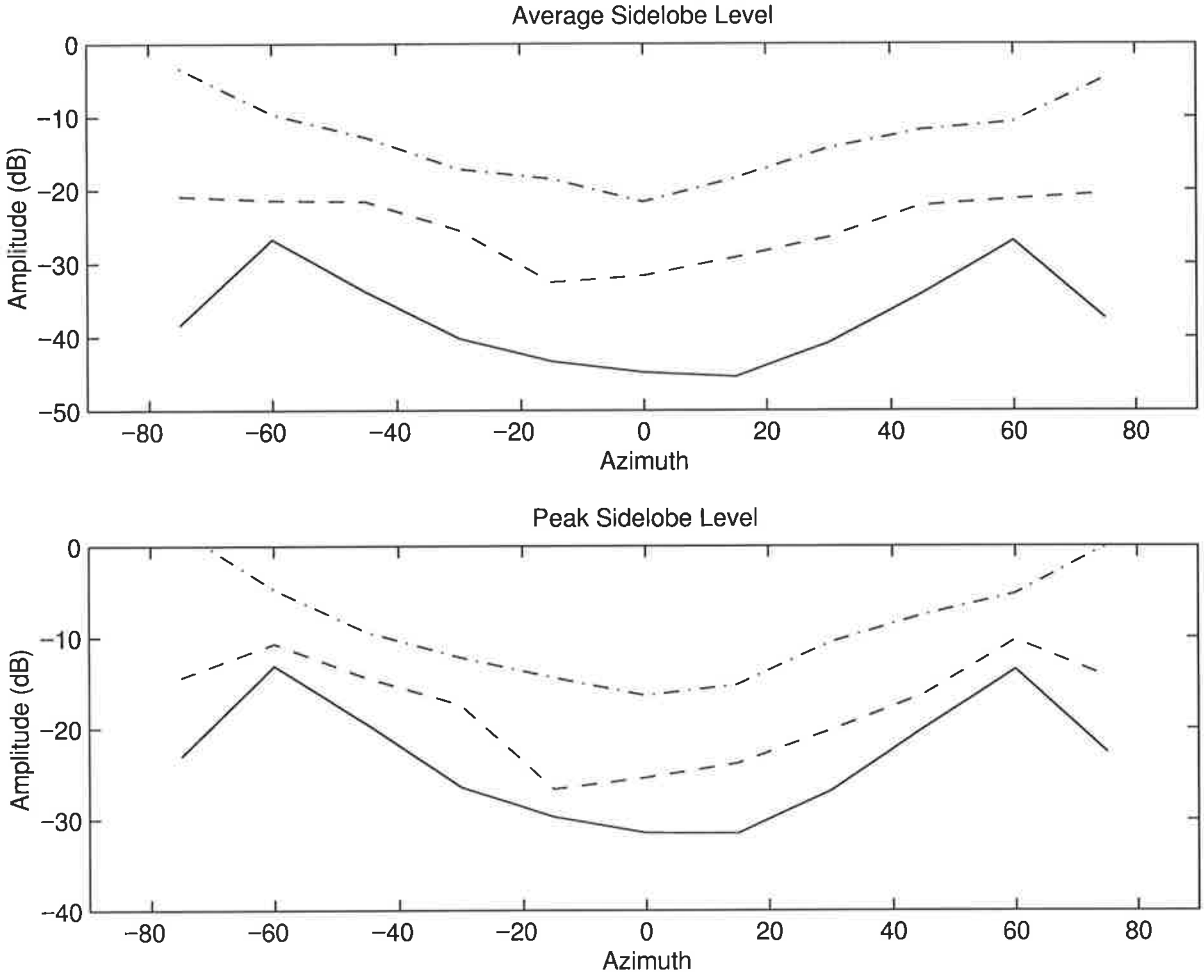

Figure 4.4: Average and peak sidelobe levels for parameters estimated in figure 4.3 - nominal parameters (—.—), estimated parameters (— —) and actual parameters (—).

unlike a symmetric Toeplitz model, does not restrict the coupling, between all equally spaced elements, to be the same. Further this model is applicable for arrays of arbitrary geometry.

Modifications to the generalised Weiss-Friedlander method are made : (a) so that a symmetric coupling matrix can be estimated; and (b) so that disjoint (single-mode) sources (in the form of meteor trail echoes) can be used for performing array calibration. Recall disjoint here means that the sources do not occupy both the same time snapshots and the same radar range cells.

For a single source, the vector of sensor outputs is

$$\mathbf{z}_1(t) = \mathbf{C}\mathbf{\Gamma}\mathbf{a}(\theta_1)s_1(t) + \mathbf{n}(t) \tag{4.34}$$

The covariance matrix for this signal, assuming zero mean noise, is

$$\mathbf{R}_1 = E\{\mathbf{z}_1(t)\mathbf{z}_1^H(t)\} \tag{4.35}$$

Now consider $N$ disjoint sources/echoes. As will be shown in chapter 7 most meteor trail echoes observed are resolvable in time and range, indicating different underlying physical mechanisms, and hence these sources will be represented here as statistically disjoint sources. The exact covariance matrix for the $n$th disjoint source/echo is

$$\mathbf{R}_n = E\{\mathbf{z}_n(t)\mathbf{z}_n^H(t)\} \tag{4.36}$$

where $\mathbf{z}_n(t)$ is the vector of $M$ sensor outputs for the $n$th disjoint source/echo.

The problem is then to estimate the sensor positions and coupling matrix, given the $N$ estimated covariance matrices. It is assumed here that the data $\mathbf{z}_n(t)$ have been corrected for receiver gain/phase errors (so $\mathbf{\Gamma} = \mathbf{I}_M$), by injecting signals internally at the receiver inputs.

The modified cost function used is

$$Q = \sum_{n=1}^{N} \left\|\hat{\mathbf{U}}^H(n)\mathbf{C}\mathbf{a}(\theta_n)\right\|^2 \tag{4.37}$$

where $\hat{\mathbf{U}}(n)$ is obtained from the eigendecomposition of the $n$th estimated covariance matrix $\hat{\mathbf{R}}_n$. Note in the generalised Weiss-Friedlander method $\hat{\mathbf{U}}$ is independent of $n$, and is created from the single covariance matrix of the non-disjoint sources.

The cost function in (4.37) is a least squares formulation of $N(M-1)$ complex equations. There are $2M-3$ unknown sensor positions, $N$ unknown DOAs, and $(M(M+1)-2)$ unknown coupling parameters (since one estimates a complex symmetric coupling matrix up to an arbitrary complex scalar). Hence a solution can exist only if $(2M-3)+N+(M(M+1)-2) \leq 2N(M-1)$ which implies $N \geq (M^2+3M-5)/(2M-3)$; for example for a 16-element array $N \geq 11$. Note if non-disjoint sources are used, the number of complex equations would be $N(M-N)$, so clearly by using disjoint sources one can estimate many more parameters for a given number of sources. (Note also for disjoint sources $N$ can be greater than $M$).

The proposed iterative procedure for minimising cost function (4.37) again contains three steps. The **first step** uses the best estimates of sensor positions and coupling values available, and estimates the $N$ DOAs using the MUSIC algorithm for each disjoint source, as follows

$$p_n(\theta) = \frac{1}{\|\hat{\mathbf{U}}^H(n)\mathbf{C}\mathbf{a}(\theta)\|^2} \quad n = 1, 2, ..., N \tag{4.38}$$

The DOA corresponding to the peak value of $p_n(\theta)$ is the estimated DOA for the $n$th signal.

The DOAs estimated, and the best available values of the coupling parameters, are then used in the **second step** to estimate the sensor positions. The sensor positions are estimated as in the generalised Weiss-Friedlander method, as

$$\mathbf{v_{xy}} = [Re\{\mathbf{B}^H\mathbf{B}\}]^{-1} Re\{\mathbf{B}^H\mathbf{Z}\} \tag{4.39}$$

where $\mathbf{B} = [\mathbf{B}^T(1), \mathbf{B}^T(2), ..., \mathbf{B}^T(N)]^T$, $\mathbf{Z} = [\mathbf{Z}^T(1), \mathbf{Z}^T(2), ..., \mathbf{Z}^T(N)]^T$, but here $\mathbf{B}(n) = -[\hat{\mathbf{U}}^H(n)\mathbf{C}\, diag\{\mathbf{a}_1(\theta_n)\}, \hat{\mathbf{U}}^H(n)\mathbf{C}\, diag\{\mathbf{a}_2(\theta_n)\}]$, $\mathbf{Z}(n) = \hat{\mathbf{U}}^H(n)\mathbf{C}\, \mathbf{a}_0(\theta_n)$, $\mathbf{a}_1(\theta_n) = j\mathbf{a}_0(\theta_n)(w/v)\sin(\theta_n)$, $\mathbf{a}_2(\theta_n) = j\mathbf{a}_0(\theta_n)(w/v)\cos(\theta_n)$. (An alternate method for estimating sensor positions is proposed later in this chapter.)

For the **third step**, estimation of the symmetric coupling matrix, one writes $\mathbf{C}\mathbf{a}(\theta_n)$ as $\mathbf{W}(\theta_n)\mathbf{c}$ so that as before the cost function can be written as

$$Q = \mathbf{c}^H \left\{ \sum_{n=1}^{N} \mathbf{W}^H(\theta_n)\hat{\mathbf{U}}(n)\hat{\mathbf{U}}^H(n)\mathbf{W}(\theta_n) \right\} \mathbf{c} \tag{4.40}$$

and obtain the quadratic minimum for estimating $\mathbf{c}$, under the constraint $c_1 = 1$, as

$$\mathbf{c} = \frac{\mathbf{G}^{-1}\mathbf{u}}{\mathbf{u}^H\mathbf{G}^{-1}\mathbf{u}} \tag{4.41}$$

where here $\mathbf{G} = \sum_{n=1}^{N} \mathbf{W}^H(\theta_n)\hat{\mathbf{U}}(n)\hat{\mathbf{U}}^H(n)\mathbf{W}(\theta_n)$ and $\mathbf{u} = [1, 0, ..., 0]^T$. It can be shown that for the symmetric coupling matrix model employed, the $M\text{x}M(M+1)$ matrix $\mathbf{W}(\theta_n)$ is

$$[\mathbf{W}]_{mk} = \begin{cases} a_{m+k-\rho(m)} & \rho(m) \le k \le \rho(m+1) - 1 \\ a_{m-l} & k = \rho(m-l) + l \quad \forall\, 1 \le l < (m-1) \\ 0 & \text{otherwise} \end{cases} \tag{4.42}$$

where

$$\rho(u) = \begin{cases} 1 & u = 1 \\ \rho(u-1) + (M - u + 2) & 2 \le u \le (M+1) \end{cases} \tag{4.43}$$

Note the expression for matrix $\mathbf{W}(\theta_n)$ is a new contribution.

Each of the three steps above decrease the cost function, and thus the algorithm is expected to converge. Simulations are now conducted to illustrate the performance of the algorithm. Note sensor position estimation must be performed before mutual coupling estimation since good sensor position estimates are possible even when the coupling matrix is unknown, but the reverse has been experimentally found to be not true.

## 4.5 Simulation Example

The experimentally measured coupling matrix [136] from the Jindalee OTH radar's transmitting array was again used in simulations for investigating whether disjoint sources could be used to estimate the coupling matrix parameters and sensor positions using this modified algorithm. Thirty disjoint signals, equally spread from $-90^{\circ}$ to $+90^{\circ}$ in azimuth, with SNR of 30 dB, were simulated. Covariance matrices for each signal were estimated, from 500 snapshots, and noise subspaces created (see the next section for the algorithm's performance for typical number of snapshots obtainable from meteor trail echoes).

Simulations were performed for a 16 element, nominally equispaced linear array with inter-element spacing of $d = 0.4\lambda$. The actual sensor positions were randomly generated as before. Note that while the designed array is a linear array, due to sensor position errors the actual array is not linear, and hence array calibration is possible (it has been observed that the Fisher information matrix, derived in section 6.1, is invertible for $y$ position errors of the magnitude considered).

The initial sensor positions were taken to be the nominal sensor positions, and the identity matrix was used as the initial value for the coupling matrix. The termination criterion was for the algorithm to stop when the cost function Q changed in value by less than 0.1 percent.

The results obtained are displayed in figure 4.5 :

- the cost function initially decreases rapidly, and then tends to level off after about 20 iterations;
- MUSIC, for the signal shown, is much sharper in the calibrated case (–) than the uncalibrated case ($--$);
- the DOA errors are fairly small;
- the magnitude and phase of the coupling matrix used, and the coupling matrix estimated, are in close agreement (the phase is unwrapped for easy comparison);
- the errors in the $x$ and $y$ coordinates, after the final iteration ($*$), are much smaller than the errors in the nominal values (o).

Using equation (A.9) the sidelobe levels can now be calculated. The average and peak

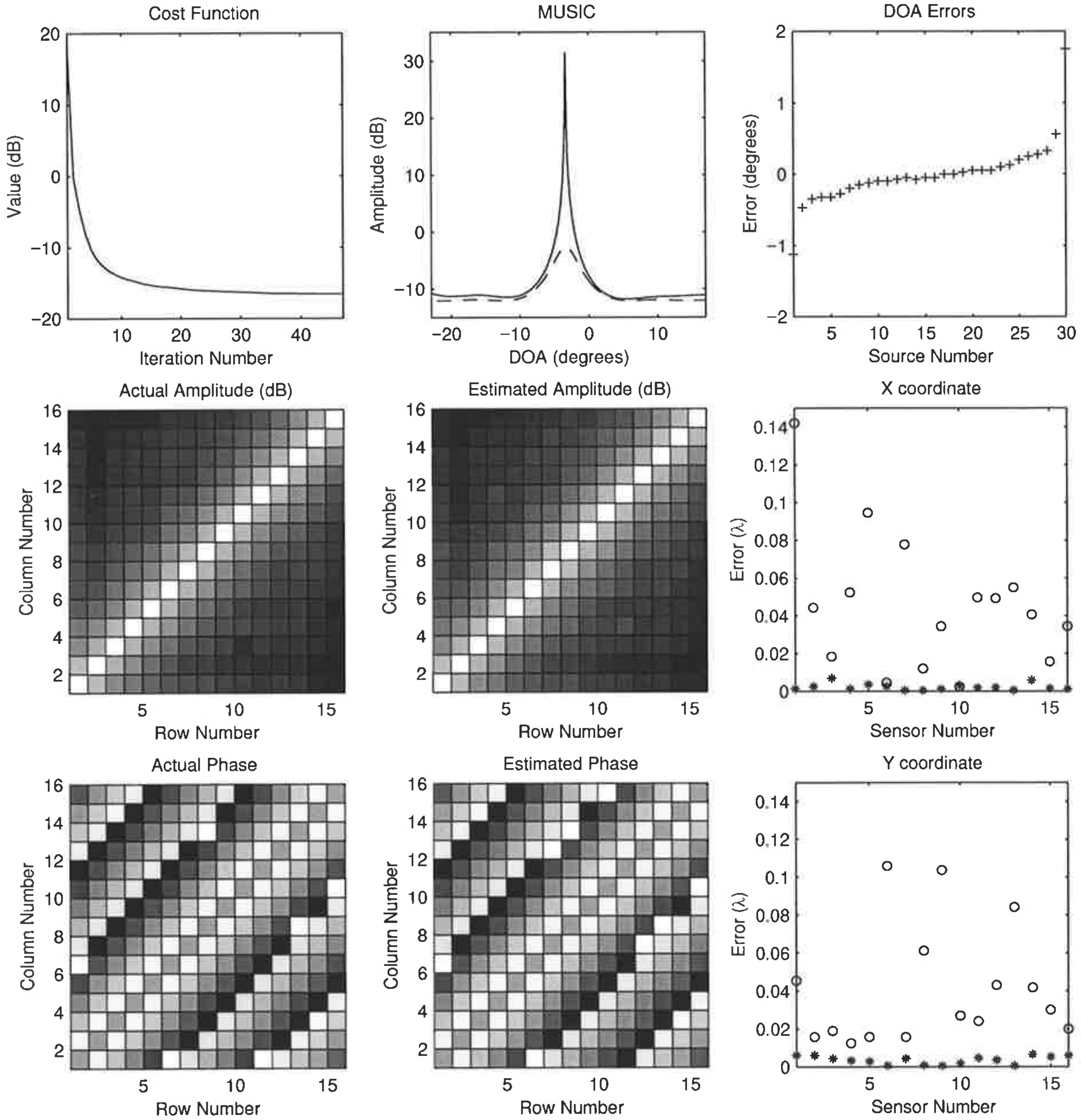

Figure 4.5: Performance of modified method - cost function decreases with iteration number; sharpening of MUSIC; errors in estimated source DOAs; actual coupling matrix and estimated coupling matrix; errors in nominal (o) and estimated (∗) sensor positions.

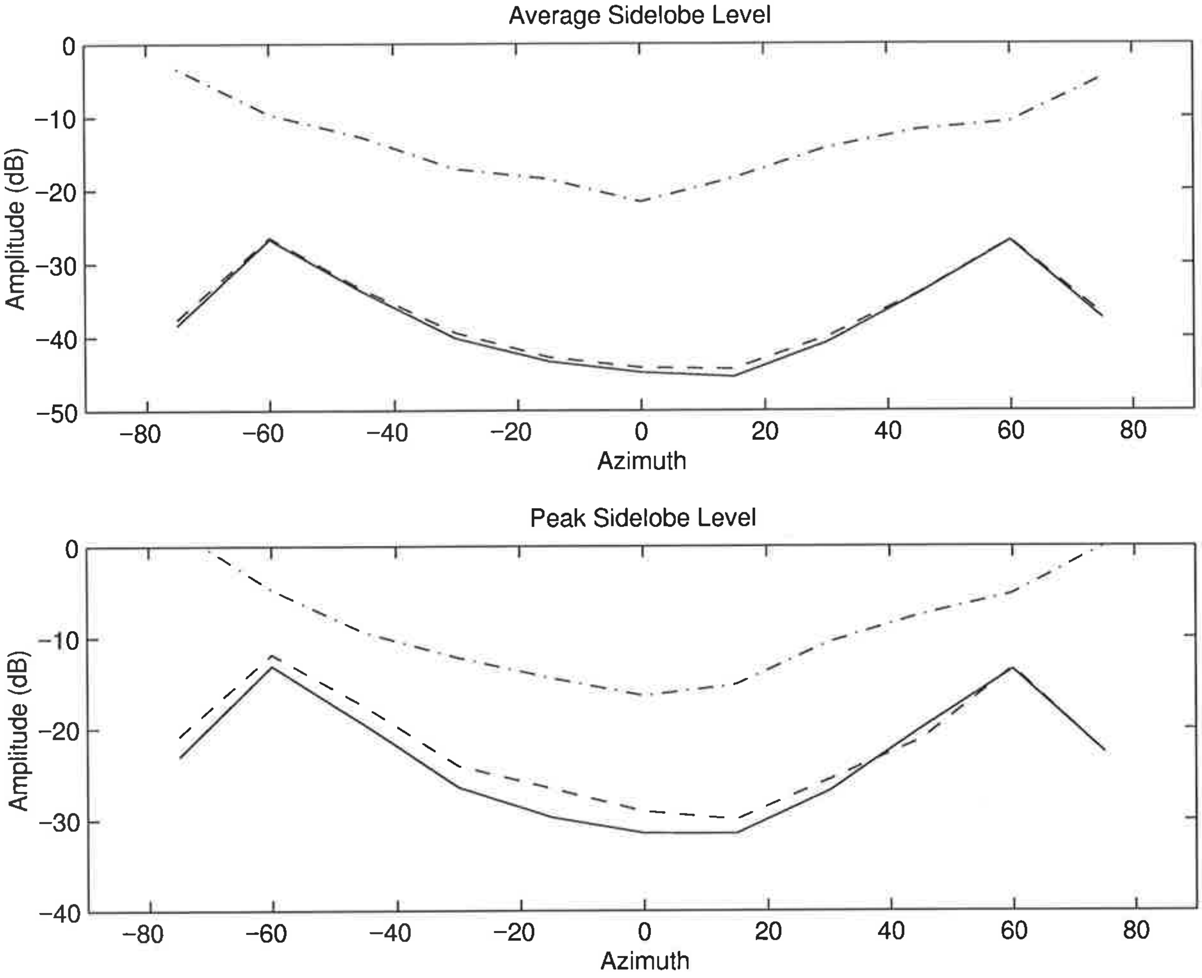

Figure 4.6: Average and peak sidelobe levels for parameters estimated in figure 4.5 - nominal parameters (–.–), estimated parameters (– –) and actual parameters (–).

sidelobe levels are shown in figure 4.6 for different look directions $\theta_o$, and hence are a function of azimuth. Clearly the algorithm has performed very well; the sidelobe levels for the estimated parameters (– –) being much better than the sidelobe levels for the nominal parameters (–.–), and being close to the sidelobe levels for the actual parameters (–). The modified algorithm has performed well in this example; further analysis of the algorithm is conducted next.

## 4.6 Monte Carlo Analysis

To analyse this algorithm's performance in detail, a Monte Carlo analysis was conducted. The performance measure considered is

$$\eta(\theta) = \frac{ASL_{nom}(\theta) - ASL_{est}(\theta)}{ASL_{nom}(\theta) - ASL_{act}(\theta)} * 100 \tag{4.44}$$

where $ASL_{nom}(\theta)$ is the average sidelobe level obtained with nominal parameters, $ASL_{est}(\theta)$ is the average sidelobe level obtained with estimated parameters, and $ASL_{act}(\theta)$ is the average sidelobe level obtained with actual parameters; each quantity expressed in dB, and a function of look direction $\theta$. Hence if $\eta(\theta)$ is small (close to zero) then the algorithm has not performed well, while if $\eta(\theta)$ is large (close to hundred) then the algorithm has performed well. This measure has been found to reflect well the performance of algorithms, and is thus used here.

Initially 100 simulations were conducted, with the sensor position errors being randomly generated in each case. The performance measure $\eta(\theta)$ is shown in figure 4.7 as a function of azimuth, for the 100 simulations. The results clearly indicate the algorithm has performed well in all cases. Note the same coupling matrix was used in all the simulations.

To test the algorithm's performance for typical SNRs and number of snapshots obtainable from meteor trail echoes (see chapter 7), simulations were conducted for different SNR-snapshot combinations. Two combinations are shown in figure 4.8; for the first case the SNRs are 20 dB and the number of snapshots are 5, while for the second case the SNRs are 30 dB and the number of snapshots are 10. Four failures (black vertical stripes) are seen in the first case, while no failures are seen in the second case. The performance measure (and hence the sidelobe level) is clearly better for the second case, where the SNRs and number of snapshots are larger. Note the algorithm's performance versus SNR is also considered in section 6.1.6, and the accuracy (standard deviations) of the estimated parameters was found to be inversely proportional to the square-root of the SNR.

Figure 4.9 shows the dependence of the algorithm on the number of sources. These simulations were performed for the same array, with 500 snapshots obtained from each of the 30 dB disjoint sources. When the number of sources is less than 16, the algorithm fails as there are insufficient sources for this algorithm to estimate the unknown parameters for 16-element arrays; note the necessary condition (see section 4.4) was for $N \geq 11$. When the number of sources is greater than about 18 the performance is essentially independent of the number of sources.

Overall, while the algorithm has done very well, one notes a few cases where it has failed. These failures could perhaps be overcome by using better initial values for the parameters being estimated, since in general one cannot guarantee convergence to the global minimum. Note for the coupling matrix, any modelled or previously estimated coupling matrix could be used as the initial value, instead of the identity matrix which has been used for these simulations.

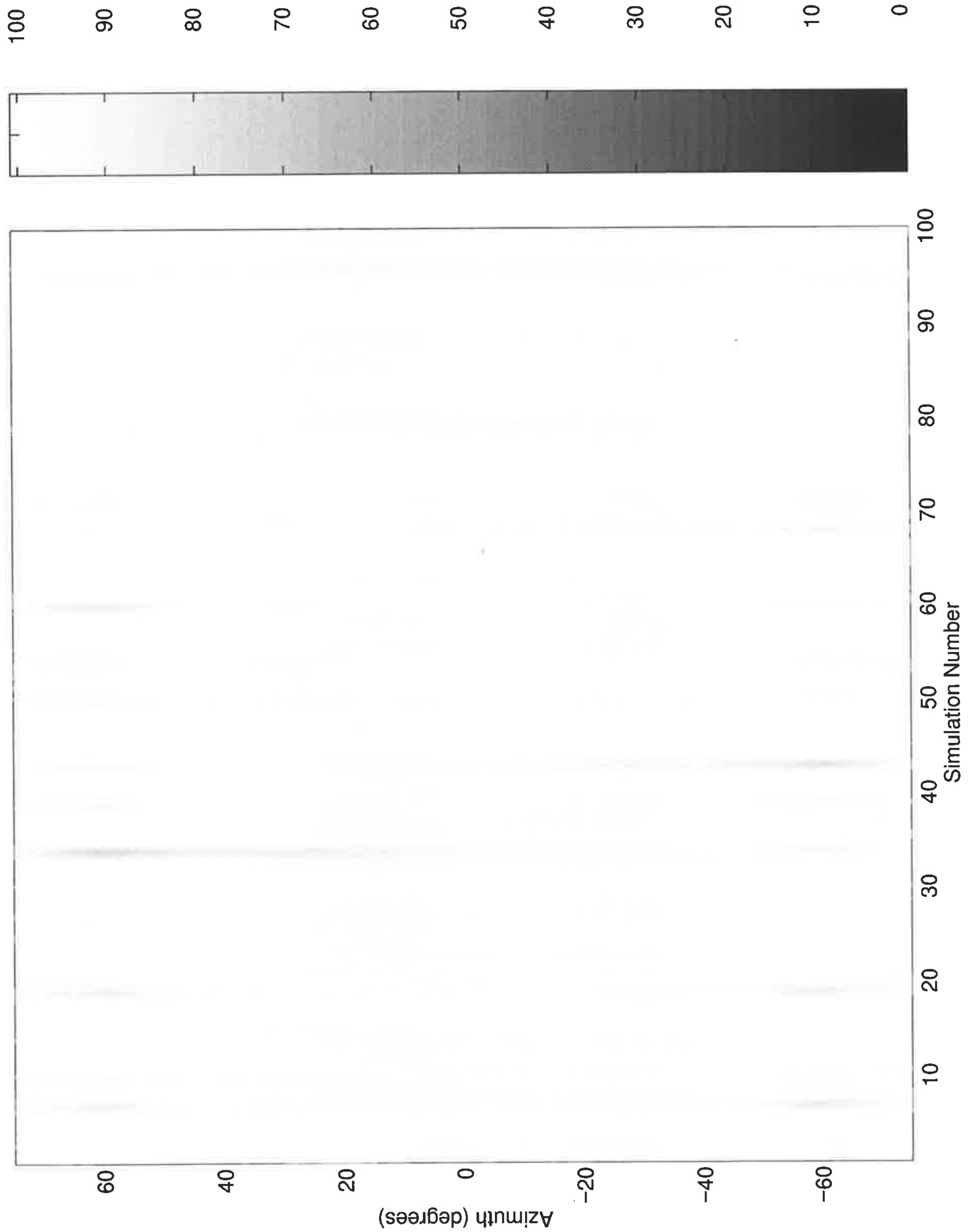

Figure 4.7: Statistical performance of algorithm.

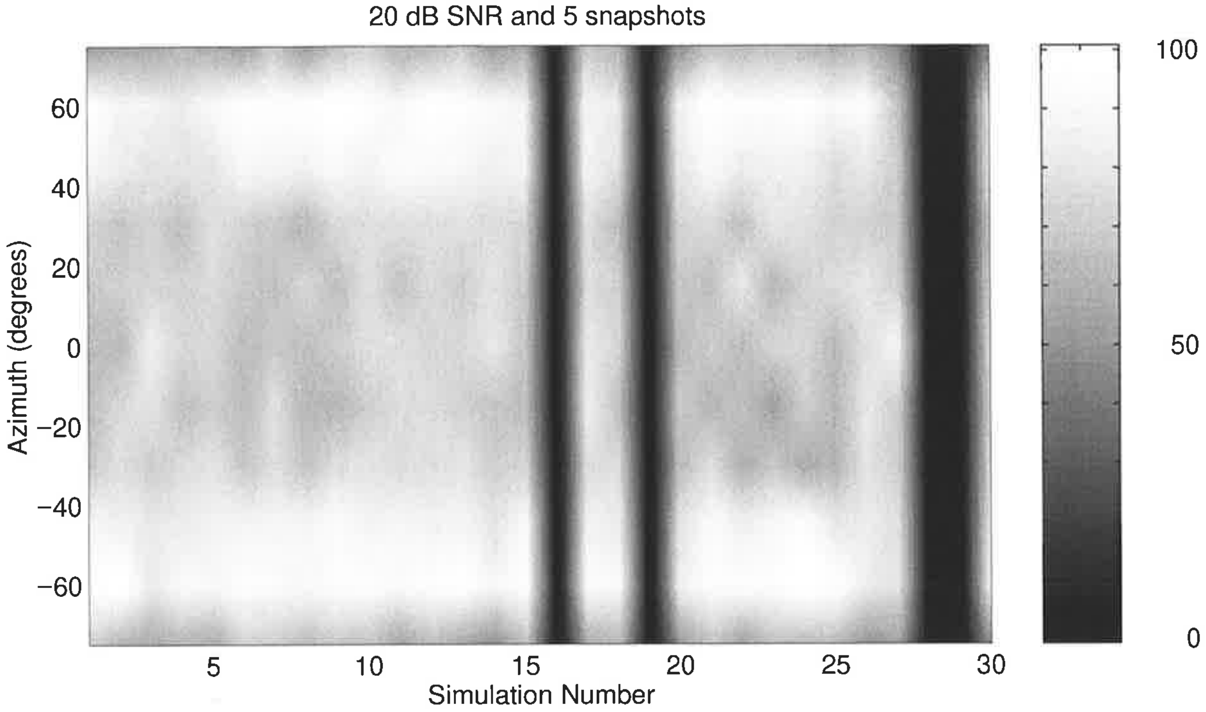

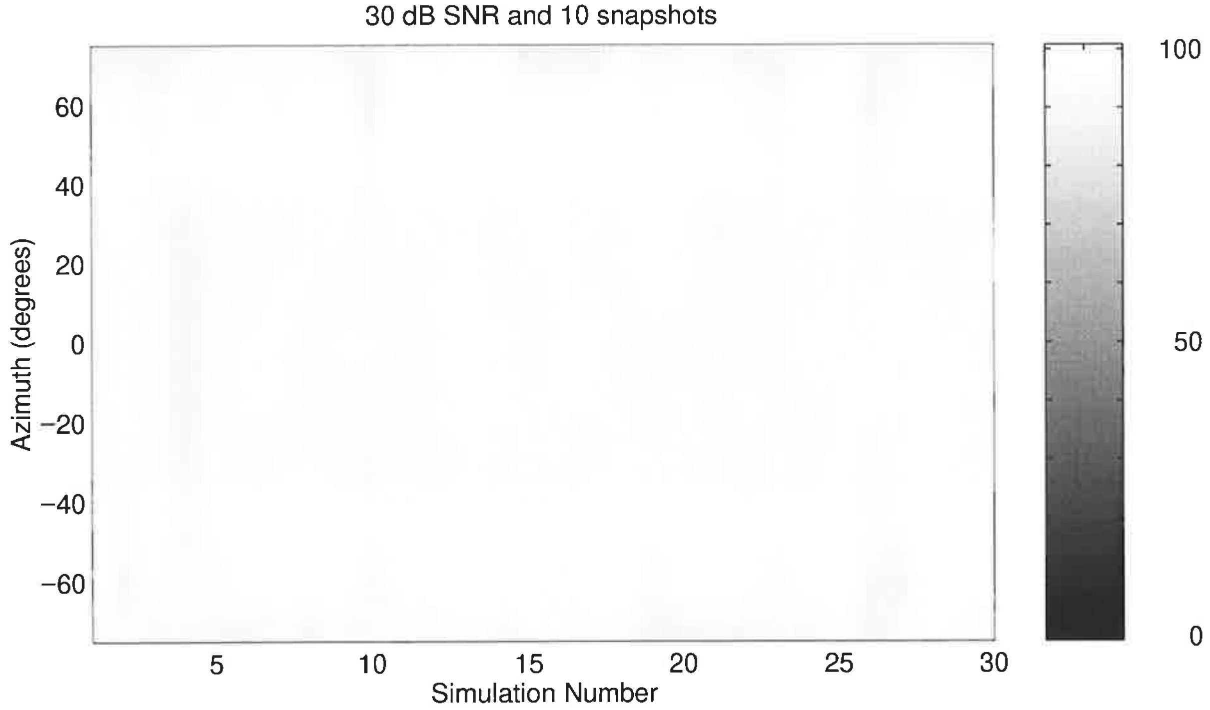

Figure 4.8: Algorithm's performance for typical SNRs and number of snapshots obtainable from meteor trail echoes.

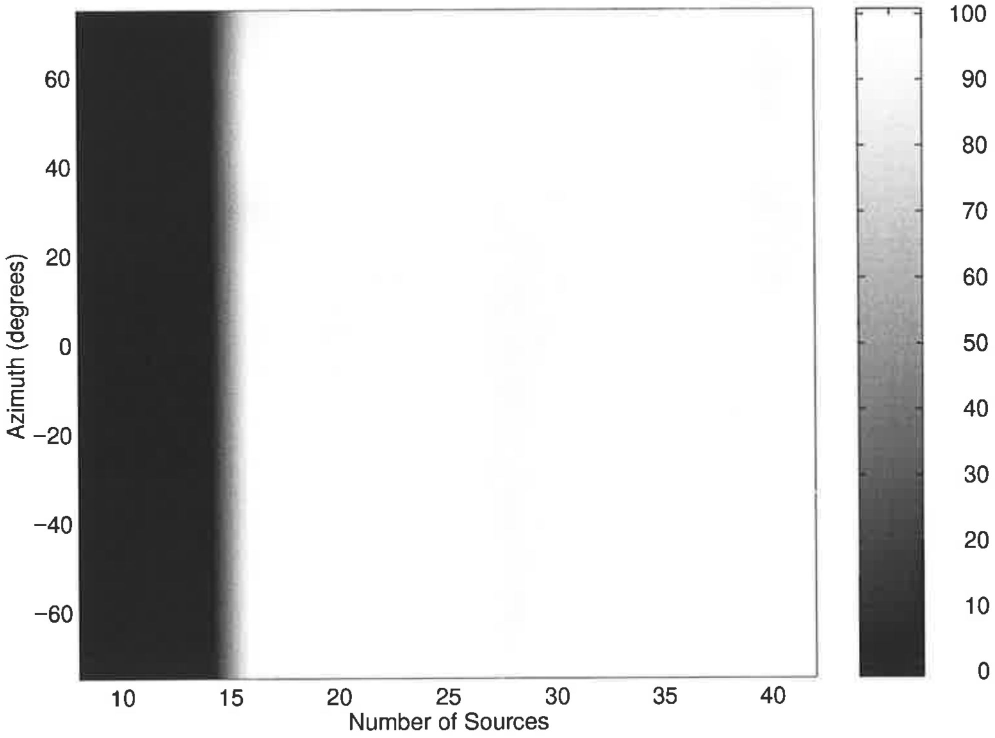

Figure 4.9: Dependence of algorithm on number of sources.

An alternate sensor position estimator, which was developed using a Newton search procedure, has been found to reduce the number of failures (i.e. the algorithm with this particular sensor position estimator had less failures). This procedure, which is the second contribution, is considered next.

## 4.7 Alternative Sensor Position Estimator

While the results obtained using the above method were good, a new sensor position estimator was developed and tested to see if the number of failures could be reduced for practical SNRs and number of snapshots.

Let $\gamma(k) = [\mathbf{x}(k)^T, \mathbf{y}(k)^T]^T$, where $\mathbf{x}(k)$ and $\mathbf{y}(k)$ are the vectors of estimated sensor positions after the $k$th iteration. Then the Newton method for obtaining the sensor positions after the $(k+1)$th iteration is

$$\gamma(k+1) = \gamma(k) - u\ \mathbf{H}(\gamma(k))^{-1}\ \mathbf{r}(\gamma(k)) \tag{4.45}$$

where $\mathbf{H}$ is the Hessian matrix for the sensor positions, $\mathbf{r}$ is the gradient vector for the sensor positions, and the step length is $0 < u < 1$. The $2M$x1 gradient vector is $\mathbf{r}(\gamma(k)) = [(\partial Q/\partial \mathbf{x}(k))^T, (\partial Q/\partial \mathbf{y}(k))^T]^T$, and the $2M$x$2M$ Hessian matrix is

$$\mathbf{H}(\gamma(k)) = \begin{bmatrix} \frac{\partial^2 Q}{\partial \mathbf{x}(k)\partial \mathbf{x}^T(k)} & \frac{\partial^2 Q}{\partial \mathbf{x}(k)\partial \mathbf{y}^T(k)} \\ \frac{\partial^2 Q}{\partial \mathbf{y}(k)\partial \mathbf{x}^T(k)} & \frac{\partial^2 Q}{\partial \mathbf{y}(k)\partial \mathbf{y}^T(k)} \end{bmatrix} \tag{4.46}$$

Now define $\dot{\mathbf{a}}_{x_p}(\theta_n) = \partial \mathbf{a}(\theta_n)/\partial x_p = \mathbf{dx_p} \odot \mathbf{a}(\theta_n)$, where $\odot$ is the Hadamard product and $\mathbf{dx_p}$ is an $M$ element vector with all but the $p$th element zero; the $p$th element is $(+2\pi j/\lambda)\sin(\theta_n)$, where $\lambda$ is the radar wavelength. Then from equation (4.37)

$$\begin{aligned}
\frac{\partial Q}{\partial x_p} &= \sum_{n=1}^{N} \left[\dot{\mathbf{a}}_{x_p}^H(\theta_n)\mathbf{C}^H\hat{\mathbf{U}}(n)\hat{\mathbf{U}}^H(n)\mathbf{C}\mathbf{a}(\theta_n) + \mathbf{a}^H(\theta_n)\mathbf{C}^H\hat{\mathbf{U}}(n)\hat{\mathbf{U}}^H(n)\mathbf{C}\dot{\mathbf{a}}_{x_p}(\theta_n)\right] \\
&= 2\Re\left\{\sum_{n=1}^{N} \mathbf{a}^H(\theta_n)\mathbf{C}^H\hat{\mathbf{U}}(n)\hat{\mathbf{U}}^H(n)\mathbf{C}(\mathbf{dx_p} \odot \mathbf{a}(\theta_n))\right\} \qquad (4.47)
\end{aligned}$$

and hence

$$\begin{aligned}
\frac{\partial^2 Q}{\partial^2 x_p} &= 2\Re\left\{\sum_{n=1}^{N} \left[(\mathbf{a}^H(\theta_n) \odot \mathbf{dx_p}^H)\mathbf{C}^H\hat{\mathbf{U}}(n)\hat{\mathbf{U}}^H(n)\mathbf{C}(\mathbf{dx_p} \odot \mathbf{a}(\theta_n))\right.\right. \\
&\qquad \left.\left. + \mathbf{a}^H(\theta_n)\mathbf{C}^H\hat{\mathbf{U}}(n)\hat{\mathbf{U}}^H(n)\mathbf{C}(\mathbf{dx_p} \odot \mathbf{dx_p} \odot \mathbf{a}(\theta_n))\right]\right\} \qquad (4.48) \\
\frac{\partial^2 Q}{\partial x_p \partial x_q} &= 2\Re\left\{\sum_{n=1}^{N} \left[(\mathbf{a}^H(\theta_n) \odot \mathbf{dx_q}^H)\mathbf{C}^H\hat{\mathbf{U}}(n)\hat{\mathbf{U}}^H(n)\mathbf{C}(\mathbf{dx_p} \odot \mathbf{a}(\theta_n))\right.\right. \\
&\qquad \left.\left. + \mathbf{a}^H(\theta_n)\mathbf{C}^H\hat{\mathbf{U}}(n)\hat{\mathbf{U}}^H(n)\mathbf{C}(\mathbf{dx_p} \odot \mathbf{dx_q} \odot \mathbf{a}(\theta_n))\right]\right\} \\
&= 2\Re\left\{\sum_{n=1}^{N} \left[(\mathbf{a}^H(\theta_n) \odot \mathbf{dx_q}^H)\mathbf{C}^H\hat{\mathbf{U}}(n)\hat{\mathbf{U}}^H(n)\mathbf{C}(\mathbf{dx_p} \odot \mathbf{a}(\theta_n))\right]\right\} \qquad (4.49)
\end{aligned}$$

where $\Re\{\}$ is the real part, $q \neq p$ and $\mathbf{dx_q}$ is an $M$ element vector with all but the $q$th element zero; the $q$th element is $(+2\pi j/\lambda)\sin(\theta_n)$.

The partial derivatives with respect to the $y$ coordinates are similarly obtained as

$$\begin{aligned}
\frac{\partial Q}{\partial y_p} &= 2\Re\left\{\sum_{n=1}^{N} \mathbf{a}^H(\theta_n)\mathbf{C}^H\hat{\mathbf{U}}(n)\hat{\mathbf{U}}^H(n)\mathbf{C}(\mathbf{dy_p} \odot \mathbf{a}(\theta_n))\right\} \qquad (4.50) \\
\frac{\partial^2 Q}{\partial^2 y_p} &= 2\Re\left\{\sum_{n=1}^{N} \left[(\mathbf{a}^H(\theta_n) \odot \mathbf{dy_p}^H)\mathbf{C}^H\hat{\mathbf{U}}(n)\hat{\mathbf{U}}^H(n)\mathbf{C}(\mathbf{dy_p} \odot \mathbf{a}(\theta_n))\right.\right. \\
&\qquad \left.\left. + \mathbf{a}^H(\theta_n)\mathbf{C}^H\hat{\mathbf{U}}(n)\hat{\mathbf{U}}^H(n)\mathbf{C}(\mathbf{dy_p} \odot \mathbf{dy_p} \odot \mathbf{a}(\theta_n))\right]\right\} \qquad (4.51)
\end{aligned}$$

$$\frac{\partial^2 Q}{\partial y_p \partial y_q} = 2\Re\left\{\sum_{n=1}^{N}\left[(\mathbf{a}^H(\theta_n)\odot\mathbf{dy_q}^H)\mathbf{C}^H\hat{\mathbf{U}}(n)\hat{\mathbf{U}}^H(n)\mathbf{C}(\mathbf{dy_p}\odot\mathbf{a}(\theta_n))\right]\right\} \quad (4.52)$$

where $\mathbf{dy_p}$ is an $M$ element vector with all but the $p$th element zero; the $p$th element is $(+2\pi j/\lambda)\cos(\theta_n)$.

The $\partial^2 Q/\partial x_p \partial y_p$ and $\partial^2 Q/\partial x_p \partial y_q$ terms are

$$\begin{aligned}\frac{\partial^2 Q}{\partial x_p \partial y_p} &= 2\Re\left\{\sum_{n=1}^{N}\left[(\mathbf{a}^H(\theta_n)\odot\mathbf{dy_p}^H)\mathbf{C}^H\hat{\mathbf{U}}(n)\hat{\mathbf{U}}^H(n)\mathbf{C}(\mathbf{dx_p}\odot\mathbf{a}(\theta_n))\right.\right.\\ &\qquad \left.\left.+\mathbf{a}^H(\theta_n)\mathbf{C}^H\hat{\mathbf{U}}(n)\hat{\mathbf{U}}^H(n)\mathbf{C}(\mathbf{dx_p}\odot\mathbf{dy_p}\odot\mathbf{a}(\theta_n))\right]\right\} \quad (4.53)\\ \frac{\partial^2 Q}{\partial x_p \partial y_q} &= 2\Re\left\{\sum_{n=1}^{N}\left[(\mathbf{a}^H(\theta_n)\odot\mathbf{dy_q}^H)\mathbf{C}^H\hat{\mathbf{U}}(n)\hat{\mathbf{U}}^H(n)\mathbf{C}(\mathbf{dx_p}\odot\mathbf{a}(\theta_n))\right]\right\} \quad (4.54)\end{aligned}$$

The algorithm's performance with this sensor position estimator is shown in figure 4.10. The cases considered here are the same as those in figure 4.8, where (a) the SNRs are 20 dB and the number of snapshots are 5, and (b) the SNRs are 30 dB and the number of snapshots are 10. The results obtained are as good as those in figure 4.8, but note no failures are present here unlike in figure 4.8 for case (a) where four failures (13 percent) were obtained (the improvements obtained here are attributed to the use of the second derivative in the Newton method).

## 4.8 Performance Criteria

In practice, after running an array calibration algorithm, it is highly desirable to know whether the algorithm has been successful in achieving accurate calibration. In other words it would be nice if there was some easy to determine performance criteria by which one can test if an array calibration procedure has in fact been successful.

One possible approach is to use a set of disjoint meteor trail echoes, distinct from the echoes used to calibrate the array. The criterion is based on the fact that if effective array calibration has been performed then the integrated sidelobe level will be much lower than without any array calibration. Consider $N$ disjoint meteor echoes, with covariance matrices $\mathbf{R}_1, \mathbf{R}_2, \ldots, \mathbf{R}_N$. It is assumed that the meteor echoes are line-of-sight echoes, or have propagated via a single ionospheric layer, and hence each covariance matrix only contains one signal (see chapter 7). The criterion proposed is the integrated sidelobe level, which for $K$ different beams (steering

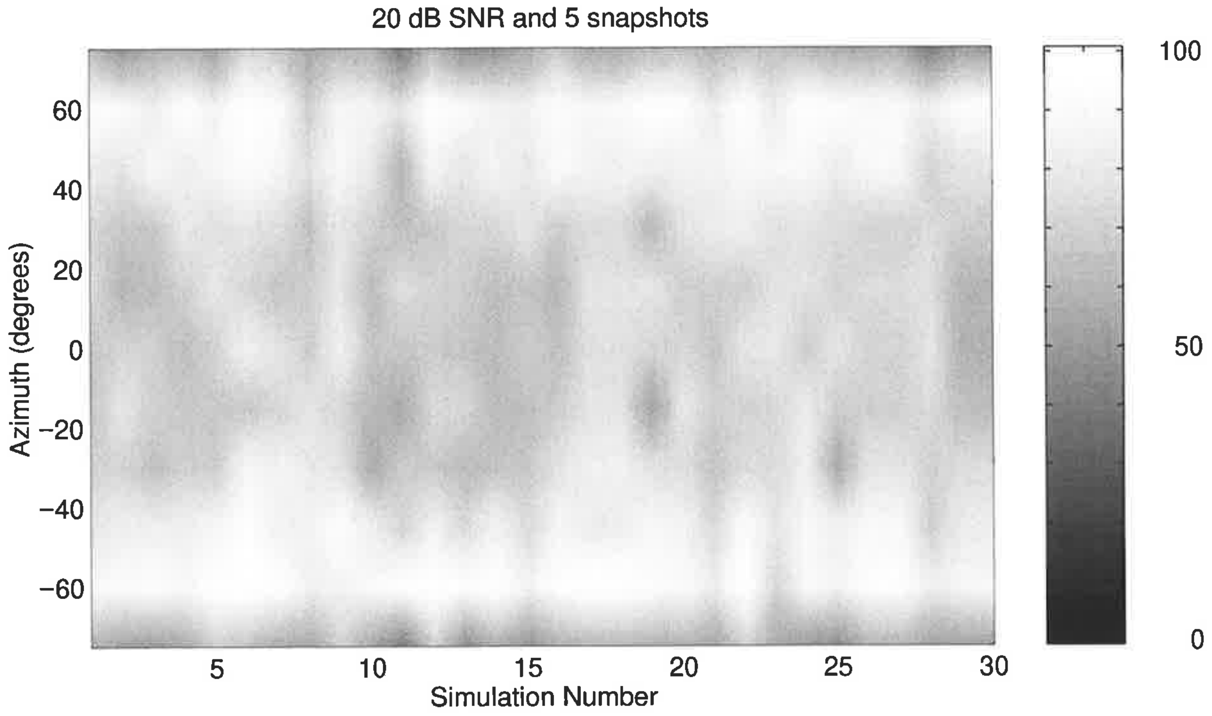

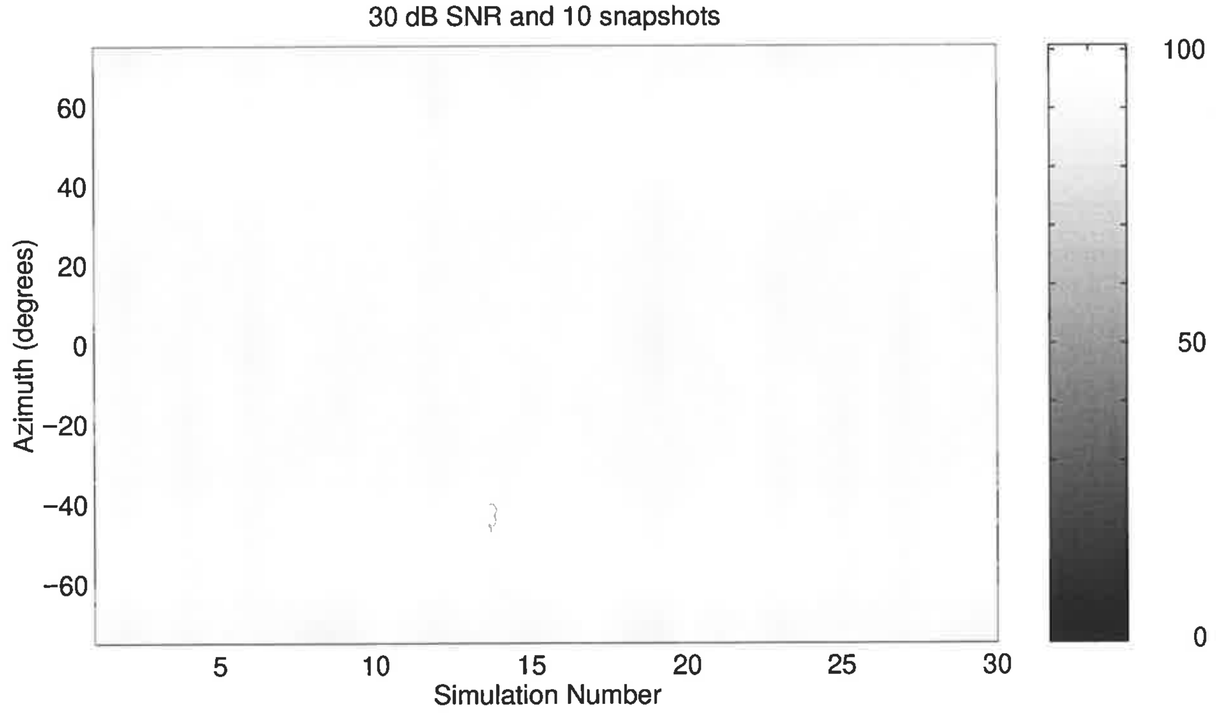

Figure 4.10: Algorithm's performance with alternative sensor position estimator, for typical SNRs and number of snapshots obtainable from meteor trail echoes.

directions) is

$$ISLB = \sum_{k=1}^{K} \sum_{l=1}^{L} B_{\theta_k}(\theta_{kl}) \cos(\theta_{kl}) \tag{4.55}$$

where $B_{\theta_k}(\theta)$ is the beampattern of the $k$th beam, and $\theta_{kl}$ is a sidelobe direction for this beam. Note for the $k$th beam, only echoes in the $k$th beam's sidelobes are to be used with this criterion, and hence this criterion requires $L$ meteor echoes to be present in the sidelobes of each beam. It is possible to determine which echoes are in the sidelobes of a given beam, since even for uncalibrated arrays, bearing errors are not large (see chapter 3). Equation (4.55) can be expressed in terms of the meteor echo principal eigenvectors as follows

$$ISLB = \sum_{k=1}^{K} \sum_{l=1}^{L} \left|\mathbf{w}^H(\theta_k)\mathbf{v}_{kl}\right|^2 \cos(\theta_{kl}) \tag{4.56}$$

where $\mathbf{v}_{kl}$ is the (normalised) principal eigenvector, for a meteor echo in the sidelobes of the $k$th beam.

The $ISLB$ using the uncalibrated optimal $\mathbf{w}$ (see section 4.3) is compared to the $ISLB$ using the calibrated optimal $\mathbf{w}$. If the $ISLB$ is sufficiently better for the calibrated case then array calibration has been successful, and if not then array calibration has been unsuccessful. In fact, the $ISLB$ level can be used to quantify the array calibration performance. Using this measure on the simulation example in figure 4.5-4.6, the ISLB is -9.6 dB for the uncalibrated case and -32.7 dB for the calibrated case (the ISLB is -32.9 dB for the perfectly calibrated case).

Note equation (4.56) consists of two components : (a) contributions from the meteor echoes towards the ISLB; and (b) white noise contributions. To get a measure of the ISLB the meteor echo powers must be well above the noise-level power. This can only be guaranteed if the echo powers are say 10dB or more above the array sidelobe levels required. An alternative approach is to use one very strong source, such as the radar transmitter signal. (Note the transmitter signal, for certain radar configurations, is seen in the early ranges (as in figure 1.2) and so the covariance matrix can be estimated for this source). The integrated sidelobe level can then be estimated as follows

$$ISLB = \sum_{k=1}^{K} |\mathbf{w}^H(\theta_k)\mathbf{v}|^2 \cos(\theta) \tag{4.57}$$

where $\mathbf{v}$ is the principal eigenvector of the source, and $\theta$ is the direction of the source.

Figure 4.11(a) shows the ISLB value for this criterion when applied to the example in figure 4.5-4.6; the uncalibrated (–.–), calibrated (– –) and perfectly known (–) cases are shown.

The ISLB values are shown as a function of the DOA of the strong source used to form the criterion. The results indicate that this criterion can clearly distinguish the uncalibrated and well calibrated cases, and also that the results are not significantly influenced by the DOA of the strong source used to form the criterion. Figure 4.11(b) shows a measure analogous to $\eta(\theta)$ in equation (4.44), applied in this case to the three curves in figure 4.11(a). The values around 100 illustrate the good discriminating ability of the criterion.

## 4.9 Mutual Coupling Estimation Investigation

The simulations conducted thus far for the modified algorithm, used the coupling matrix experimentally measured from the Jindalee transmitting array. To further test the mutual coupling estimation performance, coupling matrices from another OTH radar were considered; this radar being located in Longreach in Queensland. This radar is one of the two radars making up the Jindalee Operational Radar Network (JORN), which is currently being constructed for long range surveillance.

The coupling matrices considered were for the transmitting array, and were measured over the frequency range of 5-12 MHz. This measured data was in the form of scattering matrices. A scattering matrix relates the forward and backward voltages on antennas, and is related to the coupling matrix as follows (excluding a scaling constant) [211]

$$\mathbf{C} = \mathbf{I}_M + \mathbf{S}_C \tag{4.58}$$

where $\mathbf{I}_M$ is the identity matrix and $\mathbf{S}_C$ is the scattering matrix. Using this equation, it is possible to obtain coupling matrices from the scattering matrices.

Figure 4.12 shows the first row of a Longreach coupling matrix; that is the coupling values between each antenna element and the first antenna element. The amplitude variation in figure 4.12(a) indicates that the coupling between the first and the second elements is about -15 dB, and that the coupling between the first and other elements drop off steadily as the distance between the element and the first element increases. For the Jindalee transmitter's coupling matrix the coupling between the first two elements was about -7 dB, and the drop off in coupling values between the first element and elements further along the array was much less. In figure 4.12(a) the coupling between the first and last (fourteenth) element is about -25 dB, compared with the Jindalee coupling matrix where the coupling between the first and last element (sixteenth element) is about -16 dB. The phase variation, shown in figure 4.12(b),

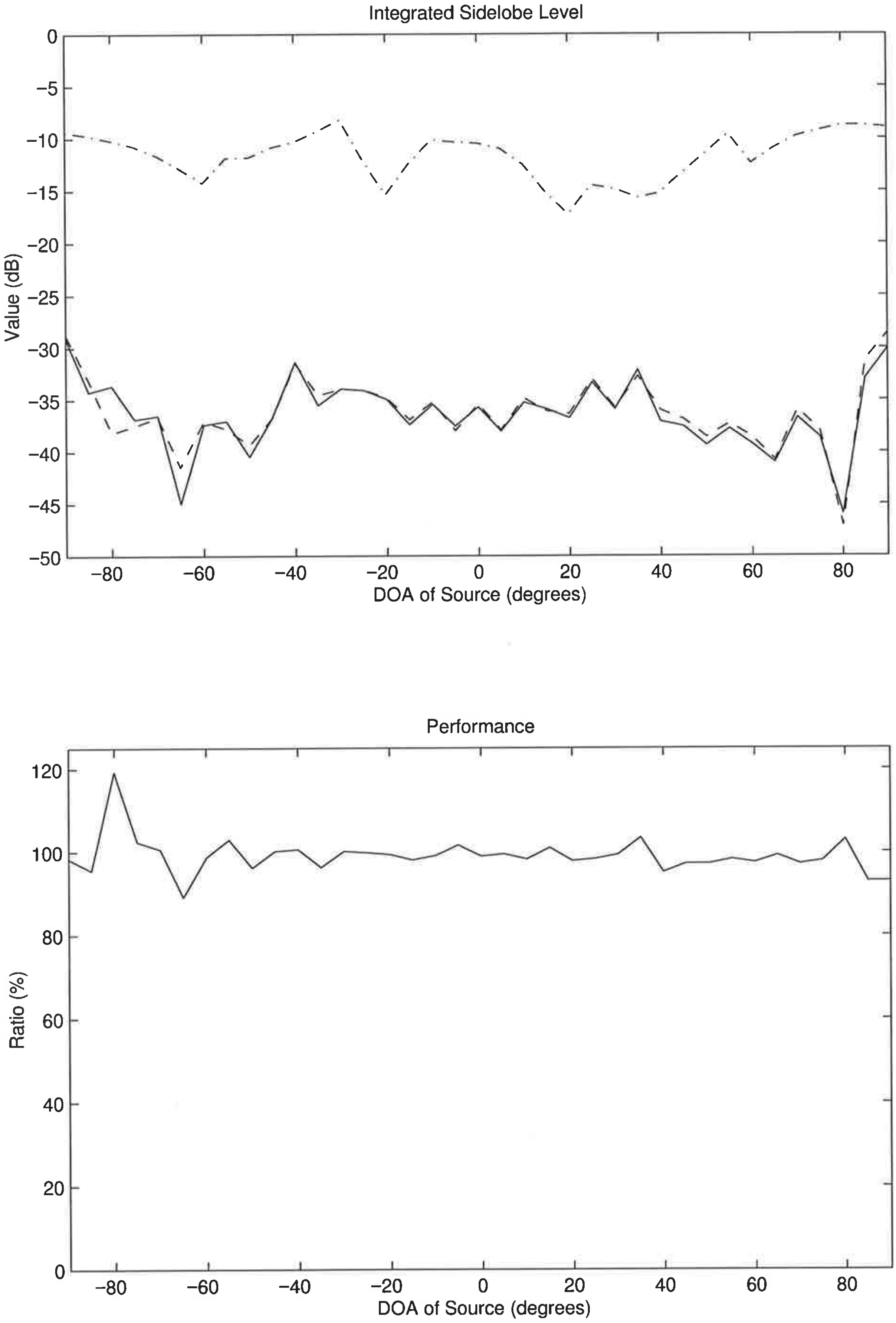

Figure 4.11: Performance Criteria - (a) integrated sidelobe level (ISLB) for uncalibrated (−.−), calibrated (− −) and perfectly known (–) cases; (b) measure of performance.

illustrates that the phase varies approximately linearly with element spacing, however some curvature is apparent.

The coupling matrix considered in figure 4.12 was for 5.0 MHz. Figure 4.13 shows the first row of all the coupling matrices obtained, from 5-12 MHz. The amplitude values shown have been normalised so that the coupling between the first element and itself is 0 dB. As would be expected, the coupling values drop off with increasing frequency (since the inter-element spacing in wavelengths, increase). The coupling between the first two elements decreases from about -15 dB at 5.0 MHz to about -25 dB at 12.0 MHz. The coupling between the two end elements in the array decreases from about -25 dB at 5.0 MHz to about -50 dB at 12.0 MHz. The coupling values for this array are much lower than those obtained for the Jindalee array, since the Longreach antennas were designed significantly better.

In order to determine the sidelobe levels that would be obtained for an array with these coupling values, the same procedure as before, using the weights given in equation (A.9), was used. However since the Longreach coupling values result in better sidelobe levels (than the Jindalee coupling values), the sidelobe region over which the matrix $\mathbf{K}$ in this equation is computed, needs to be made smaller; resulting in the sidelobe levels obtainable under ideal (error free) conditions being better. This allows the limiting sidelobe levels of the Longreach coupling matrices to be determined

The sidelobe levels obtained for the Longreach coupling values are shown in figure 4.14. The average sidelobe levels for different look directions (or azimuth's) are shown for each frequency. The average sidelobe levels clearly decrease with frequency (since the coupling values decrease with frequency) : at 5.0 MHz it is -30 dB (at worst), while at 12.0 MHz it is -50 dB (at worst).

The algorithm developed was used to estimate some of these coupling values. The algorithm was successful in reducing the sidelobe levels in all cases, the results obtained for 5.0 and 12.0 MHz are shown in figure 4.15 and 4.16 respectively. Figure 4.15 shows the 5.0 MHz coupling values have been estimated very well, and the resulting sidelobe levels have been greatly reduced. The results obtained in figure 4.16 are very good too, although some differences between the actual and estimated parameters can be observed here.

## 4.10 Error Surface

The cost function, or error surface, is analysed now to see how it varies with the unknown parameters. The smoothness of the error surface is of key importance, and it is of interest to see

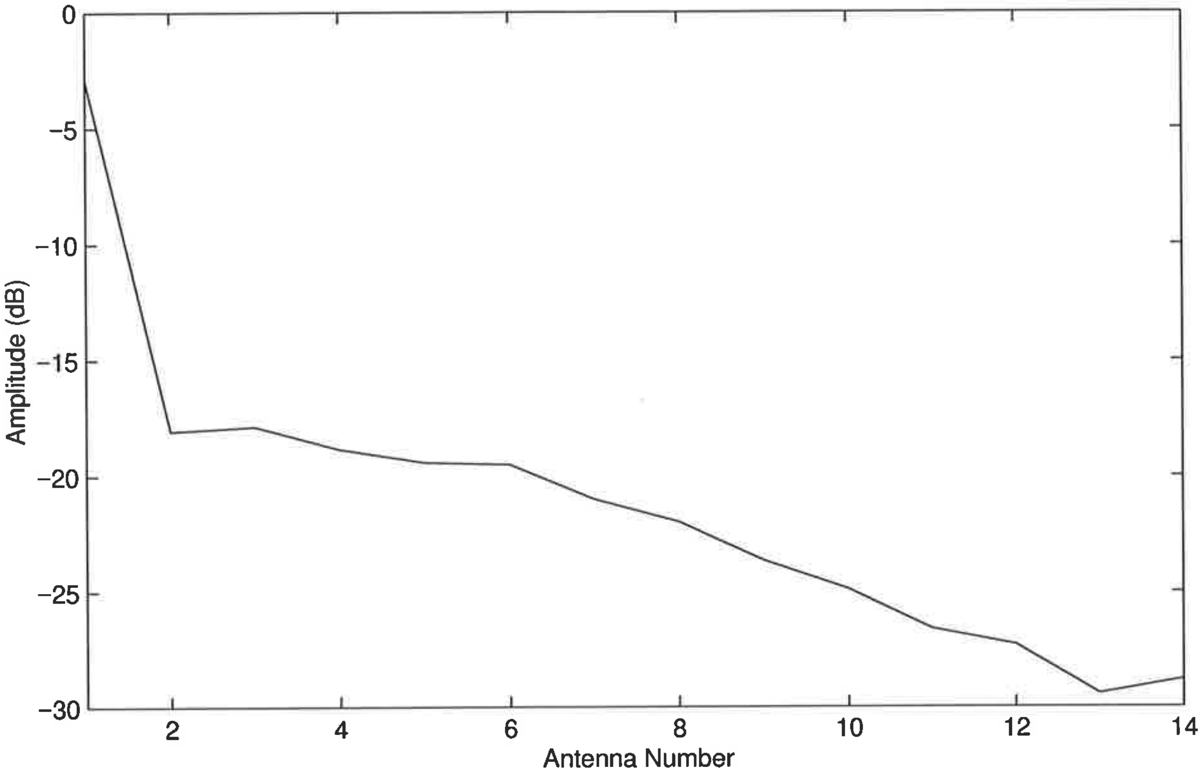

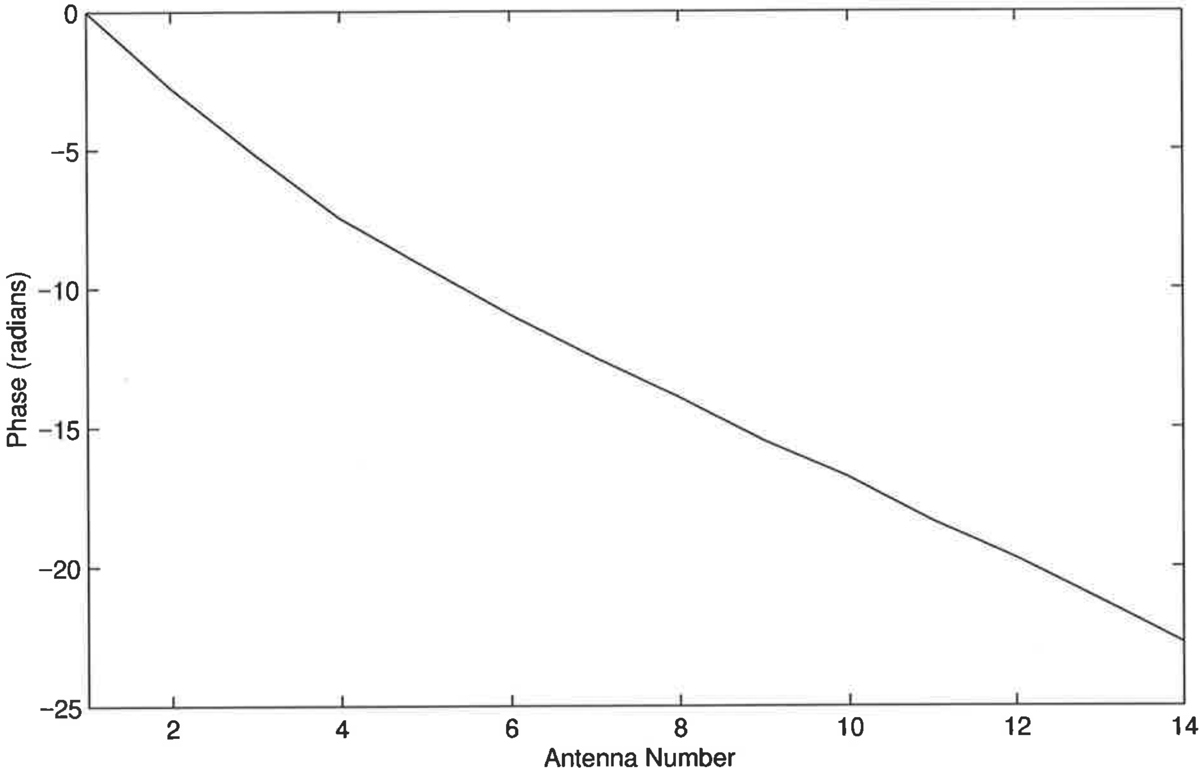

Figure 4.12: First row of Longreach coupling matrix, at 5.0 MHz.

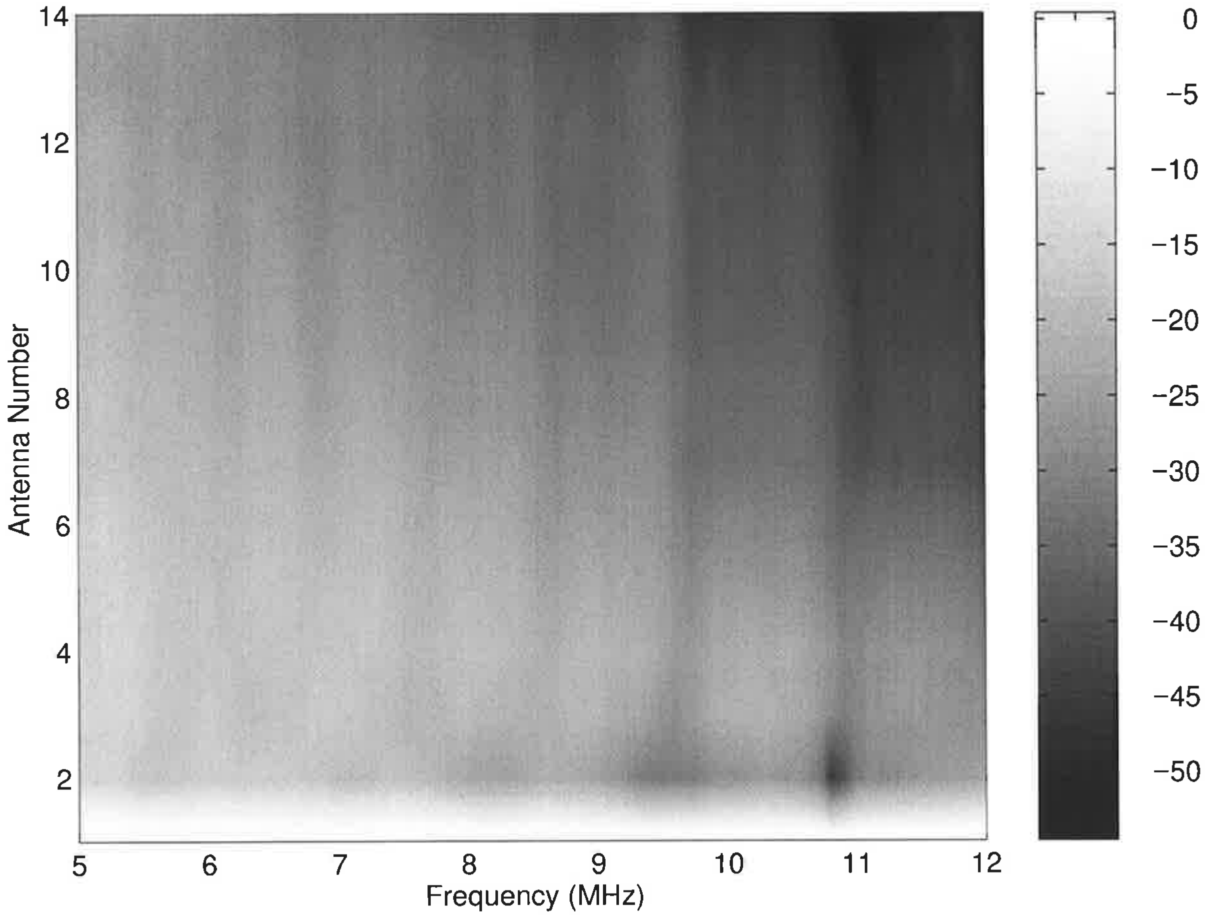

Figure 4.13: First row of Longreach coupling matrix for 5-12 MHz.

if the surface is highly multi-modal. If the surface is highly multi-modal, then the algorithm can get “stuck” and fail to get close to the global minimum.

The cost function in equation (4.37) was analysed for a nominally uniform linear 4-element array with inter-element spacing of $d = 0.4\lambda$; the randomly generated sensor position errors in the $x$-coordinate and $y$-coordinate being given in Table 4.1. The coupling matrix employed was measured from the Jindalee transmitting array. Ten sources equally spaced over 180° in azimuth were considered, and the exact covariance matrix determined for each source (see below regarding results for typical number of snapshots). The covariance matrix of each source was eigendecomposed and the matrices $\mathrm{U}(n)$ created. For the sensor positions, coupling matrix and signal bearings, in equation (4.37), initial parameter values were used as obtained in section 4.5, i.e. the nominal sensor positions ($x_m^o = md$ and $y_m^o = 0$) were used, the identity matrix was used for the coupling matrix, and the signal bearings were estimated using the MUSIC algorithm. With these quantities, the cost function can then be computed. The behaviour of the cost function is analysed below, with two parameters varied, while all other parameters are

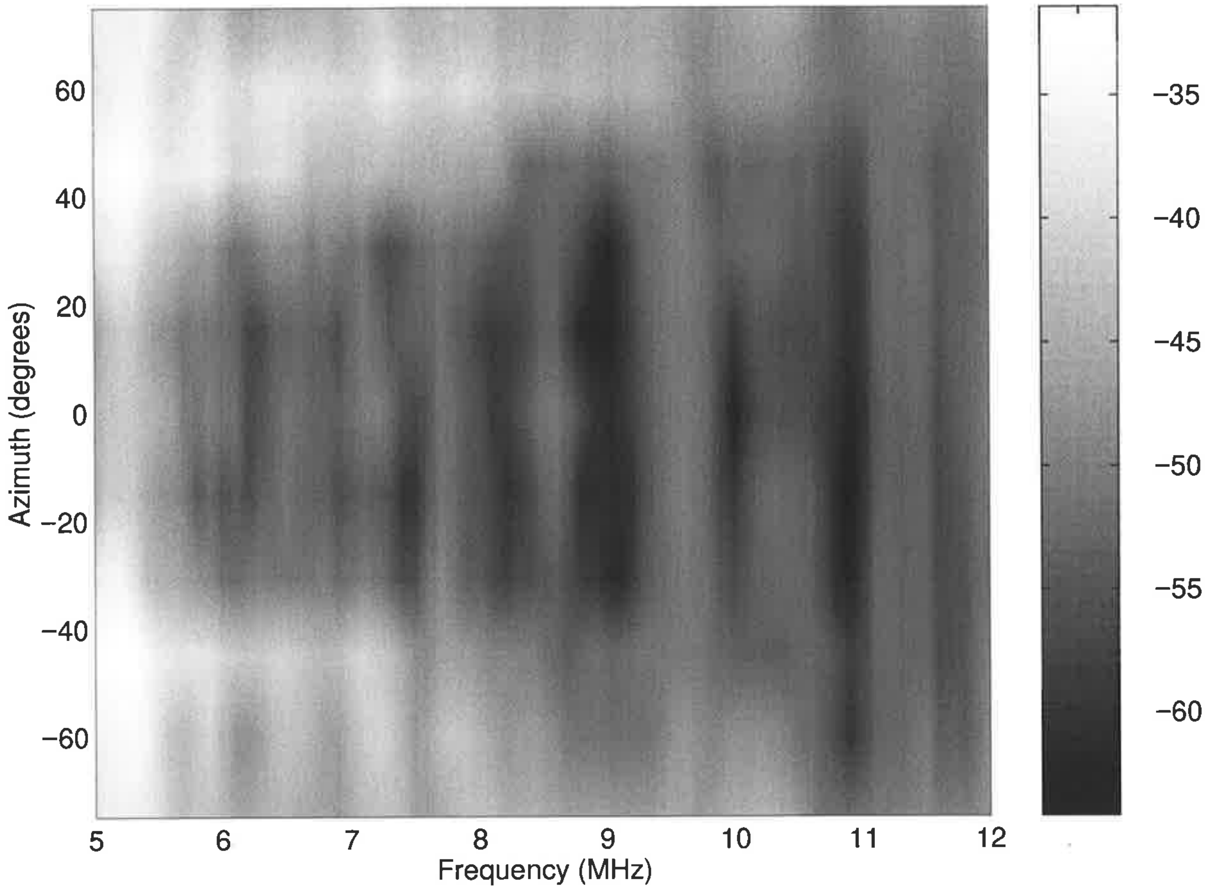

Figure 4.14: Average sidelobe levels for Longreach coupling matrices.

fixed at the values determined above.

| Sensor | 1 | 2 | 3 | 4 |
|---|---|---|---|---|
| $y$-coordinate ($\lambda$) | -0.1149 | 0.0674 | 0.0011 | -0.0361 |
| $x$-coordinate ($\lambda$) | -0.0499 | 0.0130 | 0.0156 | -0.0162 |

Table 4.1: Position Errors for 4-element Array

The cost function was first analysed as a function of the sensor position (both $x$ and $y$ coordinates) of the third sensor i.e. $Q(x_3, y_3)$. The $x$ and $y$ coordinates were varied up to $0.4\lambda$ (i.e. the size of the inter-element spacing) around the nominal sensor position, the results obtained being displayed in figure 4.17; where two sub-figures of the same error surface are shown. This error surface is clearly smooth, and is not multi-modal. Note the curvature (or slope/gradient) at any point is towards the minimum, with the minimum curvature observed at the extremes of the sub-figures. When the $x$ and $y$ coordinates were varied up to $0.8\lambda$ (twice the inter-element spacing) around the nominal sensor position (not shown), curvatures away from the minimum were observed; note however position errors as large as this are not of interest here. Similarly good surfaces were obtained for the coupling parameters.

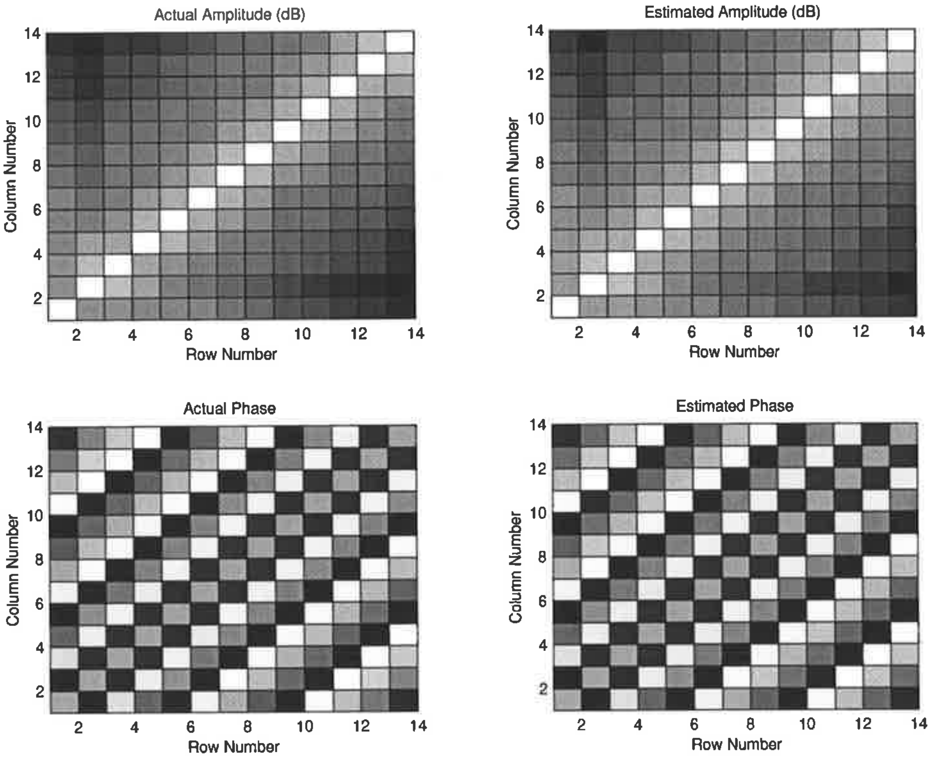

(a) actual and estimated coupling matrices

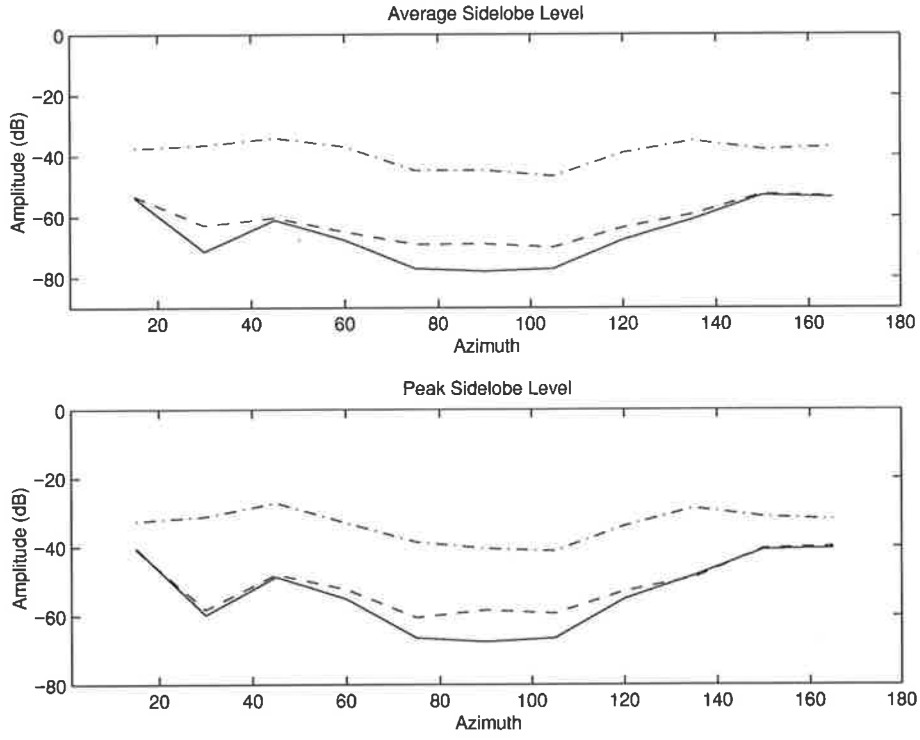

(b) average and peak sidelobe levels for nominal parameters (–.–), estimated parameters (– –) and actual parameters (–)

Figure 4.15: Longreach 5.0 MHz coupling matrix estimation.

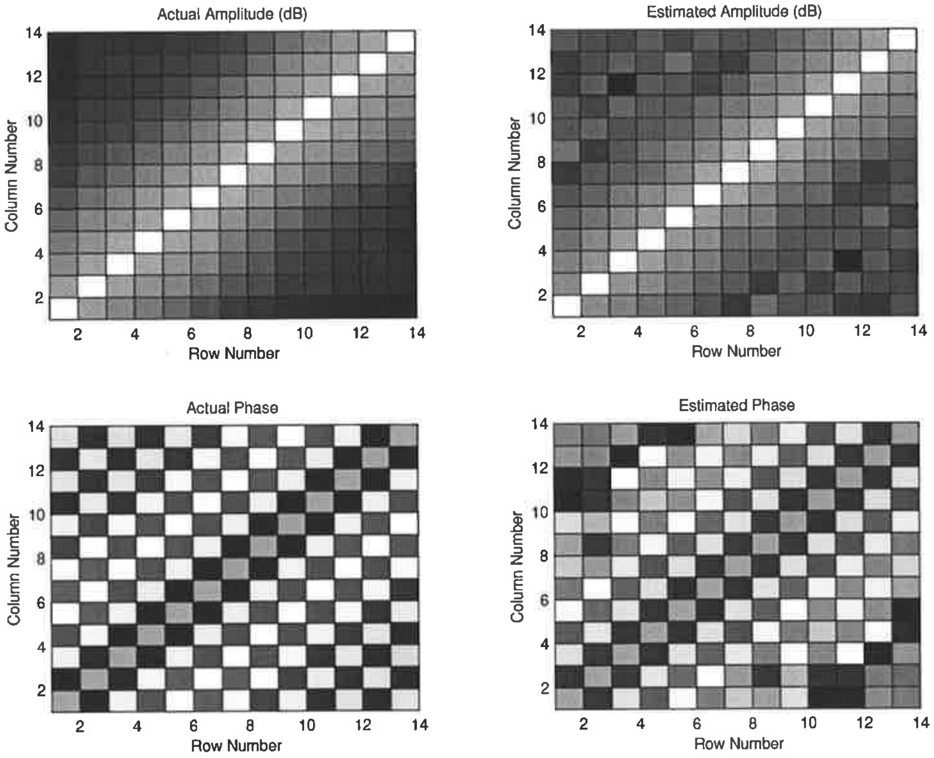

(a) actual and estimated coupling matrices

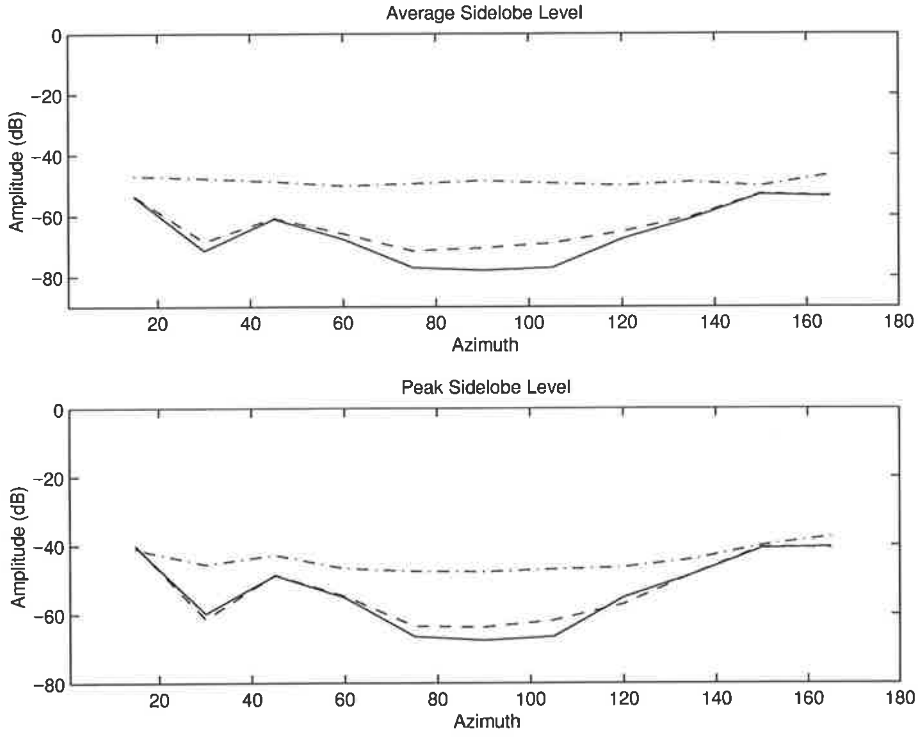

(b) average and peak sidelobe levels for nominal parameters (–.–), estimated parameters (– –) and actual parameters (–)

Figure 4.16: Longreach 12.0 MHz coupling matrix estimation.

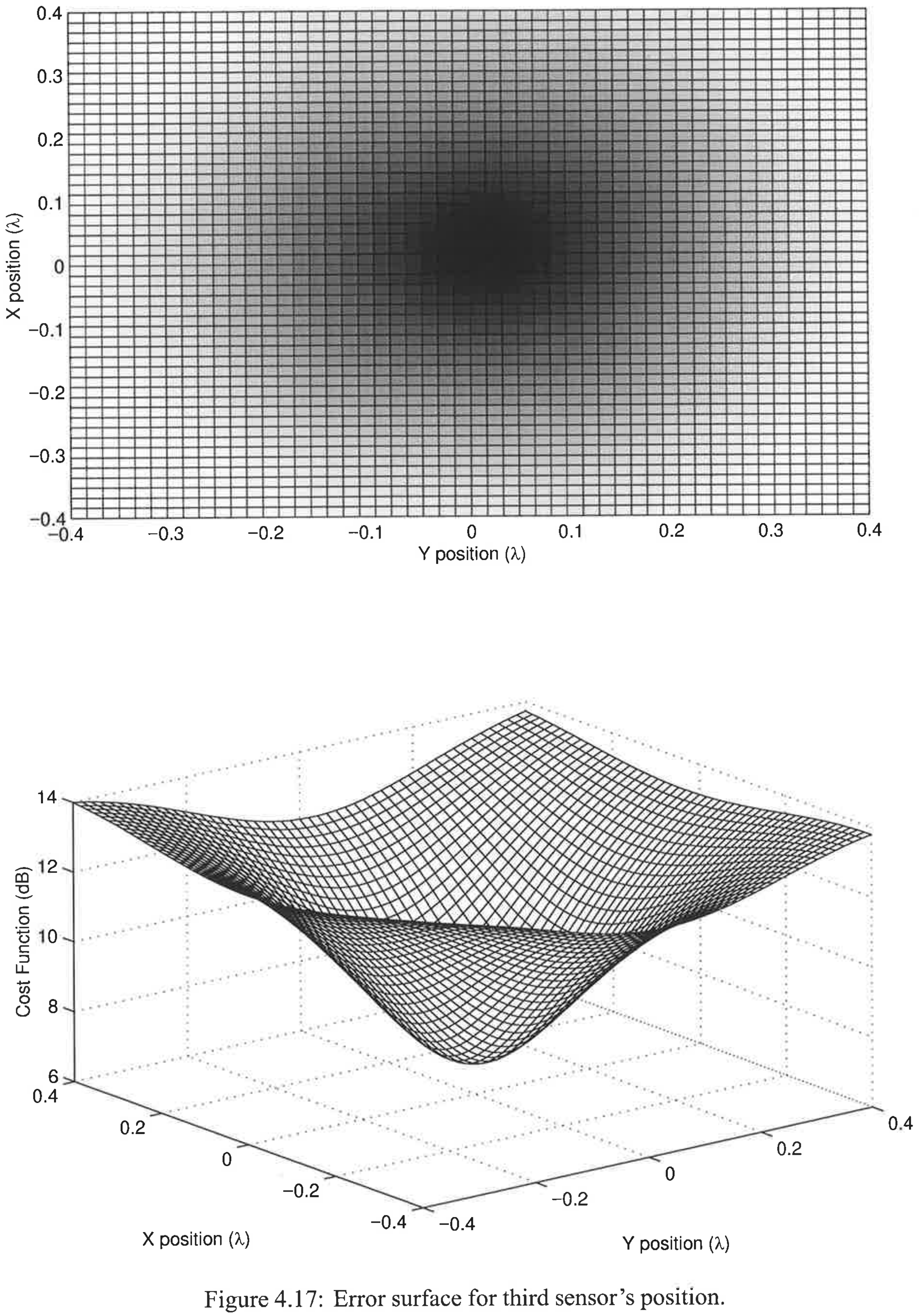

Figure 4.17: Error surface for third sensor's position.

The error surface for the bearings of two sources is shown in figure 4.18. This error surface is $Q(\theta_1, \theta_5)$, where the closest source to end-fire (at $-81^\circ$) and the closest source to broadside (at $-9^\circ$) are considered. Note the variation of this surface, if one of these two DOAs is fixed, reflects the array beampattern (as would be expected). Unlike the surface in figure 4.17, only over a small region is the curvature towards the minimum; the small region being approximately $10^\circ$-$15^\circ$ in each direction from the minimum (note the length of the region is a little smaller than the beamwidth, which is about $30^\circ$). These results indicate that, if initial bearing estimates are not possible to within $10^\circ$-$15^\circ$ of their true value, then the algorithm can diverge away from the global minimum. The error surface obtained, when the position errors were twice the amount in the above case, indicated that this critical region was even smaller. When estimated covariance matrices (from 5 snapshots and 10 dB SNR sources) were used, the error surface did not change significantly.

From these results, it is clear that the signal DOAs are the most sensitive parameters. Hence the procedure used for bearing estimation and the means used for obtaining initial bearing estimates, are of critical importance. The algorithm in this chapter used the MUSIC algorithm for bearing estimation, and has obtained good results for the size of model errors considered. The MUSIC algorithm is however not very robust to model errors, and if the model errors were to be increased, the MUSIC algorithm would be expected to produce poor DOA estimates; causing the array calibration algorithm to possibly fail. Hence for interest, larger model errors are considered, and the algorithm's performance analysed for such errors.

The performance of the algorithm for larger model errors is shown in figure 4.19. Sensor position errors with standard deviation (STD) of $0.2d$, $0.3d$ and $0.4d$, are considered here. The algorithm's performance for a STD of $0.3d$ is a little worse than that for $0.2d$; these results being almost as good as that obtained for a STD of $0.1d$ in figure 4.7. The performance for a STD of $0.4d$ is however poor, with many failures observed. Note a STD of $0.4d$ means the position errors are greater than $\lambda/10$, and since it is well known that the beampattern is robust only for errors up to $\lambda/10$, good performance is not expected for errors as large as $0.4d$.

## 4.11 Conclusion

A technique for estimating the coupling matrix and sensor position errors for OTH radars has been presented. The algorithm was developed for using scattered echoes from ionised meteor trails, which can be considered as disjoint sources of opportunity from an array calibration perspective. Simulations were conducted, using measured coupling matrices, to illustrate

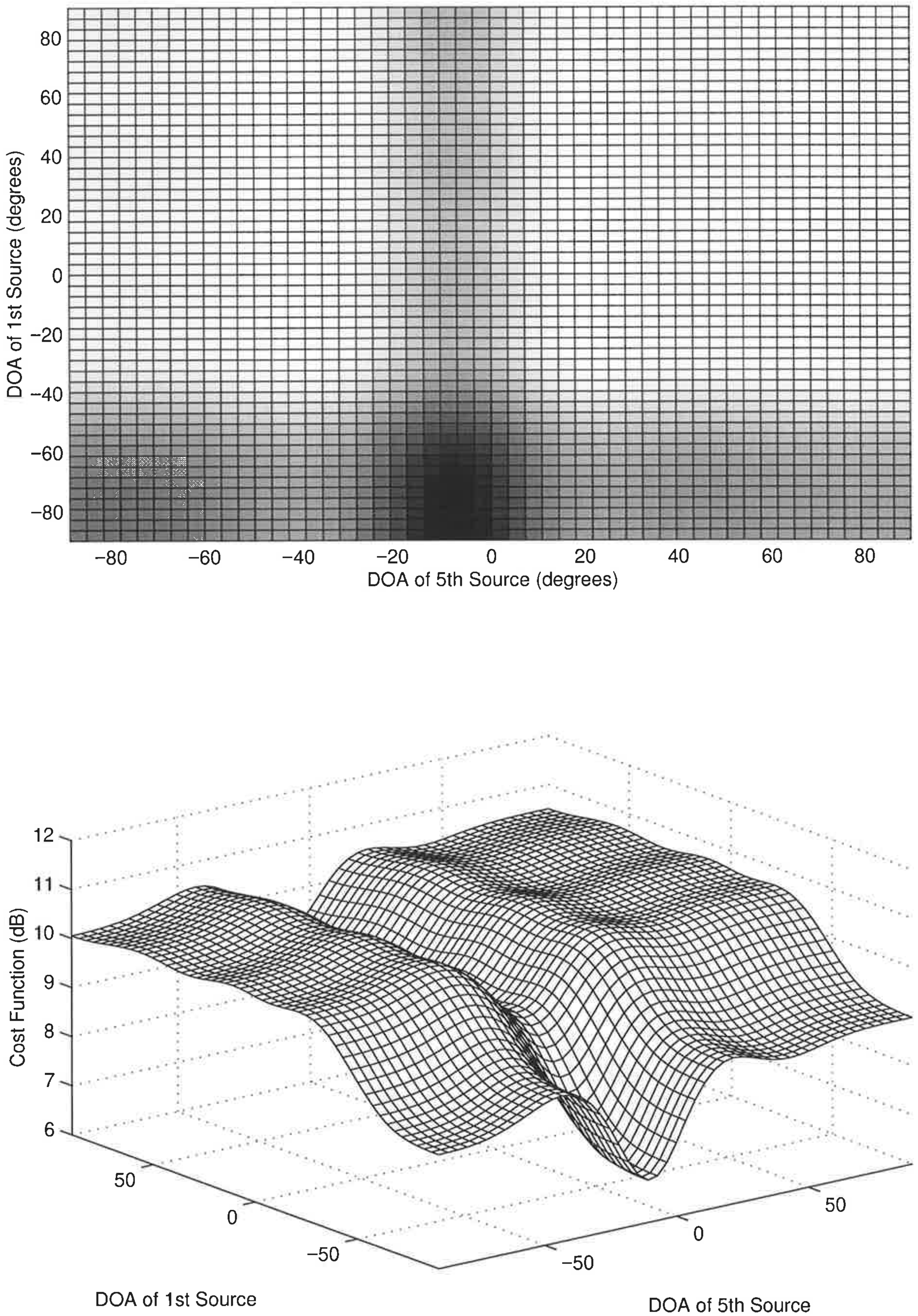

Figure 4.18: Error surface for two source DOAs.

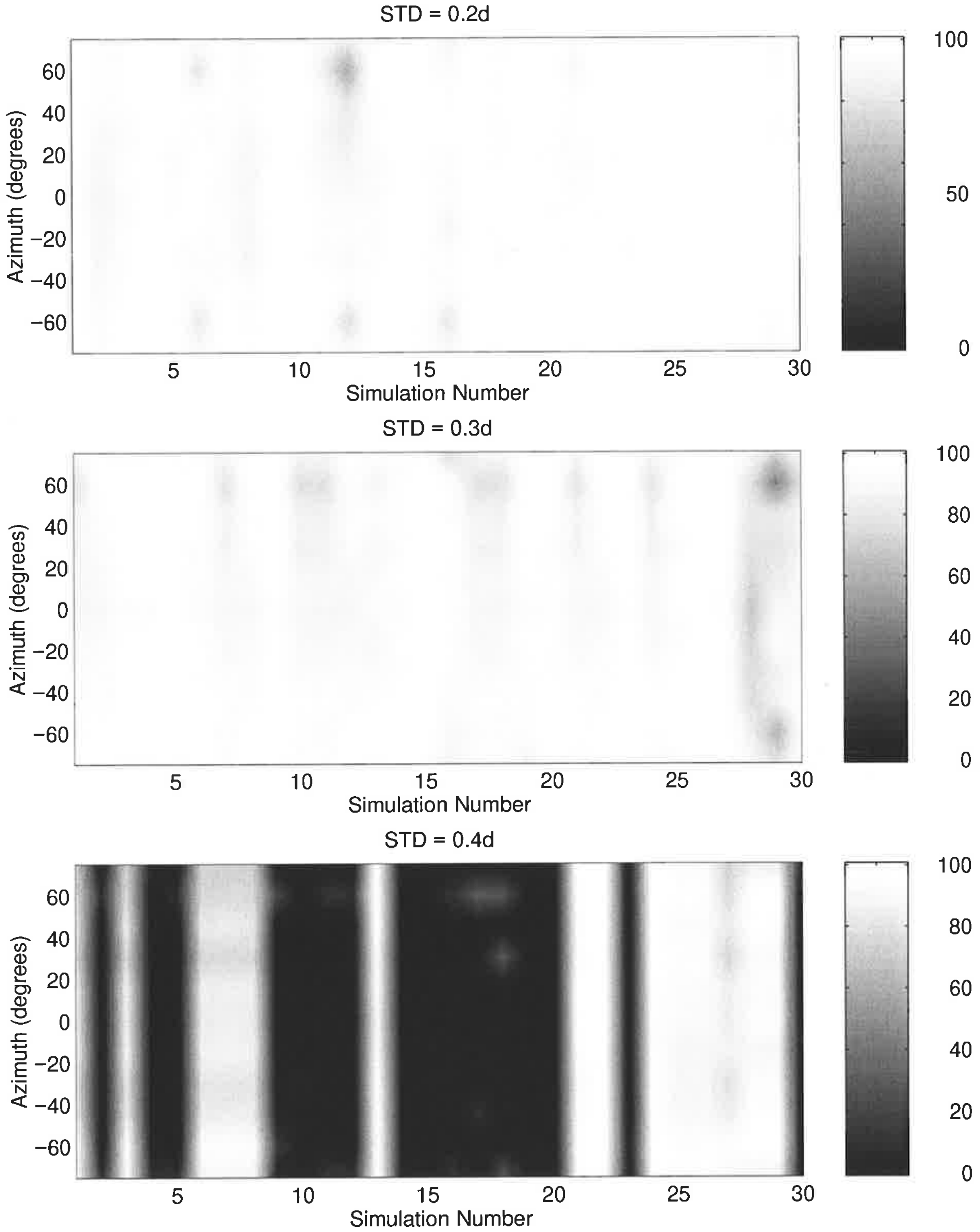

Figure 4.19: Algorithm's performance for larger model errors. Sensor position errors with standard deviation - (a) $0.2d$, (b) $0.3d$, (c) $0.4d$.

the performance of this method; the method's performance being good for typical SNRs and number of snapshots obtainable from meteor trail echoes. The algorithm was also found to be capable of estimating a variety of coupling matrices.

Performance criteria, which use sources of opportunity, were proposed for determining in practice the success achieved by an array calibration method. The algorithm's error surface was analysed and found to be in general good; the exception being for the signal DOAs, where the surfaces were good only within about a half-beamwidth of the true values.

In chapter 5 an algorithm is proposed for using disparate sources, to estimate the coupling matrix and sensor position errors; the problem considered here is a special case of that to be considered in the next chapter.

# CHAPTER 5

# Array Calibration using Disparate Sources

Unlike previous array calibration algorithms, which require a specific type or class of sources for calibrating the array, the algorithm proposed here can use all available sources for array calibration. For example, the algorithms proposed by See et. al. [182, 183, 140, 184] to estimate sensor positions and mutual coupling, need disjoint single-mode sources of known DOAs, and the DOAs must be time-invariant. The algorithm proposed here, however, can use sources present in different disjoint clusters; a cluster (see figure 5.1) being here used to denote any collection of sources which all occupy both the same time snapshots and the same radar range cells (i.e. are overlapped or non-disjoint). This algorithm can use disparate sources : multimode and near-field sources (in addition to single-mode sources), known DOA and unknown DOA sources, and sources with time-varying DOA or time-invariant DOA. Note the problem considered in chapter 4 (where single-mode, disjoint, time-invariant (unknown) DOA sources are considered), is a special case of that considered here.

As will be mentioned in chapter 7, for OTH radar array calibration, special sources such as beacons, noise sources such as radio stations, and scattered echoes from meteors, may be used. These sources have widely varying properties, which must be accounted for when they are used for array calibration. The array calibration procedure proposed here exploits multi-dimensional MUSIC for time-invariant DOA sources, while single-snapshot techniques are used for sources which have time-varying DOA. A non-linear separable least-squares solution to the array calibration problem is used to estimate the coupling matrix and sensor positions.

The problem is formulated in the first few sections, and then the algorithm is presented in section 5.6. Simulations are conducted in sections 5.7 and 5.8, using experimentally-measured

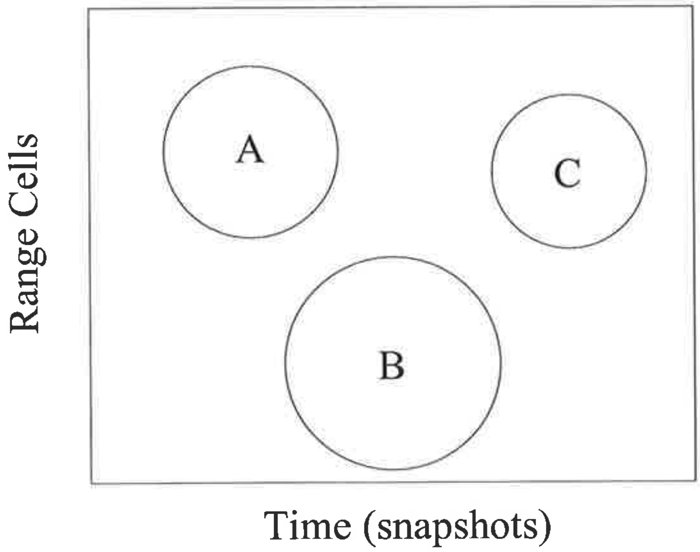

Figure 5.1: Illustration of disjoint clusters : A, B and C are disjoint clusters, each of which may contain a number of non-disjoint sources/signals.

coupling matrices, to analyse the algorithm's performance. The performance of this algorithm is analysed in section 5.9 for the special case where all the sources are single-mode, disjoint, and have time-invariant (unknown) DOAs; these results being compared to those obtained in the previous chapter. The algorithm's error surface is analysed in section 5.10, its performance with larger model errors is considered in section 5.11, and finally in section 5.12 the chapter is concluded.

## 5.1 Signal Model

For a signal impinging the array, the vector of sensor outputs is

$$\mathbf{z}(t) = \mathbf{C}\boldsymbol{\Gamma}\mathbf{a}(\theta_1)s_1(t) + \mathbf{n}(t) \tag{5.1}$$

where for a time-varying DOA signal $\theta_1 = \theta_1(t)$; however for simplicity of notation, the dependence is not shown but can be easily inferred from the context. The covariance matrix for a time-invariant DOA signal, assuming zero mean noise, is

$$\mathbf{R} = E\{\mathbf{z}(t)\mathbf{z}^H(t)\} \tag{5.2}$$

Given measurements $\mathbf{z}(t)$ and/or estimated covariance matrices $\hat{\mathbf{R}}$, for a number of signals, the problem is then to estimate both the sensor positions and coupling matrix, by formulating a cost function and minimising it with respect to these and other unknown parameters. It is assumed here again, that the data $\mathbf{z}(t)$ have been corrected for gain/phase errors (so $\mathbf{\Gamma} = \mathbf{I}_M$).

## 5.2 Time-varying DOA Sources

For time-varying DOA sources a meaningful spatial covariance matrix is difficult in general to be estimated, due to the non-stationary spatial behaviour of the source. Instead single-snapshot data can be used for array calibration, provided the signal-to-noise ratio is sufficiently high. In fact time-varying DOA sources, which have distinct DOAs each snapshot, can provide multiple single-snapshot sources for array calibration. Examples of time-varying DOA sources are meteor head echoes (see chapter 7) and calibration sources mounted on trucks or aircraft.

For the case of one single-mode source, a single-snapshot is

$$\mathbf{z} = \mathbf{C}\mathbf{a}(\theta)s + \mathbf{n} \tag{5.3}$$

for which a non-linear least squares problem is formulated, with a cost function

$$Q = ||\mathbf{z} - \mathbf{C}\mathbf{a}(\theta)s||^2 \tag{5.4}$$

Note if $s$ is deterministic and the noise white, then the parameters minimising this cost function, are deterministic maximum likelihood estimates. For the case of multiple sources, either uncorrelated or correlated (multimode) signals, which are overlapped in time (non-disjoint), equation (5.3) can be generalised as follows for (a single-snapshot of) $N$ signals

$$\mathbf{z} = \mathbf{C}\mathbf{A}\mathbf{s} + \mathbf{n} \tag{5.5}$$

where $\mathbf{A} = [\mathbf{a}(\theta_1), \mathbf{a}(\theta_2), ..., \mathbf{a}(\theta_N)]$, and the vector $\mathbf{s}$ of complex signal amplitudes is $\mathbf{s} = [s_1, s_2, ..., s_N]^T$. The cost function is then

$$Q = ||\mathbf{z} - \mathbf{C}\mathbf{A}\mathbf{s}||^2 \tag{5.6}$$

## 5.3 Time-invariant DOA Sources

Here time-invariant DOA sources refer to those sources whose DOA varies at most marginally from a nominal value. For these sources a meaningful spatial covariance matrix (as in chapter 4) can be estimated. Examples of time-invariant DOA sources are meteor trail echoes (see chapter 7) and beacons. This section starts with an outline of multi-dimensional MUSIC, and then the problem for time-invariant DOA sources is formulated.

Multi-dimensional MUSIC, proposed originally in [178] (see also [279]), is a multi-dimensional search procedure for DOA estimation. It does not have the drawback of one-dimensional search procedures, such as MUSIC, of not being able to cope with coherent signals, since it does not assume the signal covariance matrix to have full rank. Consider the eigenvectors corresponding to the largest eigenvalues of the covariance matrix (i.e. the signal subspace), and let $\mathbf{E}$ be the matrix whose columns are these eigenvectors. It can then be shown that, in uncorrelated receiver noise, there exists a matrix/vector $\mathbf{S}$ such that

$$\mathbf{E} = \mathbf{CAS} \tag{5.7}$$

where the elements of $\mathbf{S}$ are **not necessarily** the signal amplitudes (unlike the elements of $\mathbf{s}$ in section 5.2), but rather relate the actual steering vectors (columns of the product $\mathbf{AS}$) to the signal eigenvectors in $\mathbf{E}$. The category of sources that can be considered here (for a cluster) are :

- one single-mode source
- one multimode source
- multiple non-disjoint (overlapped) single-mode sources
- multiple non-disjoint (overlapped) multimode sources

A non-linear least squares problem is formulated, for each cluster of non-disjoint sources, as

$$Q = \|\hat{\mathbf{E}} - \mathbf{CAS}\|_F^2 \tag{5.8}$$

where $\hat{\mathbf{E}}$ is the estimated $M\text{x}k'$ signal subspace matrix/vector, and $\mathbf{S}$ is a $k\text{x}k'$ matrix/vector, for the cluster of non-disjoint sources. The number of signals present is $k$ and the number of signal eigenvalues is $k'$. If all the signals in the cluster are uncorrelated then $k' = k$, and if any of the signals are correlated $k' < k$.

Note that, if a source has a time-invariant DOA for some portion of its duration and has a time-varying DOA for the rest of the time, the approaches in both sections 5.2 and 5.3 can be used for the corresponding time segments.

## 5.4 Overall Cost Function

All sub-problems, for each and all of the disjoint clusters, can be combined into one problem with a single cost function, using the addition property of norms. The overall cost function is [1]

$$Q = ||\tilde{\mathbf{Z}} - \mathbf{C}\mathbf{A}\tilde{\mathbf{S}}||_F^2 \tag{5.9}$$

where matrix $\tilde{\mathbf{Z}}$ contains a column of $\mathbf{z}$ for each different cluster of time-varying DOA sources, and column(s) of $\hat{\mathbf{E}}$ for each different cluster of time-invariant DOA sources. $\tilde{\mathbf{S}}$ is made up of $s$'s from each disjoint sub-problem/cluster. Here $N_C$ will refer to the number of different sub-problems/clusters, $N_T$ to the total number of signals, and $N_{\tilde{Z}}$ to the number of columns in $\tilde{\mathbf{Z}}$. An example of the structure of $\tilde{\mathbf{Z}}$ and $\tilde{\mathbf{S}}$ are given in the next section.

While this problem cannot be solved in general, the matrices $\mathbf{C}$, $\mathbf{A}$ and $\tilde{\mathbf{S}}$ have special structures : the coupling matrix being estimated is symmetric (see chapter 4 for the details), the columns of $\mathbf{A}$ are steering vectors, and $\tilde{\mathbf{S}}$ is a sparse matrix of known structure. Thus equation (5.9) is minimised given the special structure of these matrices. Further, the algorithm proposed in this chapter, is only expected to provide a solution close to the global minimum when the initial parameter values are sufficiently close to the actual parameter values.

## 5.5 An Example

To purely illustrate the structure of $\tilde{\mathbf{Z}}$ and $\tilde{\mathbf{S}}$, the following scenario is considered. Disjoint clusters of time-varying DOA sources : one cluster of a single-mode source, one cluster of a multimode source (with three correlated signals). Disjoint clusters of time-invariant DOA sources : one cluster of a single-mode source, one cluster of three single-mode sources. For this case $N_C = 4$, $N_T = 8$, the matrix $\tilde{\mathbf{Z}}$ ($M$x6) and $\tilde{\mathbf{S}}$ (8x6) are as given below, where $\mathbf{z}_1$, $\mathbf{z}_2$ are vectors of single-snapshots and $\hat{\mathbf{e}}_1$, $\hat{\mathbf{E}}_2$ is a vector and a matrix of eigenvectors.

$$\tilde{\mathbf{Z}} = [\mathbf{z}_1, \mathbf{z}_2, \hat{\mathbf{e}}_1, \hat{\mathbf{E}}_2]$$

---

[1] For a near-field source the steering vector depends on both the source's DOA and its range from the radar. If the source's range is known, as is the case for scattered echoes and known transmitters, then the steering vector is known except for the DOA, and so this source can also be used for array calibration.

$$\tilde{\mathbf{S}} = \begin{bmatrix} s_{11} & 0 & 0 & 0 & 0 & 0 \\ 0 & s_{21} & 0 & 0 & 0 & 0 \\ 0 & s_{22} & 0 & 0 & 0 & 0 \\ 0 & s_{23} & 0 & 0 & 0 & 0 \\ 0 & 0 & s_{31} & 0 & 0 & 0 \\ 0 & 0 & 0 & s_{41} & s_{44} & s_{47} \\ 0 & 0 & 0 & s_{42} & s_{45} & s_{48} \\ 0 & 0 & 0 & s_{43} & s_{46} & s_{49} \end{bmatrix}$$

where for the first cluster $s_{11}$ relates the actual steering vector to $\mathbf{z}_1$, for the second cluster the three scalars $s_{2k}$ relate the three actual steering vectors to $\mathbf{z}_2$, for the third cluster $s_{31}$ relates the actual steering vector to $\hat{\mathbf{e}}_1$, and finally for the fourth cluster the nine scalars $s_{4k}$ relate the three actual steering vectors to the $M$x3 matrix $\hat{\mathbf{E}}_2$. Note for the fourth cluster, where uncorrelated signals are present, the number of signal eigenvectors obtained is the same as the number of signals present. However each signal eigenvector in not necessarily a scaled version of one of the actual steering vectors; each signal eigenvector instead usually being a linear combination of the actual steering vectors. Hence the reason for nine scalars $s_{4k}$ required in the fourth cluster.

## 5.6 Algorithm

The algorithm sequence, for this multi-parameter optimisation problem, was based on the observation that it was possible to improve significantly the sensor position estimates even when the coupling parameters were unknown, but it was not possible to obtain any such improvements in the estimates of the coupling parameters when the sensor position errors were large. By trying to improve the sensor position estimates (at each stage updating the DOAs and complex $s$'s) and then estimating the coupling matrix (again at each stage updating the DOAs and complex $s$'s), the cost function is minimised. The algorithm sequence is shown in figure 5.2; the order of operations was determined heuristically by comparing the results for different orders.

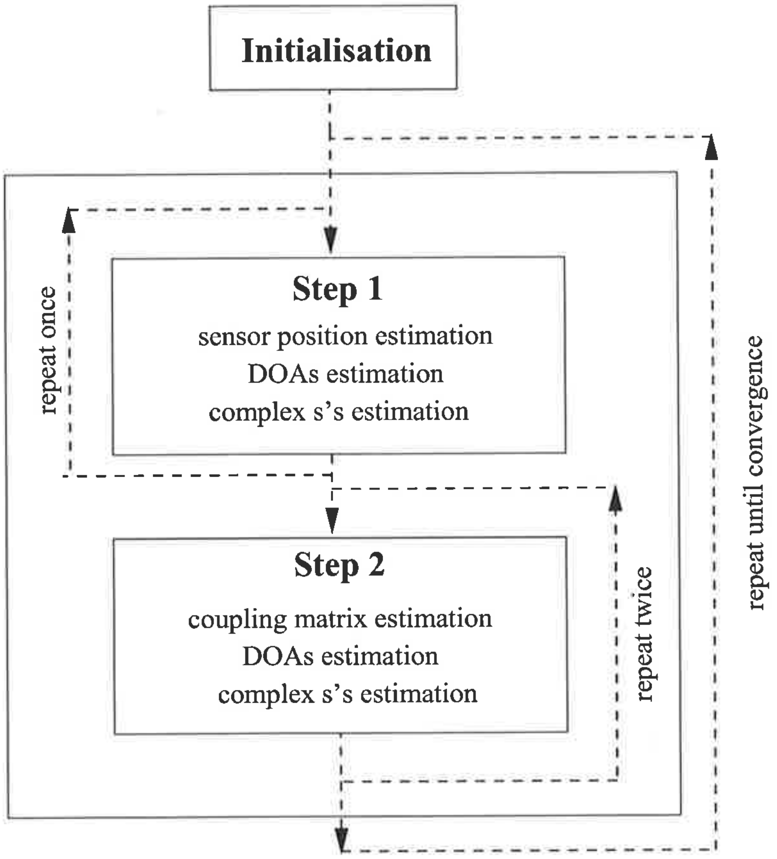

Figure 5.2: Algorithm Sequence.

### 5.6.1 Initialisation

As with most non-linear least squares problems, the initialisation is of paramount importance. The initial values for the unknowns in the cost function (5.9) are obtained by : (I) using the nominal sensor position values and nominal coupling matrix; (II) estimating the unknown signals' DOAs using the parameter values in (I), and then creating $\mathbf{A}$; and (III) estimating the complex $s$'s using the parameter values in (I) and (II), and then creating $\tilde{\mathbf{S}}$.

In step (II), the nominal sensor position values and the nominal coupling matrix, are used with the Bartlett processor (conventional beamformer) to obtain initial estimates of each of the unknown signals' DOAs. The Bartlett processor is used here, since it is capable of providing robust DOA estimates in the presence of correlated signals (unlike the MUSIC algorithm, which was used in chapter 4). For the case of each cluster of time-varying DOA sources, the Bartlett processor here is

$$p(\theta) = \mathbf{a}_o^H(\theta)\mathbf{C}_o^H\mathbf{z}_n\mathbf{z}_n^H\mathbf{C}_o\mathbf{a}_o(\theta) \qquad (5.10)$$

where $\mathbf{C}_o$ is the nominal coupling matrix, $\mathbf{a}_o(\theta)$ is the nominal array steering vector, and $\mathbf{z}_n$ is the single-snapshot of sensor outputs for the $n$th cluster of time-varying DOA sources. For the case of each cluster of time-invariant DOA sources, the Bartlett processor here is

$$p(\theta) = \mathbf{a}_o^H(\theta)\mathbf{C}_o^H\hat{\mathbf{R}}_n\mathbf{C}_o\mathbf{a}_o(\theta) \tag{5.11}$$

where $\hat{\mathbf{R}}_n$ is the estimated covariance matrix for the $n$th cluster of time-invariant DOA sources.

The peak of each spectra gives the DOA of the strongest signal in the cluster. When multiple signals exist (in a cluster) and their DOAs have to be estimated from either a single-snapshot or a covariance matrix, the projection matrix is used [269]. For example if for the strongest signal, a DOA of $\theta_m$ is obtained, then the steering vector for finding the next strongest signal's DOA is

$$\mathbf{a}_o'(\theta) = \left(\mathbf{I}_M - \frac{1}{M}\mathbf{a}_o(\theta_m)\mathbf{a}_o^H(\theta_m)\right)\mathbf{a}_o(\theta) \tag{5.12}$$

This steering vector is then used in the Bartlett processor above to obtain the next strongest signal's DOA. This procedure is repeated for obtaining any subsequent signals' DOAs in the cluster. Using this technique the limitation of the Bartlett processor, of resolving closely spaced signals (see section 2.1.2), is somewhat overcome.

Once initial values for all signals' DOAs have been obtained for the cluster, these values together with the nominal sensor positions can be used to form the matrix $\mathbf{A}(n)$, of steering vectors for the cluster. Matrix $\mathbf{A}$, in equation (5.9), is created by simply combining the matrices $\mathbf{A}(n)$ columnwise.

In step (III), the nominal coupling matrix and matrix $\mathbf{A}(n)$, are used to obtain initial values for the complex $s$'s in each cluster. For time-varying DOA sources

$$\mathbf{s}_n = (\mathbf{C}_o\mathbf{A}(n))^+\mathbf{z}_n \tag{5.13}$$

while for time-invariant DOA sources

$$\mathbf{S}_n = (\mathbf{C}_o\mathbf{A}(n))^+\hat{\mathbf{E}}_n \tag{5.14}$$

where $()^+$ is the generalised inverse operator. Once all initial complex $s$'s for all clusters, have been estimated, the matrix $\tilde{\mathbf{S}}$ in equation (5.9) can be formed. This completes the initialisation step.

### 5.6.2 Sensor Position Estimation

The last estimates of the DOAs, coupling matrix and complex $s$'s are used in this step to estimate the sensor positions. The last estimates of sensor positions are used in a Newton search to update the estimates of the sensor positions.

Let $\gamma(k) = [\mathbf{x}^T(k), \mathbf{y}^T(k)]^T$, where $\mathbf{x}(k)$ and $\mathbf{y}(k)$ are the vectors of estimated sensor positions after the $k$th iteration. Then, as in section 4.7,

$$\gamma(k+1) = \gamma(k) - u\ \mathbf{H}^{-1}(\gamma(k))\ \mathbf{r}(\gamma(k)) \tag{5.15}$$

where $\mathbf{H}$ is the Hessian matrix for the sensor positions, $\mathbf{r}$ is the gradient vector for the sensor positions, and the step length is $0 < u < 1$. Expressions for this Hessian and gradient are obtained from the cost function in (5.9), and are derived below.

The $2M$x1 gradient vector is $\mathbf{r}(\gamma(k)) = [(\partial Q/\partial \mathbf{x}(k))^T, (\partial Q/\partial \mathbf{y}(k))^T]^T$, and the $2M$x$2M$ Hessian matrix is

$$\mathbf{H}(\gamma(k)) = \begin{bmatrix} \frac{\partial^2 Q}{\partial \mathbf{x}(k)\partial \mathbf{x}^T(k)} & \frac{\partial^2 Q}{\partial \mathbf{x}(k)\partial \mathbf{y}^T(k)} \\ \frac{\partial^2 Q}{\partial \mathbf{y}(k)\partial \mathbf{x}^T(k)} & \frac{\partial^2 Q}{\partial \mathbf{y}(k)\partial \mathbf{y}^T(k)} \end{bmatrix} \tag{5.16}$$

The cost function $Q$ in equation (5.9) can be re-written as

$$\begin{aligned} Q &\approx \sum_{l=1}^{L} \|\tilde{\mathbf{z}}_l - \mathbf{C}\mathbf{A}\tilde{\mathbf{s}}_l\|^2 && (5.17) \\ &= \sum_{l=1}^{L} (\tilde{\mathbf{z}}_l^H \tilde{\mathbf{z}}_l - \tilde{\mathbf{z}}_l^H \mathbf{C}\mathbf{A}\tilde{\mathbf{s}}_l - \tilde{\mathbf{s}}_l^H \mathbf{A}^H \mathbf{C}^H \tilde{\mathbf{z}}_l + \tilde{\mathbf{s}}_l^H \mathbf{A}^H \mathbf{C}^H \mathbf{C}\mathbf{A}\tilde{\mathbf{s}}_l) && (5.18) \end{aligned}$$

where $\tilde{\mathbf{z}}_l$ is the $l$th (of $L$) column of $\tilde{\mathbf{Z}}$, and $\tilde{\mathbf{s}}_l$ is the $l$th (of $L$) column of $\tilde{\mathbf{S}}$.

Now define $\dot{\mathbf{A}}_{x_p} = \partial \mathbf{A}/\partial x_p = \mathbf{Dx_p} \odot \mathbf{A}$, where $\odot$ is the Hadamard product and $\mathbf{Dx_p}$ is an $M$x$N_T$ matrix with all but the $p$th row zero; the $n$th element of the $p$th row is $(+2\pi j/\lambda)\sin(\theta_n)$, where $\lambda$ is the radar wavelength. Also define $\dot{\mathbf{A}}_{x_p}^H = \partial(\mathbf{A}^H)/\partial x_p = \mathbf{Dx_p}^H \odot \mathbf{A}^H = (\partial \mathbf{A}/\partial x_p)^H$. Then

$$\begin{aligned} \frac{\partial Q}{\partial x_p} &= \sum_{l=1}^{L} (-\tilde{\mathbf{z}}_l^H \mathbf{C}\dot{\mathbf{A}}_{x_p}\tilde{\mathbf{s}}_l - \tilde{\mathbf{s}}_l^H \dot{\mathbf{A}}_{x_p}^H \mathbf{C}^H \tilde{\mathbf{z}}_l + \tilde{\mathbf{s}}_l^H \dot{\mathbf{A}}_{x_p}^H \mathbf{C}^H \mathbf{C}\mathbf{A}\tilde{\mathbf{s}}_l + \tilde{\mathbf{s}}_l^H \mathbf{A}^H \mathbf{C}^H \mathbf{C}\dot{\mathbf{A}}_{x_p}\tilde{\mathbf{s}}_l) \\ &= -2\Re\left\{\sum_{l=1}^{L} (\tilde{\mathbf{z}}_l^H - \tilde{\mathbf{s}}_l^H \mathbf{A}^H \mathbf{C}^H)\mathbf{C}(\mathbf{Dx_p} \odot \mathbf{A})\tilde{\mathbf{s}}_l\right\} && (5.19) \end{aligned}$$

and hence

$$\begin{aligned}
\frac{\partial^2 Q}{\partial^2 x_p} &= -2\Re\left\{\sum_{l=1}^{L}\Big[(\tilde{\mathbf{z}}_l^H - \tilde{\mathbf{s}}_l^H\mathbf{A}^H\mathbf{C}^H)\mathbf{C}(\mathbf{Dx_p}\odot\mathbf{Dx_p}\odot\mathbf{A})\tilde{\mathbf{s}}_l\right. \\
&\qquad \left. -\tilde{\mathbf{s}}_l^H(\mathbf{A}^H\odot\mathbf{Dx_p}^H)\mathbf{C}^H\mathbf{C}(\mathbf{Dx_p}\odot\mathbf{A})\tilde{\mathbf{s}}_l\Big]\right\} && (5.20) \\
\frac{\partial^2 Q}{\partial x_p \partial x_q} &= -2\Re\left\{\sum_{l=1}^{L}\Big[(\tilde{\mathbf{z}}_l^H - \tilde{\mathbf{s}}_l^H\mathbf{A}^H\mathbf{C}^H)\mathbf{C}(\mathbf{Dx_p}\odot\mathbf{Dx_q}\odot\mathbf{A})\tilde{\mathbf{s}}_l\right. \\
&\qquad \left. -\tilde{\mathbf{s}}_l^H(\mathbf{A}^H\odot\mathbf{Dx_q}^H)\mathbf{C}^H\mathbf{C}(\mathbf{Dx_p}\odot\mathbf{A})\tilde{\mathbf{s}}_l\Big]\right\} && (5.21) \\
&= 2\Re\left\{\sum_{l=1}^{L}\tilde{\mathbf{s}}_l^H(\mathbf{A}^H\odot\mathbf{Dx_q}^H)\mathbf{C}^H\mathbf{C}(\mathbf{Dx_p}\odot\mathbf{A})\tilde{\mathbf{s}}_l\right\} && (5.22)
\end{aligned}$$

where $\Re\{\}$ is the real part, and $q \neq p$. Equation (5.22) is obtained from equation (5.21) since $\mathbf{Dx_p}\odot\mathbf{Dx_q}$ is the zero matrix for $q \neq p$.

The partial derivatives with respect to the $y$ coordinates are similarly obtained as

$$\begin{aligned}
\frac{\partial Q}{\partial y_p} &= -2\Re\left\{\sum_{l=1}^{L}(\tilde{\mathbf{z}}_l^H - \tilde{\mathbf{s}}_l^H\mathbf{A}^H\mathbf{C}^H)\mathbf{C}(\mathbf{Dy_p}\odot\mathbf{A})\tilde{\mathbf{s}}_l\right\} && (5.23) \\
\frac{\partial^2 Q}{\partial^2 y_p} &= -2\Re\left\{\sum_{l=1}^{L}\Big[(\tilde{\mathbf{z}}_l^H - \tilde{\mathbf{s}}_l^H\mathbf{A}^H\mathbf{C}^H)\mathbf{C}(\mathbf{Dy_p}\odot\mathbf{Dy_p}\odot\mathbf{A})\tilde{\mathbf{s}}_l\right. \\
&\qquad \left. -\tilde{\mathbf{s}}_l^H(\mathbf{A}^H\odot\mathbf{Dy_p}^H)\mathbf{C}^H\mathbf{C}(\mathbf{Dy_p}\odot\mathbf{A})\tilde{\mathbf{s}}_l\Big]\right\} && (5.24) \\
\frac{\partial^2 Q}{\partial y_p \partial y_q} &= 2\Re\left\{\sum_{l=1}^{L}\tilde{\mathbf{s}}_l^H(\mathbf{A}^H\odot\mathbf{Dy_q}^H)\mathbf{C}^H\mathbf{C}(\mathbf{Dy_p}\odot\mathbf{A})\tilde{\mathbf{s}}_l\right\} && (5.25)
\end{aligned}$$

where $\mathbf{Dy_p}$ is an $M\mathrm{x}N_T$ element matrix with all but the $p$th row zero; the $n$th element of the $p$th row is $(+2\pi j/\lambda)\cos(\theta_n)$.

The $\partial^2 Q/\partial x_p \partial y_p$ and $\partial^2 Q/\partial x_p \partial y_q$ terms are

$$\begin{aligned}
\frac{\partial^2 Q}{\partial x_p \partial y_p} &= -2\Re\left\{\sum_{l=1}^{L}\Big[(\tilde{\mathbf{z}}_l^H - \tilde{\mathbf{s}}_l^H\mathbf{A}^H\mathbf{C}^H)\mathbf{C}(\mathbf{Dx_p}\odot\mathbf{Dy_p}\odot\mathbf{A})\tilde{\mathbf{s}}_l\right. \\
&\qquad \left. -\tilde{\mathbf{s}}_l^H(\mathbf{A}^H\odot\mathbf{Dy_p}^H)\mathbf{C}^H\mathbf{C}(\mathbf{Dx_p}\odot\mathbf{A})\tilde{\mathbf{s}}_l\Big]\right\} && (5.26) \\
\frac{\partial^2 Q}{\partial x_p \partial y_q} &= 2\Re\left\{\sum_{l=1}^{L}\tilde{\mathbf{s}}_l^H(\mathbf{A}^H\odot\mathbf{Dy_q}^H)\mathbf{C}^H\mathbf{C}(\mathbf{Dx_p}\odot\mathbf{A})\tilde{\mathbf{s}}_l\right\} && (5.27)
\end{aligned}$$

### 5.6.3 Coupling Matrix Estimation

The last estimates of the sensor positions, the signals' DOAs and complex $s$'s are used in this step to estimate the coupling matrix. It can be shown that the cost function in (5.9) can be re-written as follows

$$Q = \|\tilde{\mathbf{z}}^T - \mathbf{c}^T \mathbf{F}\|^2 \tag{5.28}$$

where $\tilde{\mathbf{z}} = vec(\tilde{\mathbf{Z}})$, the $MN_{\tilde{Z}}$ element column vector containing all entries of $\tilde{\mathbf{Z}}$ in a column-wise order. Vector $\mathbf{c}$ contains the $(M+1)M/2$ unknown complex coupling parameters, since the coupling matrix is assumed to be symmetric (see chapter 4). Matrix $\mathbf{F}$ is created from the matrix product $\mathbf{A}\tilde{\mathbf{S}}$, an expression for this $[(M+1)M/2]$x$[MN_{\tilde{Z}}]$ matrix is given below. The coupling parameters are then estimated as

$$\mathbf{c} = (\mathbf{F}^T)^+ \tilde{\mathbf{z}} \tag{5.29}$$

It can be shown that for the symmetric coupling matrix employed, the matrix $\mathbf{F}$ in equation (5.29) is given for all $1 \leq m \leq M$ and $1 \leq n \leq N_{\tilde{Z}}$ as

$$[\mathbf{F}]_{l,(n-1)M+m} = \begin{cases} T_{m+l-\rho(m),n} & \rho(m) \leq l \leq \rho(m+1) - 1 \\ T_{h,n} & l = \rho(h) + m - h \quad \forall\, 1 \leq h < (m-1) \\ 0 & \text{otherwise} \end{cases} \tag{5.30}$$

where $\mathbf{T} = \mathbf{A}\tilde{\mathbf{S}}$, and

$$\rho(u) = \begin{cases} 1 & u = 1 \\ \rho(u-1) + (M - u + 2) & 2 \leq u \leq (M+1) \end{cases} \tag{5.31}$$

### 5.6.4 DOA Estimation

The last estimates of the sensor positions, coupling matrix and complex $s$'s are used in this step to estimate the signals' DOAs. The last estimate of the signals' DOAs are used in a Newton search to update the estimates of the signals' DOAs. The vector of the signals' DOAs after the $(k+1)$th iteration is

$$\boldsymbol{\theta}(k+1) = \boldsymbol{\theta}(k) - u\ \mathbf{H}^{-1}(\boldsymbol{\theta}(k))\ \mathbf{r}(\boldsymbol{\theta}(k)) \tag{5.32}$$

where $\mathbf{H}$ is the Hessian matrix for the DOAs, $\mathbf{r}$ is the gradient vector for the DOAs, and the step length is $0 < u < 1$. Expressions for this Hessian and gradient, which are obtained from the cost function in (5.9), are given below. If any signal has a known DOA, this signal's DOA is not considered in (5.32). Note equation (5.32) could independently be used for the signals in each cluster, since the clusters are disjoint; this is what was actually done, so computation time could be minimised.

The $N_T$x1 gradient vector is $\mathbf{r}(\boldsymbol{\theta}(k)) = \partial Q/\partial\boldsymbol{\theta}(k)$, and the $N_T$x$N_T$ Hessian matrix is $\mathbf{H}(\boldsymbol{\theta}(k)) = \partial^2 Q/\partial\boldsymbol{\theta}(k)\partial\boldsymbol{\theta}^T(k)$. Now define $\dot{\mathbf{A}}_{\theta_p} = \partial\mathbf{A}/\partial\theta_p = \mathbf{D}(\theta_p)\mathbf{A}\mathbf{e}_p\mathbf{e}_p^T$, where $\mathbf{D}(\theta_p) = (+2\pi j/\lambda)diag\{\mathbf{x}\cos(\theta_p) - \mathbf{y}\sin(\theta_p)\}$, and $\mathbf{e}_p$ is the unit vector with all but the $p$th element zero. Then from equation (5.18)

$$\begin{aligned}
\frac{\partial Q}{\partial\theta_p} &= \sum_{l\in L(p)} (-\tilde{\mathbf{z}}_l^H\mathbf{C}\dot{\mathbf{A}}_{\theta_p}\tilde{\mathbf{s}}_l - \tilde{\mathbf{s}}_l^H\dot{\mathbf{A}}_{\theta_p}^H\mathbf{C}^H\tilde{\mathbf{z}}_l + \tilde{\mathbf{s}}_l^H\dot{\mathbf{A}}_{\theta_p}^H\mathbf{C}^H\mathbf{C}\mathbf{A}\tilde{\mathbf{s}}_l + \tilde{\mathbf{s}}_l^H\mathbf{A}^H\mathbf{C}^H\mathbf{C}\dot{\mathbf{A}}_{\theta_p}\tilde{\mathbf{s}}_l) \\
&= -2\Re\left\{\sum_{l\in L(p)} \left[\tilde{\mathbf{z}}_l^H\mathbf{C}\mathbf{D}(\theta_p)\mathbf{A}\mathbf{e}_p\mathbf{e}_p^T\tilde{\mathbf{s}}_l - \tilde{\mathbf{s}}_l^H\mathbf{A}^H\mathbf{C}^H\mathbf{C}\mathbf{D}(\theta_p)\mathbf{A}\mathbf{e}_p\mathbf{e}_p^T\tilde{\mathbf{s}}_l\right]\right\} \qquad (5.33) \\
&= -2\Re\left\{\sum_{l\in L(p)} (\tilde{\mathbf{z}}_l^H - \tilde{\mathbf{s}}_l^H\mathbf{A}^H\mathbf{C}^H)\mathbf{C}\mathbf{D}(\theta_p)\mathbf{A}\mathbf{e}_p\mathbf{e}_p^T\tilde{\mathbf{s}}_l\right\} \qquad (5.34)
\end{aligned}$$

where $L(p)$ is the set of all $l$ indices corresponding to the cluster containing $\theta_p$.

From equation (5.34),

$$\begin{aligned}
\frac{\partial^2 Q}{\partial^2\theta_p} = -2\Re\Bigg\{\sum_{l\in L(p)} \Big[&\tilde{\mathbf{z}}_l^H\mathbf{C}\dot{\mathbf{D}}_{\theta_p}(\theta_p)\mathbf{A}\mathbf{e}_p\mathbf{e}_p^T\tilde{\mathbf{s}}_l + \tilde{\mathbf{z}}_l^H\mathbf{C}\mathbf{D}(\theta_p)\dot{\mathbf{A}}_{\theta_p}\mathbf{e}_p\mathbf{e}_p^T\tilde{\mathbf{s}}_l \\
&-\tilde{\mathbf{s}}_l^H\dot{\mathbf{A}}_{\theta_p}^H\mathbf{C}^H\mathbf{C}\mathbf{D}(\theta_p)\mathbf{A}\mathbf{e}_p\mathbf{e}_p^T\tilde{\mathbf{s}}_l - \tilde{\mathbf{s}}_l^H\mathbf{A}^H\mathbf{C}^H\mathbf{C}\dot{\mathbf{D}}_{\theta_p}(\theta_p)\mathbf{A}\mathbf{e}_p\mathbf{e}_p^T\tilde{\mathbf{s}}_l \\
&-\tilde{\mathbf{s}}_l^H\mathbf{A}^H\mathbf{C}^H\mathbf{C}\mathbf{D}(\theta_p)\dot{\mathbf{A}}_{\theta_p}\mathbf{e}_p\mathbf{e}_p^T\tilde{\mathbf{s}}_l\Big]\Bigg\} \qquad (5.35)
\end{aligned}$$

where $\dot{\mathbf{D}}_{\theta_p}(\theta_p) = \partial\mathbf{D}(\theta_p)/\partial\theta_p = \mathbf{D}_2(\theta_p) = (-2\pi j/\lambda)diag\{\mathbf{x}\sin(\theta_p) + \mathbf{y}\cos(\theta_p)\}$. Hence

$$\begin{aligned}
\frac{\partial^2 Q}{\partial^2\theta_p} = -2\Re\Bigg\{\sum_{l\in L(p)} \Big[&\tilde{\mathbf{z}}_l^H\mathbf{C}(\mathbf{D}_2(\theta_p) + \mathbf{D}(\theta_p)\mathbf{D}(\theta_p))\mathbf{A}\mathbf{e}_p\mathbf{e}_p^T\tilde{\mathbf{s}}_l \\
&+ \Big(\tilde{\mathbf{s}}_l^H\mathbf{e}_p\mathbf{e}_p^T\mathbf{A}^H\mathbf{D}(\theta_p)\mathbf{C}^H\mathbf{C}\mathbf{D}(\theta_p) \\
&\quad -\tilde{\mathbf{s}}_l^H\mathbf{A}^H\mathbf{C}^H\mathbf{C}(\mathbf{D}_2(\theta_p) + \mathbf{D}(\theta_p)\mathbf{D}(\theta_p))\Big)\,\mathbf{A}\mathbf{e}_p\mathbf{e}_p^T\tilde{\mathbf{s}}_l\Big]\Bigg\} \qquad (5.36)
\end{aligned}$$

Now from equation (5.34),

$$\frac{\partial^2 Q}{\partial\theta_p\partial\theta_q} = +2\Re\left\{\sum_{l\in L(p)} \tilde{\mathbf{s}}_l^H\dot{\mathbf{A}}_{\theta_q}^H\mathbf{C}^H\mathbf{C}\mathbf{D}(\theta_p)\mathbf{A}\mathbf{e}_p\mathbf{e}_p^T\tilde{\mathbf{s}}_l\right\}$$

$$= \ -2\Re\left\{\sum_{l\in L(p)} \tilde{\mathbf{s}}_l^H \mathbf{e}_q\mathbf{e}_q^T\mathbf{A}^H\mathbf{D}(\theta_q)\mathbf{C}^H\mathbf{C}\mathbf{D}(\theta_p)\mathbf{A}\mathbf{e}_p\mathbf{e}_p^T\tilde{\mathbf{s}}_l\right\} \tag{5.37}$$

where $q \neq p$ but is in the same cluster, and $\mathbf{D}(\theta_q) = (+2\pi j/\lambda)diag\{\mathbf{x}\cos(\theta_q) - \mathbf{y}\sin(\theta_q)\}$. Note the fact that $\dot{\mathbf{D}}_{\theta_q}(\theta_p)$ and $\dot{\mathbf{A}}_{\theta_q}\mathbf{e}_p\mathbf{e}_p^T$ equal zero matrices has been used here.

### 5.6.5 Estimation of Complex *s*'s

The last estimates of the sensor positions, coupling matrix and the signals' DOAs are used in this step to estimate the complex $s$'s. For each disjoint cluster of time-varying DOA sources equation (5.13) is used, and for each disjoint cluster of time-invariant DOA sources equation (5.14) is used.

### 5.6.6 Assumptions

The following assumptions have been made :
- the number of signals, present in each measured snapshot of array outputs and in each estimated covariance matrix, is known [241, 6, 245, 239, 247, 242];
- a procedure is available for determining whether a signal has a time-varying DOA or a time-invariant DOA.

A possible approach is now suggested (which we proposed in [3] for non-stationary detection), to detect variations in the DOA of incident signals. The time interval over which the signal is present is divided into $L$ sub-intervals, of duration $T$. Then $L$ covariance matrices are estimated, with the $b$th covariance matrix (where $b = 1, 2, ..., L$) obtained over the interval $(1, bT)$, as follows

$$\hat{\mathbf{R}}_b = \frac{1}{bT}\sum_{t=1}^{bT}\mathbf{z}(t)\mathbf{z}^H(t) \tag{5.38}$$

Note, the duration $T$ chosen must be long enough to get a good estimate of $\hat{\mathbf{R}}_1$, and also short enough so that $\hat{\mathbf{R}}_1$ represents only information at a particular time.

Eigendecomposing each of the $L$ covariance matrices, one obtains $\hat{\mathbf{E}}_b$ the signal subspace of $\hat{\mathbf{R}}_b$, and $\hat{\mathbf{U}}_b$ the noise subspace of $\hat{\mathbf{R}}_b$. Using $\hat{\mathbf{E}}_1$ as a reference, consider the following function

$$f(b) = \|\hat{\mathbf{E}}_1^H\hat{\mathbf{U}}_b\|^2 \tag{5.39}$$

or alternatively

$$f(b) = trace[\hat{\mathbf{E}}_1 \hat{\mathbf{E}}_1^H \hat{\mathbf{U}}_b \hat{\mathbf{U}}_b^H] \tag{5.40}$$

If the signal's DOA is time-invariant, then $f$ should remain small for all $b$, while if the signal's DOA is time-varying $f$ should increase/vary with $b$. Hence by considering this function it should be possible to detect DOA variations.

Note that since mutual coupling and sensor position errors are both time-invariant over typical radar dwell durations, it is possible to conclude any DOA variation detected by the array is due to the received signal rather than the antenna array.

## 5.7 Simulation Example

As in chapter 4, simulations were performed for a 16 element, nominally equispaced linear array with inter-element spacing of $d = 0.4\lambda$. The actual sensor positions were $x_m = md + \Delta x_m$ and $y_m = \Delta y_m$, where $\Delta x_m$ and $\Delta y_m$ are zero mean Gaussian random variables, both with standard deviation of $0.1d$. The coupling matrix used was an experimentally measured coupling matrix from the Jindalee OTH radar's transmitting array (situated at Harts Range in central Australia). The initial sensor positions were taken to be the nominal sensor positions, while the identity matrix was used as the initial coupling matrix. The termination criterion was for the algorithm to stop when the cost function Q changed in value by less than 0.1 percent.

In total thirty three sources were used, with signal-to-noise ratios of 30 dB. The number of snapshots obtained from the time-invariant DOA sources was 500 (see the next section for the algorithm's performance, for typical number of snapshots). Disjoint clusters of time-varying DOA sources : a single-mode source (2 clusters), a multimode source (2 clusters), a known DOA single-mode source (several clusters); in total 10 sources (14 signals) being present. Disjoint clusters of time-invariant DOA sources : a single-mode source (2 clusters), a multimode source (2 clusters), three single-mode sources (1 cluster), a multimode source plus a single-mode source (1 cluster), a known DOA single-mode source (several clusters); in total 23 sources (28 signals) being present.

The results obtained are displayed in figure 5.3 :

- the cost function initially decreases rapidly, and then tends to level off after about 30 iterations;
- the signals' DOA estimates are good in most cases (note the first 8 DOAs are for time-varying DOA signals, while the next 22 DOAs are for time-invariant DOA signals). The largest DOA errors observed seem to be associated with clusters that have multiple signal eigenvectors (i.e.

signal DOAs 17-22), and are probably due to array ambiguities;

- the magnitude and phase of the coupling matrix used, and the coupling matrix estimated, are in close agreement (the phase is unwrapped for easy comparison);
- the errors in the $x$ and $y$ coordinates, after the final iteration ($*$), are much smaller than the errors in the nominal values (o).

As in chapter 4, to further analyse the performance of this algorithm, it is necessary to compare the sidelobe levels obtained using the estimated parameters with those of the uncalibrated array. The weighting required to obtain minimum average sidelobe levels, given the sensor positions and the coupling matrix, is (see Appendix A)

$$\mathbf{w}(\theta_o) = \frac{\left(\hat{\mathbf{C}}^H\right)^{-1}\mathbf{K}^{-1}\hat{\mathbf{a}}(\theta_o)}{\hat{\mathbf{a}}^H(\theta_o)\mathbf{K}^{-1}\hat{\mathbf{a}}(\theta_o)} \tag{5.41}$$

where $\hat{\mathbf{C}}$ is the estimated coupling matrix and $\hat{\mathbf{a}}(\phi)$ is the steering vector formed using the estimated sensor positions. The matrix $\mathbf{K} = \int \hat{\mathbf{a}}(\phi)\hat{\mathbf{a}}(\phi)^H \cos\phi d\phi$, where the range of the integral is over the sidelobe region. The array beampattern is then

$$B_{\theta_o}(\phi) = \left\|\mathbf{w}^H(\theta_o)\mathbf{v}(\phi)\right\|^2 \tag{5.42}$$

where $\theta_o$ is the steer direction of the beam, $\phi$ is the DOA considered, $\mathbf{v}(\phi)$ is the actual steering vector (including the effects of mutual coupling). Using equation (5.42) the sidelobe levels can then be calculated.

In order to obtain the sidelobe levels using the parameters estimated in figure 5.3, the sidelobe region required to compute matrix $\mathbf{K}$ was chosen so that the resulting beam had the same beamwidth as that obtainable using the Hamming window. Figure 5.4 shows the sidelobe levels for this example, where both the average and peak sidelobe levels are shown as a function of azimuth. The sidelobe levels for the estimated parameters (−−) is much better than the sidelobe levels for the nominal parameters (−.−), and is close to the sidelobe levels for the actual parameters (–). It is hence concluded that the algorithm has performed well here.

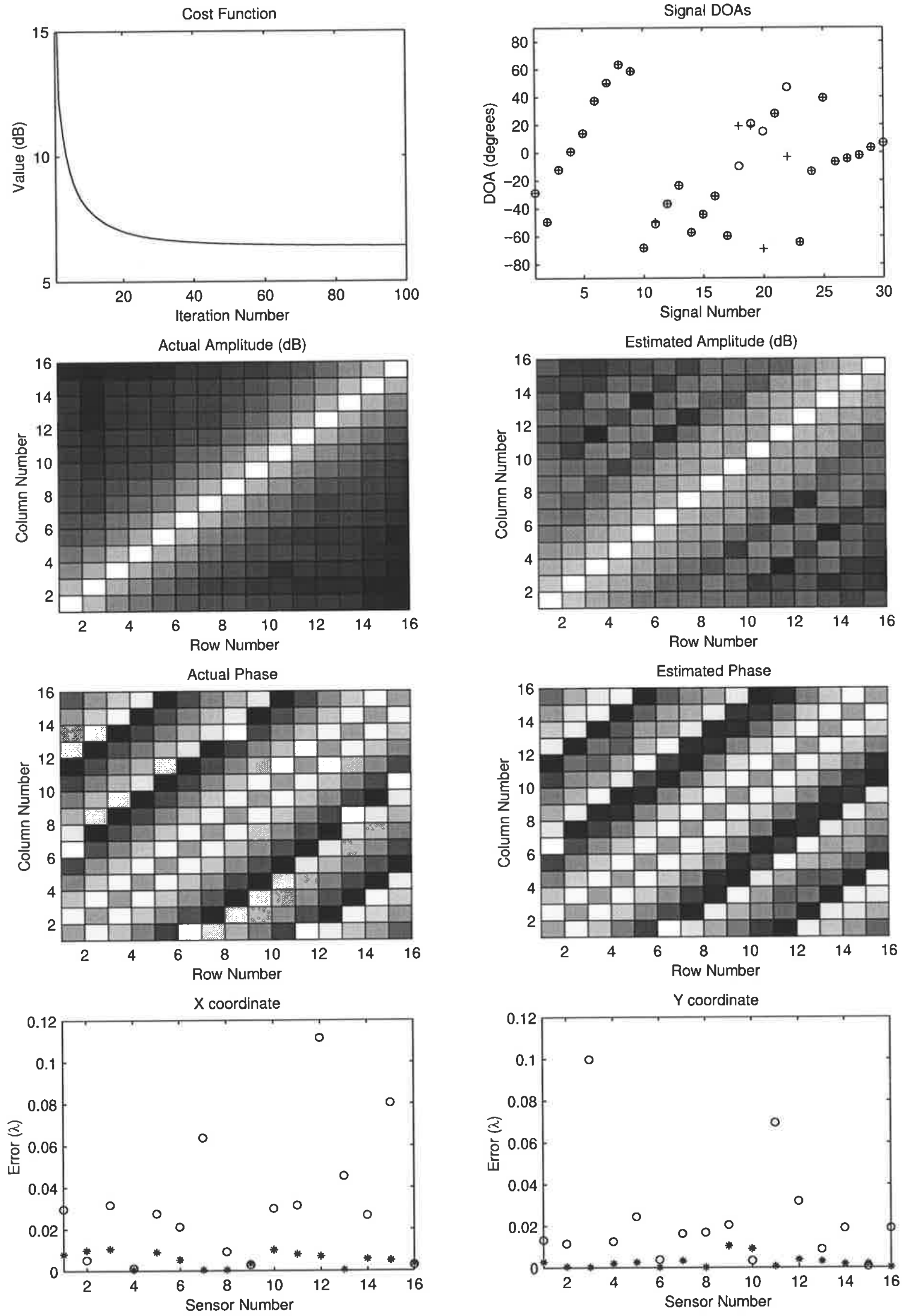

Figure 5.3: Simulation example results : cost function decreases with iteration number; the actual (o) and the estimated (+) signals' DOAs; actual coupling matrix and estimated coupling matrix; errors in nominal (o) and estimated (∗) sensor positions.

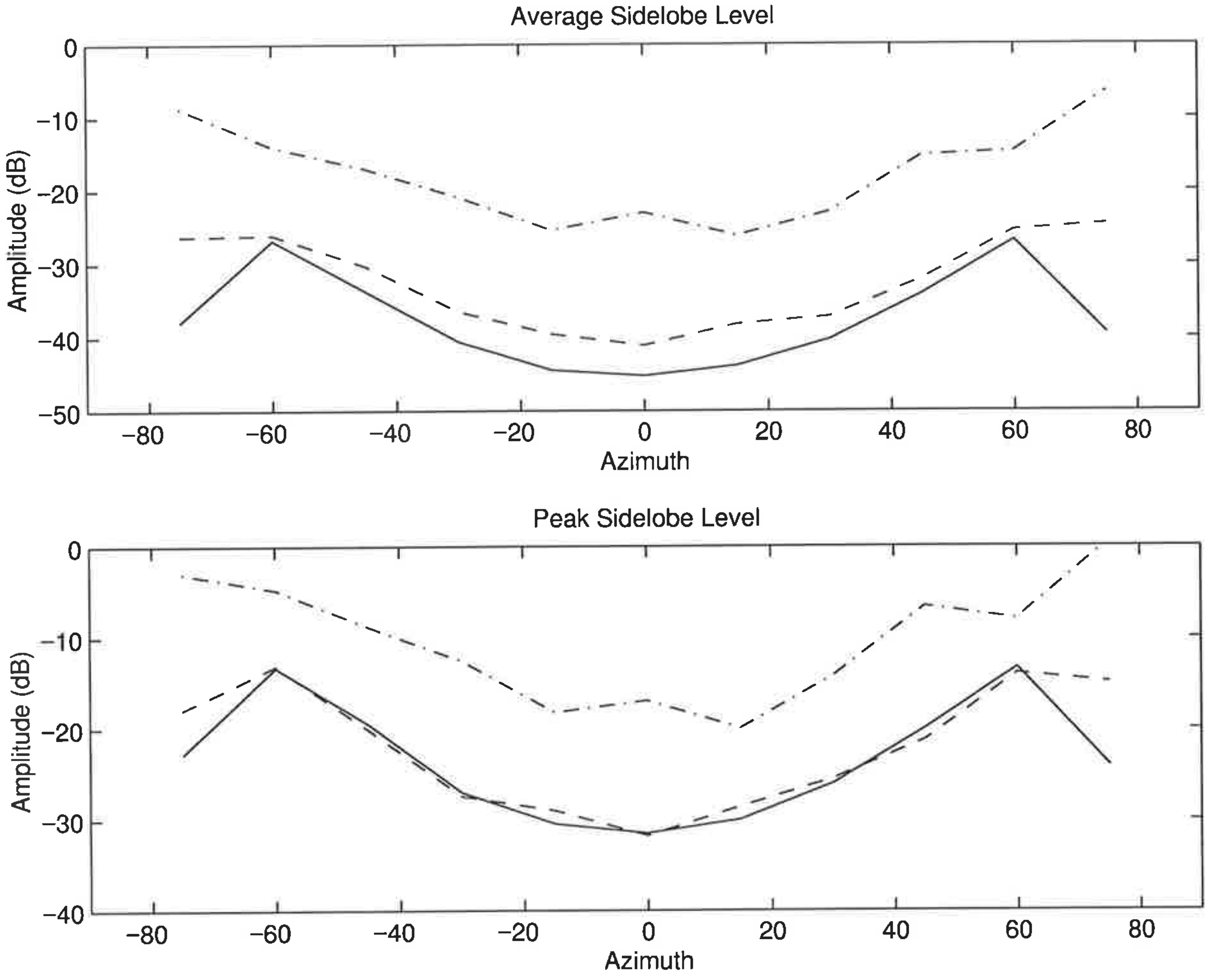

Figure 5.4: Average and peak sidelobe levels for the nominal parameters (–.–), estimated parameters (– –) and also the actual parameters (–).

## 5.8 Monte Carlo Analysis

A Monte Carlo analysis is required to analyse the algorithm's performance in detail. The performance measure considered here, as in chapter 4, is

$$\eta(\theta) = \frac{ASL_{nom}(\theta) - ASL_{est}(\theta)}{ASL_{nom}(\theta) - ASL_{act}(\theta)} * 100 \tag{5.43}$$

where $ASL_{nom}(\theta)$, $ASL_{est}(\theta)$ and $ASL_{act}(\theta)$ are the average sidelobe level obtained with nominal parameters, with estimated parameters and with actual parameters, respectively. Each quantity is expressed in dB, and as a function of look direction $\theta$. Hence if $\eta(\theta)$ is small (close to zero) the algorithm has not performed well, while if $\eta(\theta)$ is large (close to hundred) the algorithm has performed well.

Initially 100 simulations were conducted, as shown in figure 5.5, with the sensor position errors being randomly generated in each case; the same coupling matrix was used in all these simulations. As can be seen the algorithm has performed very well in all cases and there are no failures. The results obtained here are however not as good as those in chapter 4, but note different types of sources are used here. Later both algorithms, using the same type of sources, are compared.

To test the algorithm's performance for typical SNRs and number of snapshots obtainable from OTH radar sources, simulations were conducted for different SNR-snapshot combinations. Two combinations are shown in figure 5.6, where the SNRs and number of snapshots are 20 dB and 5 respectively in the top image, and 30 dB and 10 in the bottom image. Note however the SNRs of time-varying DOA sources (single-snapshot sources) are 30 dB in both cases. Clearly the algorithm has performed very well, robust results being obtained even for a few snapshots (note the performance of the algorithm is also considered in section 6.2.5, and will be shown to be good). It has, however, been observed that poor results are obtained when the SNRs of time-varying DOA sources (single-snapshot sources) is not high (below about 25 dB), as would be expected. Note the Cramer-Rao lower bound standard deviations (for high SNR), are shown in chapter 6, to be inversely proportional to the square-root of the SNR and the number of snapshots; thus the SNR of a time-varying DOA source needs to be $T$ times the SNR of a time-invariant DOA source, for both the sources to contribute equally.

The algorithm's performance can be further improved by using better initial values for the parameters being estimated. As mentioned earlier for the coupling matrix, instead of the identity matrix which has been used for these simulations as the initial value, any modelled or previously estimated coupling matrix could be used. While in general convergence to the global minimum cannot be guaranteed, the results obtained indicate that good performance has been obtained for typical initial conditions.

## 5.9 Special Case

The method presented in chapter 4 was for using disjoint single-mode meteor trail echoes to perform array calibration. With only this very important class of sources, the method in this chapter is also able to perform array calibration. Hence its performance for this special case is considered, and results obtained compared with those achieved for the method in chapter 4.

As mentioned earlier, for the case of $N$ disjoint single-mode sources (of time-invariant DOAs), $N$ covariance matrices $\hat{\mathbf{R}}_n$ can be estimated. Each of the covariance matrices contain only one single-mode source, and hence have only one signal eigenvalue. The cost function in

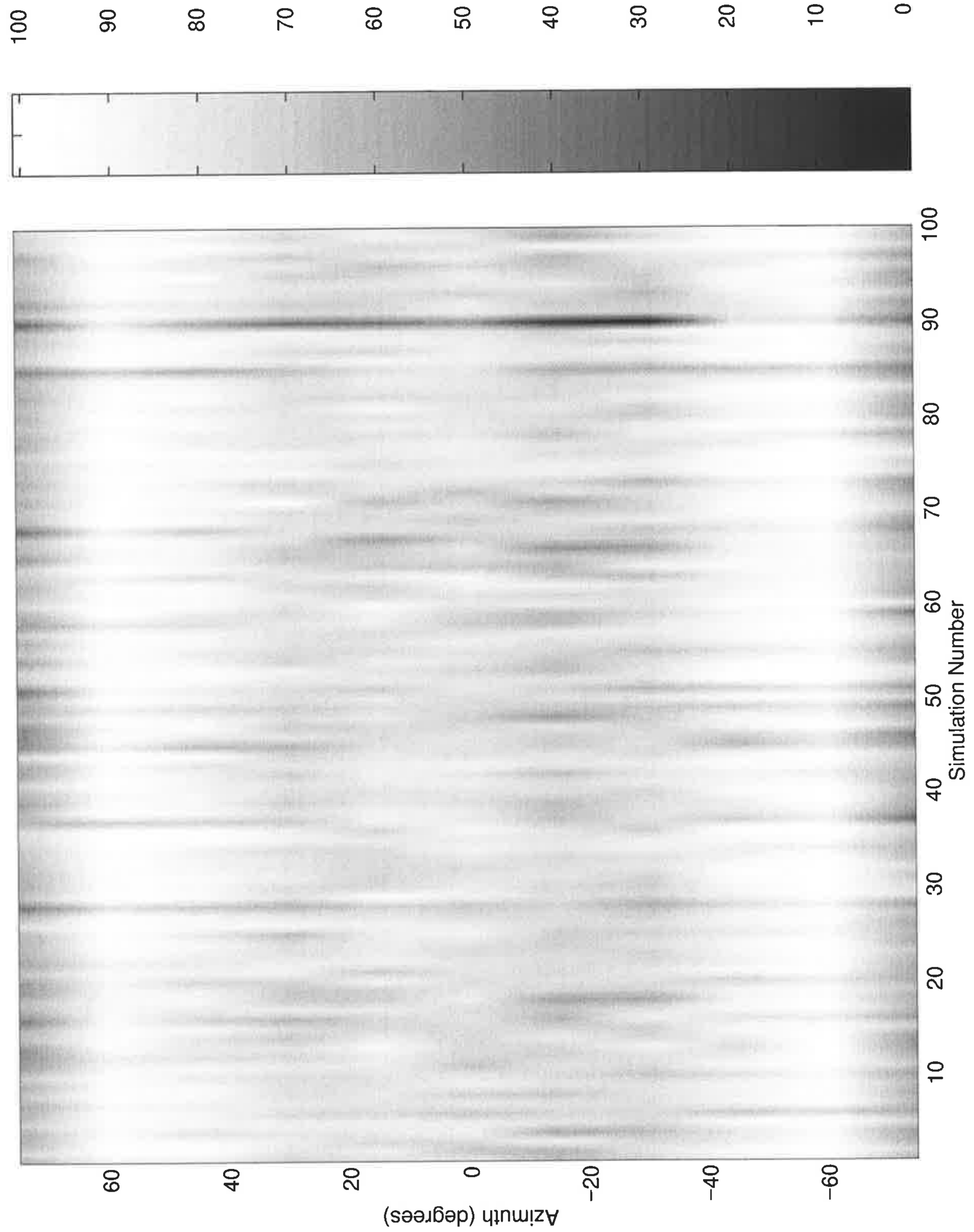

Figure 5.5: Statistical performance of algorithm.

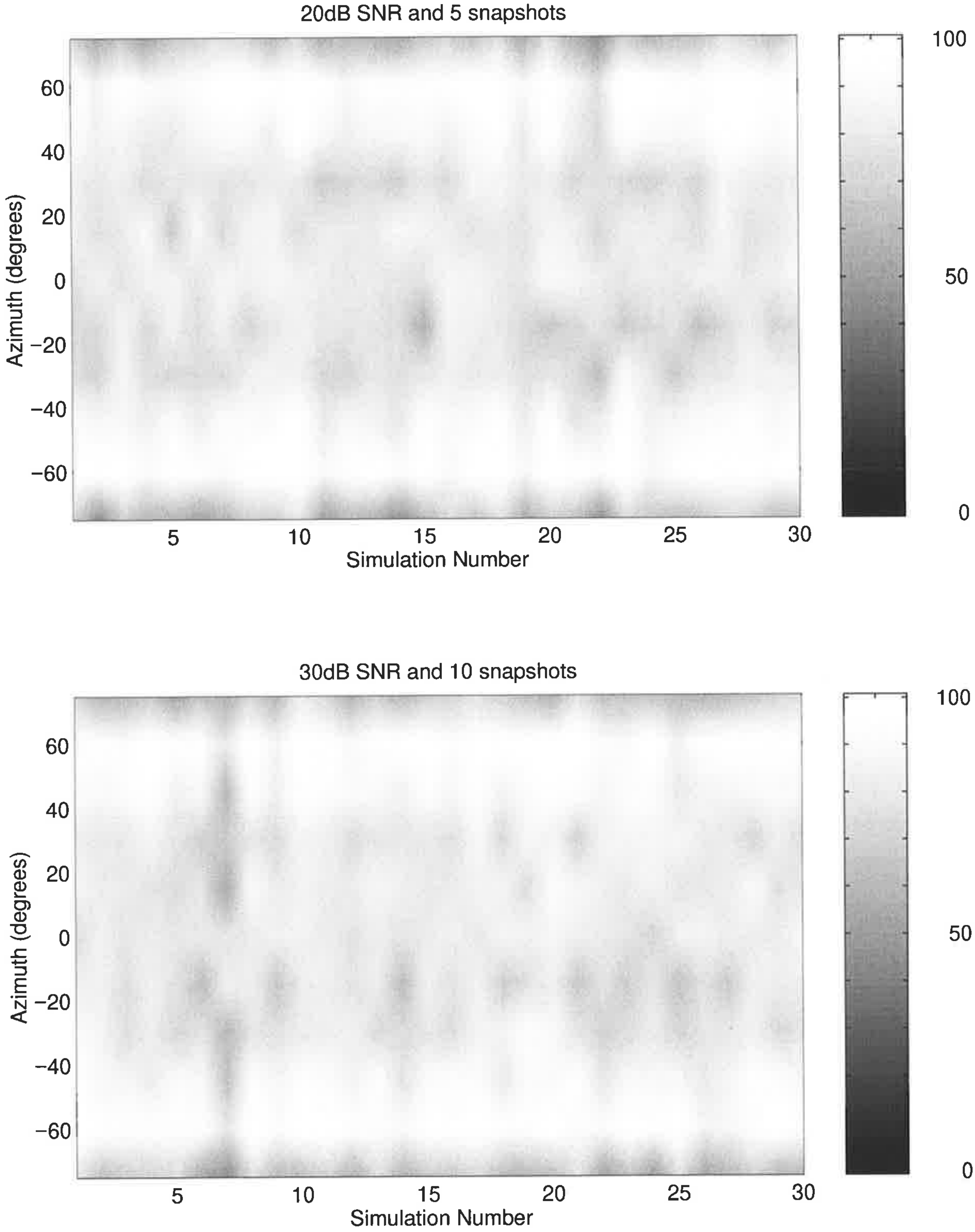

Figure 5.6: Performance of algorithm for typical number of snapshots and SNRs obtainable from OTH radar sources.

(5.9), for this scenario, simplifies to

$$Q = \sum_{n=1}^{N} \|\hat{\mathbf{e}}_n - \mathbf{Ca}(\theta_n)s_n\|^2 \tag{5.44}$$

where $\hat{\mathbf{e}}_n$ is the eigenvector corresponding to the signal eigenvalue (principal eigenvector) of $\hat{\mathbf{R}}_n$.

The cost function in equation (4.37) is formulated using the noise subspace, while the cost function in equation (5.44) is formulated using the signal subspace (in this case just the principal eigenvector). Hence similar performance is expected when the sources have high SNRs and large number of snapshots; that is both methods are expected to perform as well asymptotically. The performance of the methods for finite SNRs and snapshots however could be different.

Note further the optimisation procedure in each method are quite different. The method in chapter 4 iterates sequentially between DOA estimation, sensor position estimation and coupling matrix estimation, until the cost function changes in value by less than 0.1 percent. The method in this chapter has a complicated iteration sequence (see figure 5.2) which was obtained heuristically. The methods also use different techniques for estimating each parameter. Hence the comparative performance of the methods are illustrative of not only differences in the cost functions themselves, but also of differences in the optimisation procedures and the parameter estimators.

### 5.9.1 *Simulation Example*

The performance for the special case is first illustrated with a simulation example, and then the results obtained are compared with those in figure 5.3 which was for a variety of sources. As in chapter 4 thirty disjoint single-mode sources, with SNRs of 30 dB, are considered. The sources are equally spread from $-90^o$ to $+90^o$ in azimuth. The covariance matrices for each single-mode source is created from 500 snapshots (see below for typical number of snapshots) of the array output.

As before a 16-element nominally equispaced linear array, with inter-element spacing of $d = 0.4\lambda$, was considered. The actual sensor positions were generated as before, and the experimentally measured coupling matrix from the Jindalee transmitting array was used. The algorithm is run until convergence.

Figures 5.7 and 5.8 show the results obtained for the special case :

- the cost function decreases rapidly in the first few iterations, and then levels off by about the 30th iteration;
- the DOA estimation errors are less than about a quarter degree;
- the coupling matrix used and that estimated are very similar;
- the errors in the estimated sensor positions ($*$) are significantly better than those for the nominal sensor positions (o);
- the sidelobe levels obtained when the estimated parameters are used for array processing are very good.

These results are comparable to the results in the simulation example for the method in chapter 4, figure 4.5-4.6, and is better than those in figure 5.3-5.4 where a variety of sources were used. To obtain a good comparison, however, a Monte Carlo analysis has to be conducted.

### 5.9.2 *Monte Carlo Analysis*

Both the asymptotic performance and performance for finite/practical SNRs and snapshots (as would be the case in practice), are considered. Again the following scenarios are considered :

- case A : 30 dB SNRs and 500 snapshots;
- case B : 20 dB SNRs and 5 snapshots;
- case C : 30 dB SNRs and 10 snapshots.

Case A should illustrate the asymptotic performance, while case B and C illustrate the finite/practical performance. One hundred simulations were conducted for case A and is shown in figure 5.9. For both of the finite/practical cases, thirty simulations were conducted, the results being shown in figure 5.10. Comparing these results with those obtained in figure 4.7-4.8, one notes the performance for case A and C are very similar for both methods; both being very good in each case. Comparing the performances for case B one notes, unlike the method in chapter 4 (section 4.4), no failures are observed here. Good results are observed here, like the method in chapter 4 when no failures occur.

Hence it is concluded that both methods have good asymptotic performance and finite/practical performance, except that the method in chapter 4 tends to have a few failures. This is in accordance to what one would expect, since the method in chapter 4 has a MUSIC-like cost function; MUSIC being well known to have good asymptotic performance [212, 104, 108, 159, 30, 119], but also of being able to perform poorly when the SNR and number of snapshots are small [212, 206, 262, 189].

The dependence of the algorithm on the number of sources is shown in figure 5.11. The

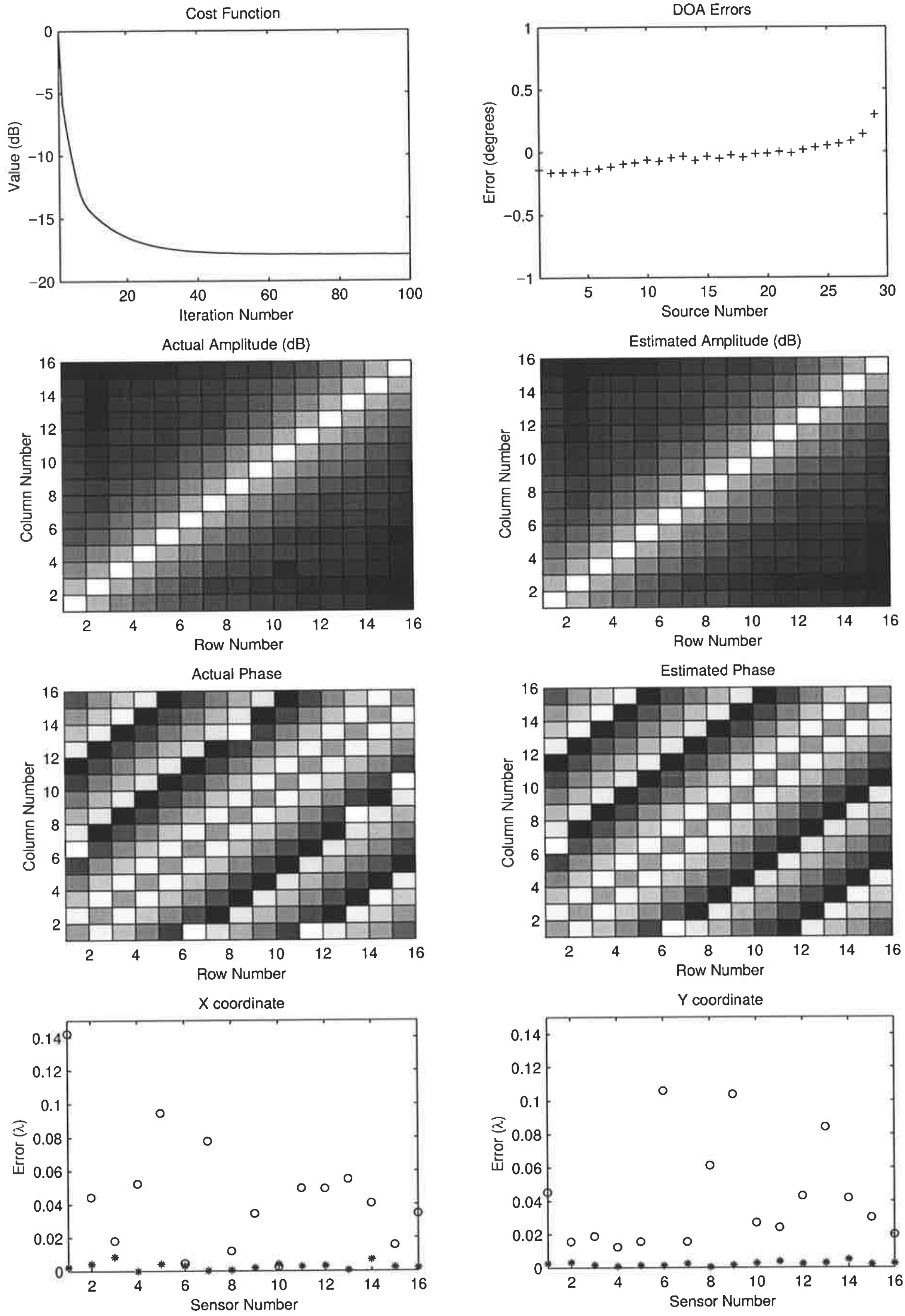

Figure 5.7: Special case simulation example : cost function decreases with iteration number; errors in estimated signals' DOAs; actual coupling matrix and estimated coupling matrix; errors in nominal (o) and estimated (∗) sensor positions.

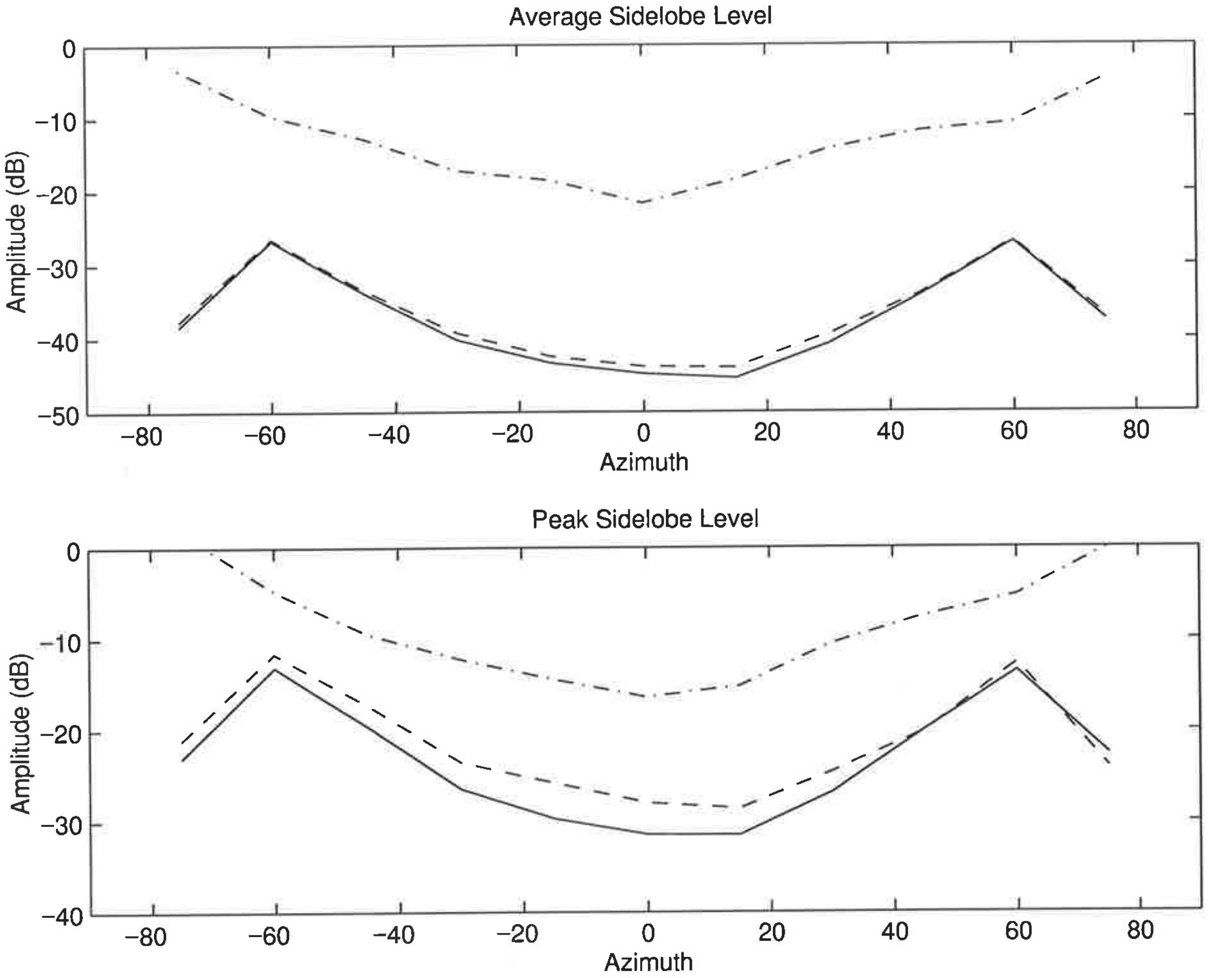

Figure 5.8: Average and peak sidelobe levels for parameters estimated in figure 5.7 - nominal parameters (—.—), estimated parameters (— —) and also the actual parameters (–)

same array is considered for each of these simulations, where 500 snapshots are obtained from each of the 30 dB disjoint sources. The algorithm fails when the number of sources is less than 16, since the number of sources is then insufficient for this algorithm to estimate the unknown parameters. These results are as good as those obtained in chapter 4 (see figure 4.9).

While ionospherically propagated meteor echoes are far-field returns, line-of-sight meteor echoes are often near-field returns (see chapter 7), and so the sensitivity of the algorithms to near-field sources is now considered. While radars can approximately estimate the range of returns, and so one can account (to some extent) for their near-field steering vectors, it is still of interest to determine how sensitive the algorithm is to unaccounted near-field sources. Thus the performance of the algorithm was investigated for the case where the source wavefronts are spherical and emanate from specified ranges (since the range effects the amount of wavefront curvature). The same array was considered for all the simulations, where 30 sources were present in the absence of any noise. The integrated sidelobe level (ISLB) obtained are shown

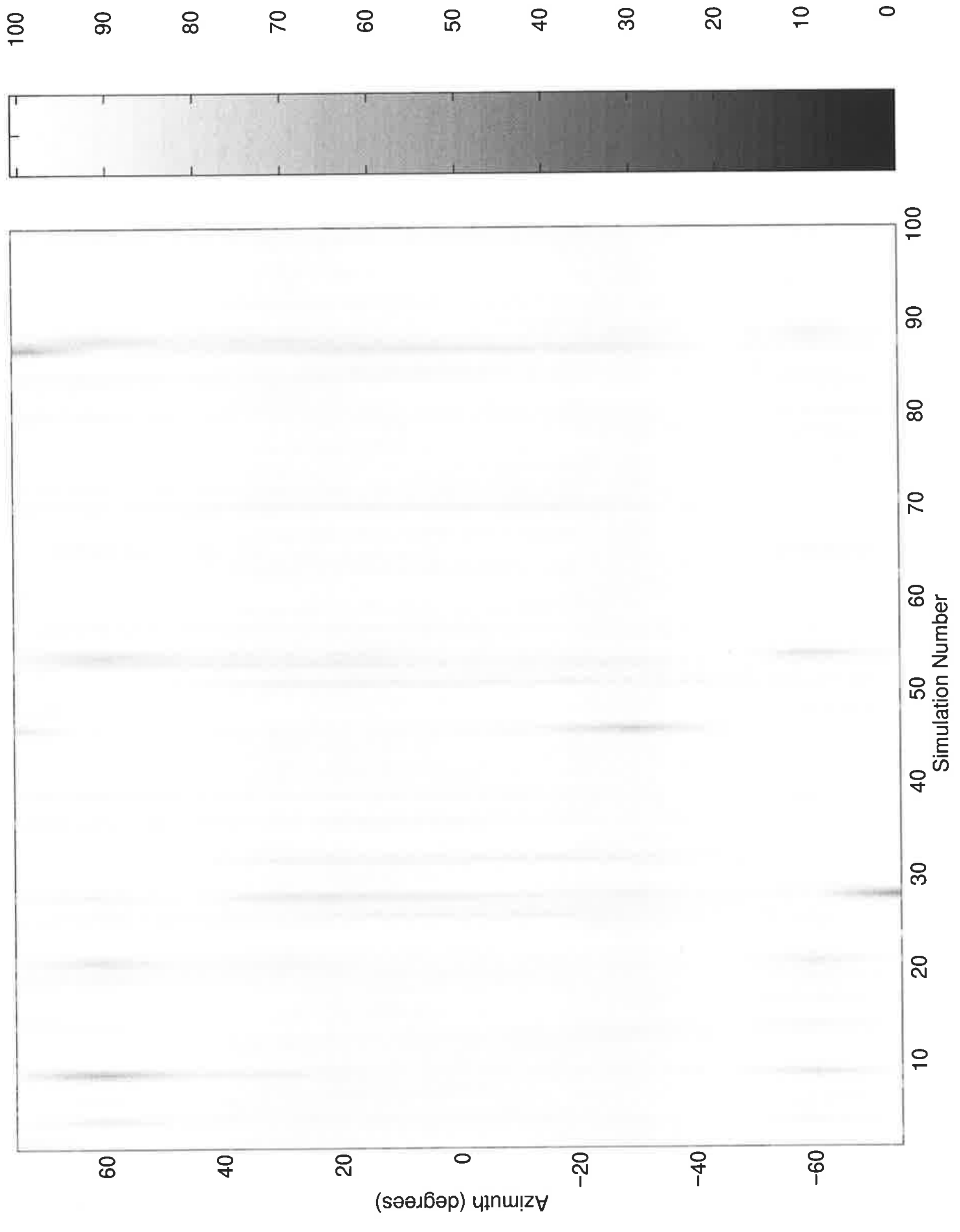

Figure 5.9: Statistical performance of special case - asymptotic scenario.

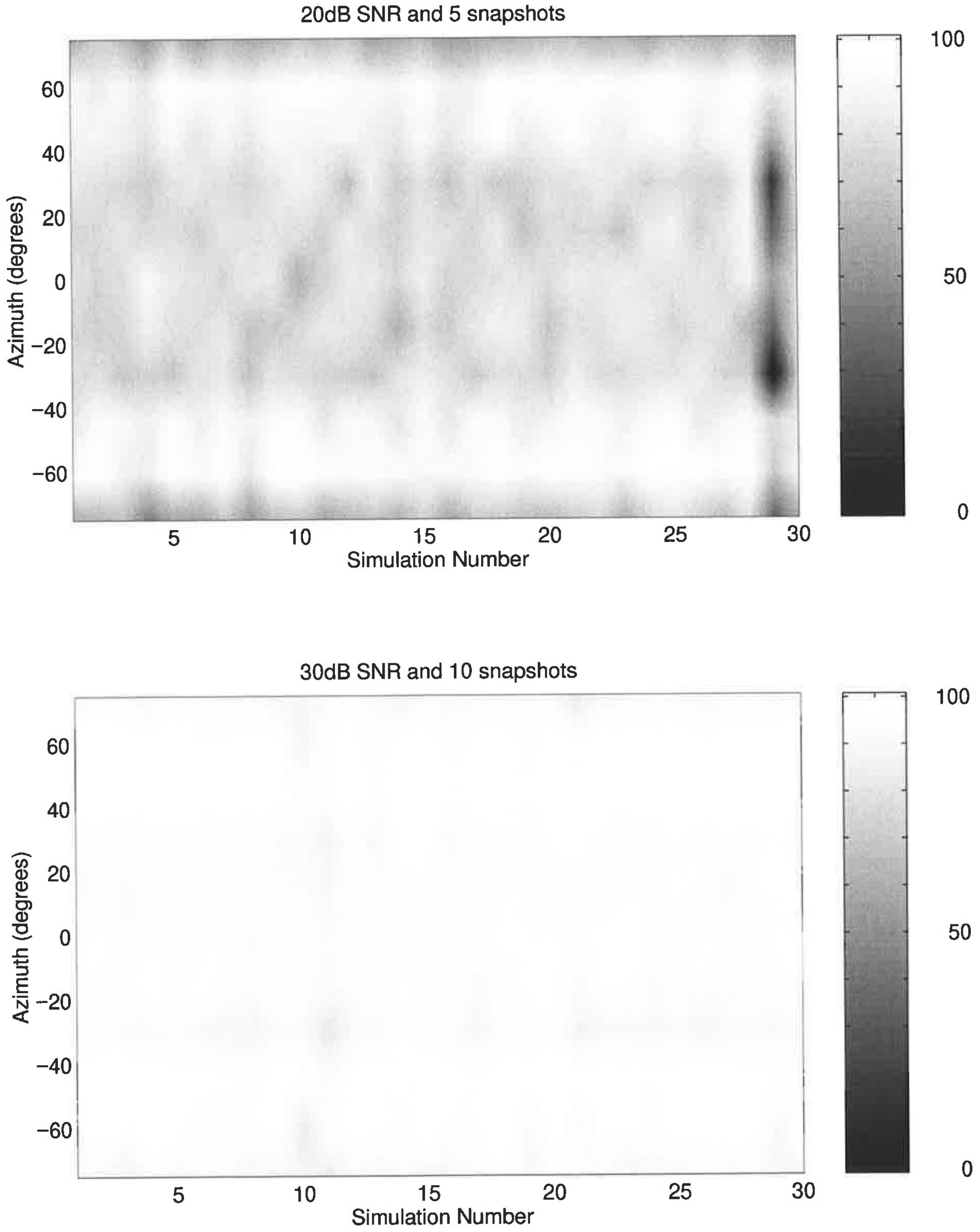

Figure 5.10: Statistical performance of special case - finite/practical scenario.

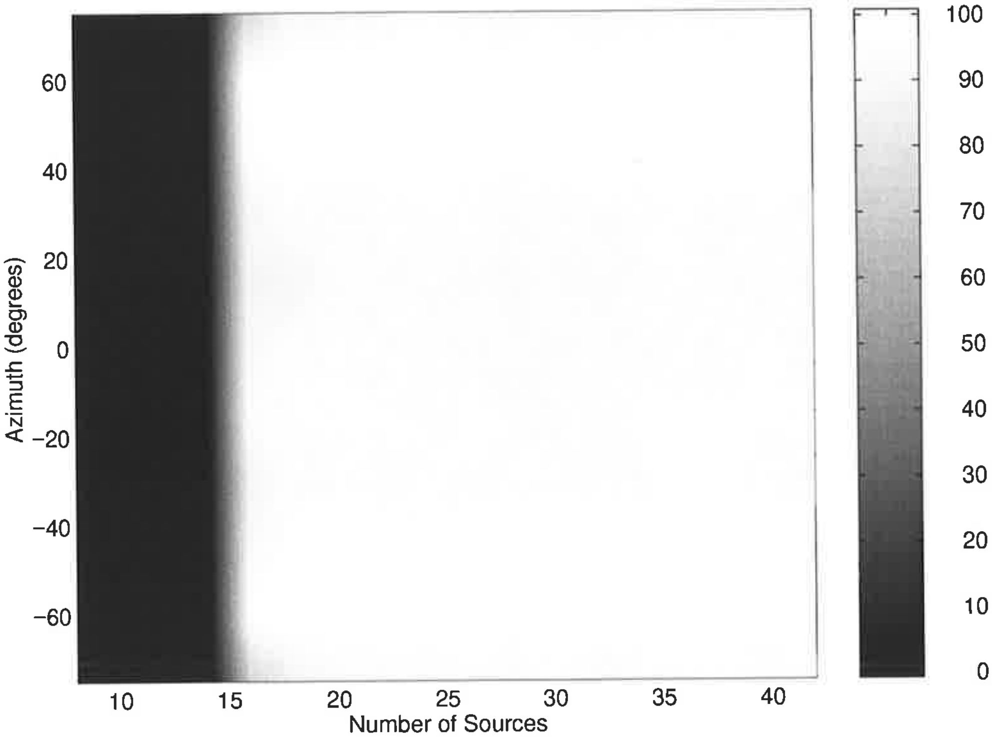

Figure 5.11: Dependence on number of sources, for the special case.

in Table 5.1, for sources at the specified ranges (note the array aperture was $6\lambda$); the ISLB for the nominal case was -9.6 dB. The algorithm failed for ranges less than about $10\lambda$, while for larger ranges the performance improved with range; the performance being range independent for ranges greater than about $250\lambda$. The performance of the algorithm in chapter 4 was very similar to that shown in Table 5.1, except that it also failed for the case where the range was less than $10\lambda$. These results indicate the algorithms are robust, provided the sources are not very close (less than about ten times the array aperture length) to the radar.

| Range ($\lambda$) | 6 | 10 | 25 | 60 | 100 | 250 | 600 | $\infty$ |
|---|---|---|---|---|---|---|---|---|
| ISLB | - | -21.7 | -28.9 | -31.8 | -32.4 | -32.7 | -32.7 | -32.7 |

Table 5.1: Effect of near-field sources on ISLB

## 5.10 Error Surface

The cost function / error surface is analysed in this section. As mentioned in chapter 4, it is important to investigate the smoothness of the error surface and to determine if it is highly multi-modal. The error surface is analysed for a 4-element array (as in chapter 4), and also a theoretical analysis is conducted for a 2-element array.

### 5.10.1 4-element Array

In this section the "special case" cost function in equation (5.44) is first analysed, and then the general cost function in equation (5.9) is analysed. As in chapter 4 the nominally uniform linear 4-element array, with the position errors in Table 4.1, is considered together with the Jindalee coupling matrix. Ten disjoint single-mode sources equally spaced over 180° in azimuth are considered, with the exact covariance matrix for each source determined (as before). The covariance matrices are eigendecomposed and the principal eigenvectors $\mathbf{e}_n$ obtained. The nominal sensor positions are $x_m^o = md$ and $y_m^o = 0$, and the identity matrix is used for the coupling matrix. Bearing estimates and the complex scalars $s_n$, are determined as in section 5.6.1. These quantities are then used to calculate the error surface; two parameters being simultaneously varied while the other parameters are fixed at the values determined above.

First the cost function was analysed while the sensor position (both $x$ and $y$ coordinates) of the third sensor was varied i.e. $Q(x_3, y_3)$. Figure 5.12 shows the error surface when the $x$ and $y$ coordinates were varied up to $0.4\lambda$ around their nominal coordinate values. Note two different sub-figures of the same error surface are shown here to better illustrate the error surface. As in chapter 4 the error surface $Q(x_3, y_3)$ is smooth, not multi-modal, and the curvature at all points are towards the minimum. Again as in chapter 4, for displacements up to $0.8\lambda$ from the nominal values (not shown), curvatures away from the minimum were observed; position errors of this size however not being of interest. Good error surfaces were also obtained for the coupling parameters and the complex scalars $s_n$.

The error surface $Q(\theta_1, \theta_5)$, for two DOAs, is shown in figure 5.13; where the true values of $\theta_1$ and $\theta_5$ are $-81^o$ and $-9^o$ respectively. As in chapter 4, only over a small region is the curvature towards the minimum. This critical region is smaller than the corresponding region in chapter 4 (figure 4.18) and so initial bearing estimates need to be closer to the true values for this algorithm than that in chapter 4. Note also the rest of the error surface in figure 5.13 is more highly multi-modal than the error surface in figure 4.18. The critical region was smaller when the position errors were twice the amount in figure 5.13, and the shape of the error surface did not change much when estimated covariance matrices (from 5 snapshots and 10 dB SNR sources) were used.

The signal DOAs are the most sensitive parameters and so the bearing estimation procedure is of most importance. The Bartlett processor is robust, and so the results obtained in this

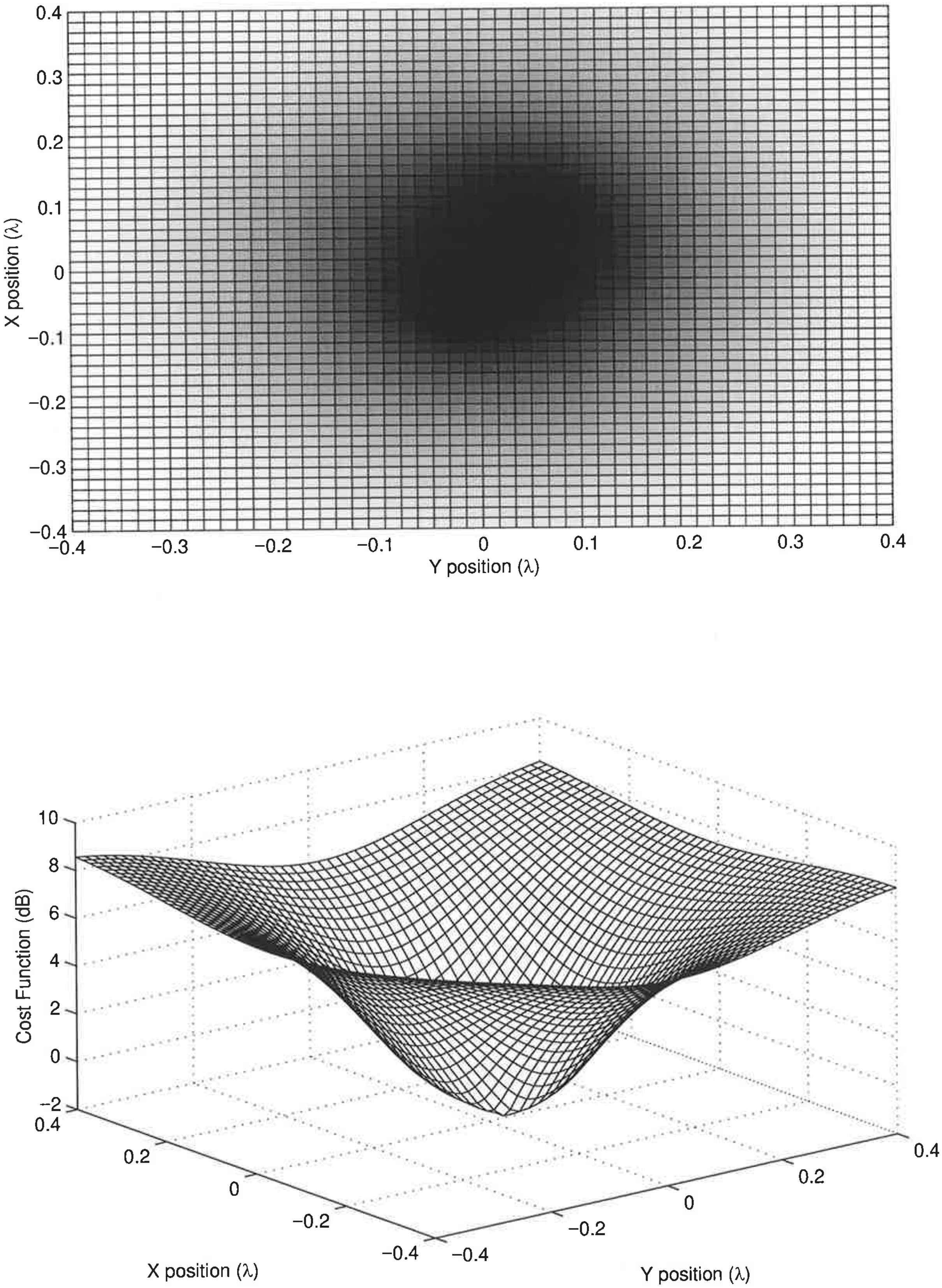

Figure 5.12: Error surface for third sensor position.

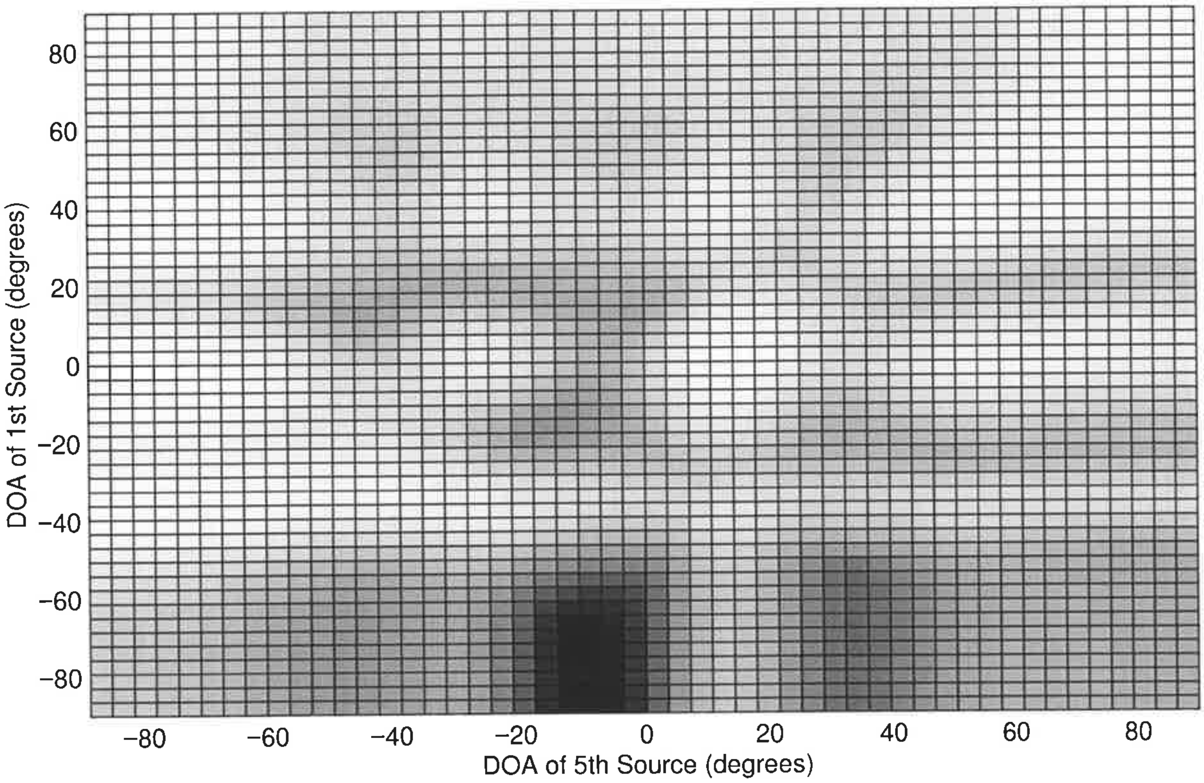

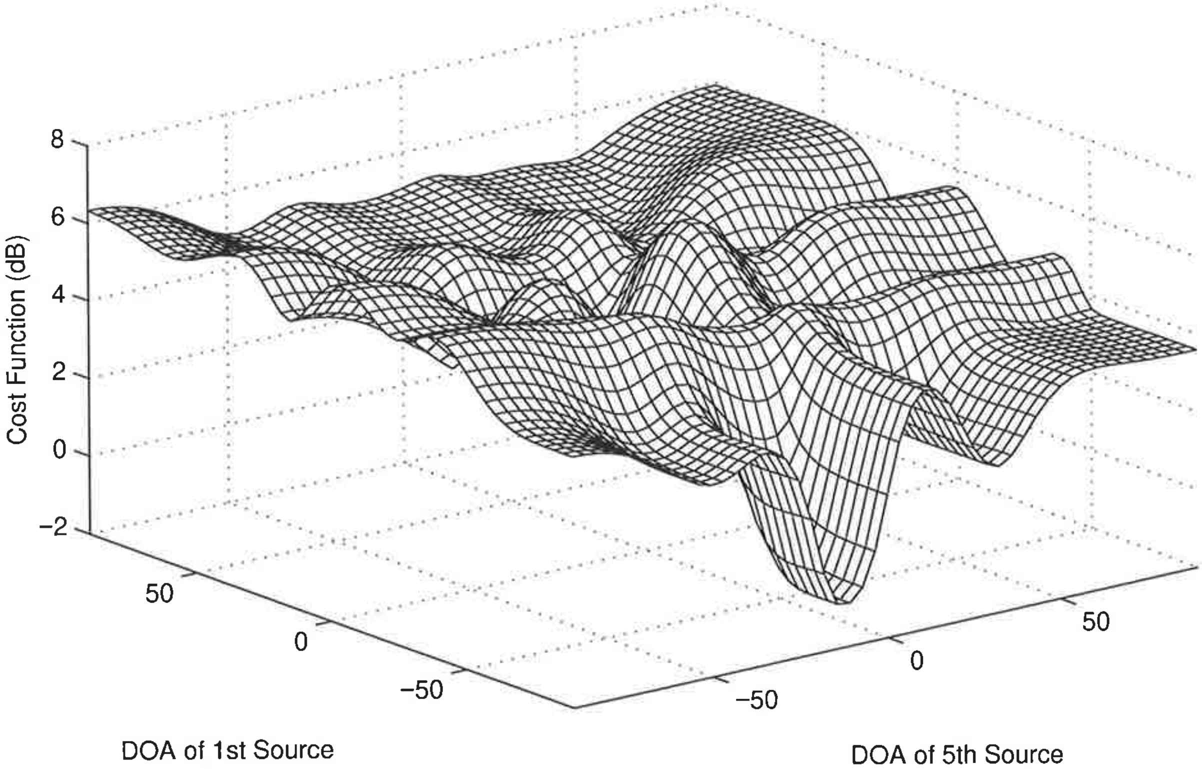

Figure 5.13: Error surface for DOAs of two sources.

chapter have been good.

The error surface for the general case (considered prior to section 5.9), with eight time-invariant DOA signals and seven time-varying DOA (single-snapshot) signals, was also considered. The surface $Q(\theta_1, \theta_5)$, for two sources with true DOAs of $-79^{\circ}$ and $-10^{\circ}$ respectively, is shown in figure 5.14. As in the special case the curvature towards the minimum occurs only over a small critical region, with the surface otherwise highly multi-modal. The critical region is somewhat bigger than that for the special case, but is flatter and hence the true minimum less well defined. The less well defined minimum (which is due to single-snapshot sources) is possibly the reason why the results for the general case were not as good as those for the special case. The results obtained for the other unknown parameters were not very different to that for the special case. Note the error surfaces for the general case differed somewhat for each realisation, since single-snapshot sources are involved.

### 5.10.2 Theoretical Analysis of 2-element Array

The error surface in equation (5.44) is now analysed analytically to determine how the unknown parameters effect the surface. In Appendix C analytic expressions are derived for this error surface. For the 2-element array considered in Appendix C, the error surface was analysed for each of the unknown parameters, while the other parameters were fixed at their true values. While this provides a simplified view of the error surface, it has been found to provide a good intuitive understanding.

One sensor was arbitrarily chosen to be at (0,0), while the other sensor was chosen to be along the $x$-axis at ($x$,0). The symmetric coupling matrix was arbitrarily chosen to have a first element of unity, the coupling matrix being

$$\mathbf{C} = \begin{bmatrix} 1 & c_1 e^{j\psi_1} \\ c_1 e^{j\psi_1} & c_2 e^{j\psi_2} \end{bmatrix} \tag{5.45}$$

As derived in Appendix C, for the source DOA estimate $\hat{\theta}_n$,

$$Q_1(\hat{\theta}_n) = K_n \left(1 - \cos\left(\frac{2\pi x}{\lambda}[\sin\theta_n - \sin\hat{\theta}_n]\right)\right) \tag{5.46}$$

$$\frac{dQ_1(\hat{\theta}_n)}{d\hat{\theta}_n} = -\frac{2\pi x}{\lambda} K_n \cos\hat{\theta}_n \sin\left(\frac{2\pi x}{\lambda}[\sin\theta_n - \sin\hat{\theta}_n]\right) \tag{5.47}$$

$$\frac{d^2Q_1(\hat{\theta}_n)}{d^2\hat{\theta}_n} = \frac{2\pi x}{\lambda} K_n \Bigg[\sin\hat{\theta}_n \sin\left(\frac{2\pi x}{\lambda}[\sin\theta_n - \sin\hat{\theta}_n]\right)$$

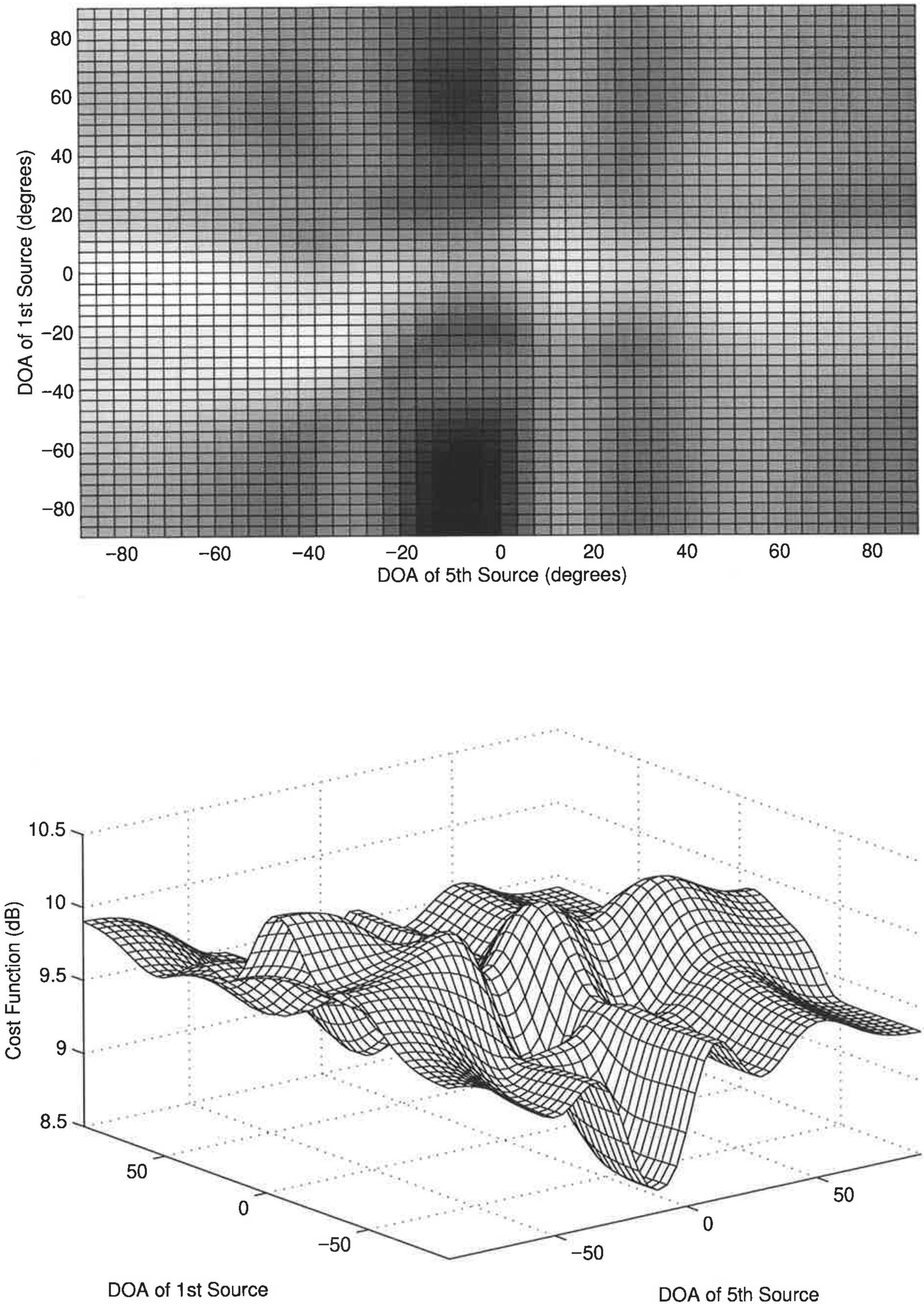

Figure 5.14: Error Surface for General Case.

$$+\frac{2\pi x}{\lambda}\cos^2\hat{\theta}_n\cos\left(\frac{2\pi x}{\lambda}[\sin\theta_n-\sin\hat{\theta}_n]\right)\Bigg] \tag{5.48}$$

where $K_n = 2|s_n|^2(c_1^2 + c_2^2)$. As expected when $\hat{\theta}_n = \theta_n$, $Q_1 = 0$ i.e. the global minimum. The location of local minima/maxima can be obtained by determining the locations where the first derivative is zero. This occurs when $\hat{\theta}_n = \pm 90^\circ$ (i.e. end-fire directions) and when

$$\begin{aligned} \frac{2\pi x}{\lambda}[\sin\theta_n-\sin\hat{\theta}_n] &= p\pi & (5.49)\\ \sin\hat{\theta}_n &= -\frac{p}{2(x/\lambda)}+\sin\theta_n & (5.50)\end{aligned}$$

where $p = 0, \pm1, \pm2, \pm3$ etc (any integer). The minima corresponding to $p = 0$ is the true solution ($\hat{\theta}_n = \theta_n$), while all other solutions are incorrect. Note for all solutions corresponding to even $p$ values $Q_1 = 0$, and the second derivative at these solutions is

$$\left.\frac{d^2Q_1(\hat{\theta}_n)}{d^2\hat{\theta}_n}\right|_{\text{p even}} = \frac{4\pi^2x^2}{\lambda^2}K_n\cos^2\hat{\theta}_n \tag{5.51}$$

which is greater than or equal to zero (note $K_n > 0$). Hence these solutions are minima. For the solutions corresponding to odd $p$ values $Q_1 = 2K_n$, and the second derivative at these solutions is

$$\left.\frac{d^2Q_1(\hat{\theta}_n)}{d^2\hat{\theta}_n}\right|_{\text{p odd}} = -\frac{4\pi^2x^2}{\lambda^2}K_n\cos^2\hat{\theta}_n \tag{5.52}$$

which is less than or equal to zero; these solutions hence are maxima. So the error surface for the source DOA has multiple minima and maxima, and good initial estimates are required to prevent convergence to an incorrect solution.

The second derivative computed at the true solution, indicates how shallow the error surface is in the vicinity of the true solution; the greater the value the less shallow the error surface. Substituting $\hat{\theta}_n = \theta_n$ into equation (5.48) gives

$$\left.\frac{d^2Q_1(\hat{\theta}_n)}{d^2\hat{\theta}_n}\right|_{\hat{\theta}_n=\theta_n} = 8\pi^2(x/\lambda)^2|s_n|^2(c_1^2+c_2^2)\cos^2\hat{\theta}_n \tag{5.53}$$

which indicates the shallowness of the error surface decreases : (a) with increasing mutual coupling; (b) with increasing inter-element spacing; and (c) as the source DOA approaches broadside direction. Note that condition (c) can be observed in figure 5.13, where the DOA closer to broadside has a less shallow minimum.

For the sensor position error $\Delta x = \hat{x} - x$,

$$
\begin{aligned}
Q_2(\Delta x) &= \sum_{n=1}^{N} K_n \left(1 - \cos\left(\frac{2\pi\Delta x}{\lambda}\sin\theta_n\right)\right) && (5.54)\\
\frac{dQ_2(\Delta x)}{d\Delta x} &= \sum_{n=1}^{N} \frac{2\pi}{\lambda} K_n \sin\theta_n \sin\left(\frac{2\pi\Delta x}{\lambda}\sin\theta_n\right) && (5.55)\\
\frac{d^2Q_2(\Delta x)}{d^2\Delta x} &= \sum_{n=1}^{N} \frac{4\pi^2}{\lambda^2} K_n \sin^2\theta_n \cos\left(\frac{2\pi\Delta x}{\lambda}\sin\theta_n\right) && (5.56)
\end{aligned}
$$

As expected $Q_2 = 0$ when $\Delta x = 0$ (i.e. the global minimum). For the case of a single calibration source ($N = 1$), the first derivative is zero when $\theta_n = 0$ or when

$$
\begin{aligned}
\frac{2\pi\Delta x}{\lambda}\sin\theta_n &= p\pi && (5.57)\\
\frac{\Delta x}{\lambda} &= \frac{p}{2\sin\theta_n} && (5.58)
\end{aligned}
$$

where again $p$ is any integer. The solution corresponding to $p = 0$ is the true solution ($\Delta x = 0$), while all other solutions are not correct. Solutions which correspond to even $p$ values result in $Q_2 = 0$, and the second derivative at these solutions is

$$
\left.\frac{d^2Q_2(\Delta x)}{d^2\Delta x}\right|_{\text{p even}} = \frac{4\pi^2}{\lambda^2} K_n \sin^2\theta_n \qquad (5.59)
$$

which is greater than or equal to zero; these solutions hence are minima. The solutions corresponding to odd $p$ values give $Q_2 = 2K_n \neq 0$, and the second derivative at these solutions is

$$
\left.\frac{d^2Q_2(\Delta x)}{d^2\Delta x}\right|_{\text{p odd}} = -\frac{4\pi^2}{\lambda^2} K_n \sin^2\theta_n \qquad (5.60)
$$

which is less than or equal to zero; these solutions are hence maxima. While the error surface for the position error is multi-modal, note the closest maxima to the true solution are at $|\Delta x/\lambda| \geq 0.5$ (see equation (5.58) and note the closest maxima are when $p = \pm 1$ and also note that $|\sin(\theta_n)| \leq 1$). Hence initial position estimates may have large errors, and so position estimates are not as critical as source DOA estimates.

The second derivative at $\Delta x = 0$ is

$$
\left.\frac{d^2Q_2(\Delta x)}{d^2\Delta x}\right|_{\Delta x=0} = \sum_{n=1}^{N} \frac{8\pi^2}{\lambda^2} |s_n|^2 (c_1^2 + c_2^2) \sin^2\theta_n \qquad (5.61)
$$

The shallowness of the error surface decreases with increasing mutual coupling, but in this case the shallowness increases as the source DOA moves towards broadside direction.

For the coupling amplitudes,

$$Q_3(\hat{c}_1) = \sum_{n=1}^{N} 2|s_n|^2(c_1^2 - 2c_1\hat{c}_1 + \hat{c}_1^2) \tag{5.62}$$

$$\frac{dQ_3(\hat{c}_1)}{d\hat{c}_1} = \sum_{n=1}^{N} 4|s_n|^2(\hat{c}_1 - c_1) \tag{5.63}$$

$$\frac{d^2Q_3(\hat{c}_1)}{d^2\hat{c}_1} = \sum_{n=1}^{N} 4|s_n|^2 \tag{5.64}$$

$$Q_4(\hat{c}_2) = \sum_{n=1}^{N} |s_n|^2(c_2^2 - 2c_2\hat{c}_2 + \hat{c}_2^2) \tag{5.65}$$

$$\frac{dQ_4(\hat{c}_2)}{d\hat{c}_2} = \sum_{n=1}^{N} 2|s_n|^2(\hat{c}_2 - c_2) \tag{5.66}$$

$$\frac{d^2Q_4(\hat{c}_2)}{d^2\hat{c}_2} = \sum_{n=1}^{N} 2|s_n|^2 \tag{5.67}$$

The first derivatives for the coupling amplitudes are zero only when $\hat{c}_1 = c_1$ and $\hat{c}_2 = c_2$. This indicates that only one minimum exists, and, as expected, the respective cost functions are zero under these conditions. The second derivatives are independent of the coupling amplitudes, since the cost functions are quadratics. Note also the shallowness of the error surface is independent of the source DOAs and the position error.

For the coupling phases,

$$Q_5(\Delta\psi_1) = \sum_{n=1}^{N} 4|s_n|^2c_1^2(1 - \cos(\Delta\psi_1)) \tag{5.68}$$

$$\frac{dQ_5(\Delta\psi_1)}{d\Delta\psi_1} = \sum_{n=1}^{N} 4|s_n|^2c_1^2\sin(\Delta\psi_1) \tag{5.69}$$

$$\frac{d^2Q_5(\Delta\psi_1)}{d^2\Delta\psi_1} = \sum_{n=1}^{N} 4|s_n|^2c_1^2\cos(\Delta\psi_1) \tag{5.70}$$

$$Q_6(\Delta\psi_2) = \sum_{n=1}^{N} 2|s_n|^2c_2^2(1 - \cos(\Delta\psi_2)) \tag{5.71}$$

$$\frac{dQ_6(\Delta\psi_2)}{d\Delta\psi_2} = \sum_{n=1}^{N} 2|s_n|^2c_2^2\sin(\Delta\psi_2) \tag{5.72}$$

$$\frac{d^2Q_6(\Delta\psi_2)}{d^2\Delta\psi_2} = \sum_{n=1}^{N} 2|s_n|^2c_2^2\cos(\Delta\psi_2) \tag{5.73}$$

where $\Delta\psi_1 = \hat{\psi}_1 - \psi_1$ and $\Delta\psi_2 = \hat{\psi}_2 - \psi_2$. As expected, the respective cost functions are zero when $\Delta\psi_1 = 0$ and $\Delta\psi_2 = 0$. The first derivatives are zero when $\Delta\psi_1 = p\pi$ and $\Delta\psi_2 = p\pi$

respectively. The true solution is clearly when $p = 0$, but other minima (even $p$'s) and maxima (odd $p$'s) exist too. Good initial estimates are however not necessary since the distance between the true minima, and the closest maxima to it, is large ($\pi$ radians).

The second derivatives, evaluated at the true solutions are

$$\left.\frac{d^2Q_5(\Delta\psi_1)}{d^2\Delta\psi_1}\right|_{\Delta\psi_1=0} = \sum_{n=1}^{N} 4|s_n|^2c_1^2 \tag{5.74}$$

$$\left.\frac{d^2Q_6(\Delta\psi_2)}{d^2\Delta\psi_2}\right|_{\Delta\psi_2=0} = \sum_{n=1}^{N} 2|s_n|^2c_2^2 \tag{5.75}$$

The shallowness of the error surfaces decrease with the increasing amplitude of the corresponding coupling coefficient, and are independent of the source DOAs and position error.

For the complex scalars $s_n$,

$$Q_7(|\hat{s}_n|) = L_n(|s_n|^2 - 2|s_n||\hat{s}_n| + |\hat{s}_n|^2) \tag{5.76}$$

$$\frac{dQ_7(|\hat{s}_n|)}{d|\hat{s}_n|} = 2L_n(|\hat{s}_n| - |s_n|) \tag{5.77}$$

$$\frac{d^2Q_7(|\hat{s}_n|)}{d^2|\hat{s}_n|} = 2L_n \tag{5.78}$$

$$Q_8(\Delta\delta_n) = 2|s_n|^2L_n(1 - \cos(\Delta\delta_n)) \tag{5.79}$$

$$\frac{dQ_8(\Delta\delta_n)}{d\Delta\delta_n} = 2|s_n|^2L_n\sin(\Delta\delta_n) \tag{5.80}$$

$$\frac{d^2Q_8(\Delta\delta_n)}{d^2\Delta\delta_n} = 2|s_n|^2L_n\cos(\Delta\delta_n) \tag{5.81}$$

where $L_n = 1 + 2c_1^2 + c_2^2 + c_1(h_n^*e^{-j\psi_1} + h_ne^{j\psi_1}) + c_1c_2(h_ne^{j(\psi_2-\psi_1)} + h_n^*e^{j(\psi_1-\psi_2)})$ and $\Delta\delta_n = \hat{\delta}_n - \delta_n$. The only minimum for $|\hat{s}_n|$ occurs when $|\hat{s}_n| = |s_n|$, and the second derivative is independent of $|\hat{s}_n|$ since the cost function is a quadratic (with the shallowness decreasing with increasing mutual coupling). The first derivative for $\Delta\hat{\delta}_n$ is zero when $\Delta\hat{\delta}_n = p\pi$. The true solution occurs when $p = 0$, with other minima (even $p$'s) and maxima (odd $p$'s) existing; initial estimates for $\Delta\hat{\delta}_n$ are not critical since the minimum at the true solution is well separated ($\pi$ radians) from its closest maxima.

## 5.11 Performance with Larger Model Errors

The algorithm's performance for larger model errors is shown, in figure 5.15 for the special case, and in figure 5.16 for the general case. In each case sensor position errors with STD of $0.2d$, $0.3d$ and $0.4d$, are considered. The performance for the special case is good, for a STD of $0.2d$, and in most cases for $0.3d$; the performance for a STD of $0.4d$ being however poor. The performance for the general case is good for a STD of $0.2d$, but is poor in many cases for $0.3d$ and in all cases for $0.4d$; the general case being worse than the special case, due mainly to only a single-snapshot being obtained from some sources (in the general case). The results for the special case is comparable to those obtained in chapter 4 (see figure 4.19).

## 5.12 Conclusion

A new array calibration approach which can use disparate sources in the HF environment, to estimate mutual coupling and sensor position errors, has been presented. The performance of the algorithm has been analysed using simulations, illustrating that the algorithm significantly reduces the array sidelobes. It was also shown that the algorithm performed well for typical SNRs and number of snapshots obtainable from OTH radar sources. In general, while convergence to the global minimum cannot be guaranteed, good results are obtained for typically available initial conditions.

The performance of the algorithm, for the special case where all the sources are disjoint and single-mode (as considered in chapter 4), was shown to be comparable to that obtained in chapter 4. The algorithm's error surface was analysed and it was shown that the source DOAs are the most critical parameter.

In chapter 6 the Cramer-Rao lower bound is derived and analysed, for the problems considered in both this chapter and chapter 4. In chapter 7 sources present in the HF environment are investigated from an array calibration perspective.

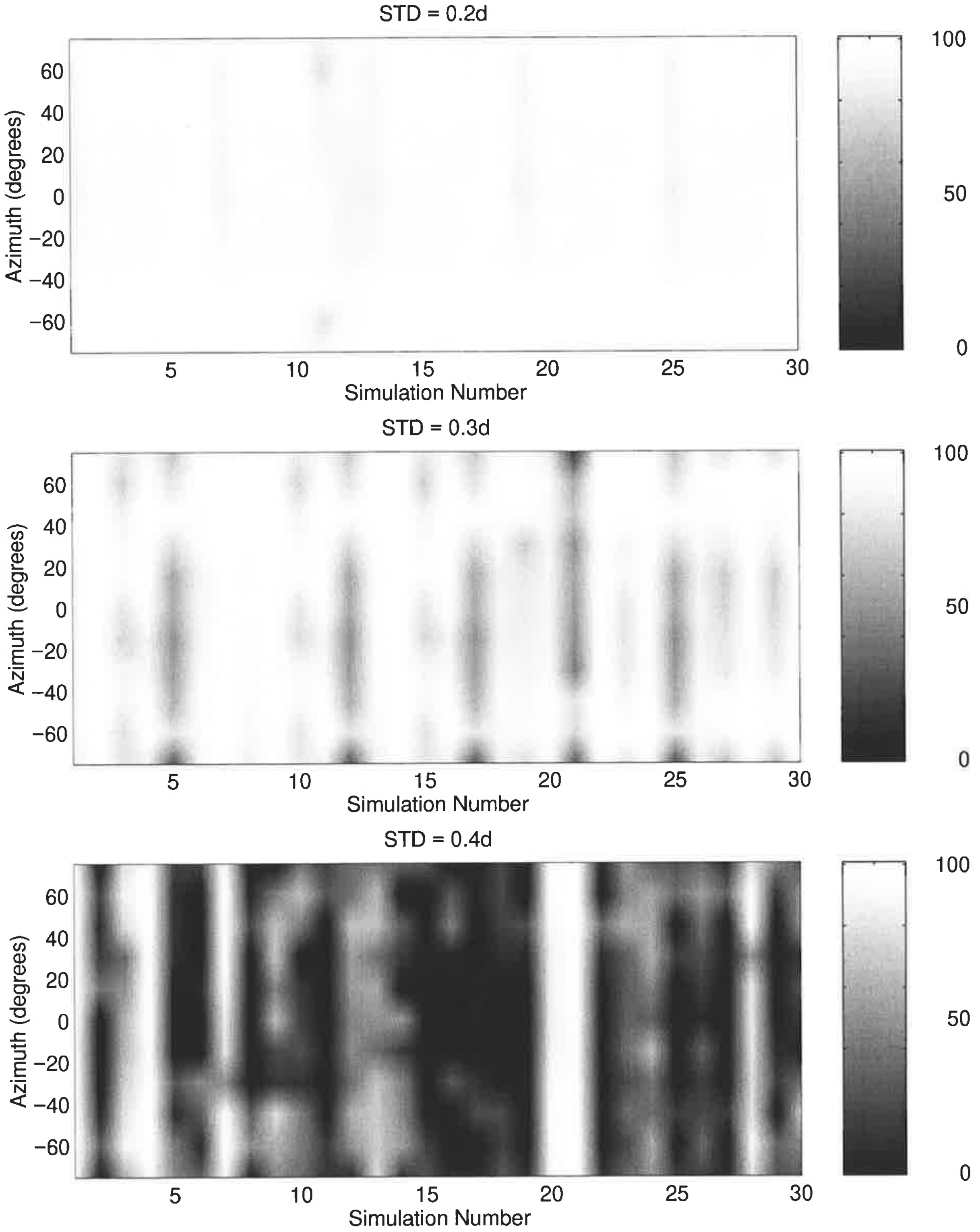

Figure 5.15: Algorithm's performance in the special case, for larger model errors. Sensor position errors with standard deviation - (a) $0.2d$, (b) $0.3d$, (c) $0.4d$.

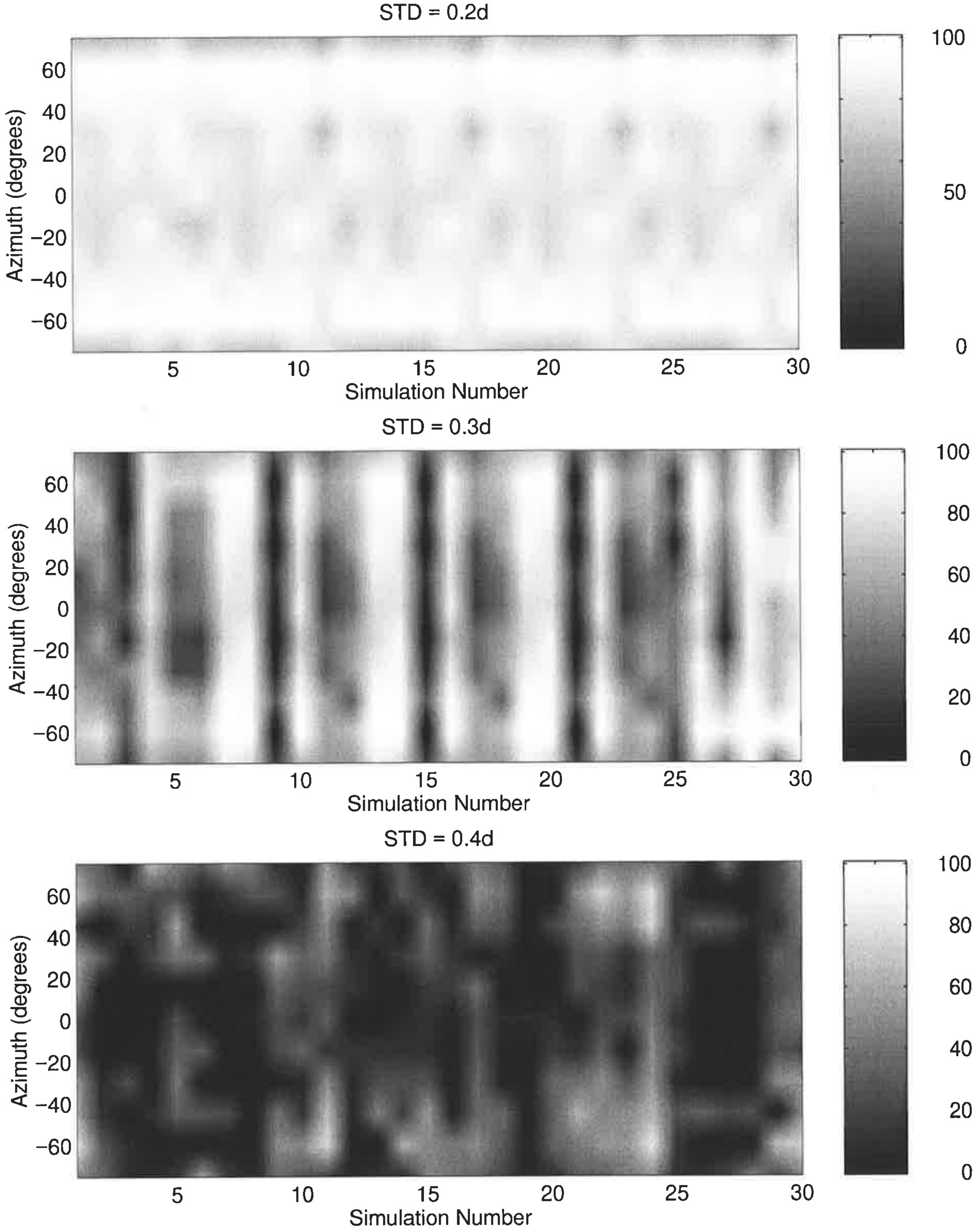

Figure 5.16: Algorithm's performance in the general case, for larger model errors. Sensor position errors with standard deviation - (a) $0.2d$, (b) $0.3d$, (c) $0.4d$.

## CHAPTER 6

# Cramer-Rao Lower Bounds

In this chapter the Cramer-Rao lower bound (CRLB) is derived and analysed for the array calibration problems considered in both chapters 4 and 5. The chapter starts with the derivation of the CRLB for the problem considered in chapter 4, i.e. for the case where all the sources are disjoint sources. This CRLB is then analysed : (a) to investigate the variation of the bound with SNR, number of snapshots, number of sources, etc; and (b) to compare the performance of the algorithm in chapter 4 with the bound. Then the CRLB expressions are generalised for the problem considered in chapter 5, and the performance of the algorithm in chapter 5 is compared with this CRLB.

The CRLB for array calibration has been considered in [148], [170, 168], [250], [83], [66], [138, 139], [235], [140], [196, 194]. Only [170, 168] and [140] consider multiple sources which are disjoint. In [170, 168], only sensor position errors are considered, and prior statistics are used in the derivation of the CRLB. In [140] the source DOAs are assumed to be known a priori and the coupling matrix is unstructured. Here the CRLB is determined for disjoint sources (and later for disparate sources), where the sensor positions, symmetric coupling matrix and source DOAs are unknown.

## 6.1 CRLB for Disjoint Sources

In this section the CRLB is derived for the problem considered in chapter 4, where disjoint (single-mode) sources are used to estimate sensor positions, mutual coupling and source DOAs. The likelihood function for the complete data set $\{\mathbf{z}_n(t), t = 1, 2, ..., T \,\&\, n = 1, 2, ..., N\}$ (see chapter 4) is given by

$$p[\check{\mathbf{z}}(1),\check{\mathbf{z}}(2),...,\check{\mathbf{z}}(T)/\mathbf{\Psi}] = \prod_{t=1}^{T}\frac{1}{\pi^{M}\|\check{\mathbf{R}}\|}\exp\left(-\check{\mathbf{z}}^{H}(t)\check{\mathbf{R}}^{-1}\check{\mathbf{z}}(t)\right) \tag{6.1}$$

where $\check{\mathbf{z}}(t) = [\mathbf{z}_1^T(t), \mathbf{z}_2^T(t), ..., \mathbf{z}_N^T(t)]^T$, the parameters being estimated $\mathbf{\Psi} = [\boldsymbol{\theta}^T, \mathbf{x}^T, \mathbf{y}^T, \mathbf{c}^T]^T$ and the $MN$x$MN$ matrix $\check{\mathbf{R}}$ is

$$\check{\mathbf{R}} = \begin{bmatrix} \mathbf{R}_1 & 0 & \cdots & 0 \\ 0 & \mathbf{R}_2 & \cdots & 0 \\ \vdots & \vdots & \vdots & \vdots \\ 0 & 0 & \cdots & \mathbf{R}_N \end{bmatrix} \tag{6.2}$$

where the exact covariance matrix of the $n$th source is $\mathbf{R}_n = \sigma_S^2\mathbf{C}\mathbf{a}(\theta_n)\mathbf{a}^H(\theta_n)\mathbf{C}^H + \sigma_N^2\mathbf{I}_M$ (for spatially white noise), assuming all trail echoes have SNR = $\sigma_S^2/\sigma_N^2$. Note it has been assumed that gain/phase errors have been calibrated out, and so the covariance matrix is free of gain/phase errors.

The likelihood function is really the probability density function of the data, viewed as a function of the unknown parameters. The "sharpness" of the likelihood function, at its peak, determines how accurately the unknown parameters can be estimated [109]. The negative of the second derivative of the logarithm of the likelihood function (at its peak), is the curvature of the log-likelihood function, and denotes the sharpness of the likelihood function. The average curvature of the log-likelihood function, is the limiting accuracy to which unknown parameters can be estimated, and defines the CRLB.

The unconditional CRLB can be shown to be

$$\mathbf{CRLB}(\mathbf{\Psi}) = \mathbf{J}^{-1}(\mathbf{\Psi}) \tag{6.3}$$

where the elements of the symmetric Fisher Information Matrix (FIM) are [213]

$$J_{kl} = J_{lk} = T\,trace\left\{\check{\mathbf{R}}^{-1}\frac{\partial\check{\mathbf{R}}}{\partial\Psi_k}\check{\mathbf{R}}^{-1}\frac{\partial\check{\mathbf{R}}}{\partial\Psi_l}\right\} \tag{6.4}$$

but since $\check{\mathbf{R}}$, $\check{\mathbf{R}}^{-1}$, $\partial\check{\mathbf{R}}/\partial\Psi_k$ are all block structured matrices

$$J_{kl} = T\sum_{n=1}^{N} trace\left\{\mathbf{R}_n^{-1}\frac{\partial\mathbf{R}_n}{\partial\Psi_k}\mathbf{R}_n^{-1}\frac{\partial\mathbf{R}_n}{\partial\Psi_l}\right\} \tag{6.5}$$

### 6.1.1 DOA - DOA Terms

Since we have disjoint sources, $\partial \mathbf{R}_n / \partial \theta_l$ is a zero matrix for $n \neq l$, and hence $J_{\theta_k,\theta_l}$ is zero for $k \neq l$. Now

$$\begin{aligned}
J_{\theta_k,\theta_k} &= T trace\left\{\mathbf{R}_k^{-1}\frac{\partial \mathbf{R}_k}{\partial \theta_k}\mathbf{R}_k^{-1}\frac{\partial \mathbf{R}_k}{\partial \theta_k}\right\} && (6.6)\\
&= T\sigma_S^4\, trace\{\mathbf{R}_k^{-1}\mathbf{C}\dot{\mathbf{a}}_{\theta_k}(\theta_k)\mathbf{a}^H(\theta_k)\mathbf{C}^H\mathbf{R}_k^{-1}\mathbf{C}\dot{\mathbf{a}}_{\theta_k}(\theta_k)\mathbf{a}^H(\theta_k)\mathbf{C}^H\\
&\qquad +\mathbf{R}_k^{-1}\mathbf{C}\dot{\mathbf{a}}_{\theta_k}(\theta_k)\mathbf{a}^H(\theta_k)\mathbf{C}^H\mathbf{R}_k^{-1}\mathbf{C}\mathbf{a}(\theta_k)\dot{\mathbf{a}}_{\theta_k}^H(\theta_k)\mathbf{C}^H\\
&\qquad +\mathbf{R}_k^{-1}\mathbf{C}\mathbf{a}(\theta_k)\dot{\mathbf{a}}_{\theta_k}^H(\theta_k)\mathbf{C}^H\mathbf{R}_k^{-1}\mathbf{C}\dot{\mathbf{a}}_{\theta_k}(\theta_k)\mathbf{a}^H(\theta_k)\mathbf{C}^H\\
&\qquad +\mathbf{R}_k^{-1}\mathbf{C}\mathbf{a}(\theta_k)\dot{\mathbf{a}}_{\theta_k}^H(\theta_k)\mathbf{C}^H\mathbf{R}_k^{-1}\mathbf{C}\mathbf{a}(\theta_k)\dot{\mathbf{a}}_{\theta_k}^H(\theta_k)\mathbf{C}^H\} && (6.7)\\
&= 2T\sigma_S^4\,\Re\Big\{trace\{\mathbf{R}_k^{-1}\mathbf{C}\dot{\mathbf{a}}_{\theta_k}(\theta_k)\mathbf{a}^H(\theta_k)\mathbf{C}^H\mathbf{R}_k^{-1}\mathbf{C}\dot{\mathbf{a}}_{\theta_k}(\theta_k)\mathbf{a}^H(\theta_k)\mathbf{C}^H\\
&\qquad +\mathbf{R}_k^{-1}\mathbf{C}\dot{\mathbf{a}}_{\theta_k}(\theta_k)\mathbf{a}^H(\theta_k)\mathbf{C}^H\mathbf{R}_k^{-1}\mathbf{C}\mathbf{a}(\theta_k)\dot{\mathbf{a}}_{\theta_k}^H(\theta_k)\mathbf{C}^H\}\Big\} && (6.8)\\
J_{\theta_k,\theta_k} &= 2T\sigma_S^4\,\Re\Big\{trace\{\mathbf{R}_k^{-1}\mathbf{C}\dot{\mathbf{a}}_{\theta_k}(\theta_k)\mathbf{a}^H(\theta_k)\mathbf{C}^H\mathbf{R}_k^{-1}\\
&\qquad \mathbf{C}(\dot{\mathbf{a}}_{\theta_k}(\theta_k)\mathbf{a}^H(\theta_k)+\mathbf{a}(\theta_k)\dot{\mathbf{a}}_{\theta_k}^H(\theta_k))\mathbf{C}^H\}\Big\} && (6.9)
\end{aligned}$$

where $\dot{\mathbf{a}}_{\theta_k}(\theta_k) = \partial \mathbf{a}(\theta_k)/\partial \theta_k = \mathbf{D}(\theta_k)\mathbf{a}(\theta_k)$ (with $\mathbf{D}(\theta_k) = (+2\pi j/\lambda) diag\{\mathbf{x}\cos(\theta_k) - \mathbf{y}\sin(\theta_k)\}$), and the property $trace\{z^H\} = conj(trace\{z\})$ has been used in equation (6.8).

### 6.1.2 Sensor Position - Sensor Position Terms

The sensor position entries are

$$\begin{aligned}
J_{x_k,x_l} &= T\sum_{n=1}^{N} trace\left\{\mathbf{R}_n^{-1}\frac{\partial \mathbf{R}_n}{\partial x_k}\mathbf{R}_n^{-1}\frac{\partial \mathbf{R}_n}{\partial x_l}\right\} && (6.10)\\
&= T\sigma_S^4\sum_{n=1}^{N} trace\{\mathbf{R}_n^{-1}\mathbf{C}\dot{\mathbf{a}}_{x_k}(\theta_n)\mathbf{a}^H(\theta_n)\mathbf{C}^H\mathbf{R}_n^{-1}\mathbf{C}\dot{\mathbf{a}}_{x_l}(\theta_n)\mathbf{a}^H(\theta_n)\mathbf{C}^H\\
&\qquad +\mathbf{R}_n^{-1}\mathbf{C}\dot{\mathbf{a}}_{x_k}(\theta_n)\mathbf{a}^H(\theta_n)\mathbf{C}^H\mathbf{R}_n^{-1}\mathbf{C}\mathbf{a}(\theta_n)\dot{\mathbf{a}}_{x_l}^H(\theta_n)\mathbf{C}^H\\
&\qquad +\mathbf{R}_n^{-1}\mathbf{C}\mathbf{a}(\theta_n)\dot{\mathbf{a}}_{x_k}^H(\theta_n)\mathbf{C}^H\mathbf{R}_n^{-1}\mathbf{C}\dot{\mathbf{a}}_{x_l}(\theta_n)\mathbf{a}^H(\theta_n)\mathbf{C}^H\\
&\qquad +\mathbf{R}_n^{-1}\mathbf{C}\mathbf{a}(\theta_n)\dot{\mathbf{a}}_{x_k}^H(\theta_n)\mathbf{C}^H\mathbf{R}_n^{-1}\mathbf{C}\mathbf{a}(\theta_n)\dot{\mathbf{a}}_{x_l}^H(\theta_n)\mathbf{C}^H\} && (6.11)\\
J_{x_k,x_l} &= 2T\sigma_S^4\sum_{n=1}^{N}\Re\Big\{trace\{\mathbf{R}_n^{-1}\mathbf{C}\dot{\mathbf{a}}_{x_k}(\theta_n)\mathbf{a}^H(\theta_n)\mathbf{C}^H\\
&\qquad \mathbf{R}_n^{-1}\mathbf{C}(\dot{\mathbf{a}}_{x_l}(\theta_n)\mathbf{a}^H(\theta_n)+\mathbf{a}(\theta_n)\dot{\mathbf{a}}_{x_l}^H(\theta_n))\mathbf{C}^H\}\Big\} && (6.12)
\end{aligned}$$

where $\dot{\mathbf{a}}_{x_k}(\theta_n) = \partial \mathbf{a}(\theta_n)/\partial x_k = \mathbf{dx_k} \odot \mathbf{a}(\theta_n)$ (see section 4.7). The $y$ coordinate and $x$-$y$ coordinate terms are similarly derived, and are

$$\begin{aligned} J_{y_k,y_l} &= 2T\sigma_S^4 \sum_{n=1}^{N} \Re\Big\{trace\{\mathbf{R}_n^{-1}\mathbf{C}\dot{\mathbf{a}}_{y_k}(\theta_n)\mathbf{a}^H(\theta_n)\mathbf{C}^H \\ &\qquad \mathbf{R}_n^{-1}\mathbf{C}(\dot{\mathbf{a}}_{y_l}(\theta_n)\mathbf{a}^H(\theta_n) + \mathbf{a}(\theta_n)\dot{\mathbf{a}}_{y_l}^H(\theta_n))\mathbf{C}^H\}\Big\} \qquad (6.13) \\ J_{x_k,y_l} &= 2T\sigma_S^4 \sum_{n=1}^{N} \Re\Big\{trace\{\mathbf{R}_n^{-1}\mathbf{C}\dot{\mathbf{a}}_{x_k}(\theta_n)\mathbf{a}^H(\theta_n)\mathbf{C}^H \\ &\qquad \mathbf{R}_n^{-1}\mathbf{C}(\dot{\mathbf{a}}_{y_l}(\theta_n)\mathbf{a}^H(\theta_n) + \mathbf{a}(\theta_n)\dot{\mathbf{a}}_{y_l}^H(\theta_n))\mathbf{C}^H\}\Big\} \qquad (6.14) \end{aligned}$$

where $\dot{\mathbf{a}}_{y_k}(\theta_n) = \partial \mathbf{a}(\theta_n)/\partial y_k = \mathbf{dy_k} \odot \mathbf{a}(\theta_n)$ (see section 4.7).

### 6.1.3 Coupling - Coupling Terms

The coupling parameter entries are

$$J_{c_k,c_l} = T\sum_{n=1}^{N} trace\left\{\mathbf{R}_n^{-1}\frac{\partial \mathbf{R}_n}{\partial c_k}\mathbf{R}_n^{-1}\frac{\partial \mathbf{R}_n}{\partial c_l}\right\} \qquad (6.15)$$

$$\begin{aligned} &= T\sigma_S^4 \sum_{n=1}^{N} trace\{\mathbf{R}_n^{-1}\dot{\mathbf{C}}_{c_k}\mathbf{a}(\theta_n)\mathbf{a}^H(\theta_n)\mathbf{C}^H\mathbf{R}_n^{-1}\dot{\mathbf{C}}_{c_l}\mathbf{a}(\theta_n)\mathbf{a}^H(\theta_n)\mathbf{C}^H \\ &\qquad +\mathbf{R}_n^{-1}\dot{\mathbf{C}}_{c_k}\mathbf{a}(\theta_n)\mathbf{a}^H(\theta_n)\mathbf{C}^H\mathbf{R}_n^{-1}\mathbf{C}\mathbf{a}(\theta_n)\mathbf{a}^H(\theta_n)\dot{\mathbf{C}}_{c_l}^H \\ &\qquad +\mathbf{R}_n^{-1}\mathbf{C}\mathbf{a}(\theta_n)\mathbf{a}^H(\theta_n)\dot{\mathbf{C}}_{c_k}^H\mathbf{R}_n^{-1}\dot{\mathbf{C}}_{c_l}\mathbf{a}(\theta_n)\mathbf{a}^H(\theta_n)\mathbf{C}^H \\ &\qquad +\mathbf{R}_n^{-1}\mathbf{C}\mathbf{a}(\theta_n)\mathbf{a}^H(\theta_n)\dot{\mathbf{C}}_{c_k}^H\mathbf{R}_n^{-1}\mathbf{C}\mathbf{a}(\theta_n)\mathbf{a}^H(\theta_n)\dot{\mathbf{C}}_{c_l}^H\} \qquad (6.16) \end{aligned}$$

$$\begin{aligned} J_{c_k,c_l} &= 2T\sigma_S^4 \sum_{n=1}^{N} \Re\Big\{trace\{\mathbf{R}_n^{-1}\dot{\mathbf{C}}_{c_k}\mathbf{a}(\theta_n)\mathbf{a}^H(\theta_n)\mathbf{C}^H\mathbf{R}_n^{-1} \\ &\qquad (\dot{\mathbf{C}}_{c_l}\mathbf{a}(\theta_n)\mathbf{a}^H(\theta_n)\mathbf{C}^H + \mathbf{C}\mathbf{a}(\theta_n)\mathbf{a}^H(\theta_n)\dot{\mathbf{C}}_{c_l}^H)\}\Big\} \qquad (6.17) \end{aligned}$$

where matrix $\dot{\mathbf{C}}_{c_k} = \partial \mathbf{C}/\partial c_k$, $c_k$ being the amplitude/phase of an element in the symmetric coupling matrix. Note $\dot{\mathbf{C}}_{c_k}$ has only one non-zero element if $c_k$ is a diagonal element, and has only two non-zero elements (of equal value) if $c_k$ is an off-diagonal element.

### 6.1.4 Cross Terms

The cross terms can be similarly derived as

$$\begin{aligned} J_{\theta_k,x_l} &= T\sigma_S^4 trace\{\mathbf{R}_k^{-1}\mathbf{C}(\dot{\mathbf{a}}_{\theta_k}(\theta_k)\mathbf{a}^H(\theta_k) + \mathbf{a}(\theta_k)\dot{\mathbf{a}}_{\theta_k}^H(\theta_k))\mathbf{C}^H \\ &\qquad \mathbf{R}_k^{-1}\mathbf{C}(\dot{\mathbf{a}}_{x_l}(\theta_k)\mathbf{a}^H(\theta_k) + \mathbf{a}(\theta_k)\dot{\mathbf{a}}_{x_l}^H(\theta_k))\mathbf{C}^H\} \qquad (6.18) \end{aligned}$$

$$\begin{aligned} J_{\theta_k,c_l} &= T\sigma_S^4 \, trace\{\mathbf{R}_k^{-1}\mathbf{C}(\dot{\mathbf{a}}_{\theta_k}(\theta_k)\mathbf{a}^H(\theta_k) + \mathbf{a}(\theta_k)\dot{\mathbf{a}}_{\theta_k}^H(\theta_k))\mathbf{C}^H \\ &\qquad \mathbf{R}_k^{-1}(\dot{\mathbf{C}}_{c_l}\mathbf{a}(\theta_k)\mathbf{a}^H(\theta_k)\mathbf{C}^H + \mathbf{C}\mathbf{a}(\theta_k)\mathbf{a}^H(\theta_k)\dot{\mathbf{C}}_{c_l}^H)\} \qquad (6.19) \\ J_{c_k,x_l} &= T\sigma_S^4 \sum_{n=1}^{N} trace\{\mathbf{R}_n^{-1}(\dot{\mathbf{C}}_{c_k}\mathbf{a}(\theta_n)\mathbf{a}^H(\theta_n)\mathbf{C}^H + \mathbf{C}\mathbf{a}(\theta_n)\mathbf{a}^H(\theta_n)\dot{\mathbf{C}}_{c_k}^H) \\ &\qquad \mathbf{R}_n^{-1}\mathbf{C}(\dot{\mathbf{a}}_{x_l}(\theta_n)\mathbf{a}^H(\theta_n) + \mathbf{a}(\theta_n)\dot{\mathbf{a}}_{x_l}^H(\theta_n))\mathbf{C}^H\} \qquad (6.20) \end{aligned}$$

### 6.1.5 *CRLB Analysis*

The array calibration problem can only be solved when the CRLB exists, hence the existence of the CRLB addresses the question of identifiability i.e. whether the sensor positions and mutual coupling can be estimated, and hence if array calibration can in fact be performed. Further, since the CRLB gives the minimum variance that an unbiased estimator can obtain, it gives the accuracy attainable under given scenarios. Analytically analysing the CRLB for this problem, to study the attainable accuracy and the identifiability conditions, is however extremely complex and hence non-analytic results can only be obtained in general; the exceptions being for simplified cases, as for example in section 6.1.7.

In this section the attainable performance is investigated (non-analytically) for a 4-element array, where both sensor position errors and mutual coupling are present. Consider a nominally uniform linear 4-element array with inter-element spacing of $d = 0.4\lambda$; the randomly generated sensor position errors in the $x$-coordinate and $y$-coordinate being given in Table 4.1. The coupling matrix employed was experimentally measured from the Jindalee OTH radar's transmitting array [136]. Unless specified otherwise, 10 sources equally spaced from $-90^o$ to $+90^o$ in azimuth, each with SNR of 30 dB and 500 snapshots are considered.

Since the location of one sensor and the direction to another sensor are assumed to be known, there are only 5 sensor position parameters, $(2M - 3)$, which are unknown. For the coupling parameters, since a symmetric coupling matrix is assumed and the constraint that $c_{11} = 1$ is placed, 18 coupling values $(M(M+1) - 2)$ are unknown. Finally since all DOAs are unknown, for 10 sources 10 DOAs $(N)$ are unknown. The total number of unknown parameters is then 33 (the signal and noise powers are assumed to be known).

Figure 6.1 shows the CRLB as a function of the number of snapshots, for the estimation of the third sensor's $y$-coordinate $(-)$ and $x$-coordinate $(--)$, and the coupling value $c_{12}$'s amplitude $(-.-)$ and phase (...). The standard deviation (STD) values for the sensor position are in units of wavelengths, while the coupling value phase is in units of radians. While the number of snapshots for meteor trail echoes is typically less than about 15-20 (see chapter

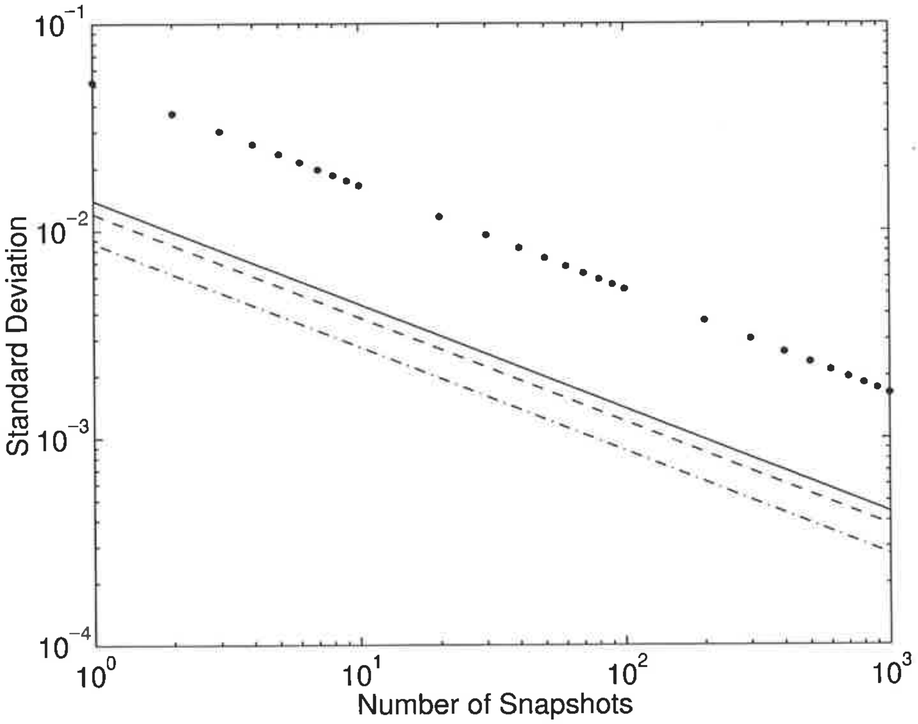

Figure 6.1: CRLB variation with number of snapshots : third sensor's $y$-coordinate ($-$) and $x$-coordinate ($--$), and $c_{12}$'s amplitude ($-.-$) and phase (...). The standard deviation values for the sensor position are in units of wavelengths, while the coupling value phase is in units of radians.

7), the behaviour for higher values gives useful insight. The STD values indicate that good array calibration accuracy can be achieved for 10 echoes with their typical 20-30 dB SNRs and typical number of snapshots (5-15) : for 10 snapshots this figure indicates, the sensor position can be estimated up to about $0.005\lambda$, coupling amplitude up to about 0.003, and the coupling phase up to about 0.015 radians.

The STD variation observed in figure 6.1 is in accordance with the $1/\sqrt{T}$ fall off expected, and indicates that if more snapshots from meteor trail echoes can be obtained, the performance can be improved. Note it has been assumed that each snapshot of a given meteor trail echo is independent, even though meteor trails are passive sources (as they reflect energy rather than transmit energy), since the scattering is a rapidly time-varying process [132].

The STD variation with SNR is shown in figure 6.2 for a range of meteor echo SNRs and for 500 snapshots : STD values for 10 snapshots are simply 50 times larger. The monotonically decreasing STD values with SNR indicates the problem is well defined, and these results indicate the STD is proportional to $1/\sqrt{SNR}$. As expected, the calibration accuracy achievable for the third sensor's $x$-coordinate and $y$-coordinate position, are similar.

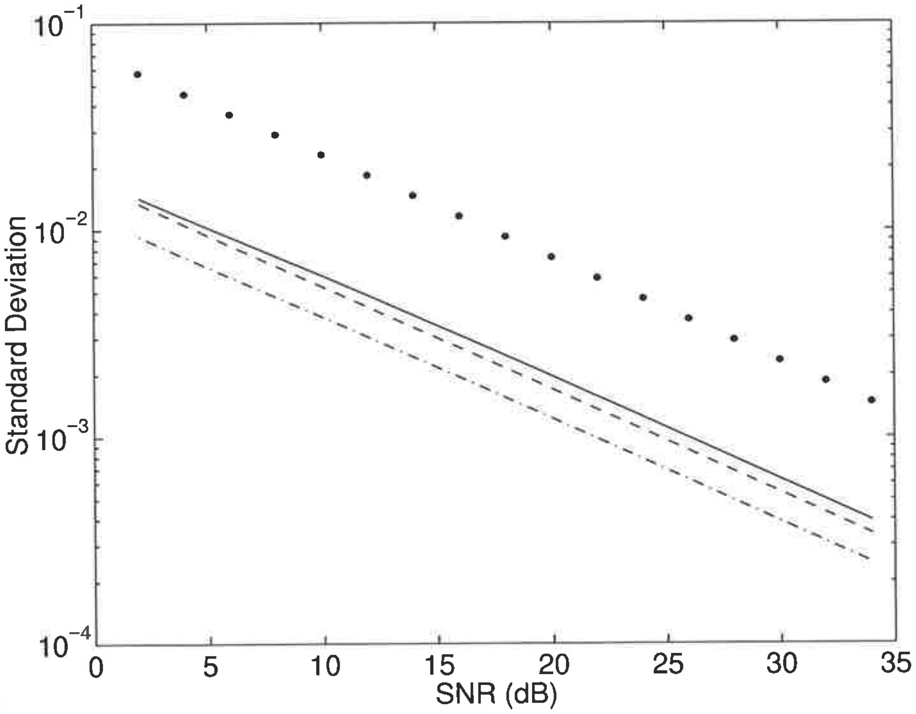

Figure 6.2: CRLB variation with SNR : third sensor's $y$-coordinate $(-)$ and $x$-coordinate $(--)$, and $c_{12}$'s amplitude $(-.-)$ and phase (...). The standard deviation values for the sensor position are in units of wavelengths, while the coupling value phase is in units of radians

Figure 6.3 shows the STD variation with number of sources. The performance attainable increases rapidly initially, and then improves more gradually. The FIM was non-invertible, and hence the problem non-identifiable, for less than four sources; indicating that for the given scenario, the information provided by less than four sources is insufficient to estimate the unknown parameters. It can be concluded from this figure that the more sources used for array calibration, the greater the achievable accuracy. However, since the curves start to flatten off for high number of sources, the improvement obtained by adding further sources becomes minimal. Note for this 4-element array, the beamwidth of the conventional beamformer is $\approx 30^{\circ}$ ($\approx (0.88\lambda)/(Md)$ radians), so there are only six independent beams : thus one would expect that the STD versus number of sources would fall off rapidly until there are six sources, assuming the sources are equally spread, and the performance improvement obtained by using more than six sources to be small. Note similar results were obtained in figure 4.9, where the algorithm's performance was investigated as a function of the number of sources (but for a 16-element array).

It has been mentioned in [138] that better array calibration accuracy can be obtained by using

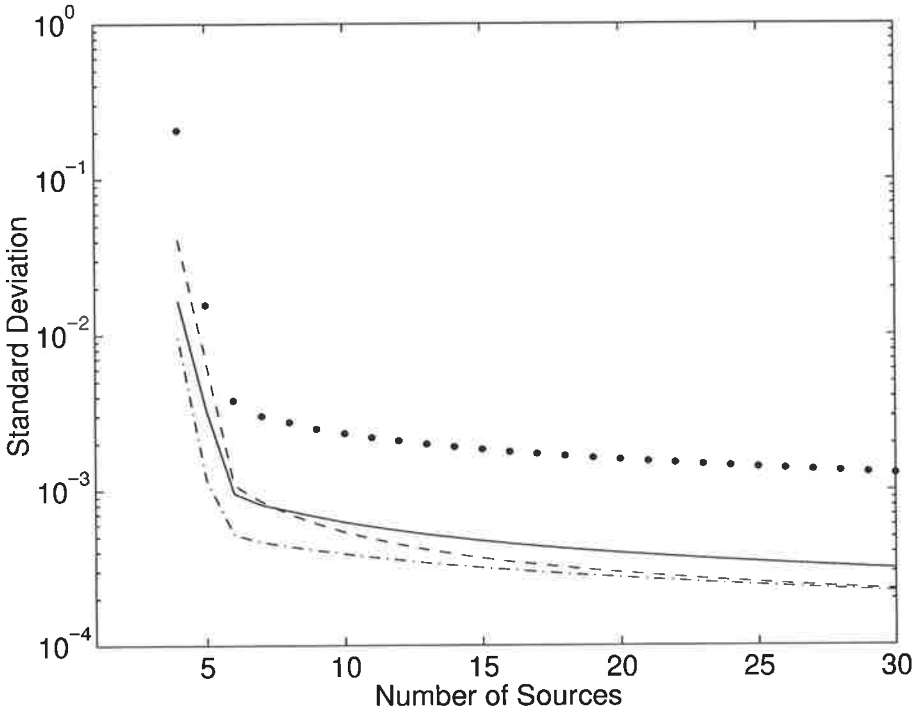

Figure 6.3: CRLB variation with number of sources : third sensor's $y$-coordinate $(-)$ and $x$-coordinate $(--)$, and $c_{12}$'s amplitude $(-.-)$ and phase $(...)$. The standard deviation values for the sensor position are in units of wavelengths, while the coupling value phase is in units of radians.

"active array calibration" (special sources with known DOAs) as compared with "passive array calibration" (sources of opportunity with unknown DOAs). Figure 6.4(a) shows the CRLB of the third sensor's $y$-coordinate, for the standard case $(-)$ together with some important special cases. The dashed curve $(--)$ shows the performance achievable if the source DOAs are known a priori. The improvement for sensor position estimation is a factor of about 2.5-3, while for the coupling amplitude (not shown) and coupling phase (see figure 6.4(b)) the improvement is a factor of about 10. Hence Active Array Calibration does perform better, but clearly the difference can be offset by the use of sources with higher SNRs and number of snapshots (and to some extent by using a larger number of sources).

Also shown in figure 6.4 is the CRLB for the case where other combinations of parameters are known a priori. For sensor position estimation, knowing the coupling values a priori $(...)$ gives slightly better results than knowing the DOAs $(--)$, while as expected knowing both the coupling and DOAs a priori $(-.-)$ gives even better performance. For the estimation of $c_{12}$'s amplitude (not shown), the difference in performance between the three cases is small, with the best accuracy obtained with both known DOAs and sensor positions (as expected). In

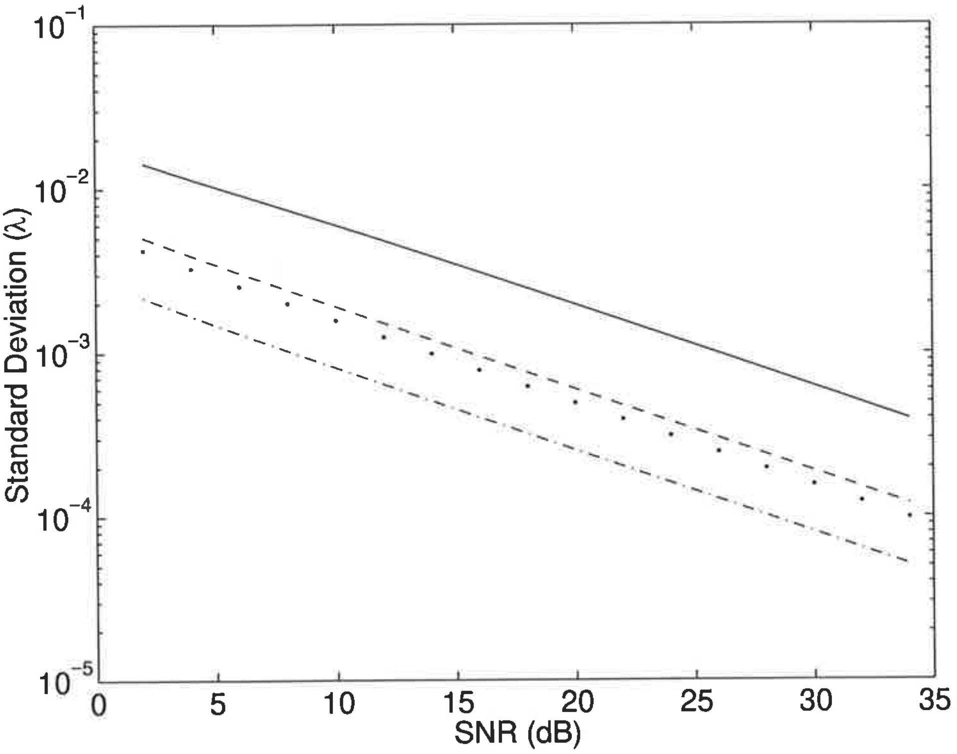

(a) third sensor's $y$-coordinate

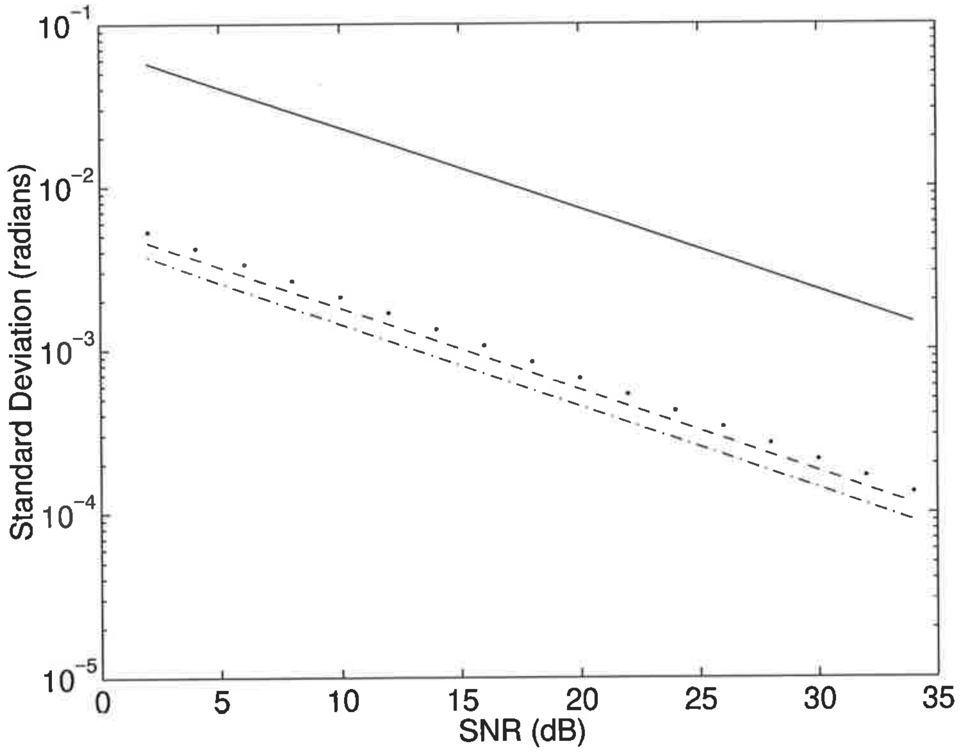

(b) phase of $c_{12}$

Figure 6.4: CRLB variation with SNR for several cases.

the case of $c_{12}$'s phase (see figure 6.4(b)), knowing the sensor positions (...) a priori is slightly worse than knowing the DOAs a priori ($--$), and again knowing both a priori ($-.-$) achieves the best results.

Meteor trails are formed when meteoroids enter the earth's atmosphere and are at altitudes of about 100 Km (see chapter 7). Hence, meteor trail echoes reach OTH radar arrays from heights of about 100 Km. Thus far it has been assumed that the sources are at zero elevation, but now one investigates how array calibration performance is affected by the elevation angle of meteor echoes. The $m$th element of the steering vector, for non-zero elevation angles, is

$$[\mathbf{a}(\theta, \phi)]_m = e^{jw(x_m \sin\theta\cos\phi + y_m \cos\theta\cos\phi)/v} \tag{6.21}$$

where here $\phi$ is the elevation angle of the source. The CRLB, obtained using this steering vector, will indicate how the elevation angle of the sources effects the attainable accuracy. Figure 6.5 shows the achievable accuracy as a function of the range (and hence elevation angle) of the meteor echoes; the closer the sources are to the radar the higher the elevation angle. These results clearly show that calibration accuracy is seriously affected for echoes from ranges less than about 100 Km, with the accuracy being independent of range for echoes from ranges greater than about 200 Km. Note as the range decreases, and hence the elevation angle increases, the effective azimuths of all the sources approach broadside (for a nominally linear array) due to the array coning effect; hence the results are expected to worsen. For simplicity, the drop off in antenna gain with elevation and the decrease in meteor echo intensity with range, have been ignored here.

It has been observed that as the azimuth spread over which the sources exist increases, the performance attainable increases. This is expected, since as the azimuth spread of the sources increases (and there are sufficiently large number of sources), the information obtained should increase, and hence the performance attainable increases. It should be mentioned that even though a linear array is considered, once sensor position errors are introduced the array is no longer linear, and hence improvement in performance is expected when the source spread is above 180° too (as has been observed).

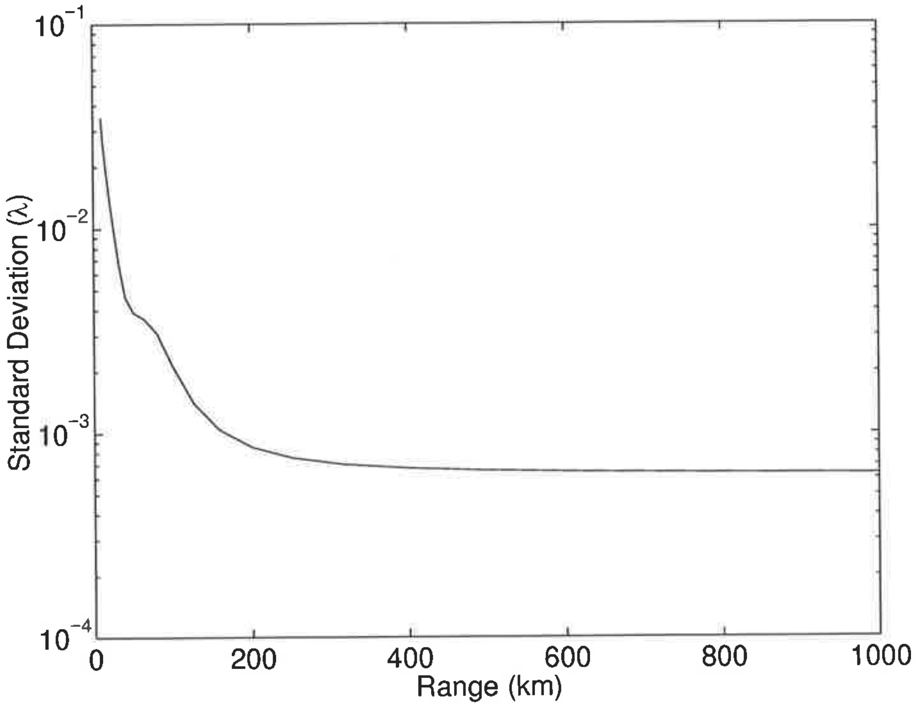

Figure 6.5: CRLB variation with range, for the third sensor's $y$-coordinate, when the elevation angle of meteor trail echoes is considered.

### 6.1.6 Algorithm Comparison with CRLB

To quantify the performance of the algorithm developed in chapter 4, the algorithm was compared with the CRLB. The comparison was performed for a 4-element array, with inter-element spacing $d = 0.4\lambda$ and position errors as given in Table 4.1. As in the previous section, since (a) the location of one sensor and the direction to another sensor are assumed to be known, (b) a symmetric coupling matrix is assumed with the constraint $c_{11} = 1$ placed, and (c) all 10 source DOAs are unknown, the total number of unknown parameters is 33.

The CRLB, for 10 sources with 500 snapshots each, is shown in figure 6.6 (solid line); the CRLB for the $x$ and $y$ coordinates of the third sensor, and the amplitude and phase of the coupling parameter $c_{12}$, being illustrated. The standard deviation (STD) values (circles) estimated from 10 algorithm runs, and the 99 percent confidence intervals (vertical bars) have been over-plotted. These results clearly indicate the algorithm is statistically efficient. Note similar results were obtained for the other unknown parameters, and the bias was small compared to the STD in all cases.

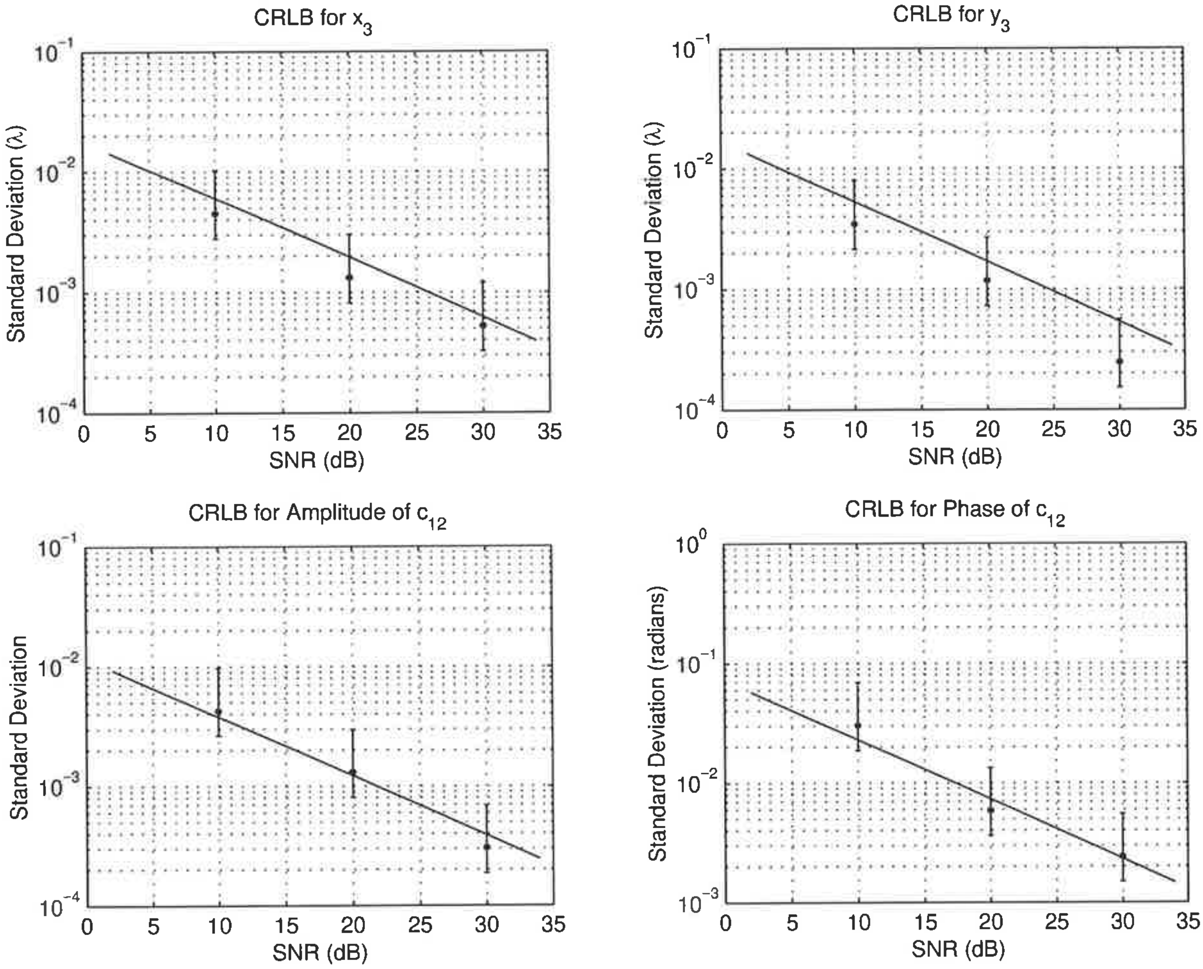

Figure 6.6: Comparison of algorithm performance with theoretical performance bound - CRLB (solid line), STD (circle) and 99 percent confidence intervals (vertical bar) as a function of SNR, for the position of a sensor and for the amplitude and phase of a coupling parameter. The STD values were obtained from 10 algorithm runs.

### 6.1.7 *Mutual Coupling Estimation using a Single Source*

For sensor position only estimation, it is well known that a single source is only capable of estimating position displacements in the direction of the source. Hence for a nominally linear array, a source in the broadside direction can only estimate position displacements orthogonal to the array; similarly a source in the end-fire directions can only estimate position displacements along the array. With mutual coupling estimation, no work has however been done to determine if a source from a particular direction is incapable of estimating the coupling parameters. Hence a theoretical analysis of the CRLB is performed, for mutual coupling only estimation using a single-mode source, to answer this question.

To obtain theoretical expressions for the CRLB, a 2-element array is considered, with the coupling matrix assumed to be Toeplitz. The unknown parameters are the source DOA ($\theta$), the coupling amplitude ($c$), and the coupling phase ($\psi$). In Appendix B the CRLB variances and the non-identifiability conditions are derived for both the passive and active array calibration cases. As a result of the complexity of this problem, specific coupling values were chosen; $c = 0.5$ and $\psi = \pi/2$ (see later regarding other coupling values).

As shown in Appendix B, the passive array calibration (unknown source DOA) problem is non-identifiable when the source is either at broadside direction, end-fire directions, or ±38.682° from broadside; the reason for these non-identifiable conditions being array ambiguities (see Appendix B). High SNR approximations for the CRLB variances were derived in Appendix B and are

$$(\sigma_\theta^2)_p \approx \frac{-0.15831}{T\cos^2(\theta)}\left[\frac{\cos(1.6\pi\sin(\theta))-1}{\cos(1.6\pi\sin(\theta))+1}\right] \quad (6.22)$$

$$(\sigma_c^2)_p \approx \frac{-0.625}{T\sigma^2\left[\cos(1.6\pi\sin(\theta))-1\right]} \quad (6.23)$$

$$(\sigma_\psi^2)_p \approx \frac{3.125}{T\left[\cos(1.6\pi\sin(\theta))+1\right]} \quad (6.24)$$

Note $\cos(1.6\pi\sin(\theta))+1=0$ when $\theta=\pm38.682^\circ$, $\cos(1.6\pi\sin(\theta))-1=0$ when $\theta=0$, and $\cos^2(\theta)=0$ when $\theta=\pm90^\circ$. Near $\theta=\pm38.682^\circ$ peaks occur in $(\sigma_\theta^2)_p$ and $(\sigma_\psi^2)_p$, near $\theta=0$ a peak occurs in $(\sigma_c^2)_p$ and a minimum occurs in $(\sigma_\theta^2)_p$, and near $\theta=\pm90^\circ$ peaks occur in $(\sigma_\theta^2)_p$. These equations give easy interpretation on how the source DOA, SNR ($\sigma^2$) and the number of snapshots $T$, effect the attainable accuracy; these expressions agreeing well with the exact expressions for high SNR. Note the CRLB variances are inversely proportional to the number of snapshots, and the CRLB variance of the coupling amplitude is also inversely proportional to the SNR; the CRLB variances for the DOA and coupling phase, being independent of SNR (for these high SNR approximation).

The active array calibration (known source DOA) problem, is shown in Appendix B, to only be non-identifiable when the source is at broadside direction. For this problem, high SNR approximations for the CRLB variances are (see Appendix B)

$$(\sigma_c^2)_a \approx \frac{-0.625}{T\sigma^2\left[\cos(1.6\pi\sin(\theta))-1\right]} \quad (6.25)$$

$$(\sigma_\psi^2)_a \approx \frac{-2.5}{T\sigma^2\left[\cos(1.6\pi\sin(\theta))-1\right]} \quad (6.26)$$

Since $\cos(1.6\pi\sin(\theta))-1=0$ when $\theta=0$, a peak occurs in both $(\sigma_c^2)_a$ and $(\sigma_\psi^2)_a$ near $\theta=0$. These equations illustrate how the source DOA, SNR and the number of snapshots, effect the estimation accuracy for active array calibration; for high SNR these expressions agree well with the exact expressions. Note these CRLB variances are inversely proportional to the number of snapshots and the SNR.

Figure 6.7 shows how the CRLB standard deviations (STD) of the unknown parameters vary with the source DOA. Plotted here are the exact expressions for passive array calibration (−) : $\sigma_\theta$ from equation (B.64), $\sigma_c$ from equation (B.68), and $\sigma_\psi$ from equation (B.72). The number of snapshots is 500 and the SNR of the source is 30 dB. The attainable DOA estimation accuracy worsens as the source DOA approaches the end-fire directions and ±38.682°. The DOA estimation accuracy improves as the source DOA approaches broadside. The coupling amplitude accuracy is reasonably constant with source DOA, but worsens as the source DOA approaches broadside. The coupling phase accuracy worsens as the source DOA approaches ±38.682°, but is otherwise fairly constant. As mentioned earlier, at broadside direction, at end-fire directions, and at ±38.682°, the problem is non-identifiable.

The CRLB STD for active array calibration have also been shown in figure 6.7 using dashed lines (−−). Plotted here are the exact expressions : $\sigma_c$ from equation (B.107) and $\sigma_\psi$ from equation (B.110). The number of snapshots is 500 and the SNR of the source is 30 dB, as for the passive array calibration case. The coupling amplitude accuracy coincides exactly with that for passive array calibration. The coupling phase accuracy is significantly better than passive array calibration, with the accuracy worsening as the source approaches broadside; broadside direction being the only direction for which the active array calibration problem is non-identifiable.

The SNR dependence is now considered when, for example, the source DOA is −45°. For this case, the high SNR approximations for the CRLBs in equation (6.22)-(6.26), become

$$(\sigma_\theta)_p = \frac{2.69}{\sqrt{T}} \tag{6.27}$$

$$(\sigma_c)_p = \frac{0.571}{\sqrt{T(SNR)}} \tag{6.28}$$

$$(\sigma_c)_a = \frac{0.571}{\sqrt{T(SNR)}} \tag{6.29}$$

$$(\sigma_\psi)_p = \frac{6.10}{\sqrt{T}} \tag{6.30}$$

$$(\sigma_\psi)_a = \frac{1.14}{\sqrt{T(SNR)}} \tag{6.31}$$

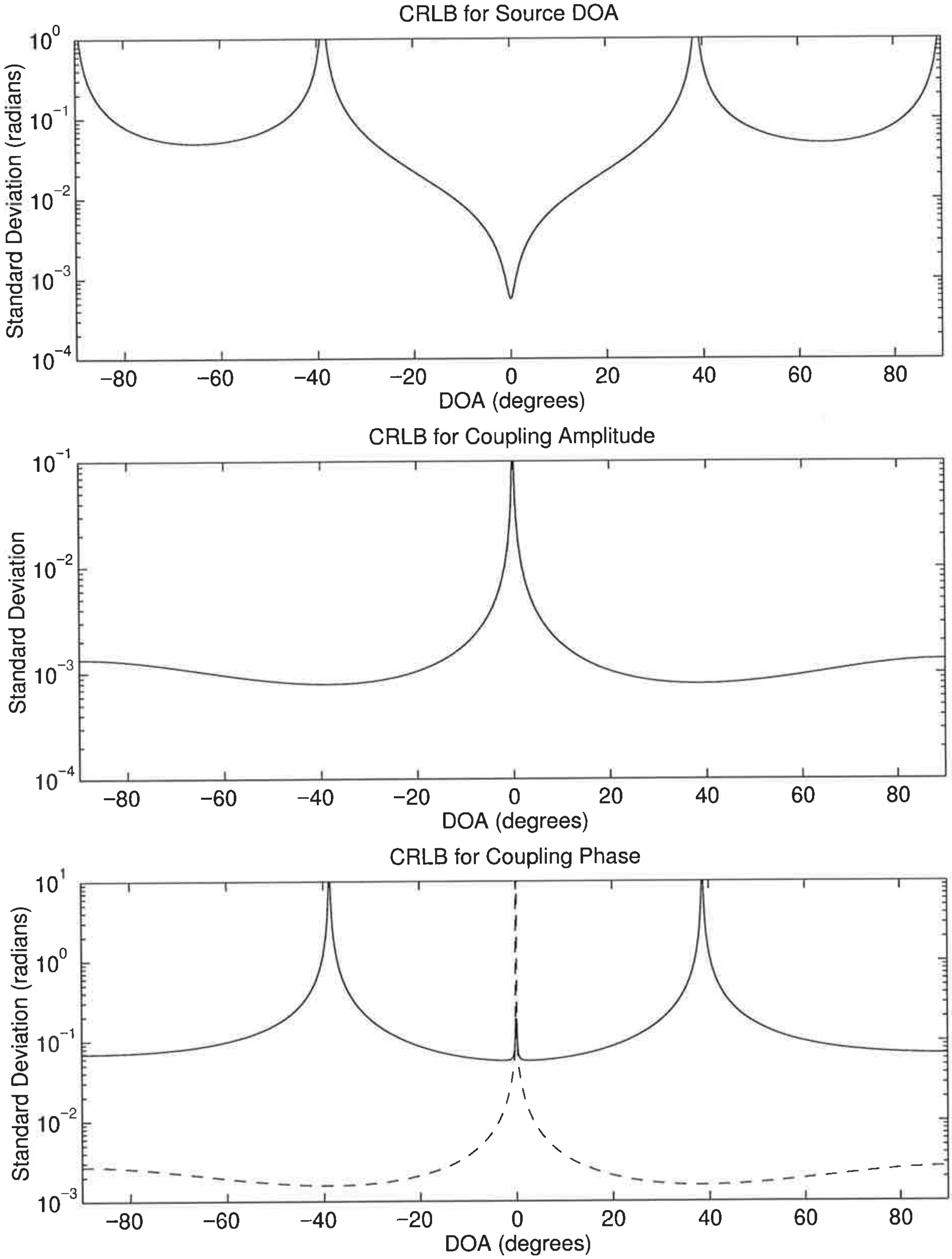

Figure 6.7: Variation of CRLB standard deviations with source DOA, for $c = 0.5$ and $\psi = \pi/2$.

If the number of snapshots is 500, then the CRLB STDs become

$$\begin{aligned}
(\sigma_\theta)_p &= 0.120 && (6.32)\\
(\sigma_c)_p &= \frac{0.0255}{\sqrt{SNR}} && (6.33)\\
(\sigma_c)_a &= \frac{0.0255}{\sqrt{SNR}} && (6.34)\\
(\sigma_\psi)_p &= 0.273 && (6.35)\\
(\sigma_\psi)_a &= \frac{0.0511}{\sqrt{SNR}} && (6.36)
\end{aligned}$$

While $(\sigma_c)_p$, $(\sigma_c)_a$ and $(\sigma_\psi)_a$ decrease with increasing SNR, $(\sigma_\theta)_p$ and $(\sigma_\psi)_p$ are independent of SNR (the exact expression for these two CRLB STDs indicate that they do decrease with SNR, but do so slowly). Equations (6.32)-(6.36) agree well with the exact expressions for high SNR.

Figure 6.8 shows the variation of the CRLB STDs (exact expressions) with the SNR of the source. The number of snapshots is 500 and the source DOA is $-45^\circ$. The results for passive array calibration ($-$) indicate that for SNRs greater than about 10 dB, the attainable accuracy for the source DOA and the coupling phase do not improve much as the source SNR increases (as indicated earlier); the accuracy for the coupling amplitude improves significantly however. Similar results were obtained for other source DOAs.

The CRLB STDs versus source SNR is shown in figure 6.8 for active array calibration using dashed lines ($--$). The number of snapshots is 500 and the source DOA is $-45^\circ$, as for the passive array calibration case. For source SNRs greater than about 5 dB, the coupling amplitude accuracy is the same as that for passive array calibration; the accuracy being marginally better than passive array calibration for SNRs less than 5 dB. The coupling phase is significantly better than that for passive array calibration (as before), with the accuracy increasing significantly with SNR (unlike passive array calibration).

Passive array calibration using a single calibration source, was shown to produce poor results when the source DOA was near $0^\circ$, $\pm 38.682^\circ$ and $\pm 90^\circ$. In general multiple sources will be used for array calibration, and hence it is of interest to see if such problems exist in the case of multiple calibration sources. The CRLB was hence analysed for the case of two disjoint single-mode sources, using the non-analytic approach used in the previous sections (but for a Toeplitz coupling matrix model). The CRLB STDs for the unknown parameters are shown in figure 6.9, where the number of snapshots is 500 and the SNRs of the sources are 30 dB.

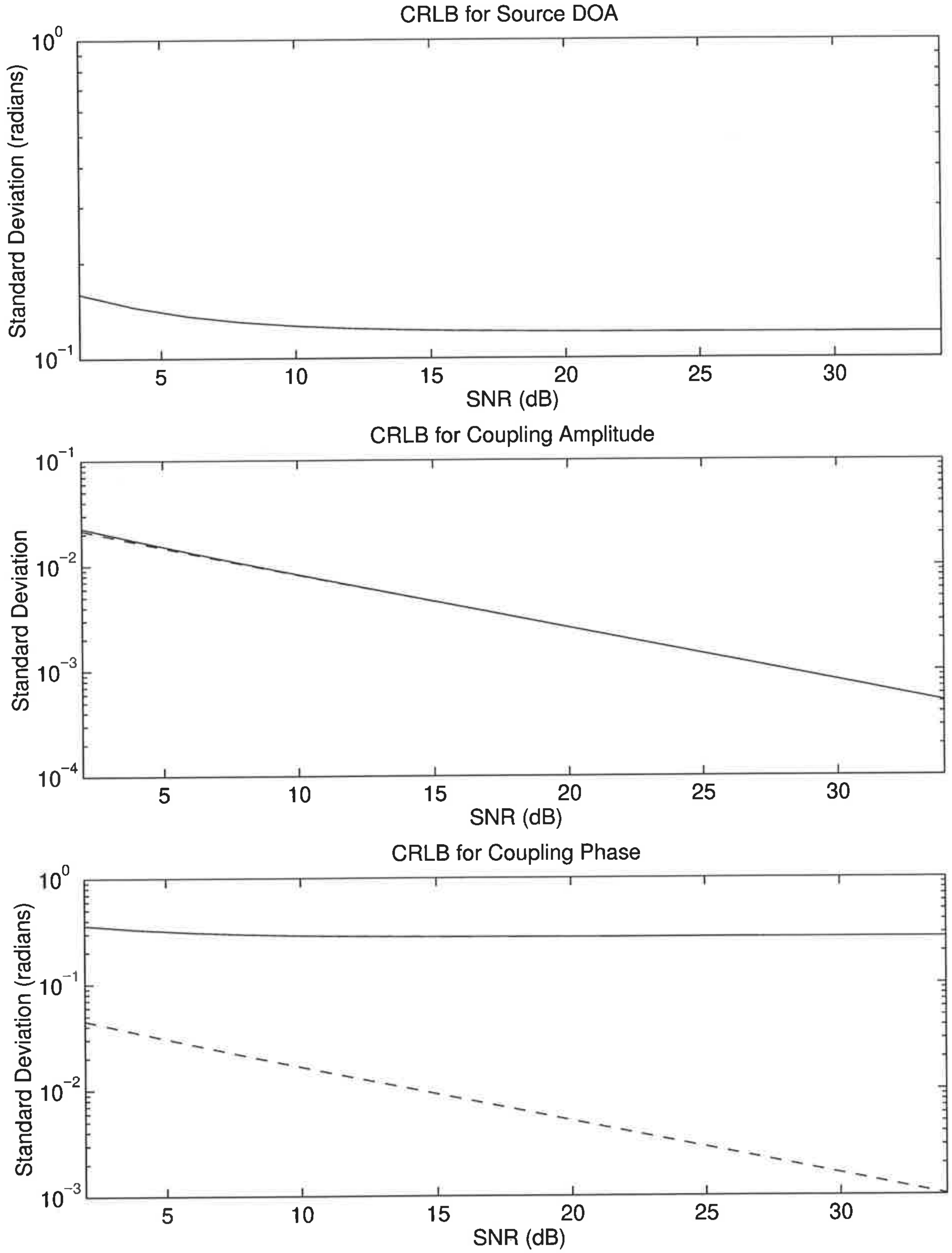

Figure 6.8: Variation of CRLB standard deviations with source SNR, for $c = 0.5$ and $\psi = \pi/2$.

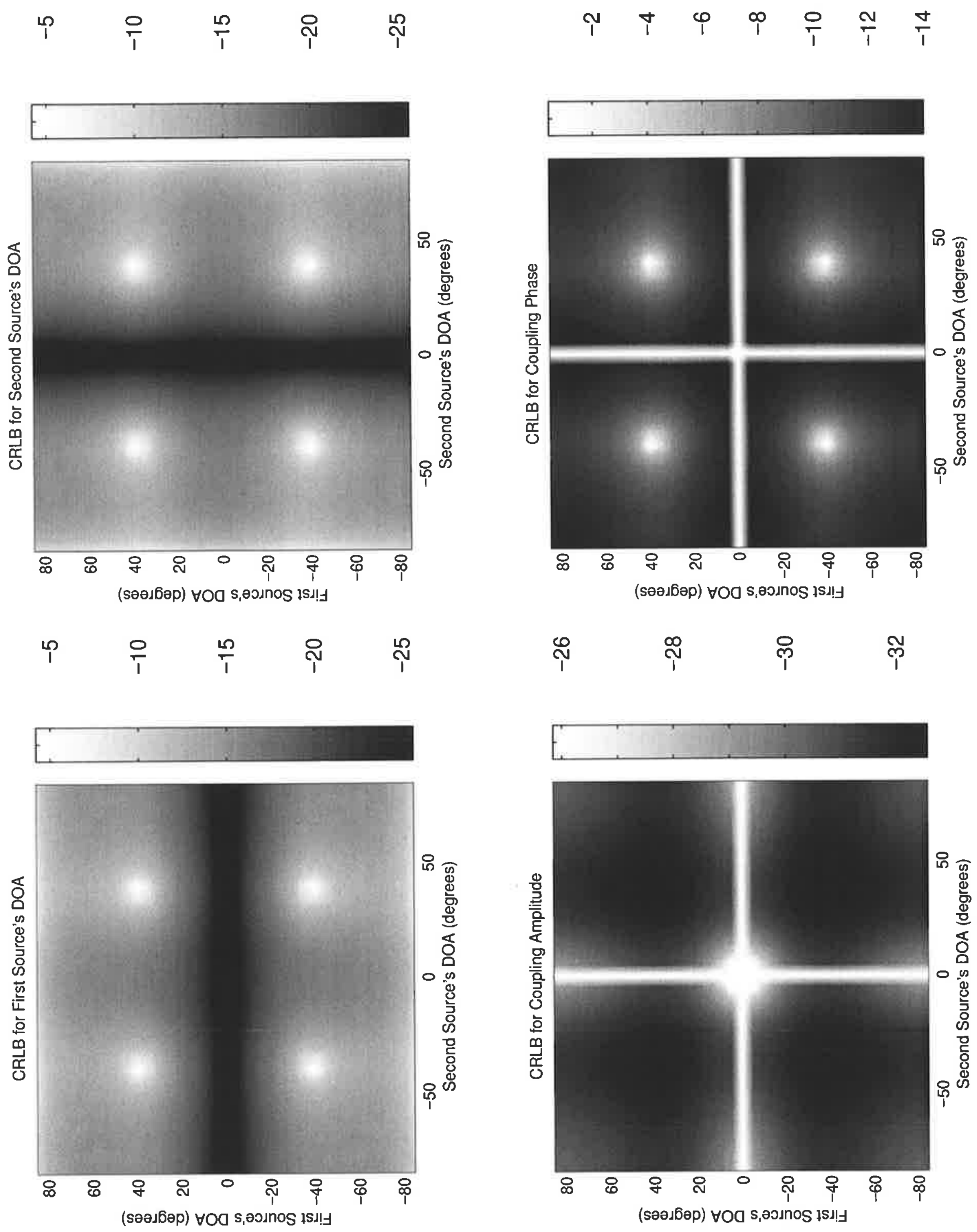

Figure 6.9: Variation of CRLB standard deviations with both source DOAs, for $c = 0.5$ and $\psi = \pi/2$.

The FIM was non-invertible when either sources' DOA was at end-fire directions, and when either sources' DOA was at broadside direction. Note however good CRLB STD values are observed for the coupling parameters in figure 6.9 near these locations, and poor STD values are observed only when both sources' DOAs are near ±38.682° (coupling phase and both source DOA STD values are poor). Hence it can be concluded for multiple sources, that provided (a) none of the sources is exactly at broadside direction, or (b) none of the sources is exactly at end-fire directions, good array calibration is possible except in the unlikely cases that all the sources are near ±38.682°. Another important observation in figure 6.9, is that unlike in the case of non-disjoint sources, for disjoint sources $\theta_1 = \theta_2$ does not cause the FIM to be non-invertible (except for the special cases mentioned above).

In order to illustrate that the CRLB results obtained above (for a Toeplitz coupling matrix with $c = 0.5$ and $\psi = \pi/2$) are representative, results are now presented for the non-Toeplitz measured coupling matrix from the Jindalee transmitting array. The first 2x2 sub-matrix of this coupling matrix is considered, and the CRLB is obtained using the non-analytic approach used in the previous sections (but for a Toeplitz coupling matrix model).

Figure 6.10 shows the CRLB STDs of the parameters being estimated as a function of the single source's DOA, as in figure 6.7. The CRLB for passive array calibration ($-$) and active array calibration ($--$) are displayed, with a grid size of one degree. The results obtained are similar to those in figure 6.7, with the problem being non-identifiable (FIM non-invertible) when the source is at broadside or end-fire directions. The problem is also (probably) non-identifiable when the source DOA is at approximately $-41°$ and at approximately $+43°$. These DOAs are non-symmetric around broadside direction, due to the coupling matrix being non-Toeplitz. The STD of the coupling amplitude is better for active array calibration, unlike in figure 6.7 where it was the same as that for passive array calibration. Note also peaks are observed near $-41°$ and near $+43°$ for the coupling amplitude STD, unlike in figure 6.7. The coupling phase STD is again better for the case of active array calibration, as compared to the case of passive array calibration.

Figure 6.11 shows the results when two disjoint single-mode sources are used for estimating this coupling matrix. The results obtained are as expected; the FIM being non-invertible when either sources' DOA is at end-fire directions, and when either sources' DOA is at broadside direction. Good CRLB STD values are observed near these locations however, and poor STD values are only observed when both sources' DOAs are near approximately $-41°$ / $+43°$. As in figure 6.9 it can be concluded that for multiple sources, provided (a) none of the sources is

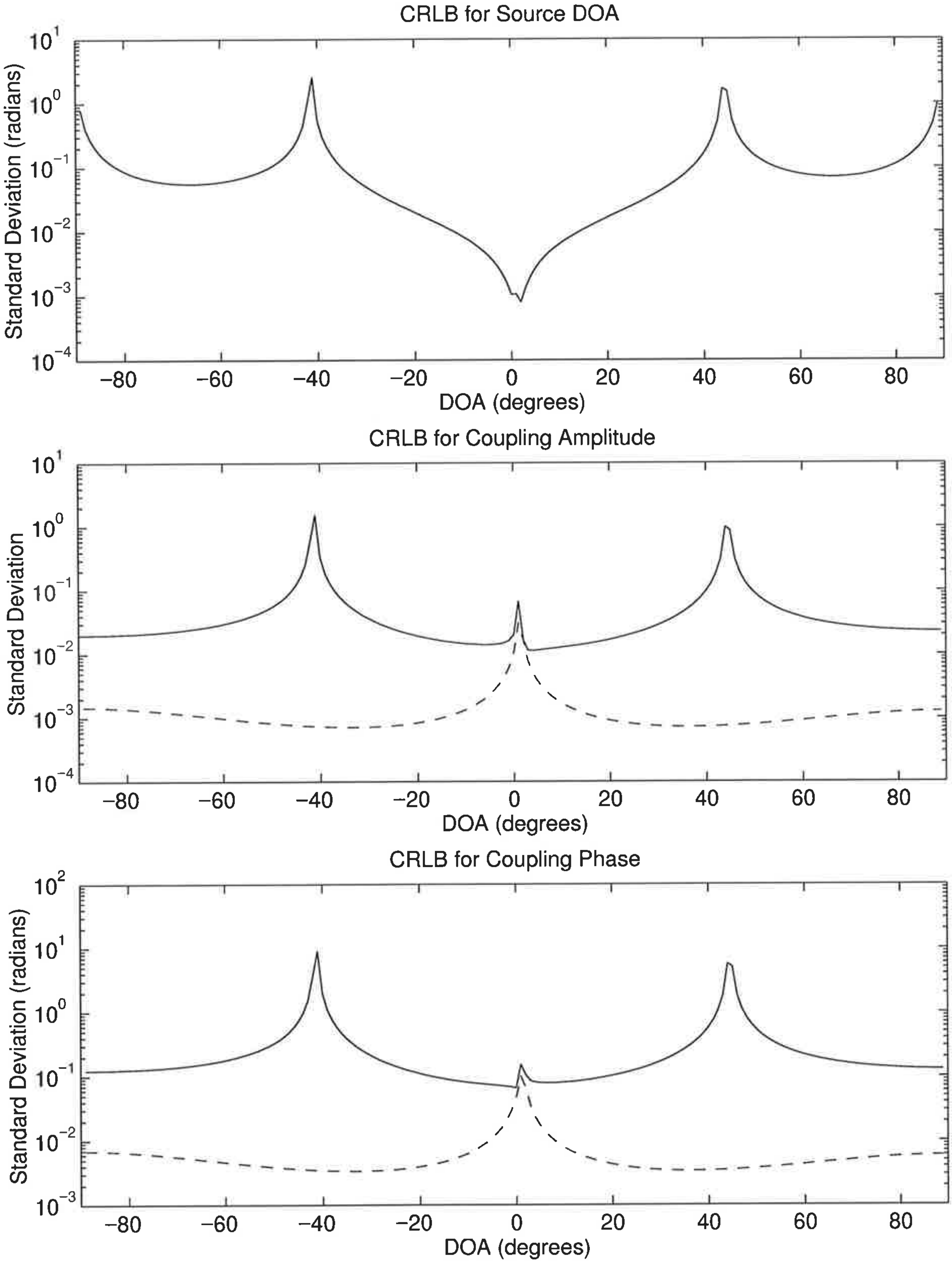

Figure 6.10: Variation of CRLB standard deviations with source DOA, for Jindalee 2x2 coupling matrix estimation.

exactly at broadside direction, or (b) none of the sources is exactly at end-fire directions, good array calibration is possible except in the unlikely cases that all the sources are near −41° / +43°.

## 6.2 CRLB for Disparate Sources

In section 6.1 the CRLB was derived for the case of disjoint single-mode sources. These expressions are now generalised for the problem considered in chapter 5, where disparate sources are used. The unconditional CRLB for estimating $\boldsymbol{\Psi} = [\boldsymbol{\theta}^T, \mathbf{x}^T, \mathbf{y}^T, \mathbf{c}^T]^T$ is

$$\mathbf{CRLB}(\boldsymbol{\Psi}) = \mathbf{J}^{-1}(\boldsymbol{\Psi}) \tag{6.37}$$

where the elements of the FIM, as in section 6.1, are

$$J_{kl} = T \sum_{n=1}^{N} trace\left\{\mathbf{R}_n^{-1}\frac{\partial \mathbf{R}_n}{\partial \Psi_k}\mathbf{R}_n^{-1}\frac{\partial \mathbf{R}_n}{\partial \Psi_l}\right\} \tag{6.38}$$

but now $\mathbf{R}_n$ is for the $n$th disjoint cluster, and is $\mathbf{R}_n = \mathbf{C}\mathbf{A}(n)\mathbf{P}_n\mathbf{A}(n)^H\mathbf{C}^H + \sigma_N^2\mathbf{I}_M$ (for spatially white noise). The matrix $\mathbf{P}_n$ is the signal covariance matrix for the $n$th disjoint cluster, and $\mathbf{A}(n)$ is the matrix of steering vectors for each of the signals in the $n$th disjoint cluster. The noise power is assumed to be the same for each cluster, and is $\sigma_N^2$.

It can be shown that for the case where different number of snapshots are obtained for each cluster, the elements of the FIM are given as

$$J_{kl} = \sum_{n=1}^{N} T_n \, trace\left\{\mathbf{R}_n^{-1}\frac{\partial \mathbf{R}_n}{\partial \Psi_k}\mathbf{R}_n^{-1}\frac{\partial \mathbf{R}_n}{\partial \Psi_l}\right\} \tag{6.39}$$

where $T_n$ is the number of snapshots obtained from the $n$th disjoint cluster. The terms derived in section 6.1 are now generalised.

### 6.2.1 DOA - DOA Terms

Since we have disjoint clusters, $\partial\mathbf{R}_n/\partial\theta_l$ is a zero matrix for $l \ni \Omega_n$, where $\Omega_n$ is the set of all signals in the $n$th cluster. Hence if $k \in \Omega_n$, then $J_{\theta_k,\theta_l}$ is non-zero only if $l \in \Omega_n$ and is

$$\begin{aligned} J_{\theta_k,\theta_l} = \; & 2T_n \Re\Big\{trace\{\mathbf{R}_n^{-1}\mathbf{C}\dot{\mathbf{A}}_{\theta_k}(n)\mathbf{P}_n\mathbf{A}^H(n)\mathbf{C}^H\mathbf{R}_n^{-1} \\ & \mathbf{C}(\dot{\mathbf{A}}_{\theta_l}(n)\mathbf{P}_n\mathbf{A}^H(n) + \mathbf{A}(n)\mathbf{P}_n\dot{\mathbf{A}}_{\theta_l}^H(n))\mathbf{C}^H\}\Big\} \end{aligned} \tag{6.40}$$

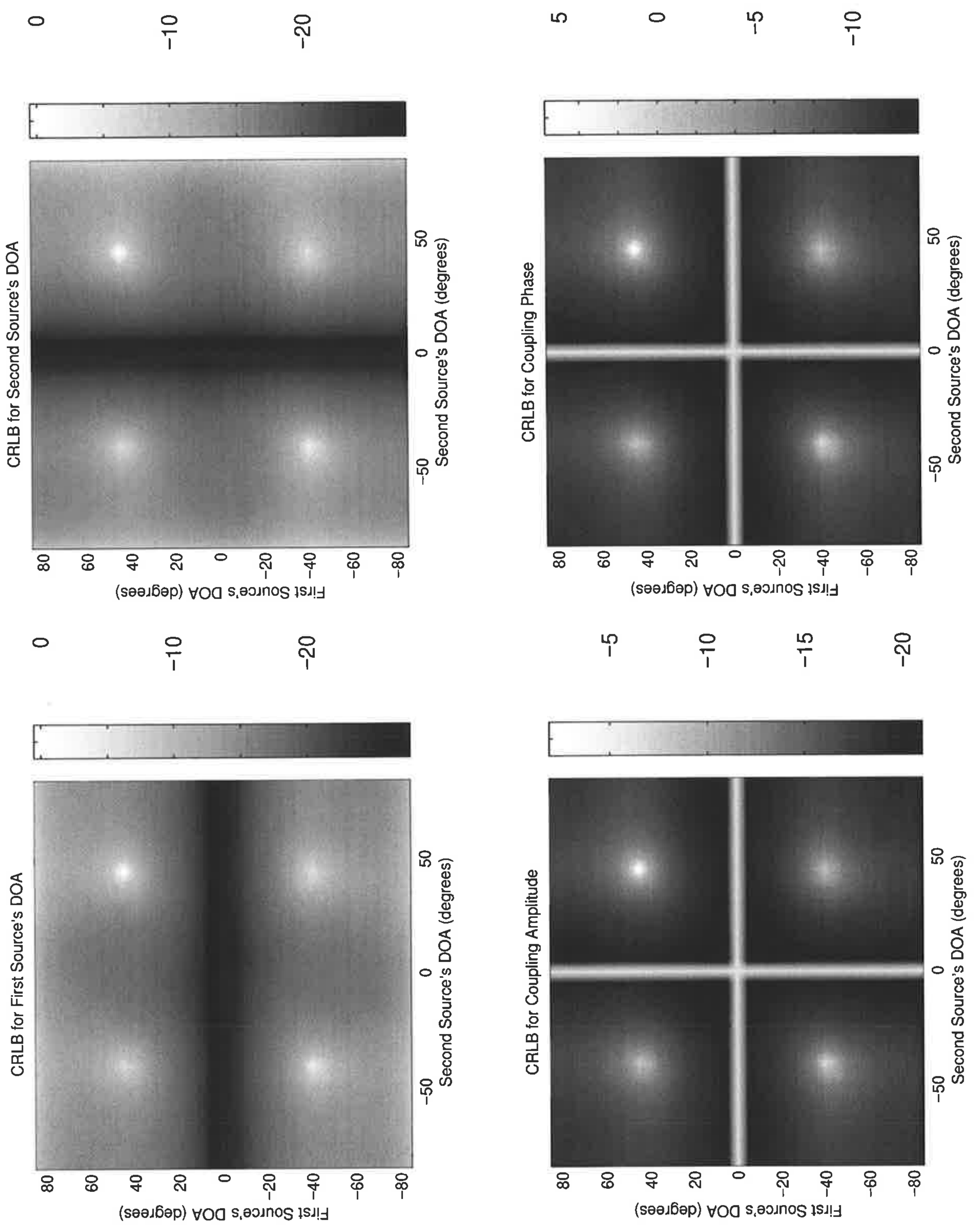

Figure 6.11: Variation of CRLB standard deviations with both source DOAs, for Jindalee 2x2 coupling matrix estimation.

where $\dot{\mathbf{A}}_{\theta_k}(n) = \partial\mathbf{A}(n)/\partial\theta_k = \mathbf{D}(\theta_k)\mathbf{A}(n)\mathbf{e}_f\mathbf{e}_f^T$. $\mathbf{D}(\theta_k) = (+2\pi j/\lambda)diag\{\mathbf{x}\cos(\theta_k) - \mathbf{y}\sin(\theta_k)\}$, and $\mathbf{e}_f$ is the unit vector with all but the $f$th element zero where $f$ is the column number of $\mathbf{A}(n)$ which contains the steering vector of the $k$th signal. (Note the signal powers are included in the matrix $\mathbf{P}_n$).

### 6.2.2 Sensor Position - Sensor Position Terms

The sensor position entries are

$$\begin{aligned} J_{x_k,x_l} &= 2\sum_{n=1}^{N} T_n \Re\Big\{trace\{\mathbf{R}_n^{-1}\mathbf{C}\dot{\mathbf{A}}_{x_k}(n)\mathbf{P}_n\mathbf{A}^H(n)\mathbf{C}^H \\ &\qquad \mathbf{R}_n^{-1}\mathbf{C}(\dot{\mathbf{A}}_{x_l}(n)\mathbf{P}_n\mathbf{A}^H(n) + \mathbf{A}(n)\mathbf{P}_n\dot{\mathbf{A}}_{x_l}^H(n))\mathbf{C}^H\}\Big\} \quad (6.41) \\ J_{y_k,y_l} &= 2\sum_{n=1}^{N} T_n \Re\Big\{trace\{\mathbf{R}_n^{-1}\mathbf{C}\dot{\mathbf{A}}_{y_k}(n)\mathbf{P}_n\mathbf{A}^H(n)\mathbf{C}^H \\ &\qquad \mathbf{R}_n^{-1}\mathbf{C}(\dot{\mathbf{A}}_{y_l}(n)\mathbf{P}_n\mathbf{A}^H(n) + \mathbf{A}(n)\mathbf{P}_n\dot{\mathbf{A}}_{y_l}^H(n))\mathbf{C}^H\}\Big\} \quad (6.42) \\ J_{x_k,y_l} &= 2\sum_{n=1}^{N} T_n \Re\Big\{trace\{\mathbf{R}_n^{-1}\mathbf{C}\dot{\mathbf{A}}_{x_k}(n)\mathbf{P}_n\mathbf{A}^H(n)\mathbf{C}^H \\ &\qquad \mathbf{R}_n^{-1}\mathbf{C}(\dot{\mathbf{A}}_{y_l}(n)\mathbf{P}_n\mathbf{A}^H(n) + \mathbf{A}(n)\mathbf{P}_n\dot{\mathbf{A}}_{y_l}^H(n))\mathbf{C}^H\}\Big\} \quad (6.43) \end{aligned}$$

where $\dot{\mathbf{A}}_{x_k}(n) = \partial\mathbf{A}(n)/\partial x_k = \mathbf{D}\mathbf{x_k} \odot \mathbf{A}(n)$, and $\dot{\mathbf{A}}_{y_k}(n) = \partial\mathbf{A}(n)/\partial y_k = \mathbf{D}\mathbf{y_k} \odot \mathbf{A}(n)$.

### 6.2.3 Coupling - Coupling Terms

The coupling parameter entries are

$$\begin{aligned} J_{c_k,c_l} &= 2\sum_{n=1}^{N} T_n \Re\Big\{trace\{\mathbf{R}_n^{-1}\dot{\mathbf{C}}_{c_k}\mathbf{A}(n)\mathbf{P}_n\mathbf{A}^H(n)\mathbf{C}^H\mathbf{R}_n^{-1} \\ &\qquad (\dot{\mathbf{C}}_{c_l}\mathbf{A}(n)\mathbf{P}_n\mathbf{A}^H(n)\mathbf{C}^H + \mathbf{C}\mathbf{A}(n)\mathbf{P}_n\mathbf{A}^H(n)\dot{\mathbf{C}}_{c_l}^H)\}\Big\} \quad (6.44) \end{aligned}$$

where matrix $\dot{\mathbf{C}}_{c_k} = \partial\mathbf{C}/\partial c_k$, $c_k$ being the amplitude/phase of an element in the symmetric coupling matrix. Note $\dot{\mathbf{C}}_{c_k}$ has only one non-zero element if $c_k$ is a diagonal element, and has only two non-zero elements (of equal value) if $c_k$ is an off-diagonal element.

### 6.2.4 Cross Terms

The cross terms are

$$\begin{aligned} J_{\theta_k,x_l} &= T_n\, trace\{\mathbf{R}_n^{-1}\mathbf{C}(\dot{\mathbf{A}}_{\theta_k}(n)\mathbf{P}_n\mathbf{A}^H(n) + \mathbf{A}(n)\mathbf{P}_n\dot{\mathbf{A}}_{\theta_k}^H(n))\mathbf{C}^H \\ &\qquad \mathbf{R}_n^{-1}\mathbf{C}(\dot{\mathbf{A}}_{x_l}(n)\mathbf{P}_n\mathbf{A}^H(n) + \mathbf{A}(n)\mathbf{P}_n\dot{\mathbf{A}}_{x_l}^H(n))\mathbf{C}^H\} \quad (6.45) \\ J_{\theta_k,c_l} &= T_n\, trace\{\mathbf{R}_n^{-1}\mathbf{C}(\dot{\mathbf{A}}_{\theta_k}(n)\mathbf{P}_n\mathbf{A}^H(n) + \mathbf{A}(n)\mathbf{P}_n\dot{\mathbf{A}}_{\theta_k}^H(n))\mathbf{C}^H \\ &\qquad \mathbf{R}_n^{-1}(\dot{\mathbf{C}}_{c_l}\mathbf{A}(n)\mathbf{P}_n\mathbf{A}^H(n)\mathbf{C}^H + \mathbf{C}\mathbf{A}(n)\mathbf{P}_n\mathbf{A}^H(n)\dot{\mathbf{C}}_{c_l}^H)\} \quad (6.46) \\ J_{c_k,x_l} &= \sum_{n=1}^{N} T_n\, trace\{\mathbf{R}_n^{-1}(\dot{\mathbf{C}}_{c_k}\mathbf{A}(n)\mathbf{P}_n\mathbf{A}^H(n)\mathbf{C}^H + \mathbf{C}\mathbf{A}(n)\mathbf{P}_n\mathbf{A}^H(n)\dot{\mathbf{C}}_{c_k}^H) \\ &\qquad \mathbf{R}_n^{-1}\mathbf{C}(\dot{\mathbf{A}}_{x_l}(n)\mathbf{P}_n\mathbf{A}^H(n) + \mathbf{A}(n)\mathbf{P}_n\dot{\mathbf{A}}_{x_l}^H(n))\mathbf{C}^H\} \quad (6.47) \end{aligned}$$

where for equation (6.45) and (6.46) $k \in \Omega_n$.

### 6.2.5 Algorithm Comparison with CRLB

The performance of the algorithm in chapter 5 was compared to the CRLB for clusters of multiple snapshot time-invariant DOA sources. As in section 6.1 it was assumed that the location of one sensor and the direction to another are known, and hence for the 4-element array considered, there were only 5 sensor positions $(2M - 3)$ unknown. Since a symmetric coupling matrix has been assumed and the constraint $c_{11} = 1$ has been placed, 18 coupling values $(M(M + 1) - 2)$ were unknown. Eleven disjoint clusters, each with a single-mode source, and another disjoint cluster, with a multimode source (with 3 correlated signals), were considered. All signals had unknown DOAs; hence 14 DOAs $(N_T)$ were unknown. The total number of unknown parameters is therefore 37 (the signal and noise powers were assumed to be known).

The solid line in figure 6.12 is the CRLB when 500 snapshots are obtained from these time-invariant DOA sources. The standard deviation (STD) values (circles) estimated from 10 algorithm runs, and the 99 percent confidence intervals (vertical bars), have been plotted. The results clearly show that the algorithm attains the CRLB, and is hence statistically efficient. Similar results were obtained for the other unknown parameters, and in each case the bias was small compared to the STD.

When multiple snapshot time-invariant DOA sources and single-snapshot time-varying DOA sources were used together (not shown), the algorithm's performance was observed to

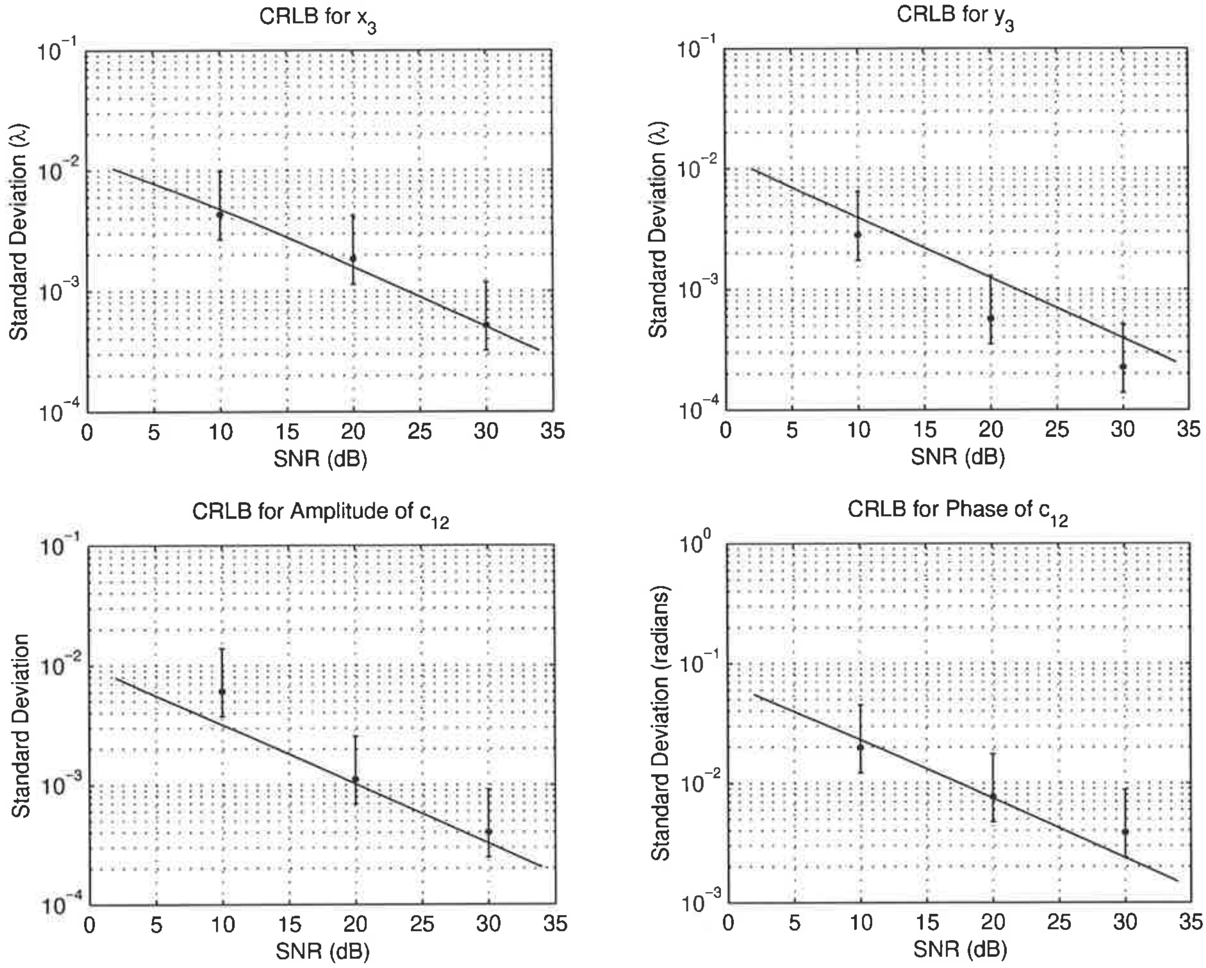

Figure 6.12: Algorithm's performance relative to theoretical performance bound : STD (circle) and 99 percent confidence intervals (vertical bar) as a function of SNR, for the position of a sensor and for the amplitude and phase of a coupling parameter. The solid line is the CRLB. Ten algorithm runs were used to obtain each STD value.

depart from the corresponding CRLB. This somewhat expected result is due to only single-snapshots being obtained from the time-varying DOA sources; the CRLB being only achieved asymptotically (i.e. for large number of snapshots and SNRs).

### 6.2.6 CRLB Analysis

The CRLB is now analysed to : (a) compare the performance of disjoint and non-disjoint sources; and (b) investigate the effect of signal correlation on the CRLB. The study was conducted for a nominally uniform linear 4-element array, with inter-element spacing of $d = 0.4\lambda$. The randomly generated sensor position errors are those in Table 4.1, and the coupling matrix used was experimentally measured from the Jindalee OTH radar's transmitting array. Unless specified otherwise, 12 signals with DOAs equally spaced from $-90^o$ to $+90^o$

in azimuth, each with SNR of 30 dB and 500 snapshots, are considered.

To compare disjoint and non-disjoint sources, three cases were considered. The cases considered are :

- case A : twelve disjoint clusters, each cluster containing only a signal (–);
- case B : six disjoint clusters, each cluster containing two non-disjoint signals (– –);
- case C : four disjoint clusters, each cluster containing three non-disjoint signals (–.–).

All the signals considered were uncorrelated. The CRLB for each case is shown in figure 6.13, as a function of the signals' SNRs. The CRLB for case A (–) is the best, the CRLB for case B (– –) is the next best, and the CRLB for case C (–.–) is the worst. This is so for all of the parameters being estimated. These results indicate that given a fixed number of sources (also SNRs, snapshots, etc), the more disjoint clusters the better the CRLB; this is as expected, since the more disjoint clusters present, the more the a priori information, and so the resulting performance should be better. Note also it was stated in section 4.4 that with disjoint sources, many more parameters can be estimated than with non-disjoint sources, for a given number of sources.

To investigate the effect of signal correlation on the CRLB, the scenario in case B above was considered. The 2x2 signal covariance matrix is now non-diagonal, and is

$$\mathbf{P}_n = \begin{bmatrix} 1-\rho & \rho \\ \rho & 1-\rho \end{bmatrix} \tag{6.48}$$

where $\rho$ determines the level of correlation ($0 \leq \rho \leq 1/2$). Figure 6.14 shows the effect of signal correlation on the CRLB for four parameters. The three cases considered are :

- case A : uncorrelated signals in each cluster (–) i.e. $\rho = 0$;
- case B : partially correlated signals in each cluster (– –), with $\rho = 1/3$;
- case C : coherent signals in each cluster (–.–) i.e. $\rho = 1/2$.

These results clearly illustrate that the CRLB worsens as the signal correlation increases, indicating the best results are obtained with uncorrelated signals. These observations agree with those of Ng and Nehorai in [138].

## 6.3 Conclusion

The CRLB has been derived for the problems considered in chapters 4 and 5, and it has been demonstrated using simulations that the algorithms in these chapters attain the corresponding

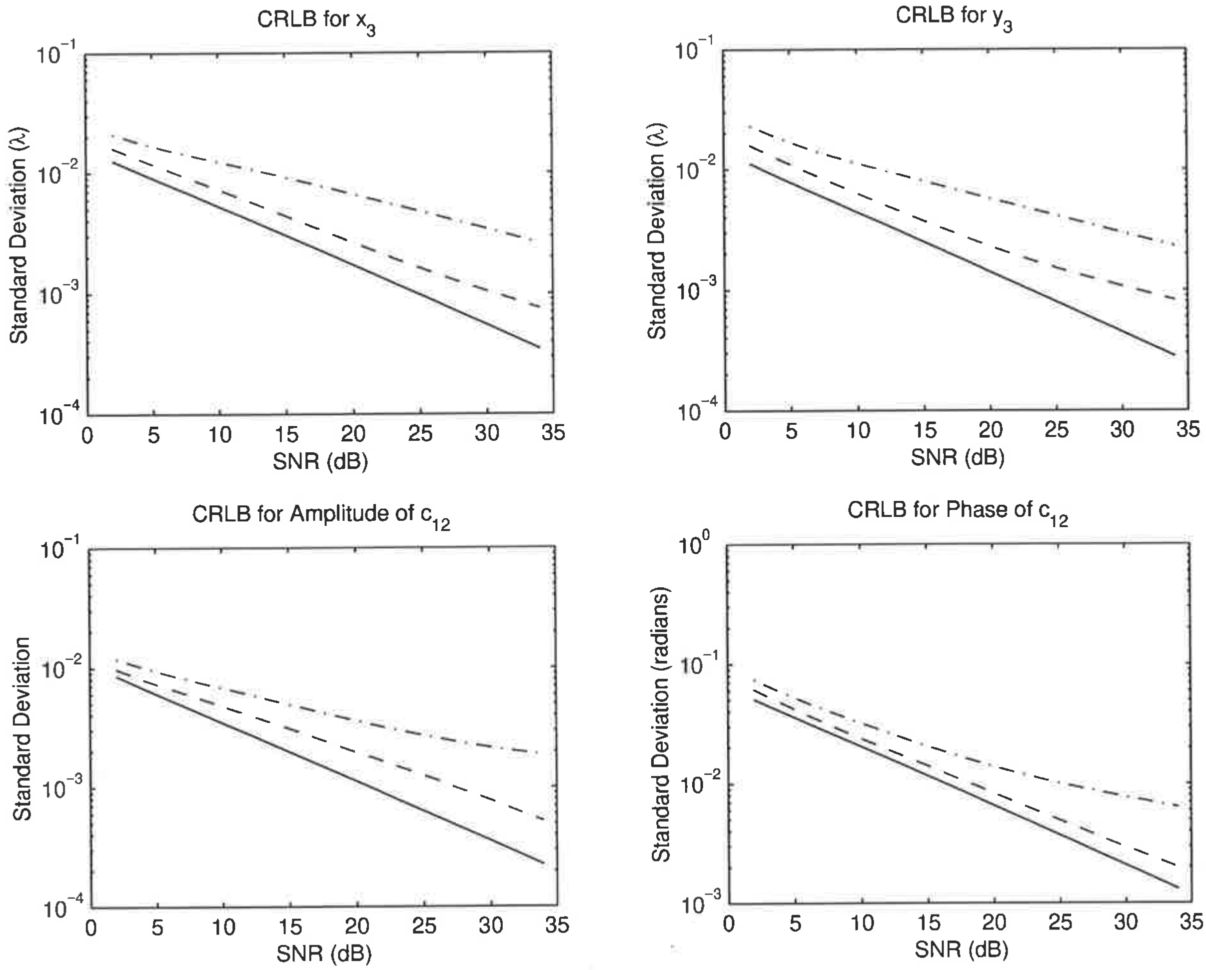

Figure 6.13: CRLB dependence on disjoint/non-disjoint sources - (a) twelve disjoint clusters, each with one signal (-); (b) six disjoint clusters, each with two non-disjoint signals (— —); (c) four disjoint clusters, each with three non-disjoint signals (—.—).

CRLBs under asymptotic conditions. The behaviour of the CRLB has been investigated as a function of SNR, number of snapshots, number of sources, signal correlation, etc. For a 4-element array, the array calibration problem was identifiable when four or more sources were used; the problem being well defined, and the CRLB STDs indicating the unknown parameters could be estimated to good accuracy. "Active array calibration" was shown to produce better accuracy than "passive array calibration", at the cost of requiring special sources. The influence of the elevation angle of meteor trail echoes on array calibration accuracy was also illustrated.

The problem of mutual coupling only estimation using a single source, was studied analytically, and it was shown that the problem is non-identifiable for certain (small number of) source DOAs; for multiple sources, except when a source is at broadside or end-fire directions these non-identifiable conditions were shown to however be very unlikely.

In chapter 7 sources present in the HF environment are investigated from an array calibration

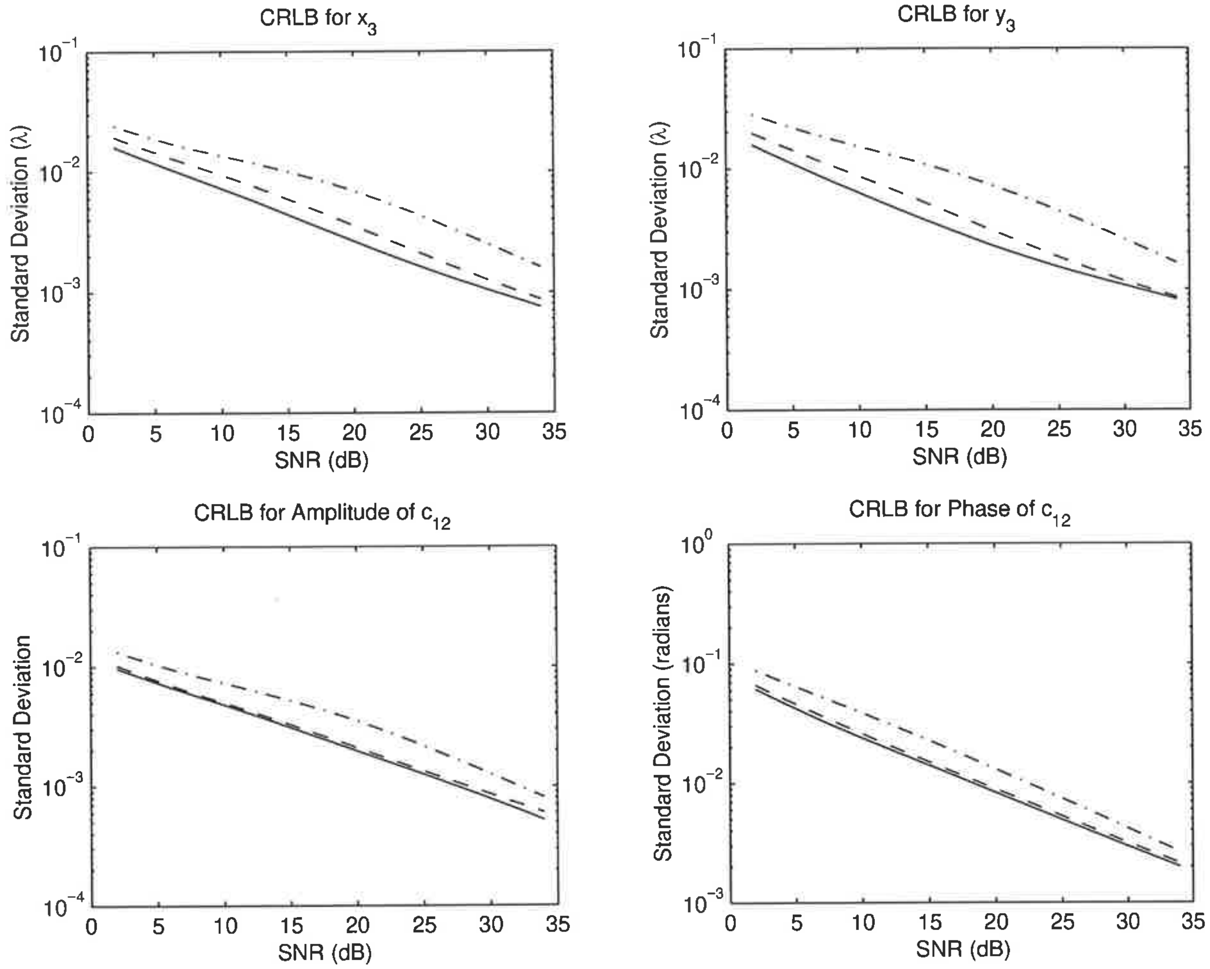

Figure 6.14: CRLB dependence on signal correlation - (a) uncorrelated signals (-); (b) partially correlated signals (— —); (c) coherent signals (—.—).

perspective, and finally in chapter 8 the thesis is concluded.

# CHAPTER 7

# Sources for HF Array Calibration

For OTH radar array calibration one may use discrete sources such as noise sources, beacons (special sources), meteor echoes and ship/aircraft returns. While all of these sources can provide sufficiently strong signals for array calibration, meteor echoes are the most attractive. Meteor echoes are sources of opportunity, and are also observed by OTH radars in great numbers; thus providing numerous sources for array calibration. Hence meteor echoes are the most desirable sources for array calibration, and so are considered in detail here.

This chapter starts with an overview of the Jindalee OTH radar, which has been instrumental in the analysis of the various sources. This is followed in section 7.2 by a description of the physical and temporal properties of meteor echoes, which is primarily from the existing literature; then a spatial analysis of their wavefronts is given which indicates how often meteor echoes can be used as sources of opportunity for array calibration. Noise sources for array calibration is discussed in section 7.3, while other sources are discussed in section 7.4. Finally in section 7.5 meteor echoes are used to calibrate the Jindalee OTH radar; demonstrating, using a real radar system, the capability of these sources.

## 7.1 Jindalee Radar Overview

The Jindalee OTH radar [190, 191, 192, 193, 115, 103, 116, 10] is located in central Australia; the transmitting array is located in Harts Range and the receiving array in Mount Everard. This radar is called a skywave radar, see figure 7.1, since it uses the ionosphere to propagate signals beyond line-of-sight by operating in the HF band (i.e. 3-30 MHz). Jindalee is capable of detecting air and surface targets, over a 90° coverage, and at ranges of 800-2800 Km.

The transmitting array is a linear array of 16 Log-periodic antennas, which produces a

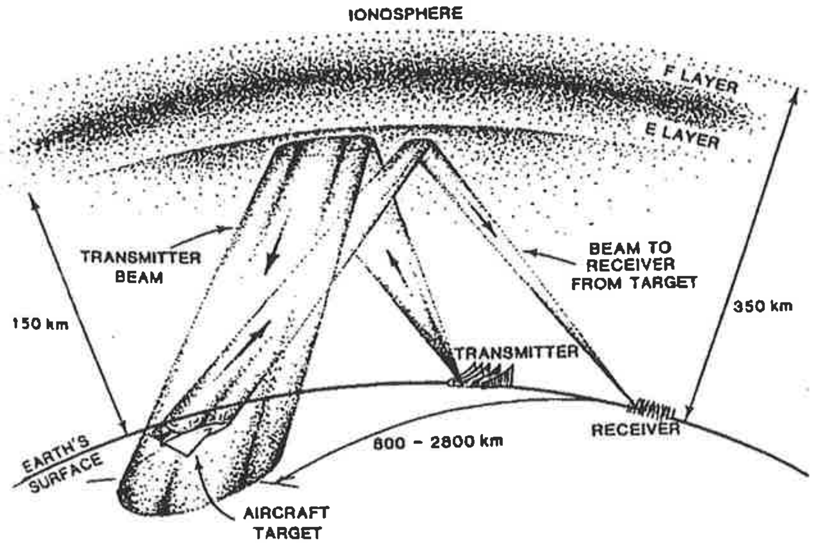

Figure 7.1: Skywave radar propagation environment (Lees et. al.).

steerable wide beam of energy. The Log-periodics produce a fairly constant power output over all frequencies in the HF band. The receiving array is a 2766 metre long uniform linear array of 462 twin-fan monopoles, which makes up 32 fully overlapped subarrays (see figure 7.2). Each of the 28 monopoles in a subarray is connected to an analogue hardware beamformer, with the output of each subarray (or hardware beamformer) then processed by a HF receiver. The hardware beamformers are time-delay beamformers, with the time-delays such that signals are received over the same azimuthal region that the transmit beam is illuminating.

The transmitting array sends out a frequency modulated continuous wave (FMCW), and the receiving array receives signals scattered by targets, the ground and the sea. Computerised processing of received signals is done in three steps, as shown in figure 7.2. The signals received by each subarray/receiver is compared to a replica of the transmitted signal to obtain "range formed" data, i.e. signals over discrete range bins called "range cells". The subarray/receiver outputs for each range cell are then digitally beamformed to produce fine beams, called "finger beams", within the subarray beampattern. Then the signals in each range cell - finger beam, over several FMCW periods (sweeps), are processed to obtain signals as a function of discrete Doppler bins. Data is processed in such a manner, over a coherent transmission interval called a "dwell".

A typical example of the radar output is shown in figure 7.3; the power output for 10 finger beams being shown as a function of range cell and Doppler cell. In each finger beam, strong

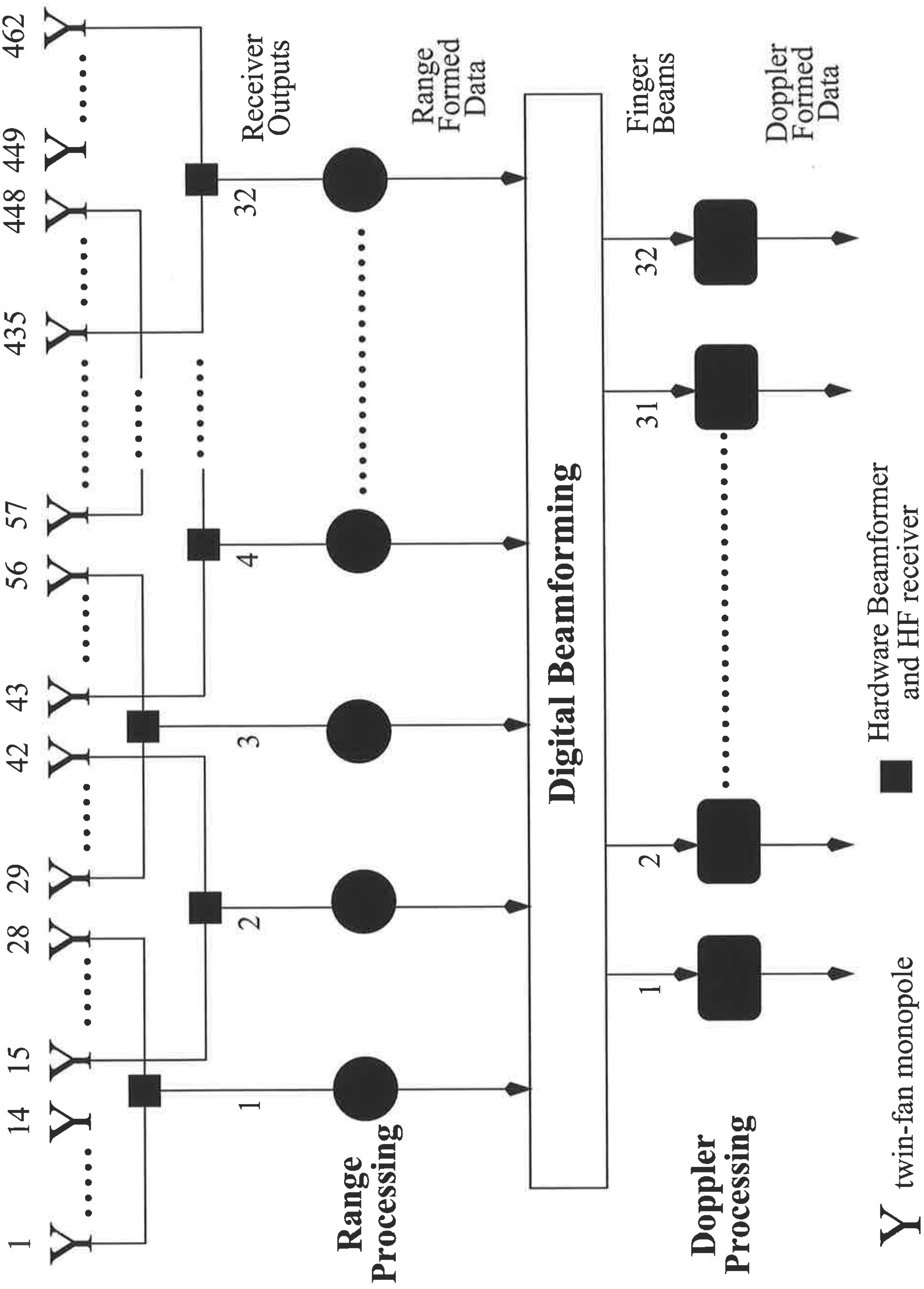

Figure 7.2: Jindalee radar processing of received signals - range processing, digital beamforming and Doppler processing.

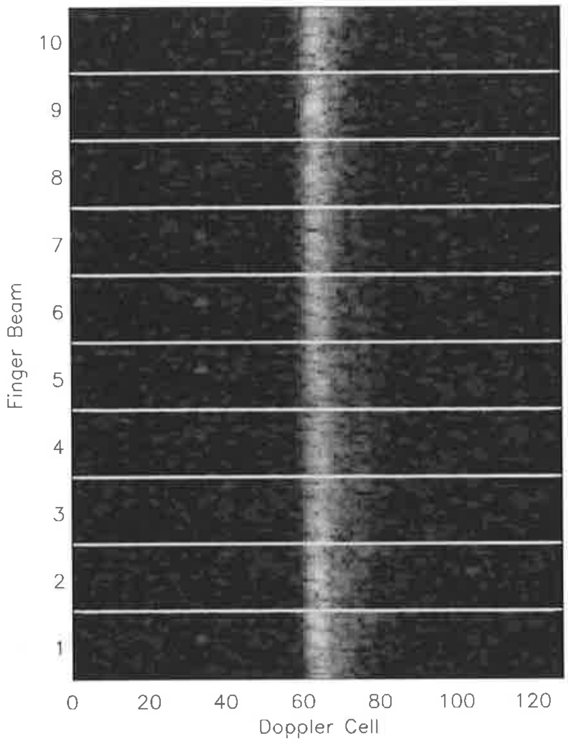

Figure 7.3: Example of Jindalee radar output. The received power is displayed, for each of the 10 finger beams, as a 2-dimensional image; each image comprising of 20 range cells (vertical axis) and 128 Doppler cells (horizontal axis).

energy exists at all ranges around zero Doppler (Doppler cell 64). This is energy scattered from the ground; since the ground has zero velocity, the energy appears at zero Doppler. Returns from the ground and the sea are referred to as clutter.

The data in figure 7.3 was collected in air-mode, where the radar parameters are set for detecting aircraft. Data obtained in this mode consists of short dwells, so the progress of aircraft can be tracked. Data collected in ship-mode, where the radar parameters are chosen for detecting ships, consist of long dwells (with a large number of sweeps) so that good Doppler resolution can be obtained for resolving ships from the sea clutter.

Sampled subarray outputs from the Jindalee radar are stored on tapes; the tapes for all radar runs being archived. This enables post-processing to be performed on radar data, making the Jindalee radar also a very powerful research tool.

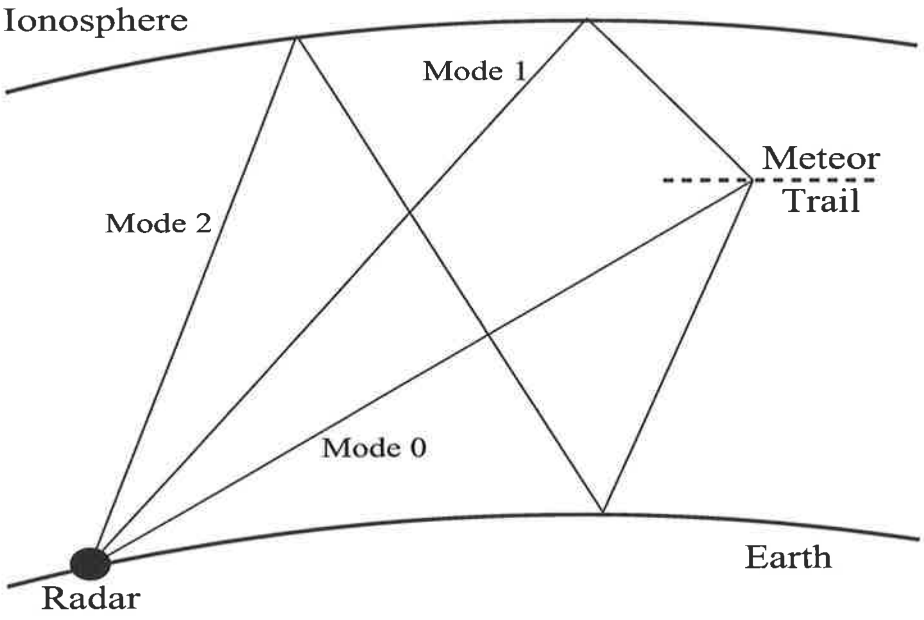

Figure 7.4: Propagation modes for meteor echoes.

## 7.2 Meteors

Possible propagation modes by which HF radar may detect meteors are shown in figure 7.4, when only a single ionospheric layer exists. Mode 0 is direct scatter along the line-of-sight path, Mode 0 echoes being observed in close-in radar ranges. Mode 1 relies on forward scattering by the ionosphere while Mode 2 relies on both ionospheric and ground forward scattering. Mode 1 echoes appear at greater ranges than Mode 0 echoes, while Mode 2 echoes appear at even greater ranges. Mode 0 echoes are often near-field echoes, while Mode 1 and Mode 2 echoes are far-field returns. (Mode 3 echoes, where the propagation modes to and from the meteors are different, are also possible).

Mode 0 meteor echoes will be observed in the data, for skywave radars, at ranges prior to the ranges at which the sea/ground clutter is observed. The range at which clutter starts appearing is frequency dependent, and this start range value is obtainable from the radar's frequency management system (FMS) [45, 46].

Now some of the properties of meteor echoes, which have been described in [132, 220, 221, 222, 223, 146, 217, 26] are outlined, and results from the analysis of meteor echo wavefronts that one has conducted is presented. The properties required for obtaining scattered echoes from meteors, the difference between underdense and overdense echoes, the difference between shower meteors and sporadic meteors, the wavefronts of both line-of-sight and ionospherically propagated meteor echoes, the effects of radar frequency on meteor observations, the diurnal variation of meteor echoes and the variation of echo rates with range, are described.

### 7.2.1 Visual Observations

The word meteor refers to the “shooting star” seen when a meteoroid, enters the earth’s atmosphere, and dissipates its energy. The visible radiation from a meteor emanates mainly near the vaporising meteoroid, and hence the meteor looks like a travelling light source. After the passage of a bright meteoroid, a glowing trail can sometimes still be seen.

### 7.2.2 Radar Observations

Two echoes, of different physical origin, are observed from a single meteor when a radar transmits a radio wave and obtains energy back. The two echoes are known as “head echo” and “trail echo”. The head echo is associated with the meteoroid, and is hence an echo that moves in space. This echo is short-lived since the meteoroid burns up fairly quickly, due to frictional heating, upon entering the earth’s atmosphere. The physical mechanism for the head echo is not yet fully understood, but the echo seems to originate from a cloud of ionisation around the meteoroid. The radar does not obtain an echo from the meteoroid itself, since the cross-section of the meteoroid is too small to be detected by the radar.

The trail echo is a specular reflection from the trail of ionisation, created by the collision of meteor atoms with the surrounding air molecules when a sufficiently large meteoric object descends into the earth’s atmosphere. No significant ionisation occurs until the meteoric object descends to heights about 120 Km above the earth, since the air is not dense enough and hence collisions with air molecules are not sufficiently frequent. Most of the ionisation occurs between 80-120 Km because the air density is large here, and also because most of the meteoric object vaporises prior to reaching a height of 80 Km (note higher velocity meteoroids produce trails at higher heights). The trail echo is seen just after the head echo, and is of much longer duration. Note the trail echo is an aspect sensitive return, whereas the head echo is an aspect insensitive return.

A long trail of ionisation can be created when even a very small meteoric object (smaller than even a pinhead) enters the atmosphere. The total backscattered radio energy from all areas of the column of ionisation, which is radar target like and has cross-sectional area much larger than the object itself, can result in a substantial echo. The trail of ionisation can be tens of

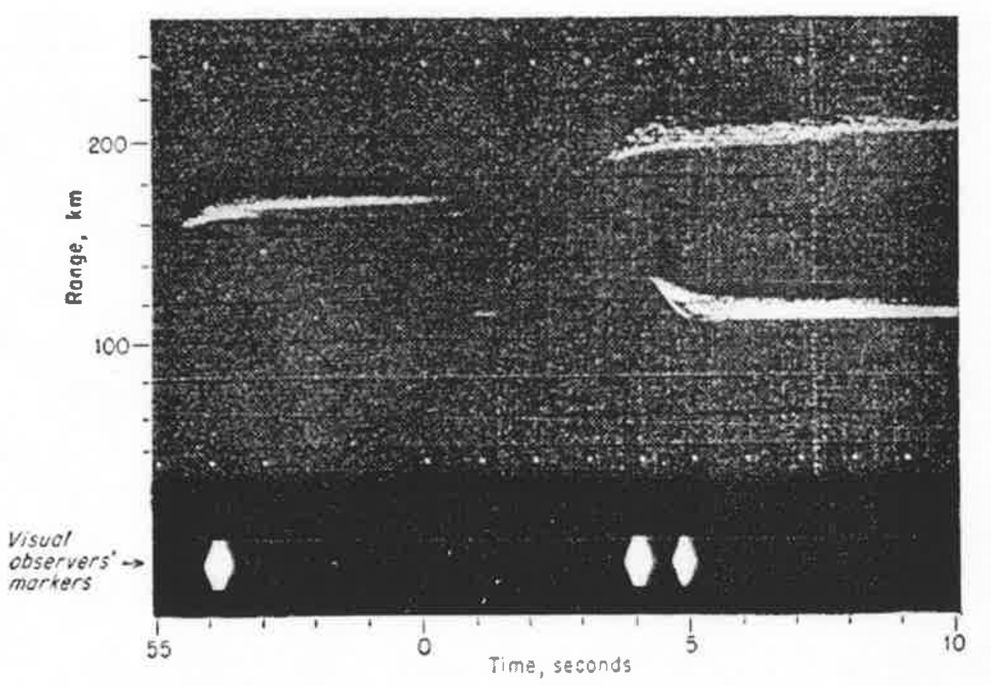

Figure 7.5: Examples of radar meteor echoes (McKinley).

kilometres long, be present over 10-15 Km in altitude, and exist in space for several seconds or minutes after the meteoroid has vaporised, before finally disappearing due to rapid diffusion. Although the trail of ionisation may be many radar wavelengths long, the trail echo is (and is modelled as) a point source due to the aspect sensitivity of the return.

Examples of radar meteor echoes are shown in figure 7.5, in a range-time display. Note since meteor echoes are scattered radar signals, the range of the meteor can be determined. The closest return in figure 7.5 is due to a meteoroid approaching the radar, while the other two returns are due to meteoroids going away from the radar. For each return the slanted narrow line at the start of the return is the head echo, while the more persistent echo which spreads in range is the trail echo.

### *7.2.3 Underdense versus Overdense Echoes*

When meteor trail reflection properties are considered, meteor trails are conveniently divided into two major subdivisions : underdense trails and overdense trails. Underdense trails are those in which the electron density (proportional to the meteor's mass) is sufficiently low so that the radio wave penetrates the trail and each electron acts as an individual scattering source. Overdense trails are those where the electron density is sufficiently high to prevent complete penetration of the radio wave, and cause reflection of the radio waves like ionospheric reflection. The duration of underdense trails is typically of the order of a tenth of a second, and the duration of overdense trails may be from a tenth of a second to many minutes.

### 7.2.4 *Shower Meteors and Sporadic Meteors*

The sky location from which a meteor appears to originate is called the radiant of the meteor. Meteors which originate from the same radiant are called shower meteors, while meteors which do not belong to recognised showers are called sporadic or non-shower meteors. Sporadic meteors have a large distribution of velocities, with a mean value of about 40 Km/s. Meteors which are part of a shower, however, move as a collection of particles and travel at the same velocity; hence shower meteors have well-defined velocities. Meteors entering the earth's atmosphere have velocities between 11 and 72 Km/s, and decelerate by a small amount during ablation.

Thomas tracked a meteor shower using the Jindalee OTH radar, on the 6th of May 1986 [222]. By measuring the radar's noise floor level, provided by the radar at each dwell, he could obtain the total backscattered power level from all meteors present during any dwell. Using this data he was able to continuously monitor meteor activity, and hence detect meteor showers over range, azimuth and time.

Figure 7.6 shows the results Thomas obtained in tracking the Eta Aquarid shower over azimuth and time. The solid curve shows the predicted position of the shower radiant, while the dashed curves on either side correspond to a standard deviation of the radiant position. The observed data positions have error bars which indicate, the time interval over which data averaging was performed (12 minutes) and also the uncertainty in the azimuth (6°). For array calibration one not only has many meteor echoes when a shower is present but also, since the shower meteors appear at different azimuths during the day, one has echoes from all azimuths for performing calibration. Note further, Thomas has observed that the proportion of strong echoes was greater for shower meteors than for sporadic meteors (at least for this shower).

### 7.2.5 *Radio Frequency Dependence*

Radar meteor echo rates are biased by the observation tool [85, 86], and radars have been known to detect only a small fraction of the meteors observed by satellites [146]. Figure 7.7 shows the relative echo rates as a function of frequency, modelled and observed by Thomas et.

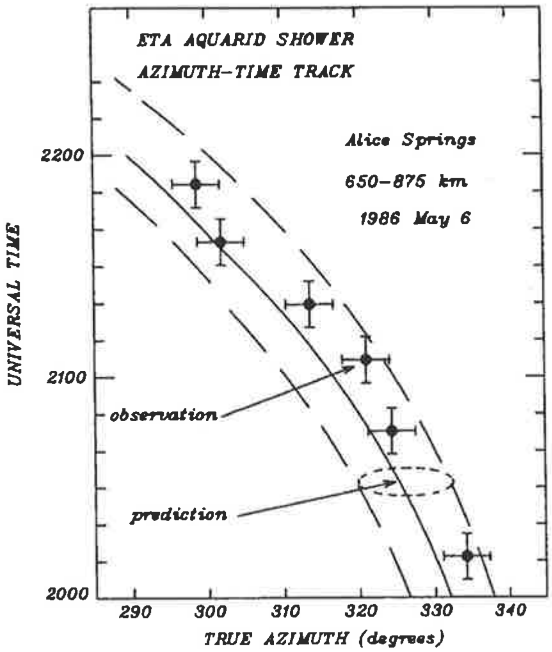

Figure 7.6: Tracking of Eta Aquarid shower over azimuth and time (Thomas et. al.).

al. using the Jindalee radar on day 296, 1985, between the hours of 0230 and 0730 local time. Also shown are the rates predicted by Greenhow ([85, 86]). The observed data was corrected for the frequency dependence of both the antenna polar diagram and radar sensitivity, and hence it is concluded that the remaining frequency dependence is purely due to the frequency of the transmitted radar signal (and is termed the "echo ceiling" effect).

The sporadic meteor echo power variation with frequency, obtained by Thomas et. al., is shown in figure 7.8 ($*$). Curve A is modelled results when the height distribution of Olsson-Steel et. al. [146] is used with a full treatment of the underdense echo ceiling, while curve B is modelled results when previously accepted height distributions are used and the underdense echo ceiling is not considered. The frequency variation observed by Thomas et. al. clearly supports the modelled results in curve A, and illustrates how the meteor echo rates (proportional to observed power) fall off at higher frequencies in the HF band. These results indicate, that for array calibration using meteor echoes, one has to collect meteor data for a longer period at the high-end of the HF band as compared to the low-end of the HF band.

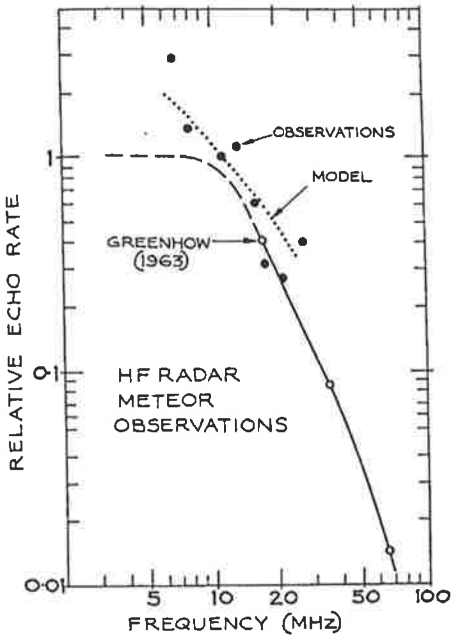

Figure 7.7: Variation of echo rates with frequency (Thomas et. al.).

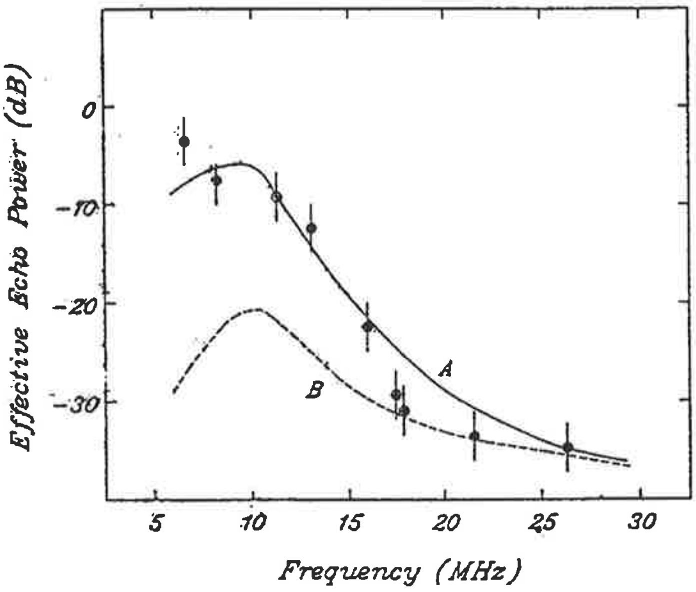

Figure 7.8: Sporadic meteor echo power variation with frequency (Thomas et. al.). Curve A and B are modelled results, while the circles show measured values.

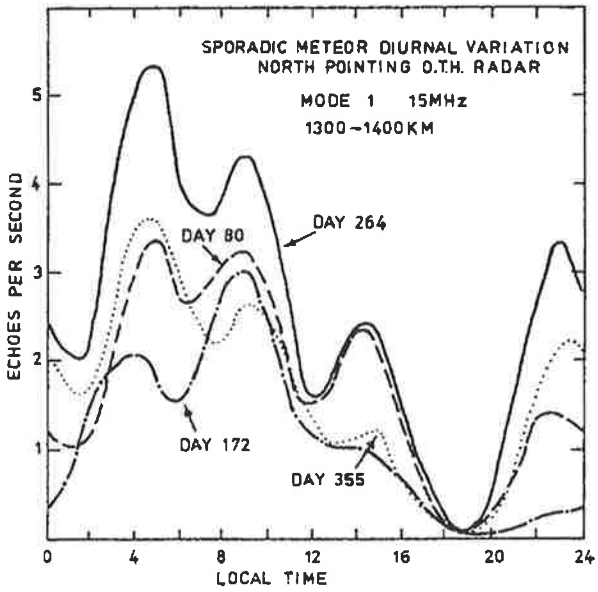

Figure 7.9: Predicted diurnal variation of sporadic meteor echo rates for different days in the year (Thomas et. al.).

### 7.2.6 Diurnal Variation

Thomas et. al. used their computer model to predict the diurnal variation of sporadic meteor echo rates, that would be observed using the Jindalee radar, via single-mode ionospheric propagation [223]. Figure 7.9 shows the echo rates predicted for a north pointing radar for several days during the year. Clearly non-zero meteor echo rates are expected throughout the day, with the peak intensity of echoes occuring near dawn and a trough occuring near sunset. Due to the orbital motion of the earth, at dawn (when the earth is rotating towards the sun) the meteor rates are high, and at sunset (when the earth rotates away from the sun) the meteor rates are low. For array calibration using meteor echoes, the results in figure 7.9 indicate that near sunset one has to collect meteor data for a greater time.

Variation of meteor echo rates from month-to-month are mainly determined by the variation of meteoroid activity itself.

### 7.2.7 Range and Altitude Dependence

The number of meteors observed by radars fall off with range, due to the decreasing detection ability of radars with range. The height distribution of trail echoes has been determined by Olsson-Steel et. al. to be non-Gaussian, with a peak at 105 Km (at 2 MHz), and most of the meteor trails present have been found at or above this altitude of 105 Km [146].

### 7.2.8 Numerous Disjoint Sources of Opportunity

In this section, and the next two sections, one analyses the spatial properties of meteor echoes. The wavefronts of meteor echoes is analysed in this section, while the spatial stationarity of meteor echoes, and multimode meteor echoes, are studied in the following two sections. All these results were obtained using the well calibrated Jindalee receiving array. This section starts with a typical example of data analysed, in order to determine if meteor echoes have "good enough" wavefronts to perform array calibration, and then results are presented for a number of echoes.

Figure 7.10(a) shows the output of a single subarray/receiver (after the clutter has been filtered out), for a dwell obtained during ship-mode data collection. The horizontal axis is sweep number (time snapshot), and the vertical axis is the radar range cell number. The strong signals (SNRs 10-30 dB) observed here are ionospherically propagated meteor trail echoes. As can be seen several echoes exist in this data, which was collected in 30 seconds. Many of these echoes occur over a few sweeps and range cells, and are well separated from other echoes. Since most echoes are separable from other echoes, statistics for each echo can be obtained independently, and thus in this thesis, such meteor echoes have been called "disjoint" echoes or "disjoint" sources.

The phase variation across the array aperture (or receiver outputs), for three successive time snapshots, of an echo in figure 7.10(a) is shown in figure 7.10(b). The linearity of the phase variations across the receivers in each case is clearly seen, the three snapshots being time shifted versions of each other. This was found to be the case for many returns examined (see later).

The MUSIC algorithm applied to each range, is shown in figure 7.10(c). The covariance matrix for each range was estimated from the vector of receiver outputs for that range; averaging of the covariance matrix occuring over the sweeps. Since the wavefronts are reasonably linear, it is not surprising that meteor echoes are beamformed well. Note that time limited echoes in a particular range in figure 7.10(a) are seen in figure 7.10(c) as spatially localised echoes.

Several dwells from the Jindalee OTH radar were analysed, to determine the linearity of meteor echo wavefronts. Both ionospherically propagated and line-of-sight meteor echoes, were considered. In all dwells considered, the covariance matrix was estimated for each echo in the dwell, in order to obtain an estimate of the wavefront of the echo. The covariance matrix

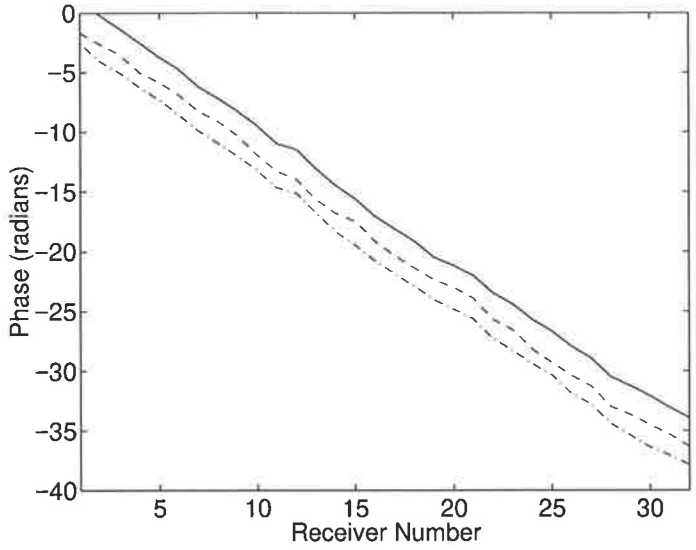

(b) phase variation across the aperture for a single echo

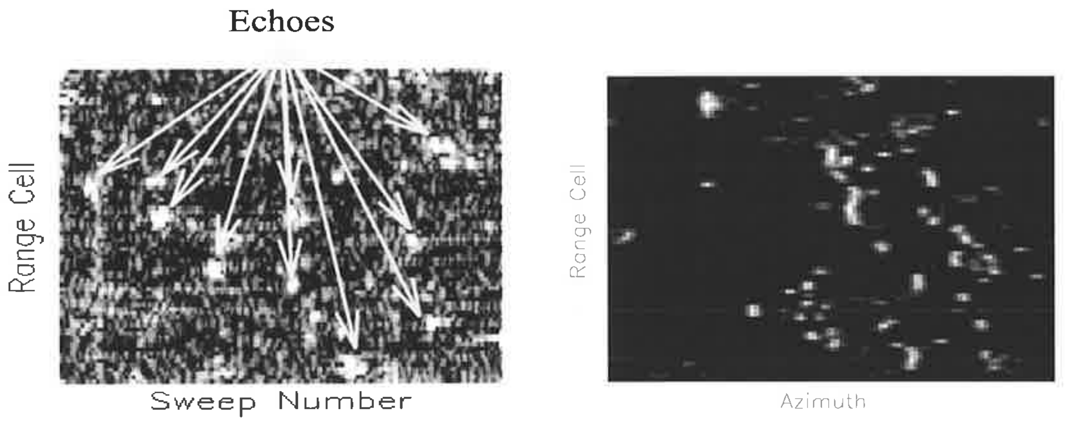

(a) single receiver output

(c) MUSIC

Figure 7.10: Example data set analysed for investigating wavefront of meteor echoes.

for an echo was estimated as

$$\hat{\mathbf{R}} = \frac{1}{T}\sum_{t=1}^{T} \mathbf{z}(t)\mathbf{z}^{H}(t) \tag{7.1}$$

where $\mathbf{z}(t)$ is the vector of receiver outputs at time snapshot $t$, and the summation is performed over all sweeps / range cells over which the echo is present. The analysis conducted is now described, with the results obtained for a particular echo, presented to illustrate the analysis.

Once the covariance matrix for an echo has been obtained, the covariance matrix is eigendecomposed; obtaining eigenvectors and eigenvalues. The eigenspectrum for an echo is shown in figure 7.11(a), which indicates there is one dominant (signal) eigenvalue. In cases where there were two overlapped echoes, hence resulting in two dominant eigenvalues, the echoes were omitted from the analysis. Further echoes with SNRs, given by the difference between the largest two eigenvalues, which were less than 10 dB were also not considered.

The principal eigenvector, that is the eigenvector corresponding to the largest eigenvalue, is a maximum likelihood estimate of an echo's wavefront [83]. Figure 7.11(b) shows the phase values ($*$) of the principal eigenvector for the echo considered. A straight line is then fit to these phase values ($-$) to estimate wavefront phase errors (deviations from the straight line). The phase errors are determined, as given in figure 7.11(c), and then the standard deviation of the phase errors computed. The wavefront amplitude errors are determined, for each echo, by estimating the amplitude deviations of the principal eigenvector elements from their average value (not shown). From the amplitude deviations for an echo, the standard deviation of the amplitude errors is computed; the standard deviation computed is then normalised by the average amplitude value.

The wavefronts of *ionospherically propagated trail echoes* were analysed from 48 radar dwells, covering 11 days during 1986-1990. The wavefronts of *line-of-sight trail echoes* were analysed from 36 radar dwells, from a day in 1989. The wavefronts of *head echoes* (all line-of-sight) were analysed from a day in 1987 and a day in 1989. Histograms for the wavefront phase and amplitude errors are shown in figures 7.12 and 7.13 respectively.

The first two sub-plots in both figure 7.12 and 7.13 are for *ionospherically propagated trail echoes*. In each of these figures the first sub-plot is for "bad" echoes which were obtained during five of the eleven days, and the second sub-plot is for "good" echoes which were obtained during the other six days. Here "good" echoes refer to those echoes obtained from data in which the ground/sea clutter is of good quality (i.e. the clutter is narrow and only single-mode clutter is obtained), while "bad" echoes refer to echoes obtained from data in which the clutter is not of good quality. The phase errors for the "good" echoes are distributed around 6°, while the phase errors for the "bad" echoes are broadly distributed around 14°. The amplitude errors for the "good" echoes are located around 0.12, while for the "bad" echoes the distribution is flatter.

In figures 7.12 and 7.13 the third sub-plot is for *line-of-sight trail echoes*. The phase errors are distributed around 7°, in comparison with the *ionospherically propagated "good" echo* phase errors which are distributed around 6°. The amplitude error histogram is somewhat similar to that for *ionospherically propagated "good" echoes*, with a peak near 0.1. Note *line-of-sight trail echoes* originate (often) from meteors in the radar's near-field, and so have wavefronts with a small amount of curvature; as a result of this a quadratic (instead of a straight

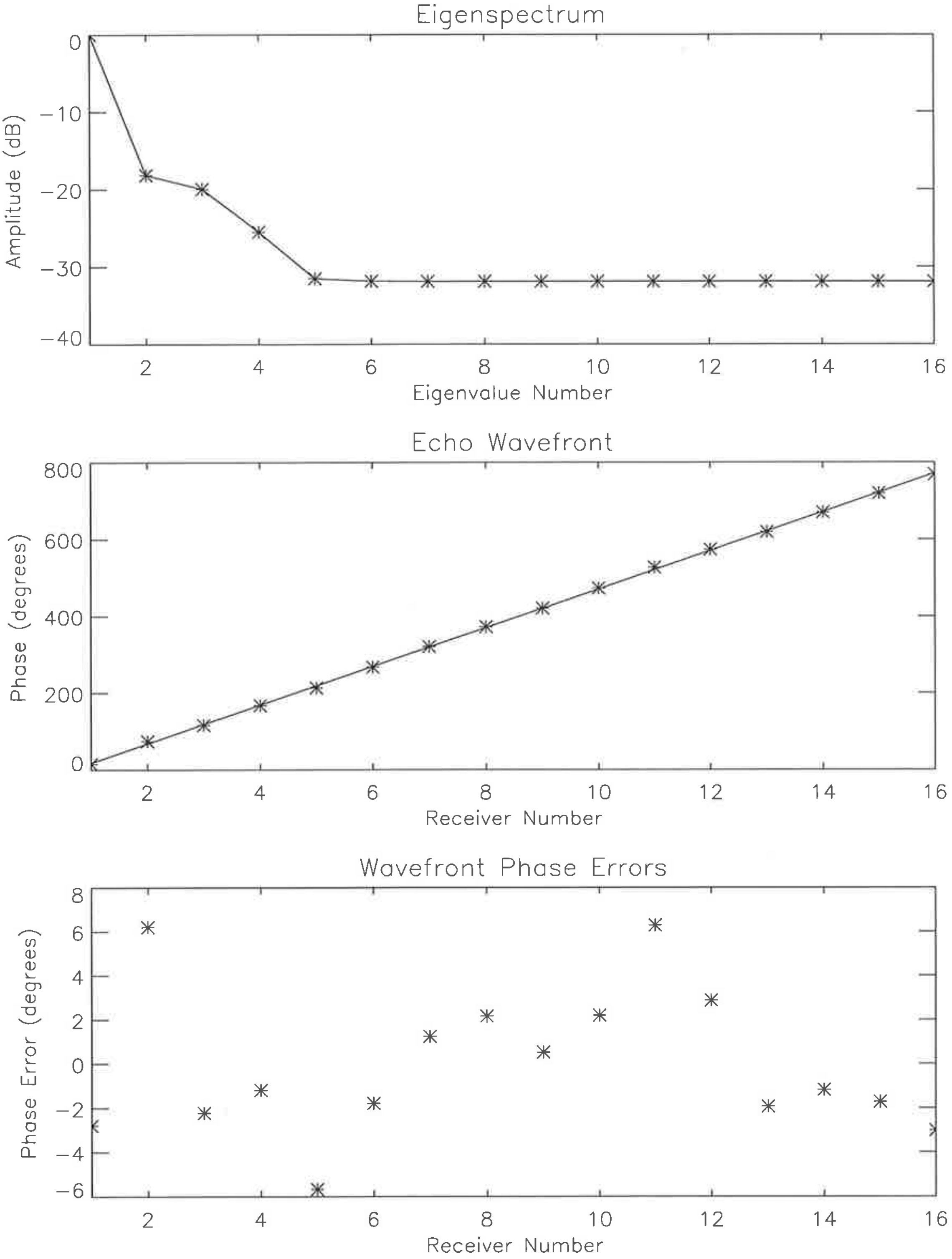

Figure 7.11: Example illustrating meteor echo wavefront analysis - (a) eigenspectrum for echo; (b) phase values of principal eigenvector ($*$) and straight line fit ($-$); (c) wavefront phase errors.

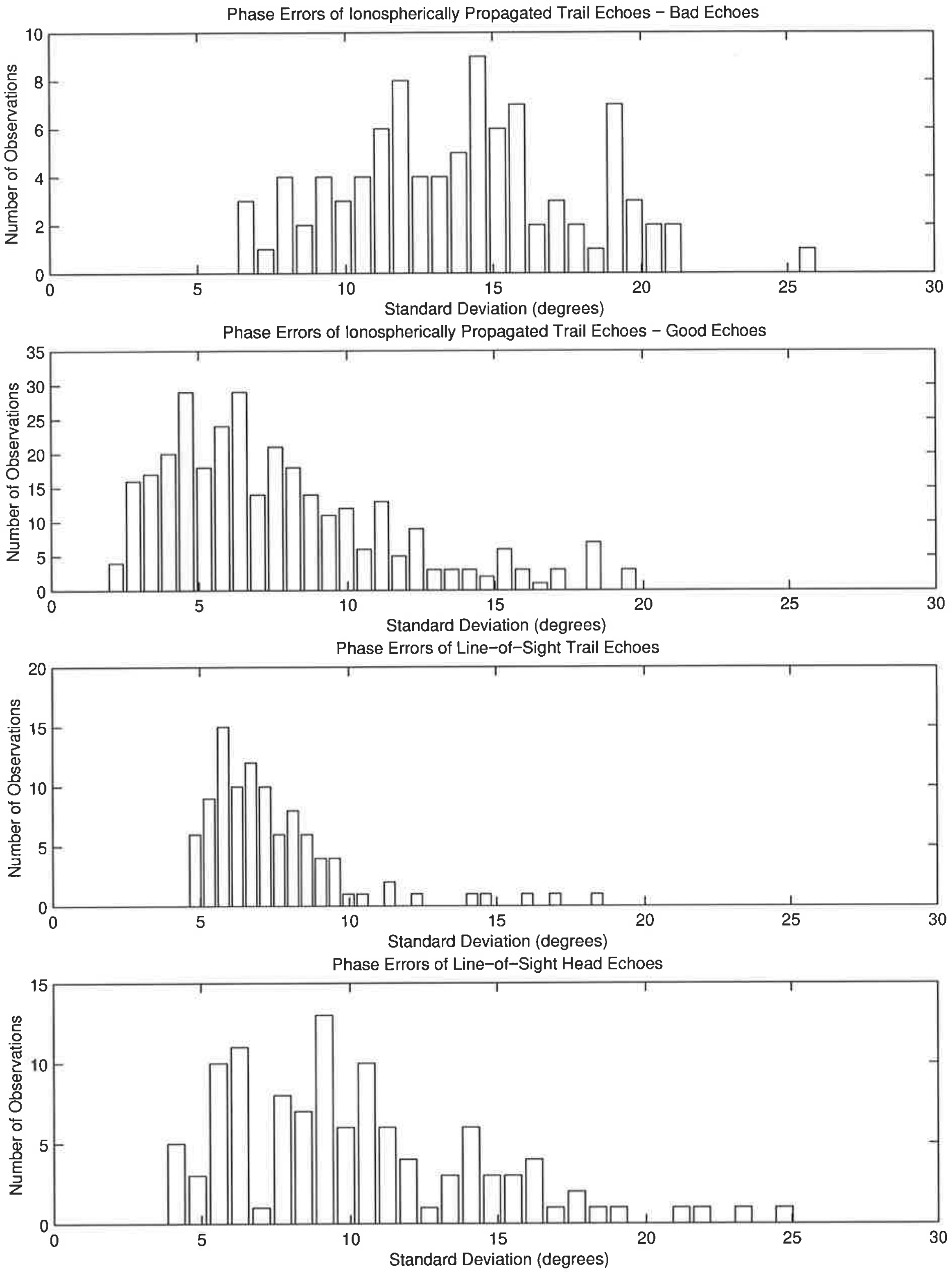

Figure 7.12: Wavefront phase errors for meteor echoes - (a) ionospherically propagated "bad" trail echoes; (b) ionospherically propagated "good" trail echoes; (c) line-of-sight trail echoes; (d) line-of-sight head echoes.

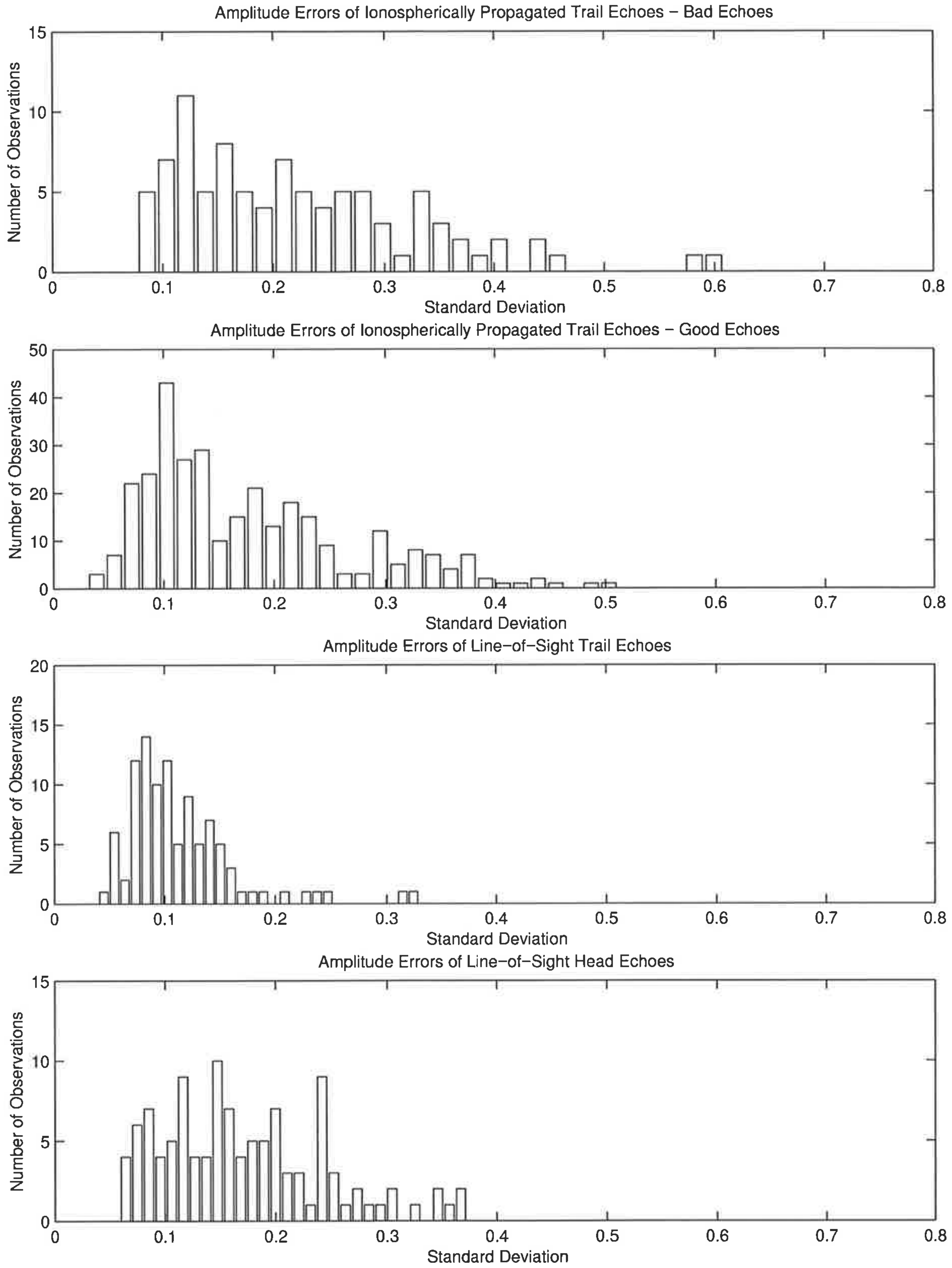

Figure 7.13: Wavefront amplitude errors for meteor echoes - (a) ionospherically propagated "bad" trail echoes; (b) ionospherically propagated "good" trail echoes; (c) line-of-sight trail echoes; (d) line-of-sight head echoes.

line) was fit to the wavefront phase values of these echoes (for obtaining the phase errors).

The fourth sub-plot in both figure 7.12 and 7.13 are for *line-of-sight head echoes*. These histograms have large spread, since only a single-snapshot is obtained for each echo. The phase errors are distributed around 10°, while the amplitude errors are distributed around about 0.18. Note for these *line-of-sight head echoes*, as in the case of *line-of-sight trail echoes*, a quadratic (instead of a straight line) was fit to the wavefront phase values (since these echoes originate from near-field meteors).

Theoretical results have been derived in [109] which give the standard deviations obtainable from sources with finite signal-to-noise ratio and snapshots. Given $T$ snapshots from a source of signal-to-noise ratio $SNR$, the standard deviation of the amplitude and phase errors are

$$\sigma_a = \sigma_\psi = \sqrt{\frac{2}{T(SNR)}} \tag{7.2}$$

where $\sigma_a$ is for a signal with mean amplitude of unity, and $\sigma_\psi$ is in radians. Hence for trail echoes, for a worse case situation where $T = 5$ (see below) and $SNR$ = 10 dB, the amplitude error standard deviation will be 0.2 and the phase error standard deviation will be 11.5°. Thus it can be concluded the wavefront errors, for both *ionospherically propagated "good" trail echoes* and *line-of-sight trail echoes*, are due only to both the limited number of snapshots and the finite signal-to-noise ratio of the echoes. Hence these echoes are suitable for array calibration. The *ionospherically propagated "bad" trail echoes* have wavefront errors which are due, not only to finite number of snapshots and finite SNRs, but in addition to ionospheric perturbation [55, 166, 79] of the wavefronts. These echoes are not expected to be suitable for array calibration.

Since only one snapshot is obtained from each *head echo*, the standard deviation (given in equation (7.2)) for amplitude errors is 0.45 and for phase errors is about 25°. The results in figure 7.12 and 7.13 indicate the wavefront errors of *head echoes* are due to finite signal-to-noise ratio and also due to only a single-snapshot being obtained from these echoes. Hence *head echoes* are suitable for array calibration.

Note the above results indicate that *ionospherically propagated meteor echoes* may be used as sources of opportunity for array calibration, when the propagation conditions are good. The quality of the propagation conditions can be assessed by investigating the quality of the ground/sea clutter : when single-mode clutter is present, and the clutter is narrow, the propagation conditions can in general be considered to be of good quality. Hence by operating

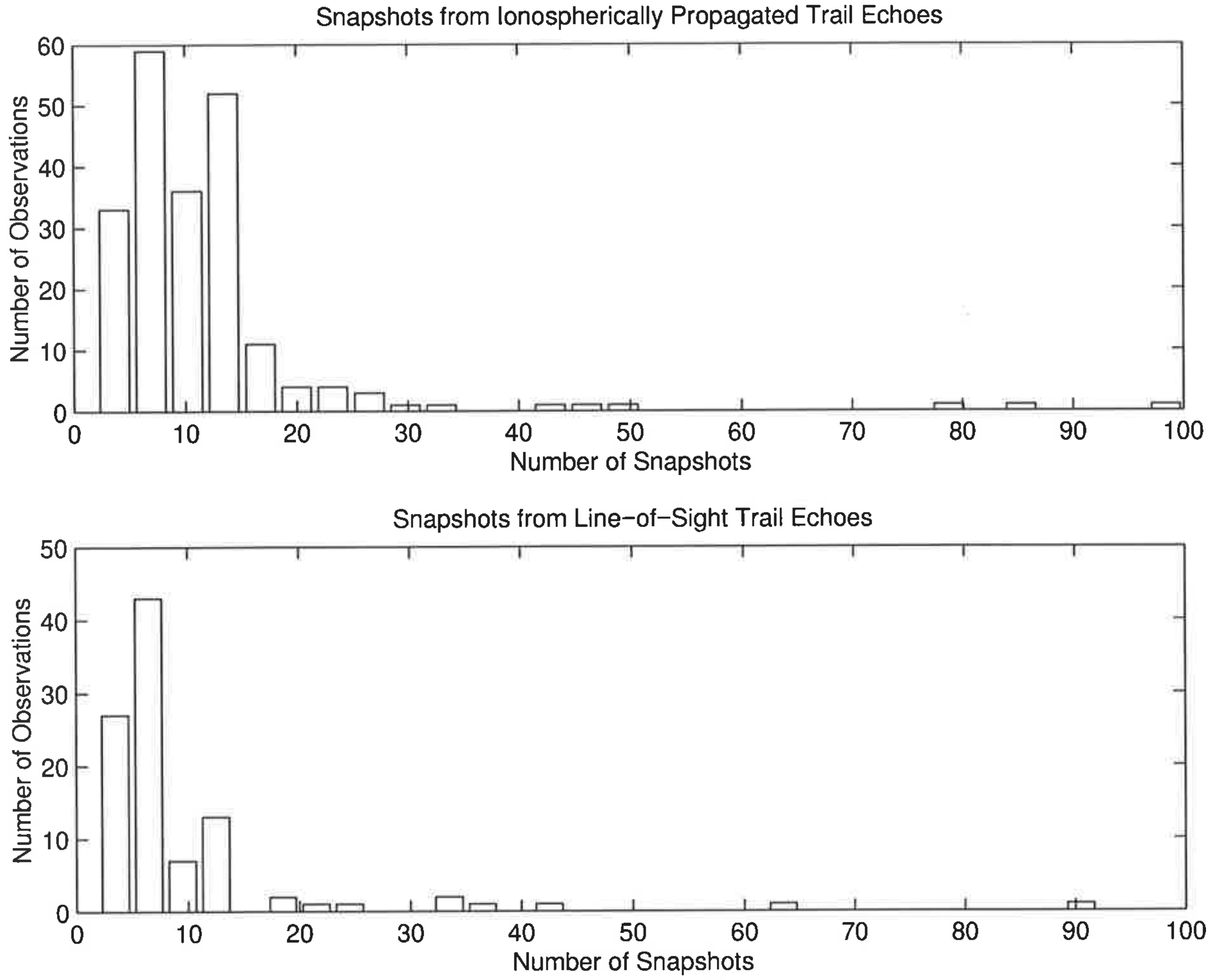

Figure 7.14: Histogram of number of snapshots obtained from meteor trail echoes - (a) ionospherically propagated echoes; (b) line-of-sight echoes.

the radar in a regime where the clutter observed is of good quality, one is likely to receive satisfactory ionospherically propagated meteor echoes.

The number of snapshots, which is proportional to the echo duration, used above to obtain the covariance matrix for each trail echo was noted. This is a useful statistic since it indicates the number of snapshots array calibration algorithms have, for estimating the unknown parameters. A histogram of the number of snapshots is shown in figure 7.14 for both ionospherically propagated and line-of-sight trail echoes. In most cases 5-10 snapshots are only obtainable.

Note the number of sources required for array calibration will dictate the duration for which the radar must be run to collect calibration data. This duration will be of the same order as a normal ship-mode dwell.

### 7.2.9 *Spatial Stationarity Analysis of Head and Trail Echoes*

The spatial stationarity of sources is of critical importance. If the source is spatially stationary then a covariance matrix can be estimated from the data, but if the source is spatially non-stationary then only snapshots of the source may be used for array calibration. In order to analyse the spatial behaviour of meteor echoes (over time) single-snapshot spatial processing was performed, which is possible due to the good SNRs many echoes posses. It was necessary however to first overcome the effects of signal correlation.

Correlation between signals impinging an array can destroy the spatial stationarity, and can affect spatial processing. It is well known that high resolution subspace techniques (such as that used below) perform poorly when signals are correlated [212, 186]. To overcome this, spatial smoothing can be performed [186]. Since the Jindalee receive array is a linear equally spaced array of similar elements, spatial smoothing is possible using a sliding window to estimate the covariance matrix.

The covariance matrix at time snapshot $t$, for a given range cell, is estimated as

$$\hat{\mathbf{R}}(t) = \frac{1}{M-K+1} \sum_{m=1}^{M-K+1} \bar{\mathbf{z}}_m(t)\bar{\mathbf{z}}_m^H(t) \tag{7.3}$$

where $\bar{\mathbf{z}}_m(t) = [z_m(t), z_{m+1}(t), ..., z_{m+K-1}(t)]^T$, $z_k(t)$ is the output of the $k$th receiver at time snapshot $t$ for the range cell considered, and $K$ is the sliding window length. The spatially smoothed MUSIC algorithm at time snapshot $t$, is obtained by eigendecomposing $\hat{\mathbf{R}}(t)$, and is

$$p_t(\theta) = \frac{1}{||\hat{\mathbf{U}}_t^H \mathbf{a}(\theta)||^2} \tag{7.4}$$

where $\hat{\mathbf{U}}_t$ is the estimated noise subspace of $\hat{\mathbf{R}}(t)$, and $\mathbf{a}(\theta)$ is the array steering vector. The temporal variation (i.e. over $t$) of a spatially smoothed MUSIC algorithm, for a single range cell, is here called a TSSM (Temporal-Spatial-Smoothed-Music) plot. Head and trail echoes are now analysed using TSSM plots.

Figure 7.15 shows two examples of TSSM plots. The power-time displays indicate that there are at least three underdense meteor trail echoes present. The TSSM plot shows horizontal lines for these echoes, indicating that these echoes have time-invariant DOAs, and so are spatially stationary. This is a property that one would expect from a meteor trail echo, since specular scattering from the ionised trail only occurs when the trail is orthogonal to the radar beam; so if the trail does not fluctuate in azimuth over time, then a time-invariant DOA echo will be

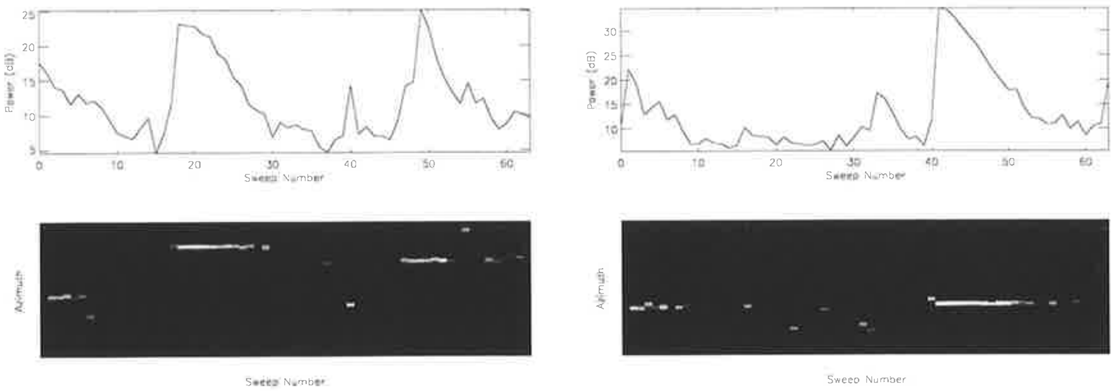

(a) (b)

Figure 7.15: Two examples of TSSM plots showing meteor trail echoes.

observed.

Figure 7.16(a) shows a range-time display, which contains a head and trail echo, definitely from the same meteoroid (it has a characteristic signature). Since the head echo has a varying Doppler (which reduces to zero at the same time the trail is formed), unlike the trail echo the head echo is observed in increasing range cells with time, and in only a few sweeps of each range cell. Figure 7.16(b)-(d) show the power-time plots and TSSM plots for three consecutive range cells.

In figure 7.16(b) the head echo is observed just before sweep 10. In figure 7.16(c) the head and trail echo are observed, at approximately the same azimuth, with the trail echo lasting for a few sweeps. In figure 7.16(d) the trail echo is stronger, exists for much longer, and clearly has a time-invariant DOA (as seen before). The DOA variation of the head echo was analysed over ranges and sweeps, and the TSSM plot in figure 7.16(e) was obtained, which illustrates the time-varying DOA [1] (and so the spatial non-stationarity) of this head echo. Note that the head echo was not as strong as the trail echo (compare figure 7.16(d) and figure 7.16(b)), as is normally the case. It should be mentioned that Thomas et. al. have also observed meteor head echoes using the Jindalee radar [221], not using high resolution spatial processing, but rather via conventional Fourier techniques.

These observations have been made in numerous data sets, obtained under single-mode propagation conditions. Note the algorithm in chapter 5 was developed to work with both spatially stationary sources (such as trail echoes) and spatially non-stationary sources (such as

---

[1] for a meteor which is 100 Km from the radar and travelling tangential to the radar's beam at 40 Km/s, the DOA of the head echo will vary by about 5° in a typical (ship-mode) sweep duration of 0.25 seconds.

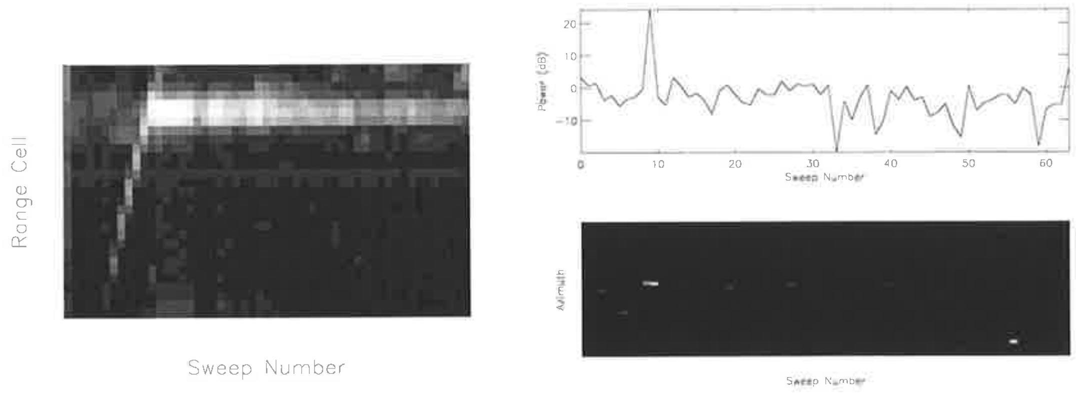

(a) range variation over time

(b) TSSM plot for a particular range cell

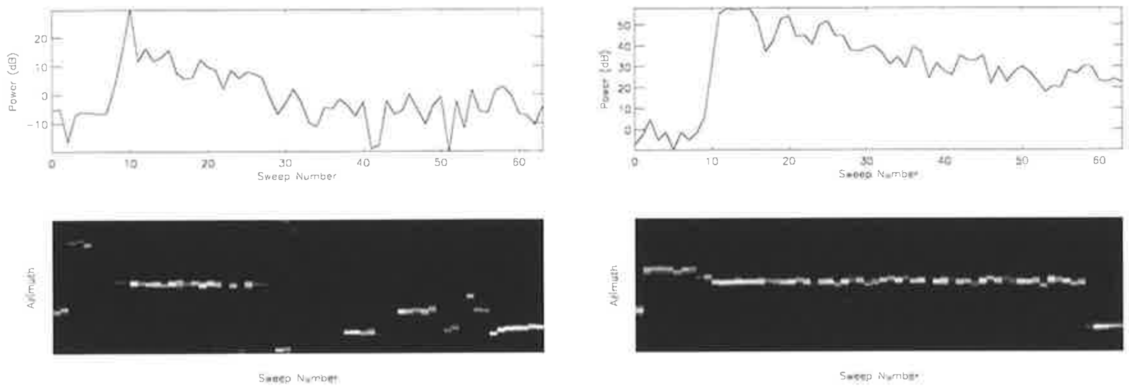

(c) TSSM plot for a particular range cell

(d) TSSM plot for a particular range cell

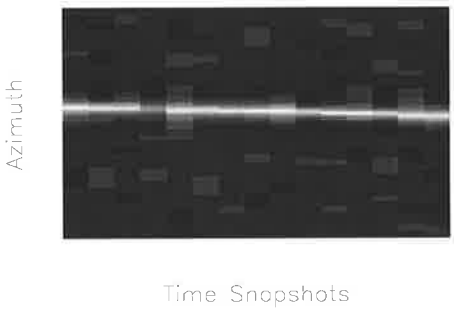

(e) TSSM plot showing time-varying DOA for head echo

Figure 7.16: Meteor head-trail echo pair.

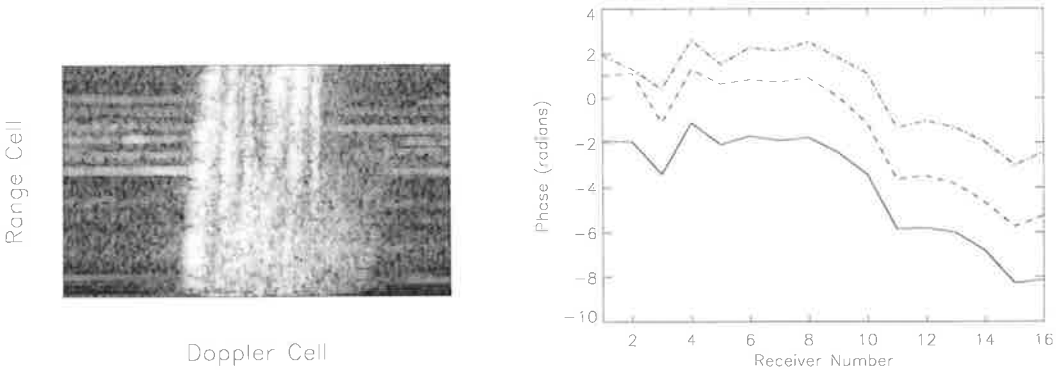

(a) ship data

(b) phase variation

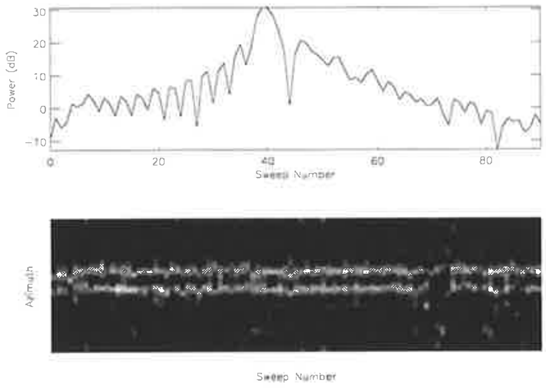

(c) TSSM plot

Figure 7.17: Multimode ionospheric propagation conditions.

head echoes); the algorithm in chapter 4 was developed specially for the spatially stationary trail echoes.

### 7.2.10 Multimode Echoes

During the night time, multiple ionospheric layers are often present. As shown in figure 7.1 two of the ionospheric layers are denoted as the E and the F layer. Under such multimode ionospheric propagation conditions multiple Bragg-line pairs are often observed in ship-mode data, when the E and F layers rise/fall at different rates. An example of this is shown in figure 7.17(a). The meteor echoes present in this data were analysed to investigate their wavefronts.

The phase variation across the aperture of a typical echo, for three snapshots, is shown in figure 7.17(b). The wavefront is crinkled, but the wavefront at each snapshot is a shifted version of the others. This could perhaps mean that one signal is present with a crinkled wavefront, or that multiple overlapped (correlated) signals are present.

Figure 7.17(c) shows the TSSM plot for this echo which illustrates that not only is a trail echo present (time-invariant DOA), but that this echo consists of two plane wavefront (localised in azimuth) signals. The distinct DOAs are believed to be due to the array coning effect; where different DOAs are observed by a linear array for signals emanating from the same azimuth, but from different heights. Some of the backscattered energy reaching the radar has been reflected by the E layer, while the rest has been reflected by the F layer; hence the reason for the number of signals observed being two.

Many observations have been made of two DOAs under multimode ionospheric propagation conditions. On some occasions two DOAs were observed even when only a single Bragg-line pair was present in the ship-data, since when the E and F layers rise/fall together (at the same velocity) only a single Bragg-line pair is observed even though multimode ionospheric propagation conditions may exist. The algorithm detailed in chapter 5 was developed to work with multimode meteor echoes.

## 7.3 External Noise

Some of the different types of noise present in the HF environment (as given in [79]), and the HF noise statistics obtained by Ward in [240], are outlined in this section. Noise at HF consists of atmospheric, galactic and man-made noise [79]. An example of HF noise observed by the Jindalee OTH radar, is shown in figure 7.18(a). The noise is strongest in finger beam 6 and 7, and is seen to be present in all range-Doppler cells of these beams.

Atmospheric noise is caused mainly by lightning strikes, resulting in broadband noise during thunderstorms. Atmospheric noise can propagate over large distances beyond line-of-sight; major contributors to the atmospheric noise level being from the opposite hemisphere or from across the day-night terminator. Galactic (or cosmic) noise has its origin outside the ionosphere, but since it has to penetrate the ionosphere for the signals to be received on earth the ionosphere influences the noise received.

Man-made noise is influenced by both the density and technological sophistication of the population. Coherent transmitters are the strongest class of man-made noise, and are present in broadcasting, aerospace/land/maritime, mobile-radio, fixed-point communication, radio navigation and meteorological monitoring. Coherent transmitters are always present or present for long durations. Other classes of man-made noise are : devices which provide localised control and communication functions; out of band emissions from Industrial, Scientific and Medical

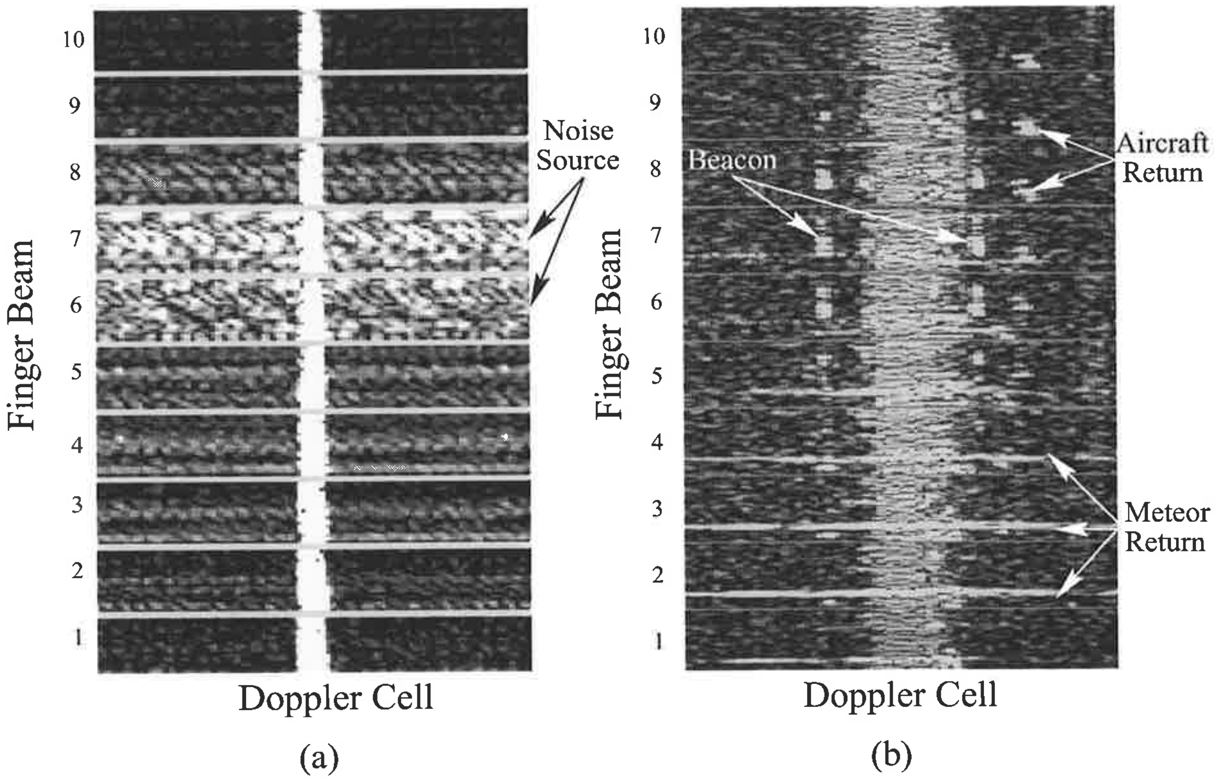

Figure 7.18: Jindalee data showing sources in the HF environment : (a) noise source; (b) beacon, aircraft return and meteor return.

(ISM) equipment; and incidental electrical/electromechanical radio-noise sources. Note for example ISM devices have been observed providing HF signals as high as 30 dB above the noise floor [232].

### 7.3.1 Suitable Noise Sources

Of all noise sources, it is expected that only man-made noise sources, of narrow bandwidth and with sufficient power levels, can be used for array calibration. Further, for ionospherically propagated noise it is only expected that noise propagating through a well behaved ionosphere can be used

In section 7.2.8 it was mentioned that if the radar clutter is of good quality, in a particular region, then scattered signals from meteors in that region may be used for array calibration; so choosing appropriate meteor echoes is easily done, since radars can estimate the range (and azimuth) from which meteor echoes emanate. The range from which noise signals emanate cannot however be estimated directly by radars, hence making the selection of appropriate noise sources for array calibration difficult.

Indirect methods for determining the location of noise sources however exist. In the case of audio coherent transmissions one can listen to the noise source, using a short-wave receiver connected to the radar antennas, and determine if the noise source can be identified as a coherent transmission originating from a known location. In the case of non-audio signals, one can determine if the signal signature received is known to be from a noise source in a known location. This could be implemented by correlating received signals, possessing adequate power levels, with signal signatures stored in memory.

### *7.3.2 HF Noise Statistics*

Some statistical results on HF coherent transmissions from a study conducted by Ward [240], are now outlined. This study was on the HF signal environment at Alice Springs (Australia). Ward presented results on the signal powers and the SNR distribution (ratio of strong signals to the level of atmospheric noise). The HF bands he considered were broadcast, maritime, aeronautical, fixed, amateur and radioastronomy. He observed large spread in the signal powers, over any typical month, and said the large spread reflects the changes in propagation conditions with time of day. The strongest signals at low frequencies were observed in the night time, due to the large attenuation of low frequencies during the day. High frequency signals do not propagate far during the night and hence the strongest high frequency signals were observed during the day.

Broadcast bands had the biggest percentage of strong signals, but large numbers of strong signals existed in the fixed service bands (some of which were broadcast stations operating adjacent to the international broadcast bands). The largest SNR distribution was observed in the broadcast bands, particularly at 7, 9, 11, 15 and 17 MHz. Signals with SNR as high as 50-80 dB were seen to occur, with the proportion of signals with such SNRs being as high as 20 percent (in some occasions). At frequencies over 20 MHz, a large proportion of the frequency spectrum was free from strong signals.

The above results indicate there should be a good number of strong noise sources for array calibration. However as mentioned earlier, since sources for array calibration must propagate via a well behaved ionosphere, the number of noise sources that can be used will be much less than that indicated here.

## 7.4 Other Sources

Beacons are special sources, located in the radar's coverage, that are used for calibrating a radar. Figure 7.18(b) shows a beacon, observed by the Jindalee OTH radar; the beacon being clearly observed in finger beams 6, 7 and 8. Beacons have three significant advantages over all other sources. Firstly the signal parameters of the beacon (signal-to-noise ratio and duration of signal) can be controlled. Secondly the location of the source is known, and can be placed in a location of choice. Thirdly, in the case of repeaters at least, returns are observed for all frequencies. Note, while for skywave returns, the location of the beacon may not imply that the DOA of the source is known, it may still provide a good nominal DOA value.

Beacon signals via surface-wave mode may also be used for array calibration. While such beacon signals may imply the beacon has to be in the radar's near-field, this does not matter since the location of the beacon is known; so the beacon's steering vector can be specified in terms of the array parameters. Note also for surface-wave radars, located near the sea, the beacon may be placed behind the radar if a reversible array is used or if the radar's "front-to-back" antenna ratio is not substantial.

Strong scattered returns from ships, aircraft, vehicles etc may also be used. These signals may propagate via either surface-wave or skywave modes. If the signal reaches the radar via surface-wave mode and the location of the source is known, then as for beacons, the source can be used for array calibration even if it is located in the near-field of the radar. Figure 7.18(b) shows an aircraft return in finger beams 8 and 9.

## 7.5 Jindalee Array Calibration

The Jindalee radar's receiving antenna array has no significant mutual coupling and the positions of the antennas are very accurately located in their designed positions. Amplitude (gain) and phase mismatch/errors however exists between the receivers, over the passband of each receiver and between the unequal length cables which connect the antennas to the receivers. To compensate for this mismatch, the Jindalee radar's receiving array is calibrated using an internal signal which is injected via equal length "calibration cables" to each of the receivers [115, 103]. The result of this calibration is a "calibration table", which is applied to data received by the array, to obtain well calibrated radar data.

The calibration table is a two-dimensional array of complex weights. Weights are stored for each receiver - range cell pair. The variation of the weights over the range cells, for a given receiver, is a result of variation in the gain/phase of the receiver frequency response over its passband and attenuation/delays in the cable. The variation of the weights over the receivers, for a given range cell, is due to gain/phase mismatch between the different receivers and also due to variations in attenuation/delays between the unequal length cables.

An example of the calibration weights for a receiver, as a function of range cells, are shown in figure 7.19. The amplitude variation in figure 7.19(a) is flat except for the early range cells. This is because the receiver's gain response is flat within the passband, and drops off rapidly before and after the passband. The early range cells have been obtained from just prior to the receiver's passband, and hence the amplitude of the calibration weights need to be high to compensate for the low gain in this region. The phase variation of the calibration weights, shown in figure 7.19(b), is fairly linear over the range cells.

The calibration weights for a range cell, as a function of receiver number, are shown in figure 7.20. The amplitude variation shown in figure 7.20(a), indicates that some variation is observed, with the amplitude of receiver number two and four being somewhat different from the others. The phase, shown in figure 7.20(b), has large variation since the cables are nominally of different lengths.

### 7.5.1 Calibration over Receivers

In order to see if meteor echoes can be used to perform array calibration for the Jindalee OTH radar, some data collected on day 297 in 1986 was analysed. This data was collected at 14.8 MHz and at ranges of about 1000-2000 Km from the radar. Nine dwells from 05:21 UT to 05:29 UT were analysed, and thirty three ionospherically propagated meteor trail echoes obtained. This data was calibrated only over the range cells, using the standard Jindalee calibration weights; calibration over the receivers was not performed, since the calibration weights over the receivers are to be estimated using the meteor echoes.

In order to estimate these calibration weights, the principal eigenvector of the covariance matrix of a selected echo (of SNR 23dB and 10 snapshots), was used. The covariance matrix was estimated by averaging the array receiver outputs over all range-time samples for which the meteor echo was present. The estimated calibration weights are then simply the inverse of the principal eigenvector element values i.e. the estimated calibration weights are $w_k = 1/v_k$, where $v_k$ is the $k$th element of the principal eigenvector.

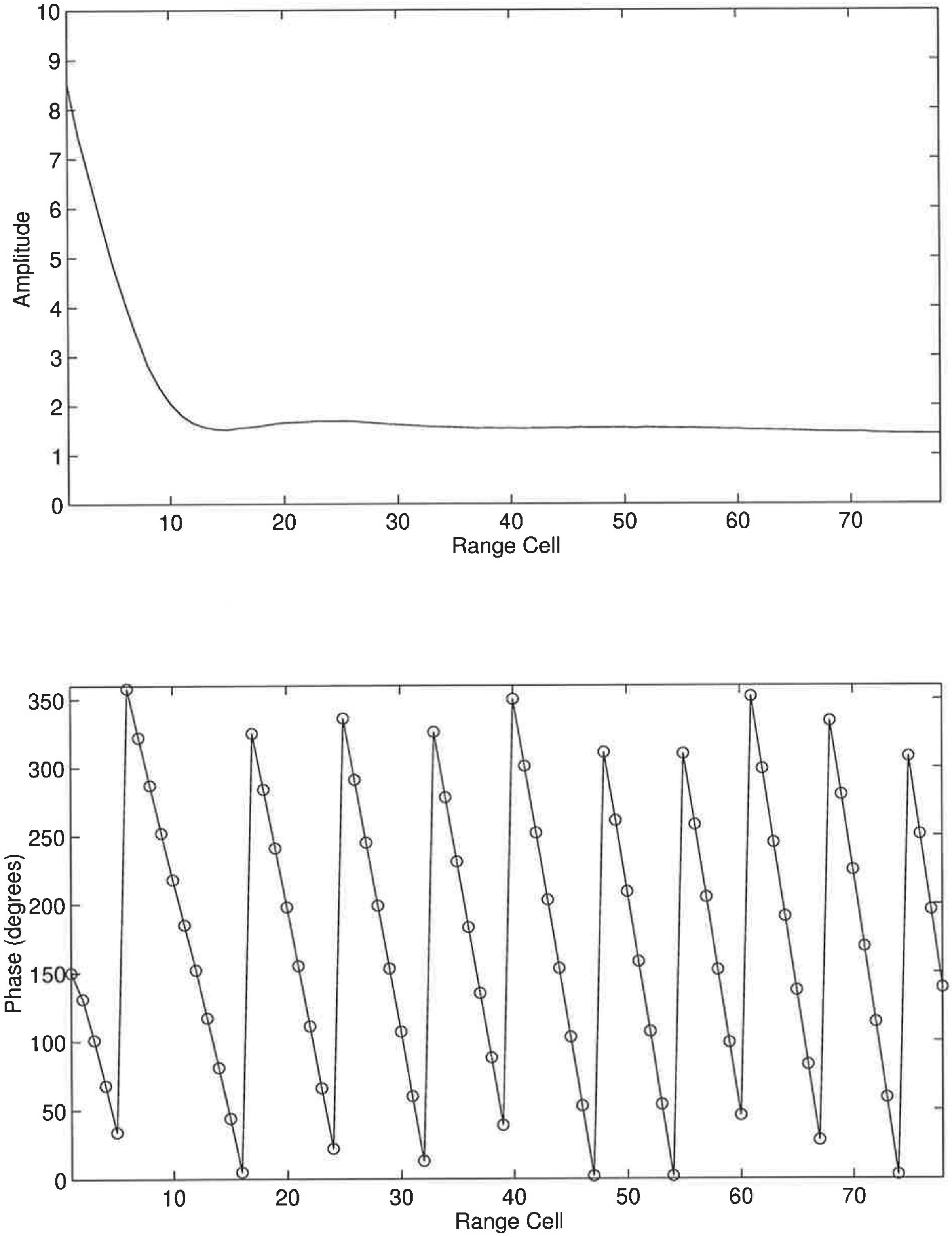

Figure 7.19: Jindalee calibration weights versus range, for a particular receiver.

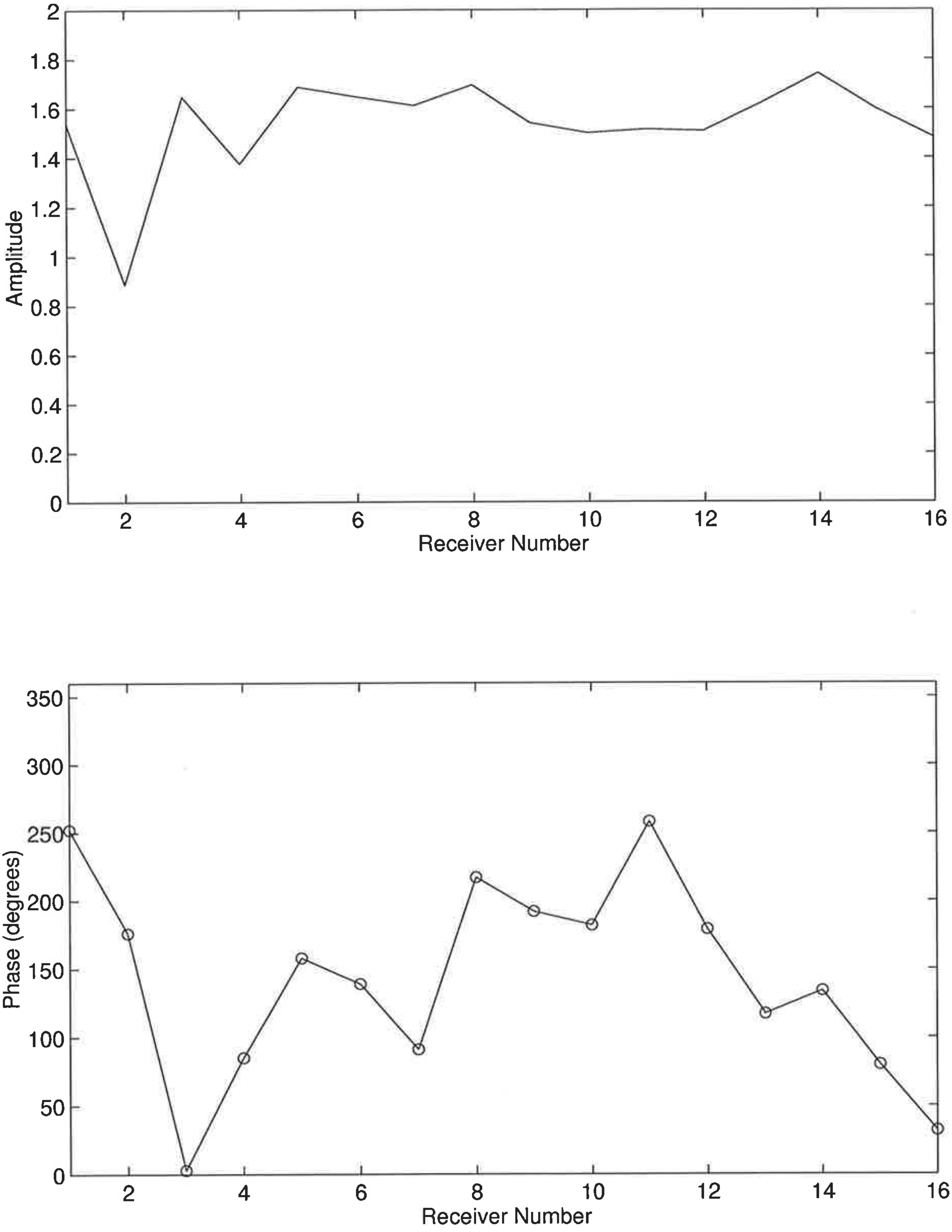

Figure 7.20: Jindalee calibration weights versus receiver number, for a particular range.

### 7.5.2 Performance Determination

The estimated calibration weights (+) together with the standard calibration weights (o), are as shown in figure 7.21. The amplitude comparison shown in figure 7.21(a), indicates that the estimates are fairly close, the biggest difference being for receiver number three and twelve. The phase comparison is shown in figure 7.21(b), which indicates the estimates are good.

To further compare the calibration weights the sidelobe levels, achieved when the array is calibrated over the receivers using the standard and estimated calibration weights, were determined. The other thirty two echoes present during this period were used as sources for measuring the sidelobe levels (gain/phase variation over this 10 minute interval will be minimal). A Hamming window was used to weight the receiver outputs, and then the average and peak sidelobe levels were calculated for each echo when a beam was digitally steered over azimuth. Since the Jindalee sidelobe levels are classified, the difference in the sidelobe levels for the standard calibration weights and the estimated calibration weights is considered.

The sidelobe level difference for each of the thirty two echoes are shown in figure 7.22. For the average sidelobe level, the difference is at most 1.5 dB and at worst -3 dB. For the peak sidelobe level, the difference is at most 1.5 dB and at worst -3.5 dB.

Figure 7.23 shows the results obtained when twenty different echoes were each separately used to calibrate the radar. The sidelobe level differences are given, for both the peak and average sidelobe levels, from ten separate echoes present during this period. The SNRs of the echoes used to calibrate varied from 10 dB to about 25 dB; better results being obtained for the stronger echoes. These results indicate that the average/peak sidelobe levels are in most cases within 2 dB of the standard calibration approach.

## 7.6 Conclusion

The propagation modes by which HF radar may obtain head/trail echoes, the difference between shower and sporadic meteors, the effect of radar frequency on echo rates observed, and the diurnal variation of echo rates, have been described. Analysis of head/trail echo wavefronts was conducted, which illustrated that often these echoes can be used as sources of opportunity for array calibration. Trail echoes, which can be considered as disjoint sources, were found to be present in most cases for 5-10 snapshots. The spatial stationarity of head/trail echoes was examined; trail echoes being found to have time-invariant DOAs, while head echoes in general had time-varying DOAs. Under multimode propagation conditions, multiple correlated signals

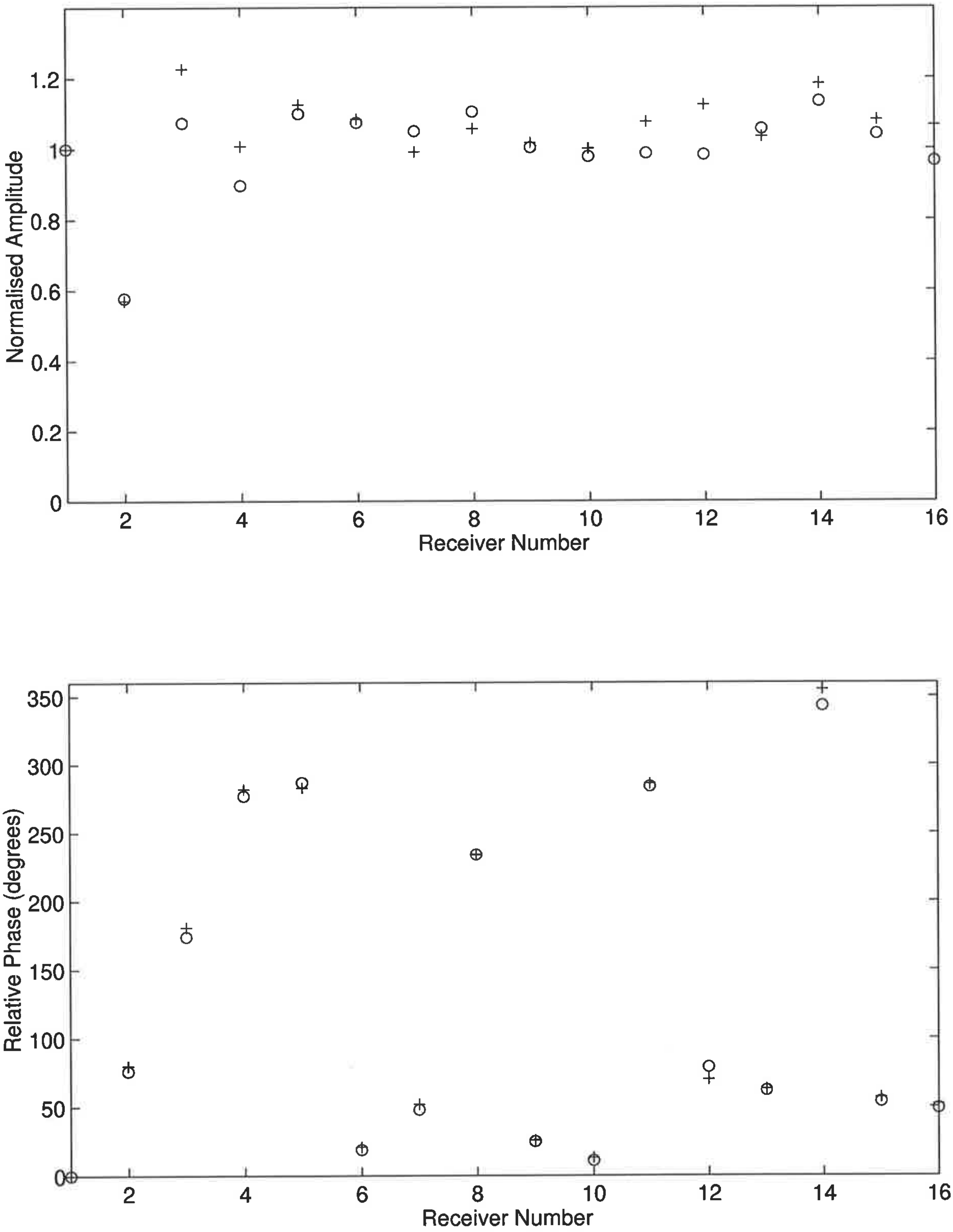

Figure 7.21: Actual (o) and estimated (+) calibration weights.

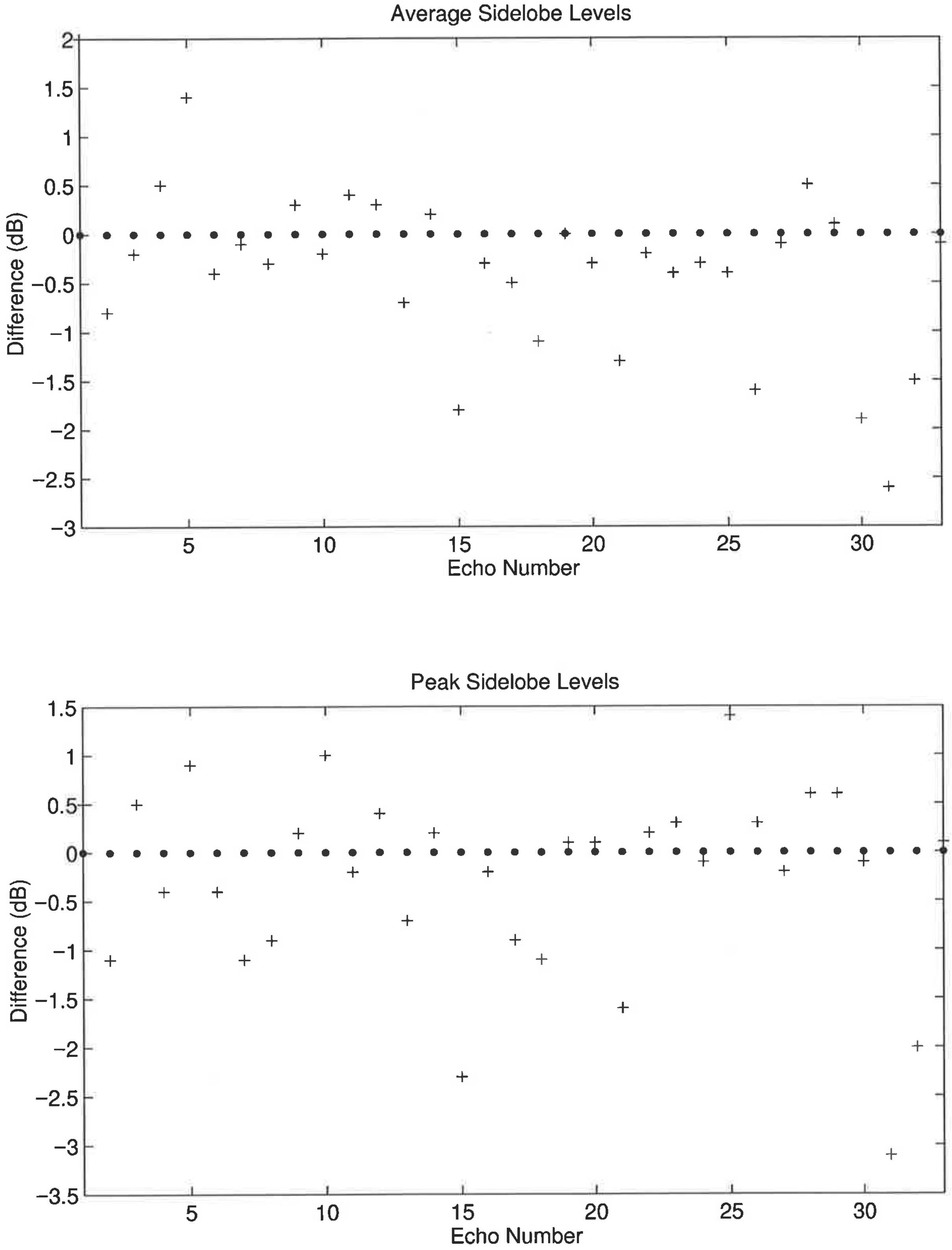

Figure 7.22: Average and peak sidelobe level difference (+) between the two methods. Positive difference values indicate calibration using meteor echoes is better.

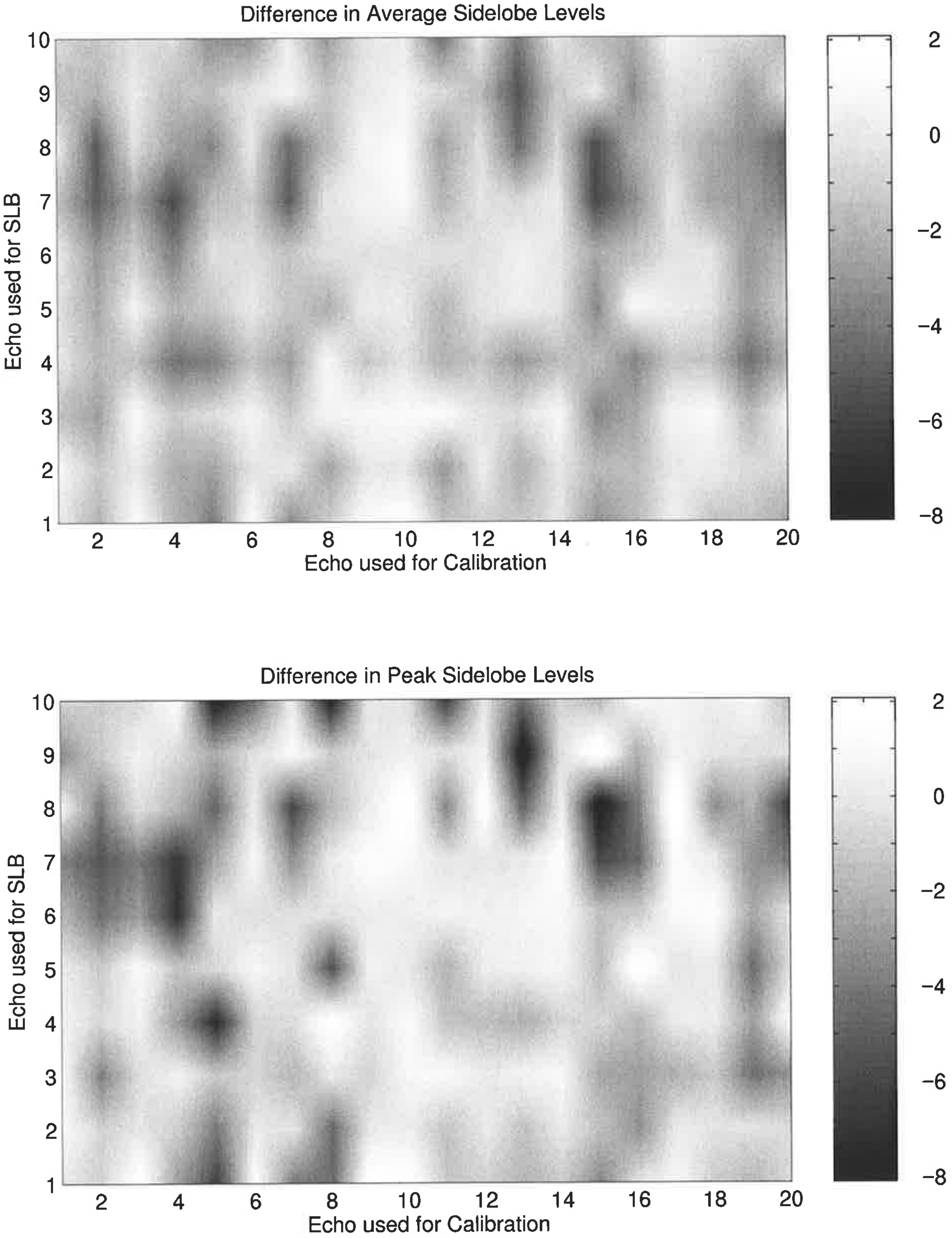

Figure 7.23: Comparison between the methods - statistical performance. Positive difference values indicate calibration using meteor echoes is better.

(with distinct DOAs) were observed for meteor echoes.

Different types of noise sources present in the HF environment, some HF noise statistics, and methods for determining the suitability of noise sources for array calibration, were discussed. The properties of beacons, and other possible sources for array calibration, were also outlined.

Array calibration using meteor echoes was investigated, using the Jindalee OTH radar. The results obtained indicate that array calibration using meteor echoes has been almost as good as the standard calibration (using a special signal injected via cables to the receivers). Since it is known that the standard calibration of the Jindalee OTH radar is good, it is clear that one has been very successful in calibrating this radar.

# CHAPTER 8

# Conclusion

In this chapter the thesis is concluded. An overview of the thesis, an outline of the main contributions, and a description of future work that could be performed, are given.

## 8.1 Overview and Contributions

Modern OTH radar receiving arrays, which are being designed to be rapidly relocated, require accurate array calibration. In this thesis, the effect of array model errors on the performance of such radar arrays has been determined, and signal processing algorithms have been developed (and tested) to correct for these imperfections using sources in the HF environment.

In **chapter 3** the effect of array model errors on the performance of OTH radar arrays was analysed. The effect of gain/phase mismatch between the receivers, sensor position errors and mutual coupling between the antenna elements, were considered. The performance degradation in the signal-to-noise ratio, array gain, bearing estimation and array sidelobe levels, were obtained in terms of the standard deviation of the model errors. The main degradation was the array sidelobe levels, which was shown to cause the sub-clutter visibility (and so target detectability) to be degraded when non-stationary interferers were present. In this chapter it was concluded that array calibration was necessary so the array sidelobe levels could be improved. **The main contributions were : (a) obtaining the performance degradations in terms of the model error standard deviations; (b) showing that model errors could degrade target detectability in the HF radar scenario.**

In **chapter 4** a signal processing algorithm was developed for using disjoint (single-mode) sources (such as meteor trail echoes) to estimate sensor position errors and mutual coupling. This algorithm was obtained by modifying and extending a method proposed in the literature by Weiss and Friedlander. The new algorithm was analysed for a variety of scenarios, using simulations, and found to perform well. Also in this chapter performance criteria were proposed for determining in practice if an array calibration algorithm has been successful, and the error surface for this algorithm was analysed. **The main contribution was developing an array calibration algorithm, for utilising echoes from meteor trails, to estimate sensor position errors and mutual coupling.**

In **chapter 5** a signal processing algorithm was developed for using disparate sources, present in the HF environment, to estimate sensor position errors and mutual coupling. Unlike the algorithm in chapter 4, which uses disjoint sources, the algorithm developed in chapter 5 can use (non-disjoint) sources present in different disjoint clusters. Further the algorithm in chapter 5 can use multimode and near-field sources (in addition to single-mode sources), sources with time-varying or time-invariant bearings, and the bearing of each source may be either known or unknown. The algorithm was analysed using simulations, and its performance was found to be good. Also in this chapter the performance of the algorithm was investigated for the case (considered in chapter 4) where all sources are disjoint (and single-mode), and found to compare well with the performance of the algorithm in chapter 4. The chapter ends with an analysis of the algorithm's error surface. **The main contribution was the development of an array calibration algorithm, for using disparate sources, to estimate sensor position errors and mutual coupling.**

In **chapter 6** the theoretical Cramer-Rao lower bound was determined for each of the problems considered in chapter 4 and 5, and the algorithms were found to achieve the corresponding bound. The variation of the bound with signal-to-noise ratio, number of snapshots, number of sources, etc, was investigated; the results obtained indicate that the problems are well defined, and that good accuracy can be achieved in estimating the unknown parameters. **The main contribution was the determination of the Cramer-Rao lower bounds for the array calibration problems considered in chapter 4 and 5.**

In **chapter 7** sources present in the HF environment were considered from an array calibration perspective. Scattered echoes from meteor trails were shown to be excellent sources of opportunity for array calibration : these sources in general have planar wavefronts at the ranges of interest, are received in large numbers over the entire HF band, are disjoint sources, have sufficiently high SNRs, and are of adequate duration for sufficient number of snapshots to be obtained for array calibration. Meteor head echoes were also shown to be good sources of opportunity, and their properties along with that of other sources (beacons and noise sources) were outlined. Array calibration was performed on the Jindalee OTH radar's receiving array using ionospherically propagated echoes from meteor trails; amplitude and phase errors being calibrated, and results obtained were found to compare well with those for the standard (expensive) Jindalee calibration. **The main contributions were showing that the spatial properties of meteor head and trail echoes allow them to be used for OTH radar array calibration, and demonstrating that meteor trail echoes can be used to calibrate the amplitude and phase errors in the Jindalee radar's receiving array.**

In the **appendices** the array weighting required to obtain minimum sidelobe levels for a two-dimensional array with known mutual coupling is first given. Next a theoretical analysis of the Cramer-Rao lower bound is conducted, for the problem of mutual coupling only estimation. Finally error surface theoretical expressions are derived, for the analysis presented in chapter 5. **The main contributions were obtaining both the identifiability conditions and theoretical Cramer-Rao lower bound variance expressions, in the mutual coupling only estimation problem.**

## 8.2 Future Work

The algorithms developed need to be analysed, using real data collected from an OTH radar receiving array with both sensor position errors and mutual coupling. The emphasis should be placed on using meteor trail echoes for performing array calibration, but other sources should also be examined since in practice if other sources are present they should also be used if possible.

In particular note :

- different combinations of position errors should be considered;
- different array geometries should be considered;
- array calibration should be attempted at several frequencies in the HF band, since the coupling matrix varies with frequency;
- performance criteria proposed in section 4.8 should be investigated.

Also it should be investigated how well coupling matrices estimated at a given frequency are in calibrating the radar at other frequencies in the HF band. The coupling matrix estimated at one frequency may have to be modified in some manner for it to be appropriate for calibrating the radar at other frequencies. This modification may need to be obtained from modelled information or previous results.

# APPENDIX A

# Sidelobes for 2-D Array with Mutual Coupling

The optimal array weights for a two-dimensional array with mutual coupling, are now derived; the criterion considered being minimum average sidelobe levels. The determination of the optimal weights, for the sensor positions and coupling matrix estimated, enables the sidelobe levels (obtainable using these estimates) to be determined.

Let $\hat{\mathbf{a}}(\phi)$ be the steering vector formed using the estimated sensor positions, and let $\hat{\mathbf{C}}$ be the estimated coupling matrix. The total sidelobe power expected, for the beam steered in direction $\theta_o$, is

$$p = \int \left\|\mathbf{w}^H(\theta_o)\hat{\mathbf{C}}\hat{\mathbf{a}}(\phi)\right\|^2 \cos\phi \, d\phi \tag{A.1}$$

where the range of the integral is over the sidelobe region. Equation (A.1) can be re-written as

$$p = \mathbf{w}^H(\theta_o)\hat{\mathbf{C}}\int \hat{\mathbf{a}}(\phi)\hat{\mathbf{a}}^H(\phi)\cos\phi \, d\phi \, \hat{\mathbf{C}}^H\mathbf{w}(\theta_o) \tag{A.2}$$

$$p = \mathbf{w}^H(\theta_o)\hat{\mathbf{C}}\mathbf{K}\hat{\mathbf{C}}^H\mathbf{w}(\theta_o) \tag{A.3}$$

where $\mathbf{K} = \int \hat{\mathbf{a}}(\phi)\hat{\mathbf{a}}^H(\phi)\cos\phi \, d\phi$.

Now $p$ has to be minimised subject to the constraint that the gain in the look direction is one, i.e. $\mathbf{w}^H(\theta_o)\hat{\mathbf{C}}\hat{\mathbf{a}}(\theta_o) = 1$. Substituting $\mathbf{u}^H(\theta_o) = \mathbf{w}^H(\theta_o)\hat{\mathbf{C}}$, ($\mathbf{u}(\theta_o) = \hat{\mathbf{C}}^H\mathbf{w}(\theta_o)$) into (A.3) gives

$$p = \mathbf{u}^H(\theta_o)\mathbf{K}\mathbf{u}(\theta_o) \tag{A.4}$$

with the constraint $\mathbf{u}^H(\theta_o)\hat{\mathbf{a}}(\theta_o) = 1$. Using Lagrange multipliers this is solved by defining

$$f = \mathbf{u}^H(\theta_o)\mathbf{K}\mathbf{u}(\theta_o) + \lambda_l(1 - \mathbf{u}^H(\theta_o)\hat{\mathbf{a}}(\theta_o)) + \lambda_l(1 - \hat{\mathbf{a}}^H(\theta_o)\mathbf{u}(\theta_o)) \tag{A.5}$$

Then the derivative of $f$ with respect to $\mathbf{u}$ is taken,

$$\frac{df}{d\mathbf{u}} = 2\mathbf{K}\mathbf{u}(\theta_o) - 2\lambda_l\hat{\mathbf{a}}(\theta_o) \tag{A.6}$$

Setting this to zero,

$$\mathbf{u}(\theta_o) = \lambda_l\mathbf{K}^{-1}\hat{\mathbf{a}}(\theta_o) \tag{A.7}$$

But also $\mathbf{u}^H(\theta_o)\hat{\mathbf{a}}(\theta_o) = 1$, and so (since $(\mathbf{K}^{-1})^H = \mathbf{K}^{-1}$) one obtains

$$\mathbf{u}(\theta_o) = \frac{\mathbf{K}^{-1}\hat{\mathbf{a}}(\theta_o)}{\hat{\mathbf{a}}^H(\theta_o)\mathbf{K}^{-1}\hat{\mathbf{a}}(\theta_o)} \tag{A.8}$$

Hence the optimal weights are

$$\mathbf{w}(\theta_o) = \frac{\left(\hat{\mathbf{C}}^H\right)^{-1}\mathbf{K}^{-1}\hat{\mathbf{a}}(\theta_o)}{\hat{\mathbf{a}}^H(\theta_o)\mathbf{K}^{-1}\hat{\mathbf{a}}(\theta_o)} \tag{A.9}$$

The array beampattern is

$$B_{\theta_o}(\phi) = \left\|\mathbf{w}^H(\theta_o)\mathbf{v}(\phi)\right\|^2 \tag{A.10}$$

where $\theta_o$ is the steer direction of the beam, $\phi$ is the signal direction considered, $\mathbf{v}(\phi)$ is the actual steering vector including the effects of mutual coupling i.e. $\mathbf{v}(\phi) = \mathbf{C}\mathbf{a}(\phi)$. The sidelobe levels can then be calculated.

# APPENDIX B

# Mutual Coupling Estimation using a Single Source

The Cramer-Rao lower bound (CRLB) is derived here, for the problem of mutual coupling only estimation using a single-mode source. In order to obtain theoretical expressions for the CRLB, a 2-element array is considered, and it is assumed that the coupling matrix is Toeplitz (to simplify the problem). One sensor is arbitrarily placed at the origin (0,0), and the other sensor is arbitrarily placed along the $x$-axis; hence the second sensor is at ($x$,0). The first element of the coupling matrix is arbitrarily chosen to be one. The coupling matrix is then

$$\mathbf{C} = \begin{bmatrix} 1 & ce^{j\psi} \\ ce^{j\psi} & 1 \end{bmatrix} \tag{B.1}$$

where the re-radiated signal is of magnitude $c$ ($< 1$) times the signal amplitude, and the phase of the re-radiated signal is $\psi$ radians with respect to the initial signal received by both the elements.

The array steering vector is

$$\mathbf{a}(\theta) = \begin{bmatrix} 1 \\ e^{j2\pi x \sin(\theta)/\lambda} \end{bmatrix} = \begin{bmatrix} 1 \\ h \end{bmatrix} \tag{B.2}$$

where $h = e^{j2\pi x \sin(\theta)/\lambda}$.

The FIM for this problem of estimating $\Psi = [\theta, c, \psi]^T$, is

$$\mathbf{J} = \begin{bmatrix} J_{\theta\theta} & J_{\theta c} & J_{\theta\psi} \\ J_{c\theta} & J_{cc} & J_{c\psi} \\ J_{\psi\theta} & J_{\psi c} & J_{\psi\psi} \end{bmatrix} \tag{B.3}$$

where the $(k,l)$th element of the symmetric FIM is

$$J_{kl} = T\,trace\left\{\mathbf{R}^{-1}\frac{\partial\mathbf{R}}{\partial\Psi_k}\mathbf{R}^{-1}\frac{\partial\mathbf{R}}{\partial\Psi_l}\right\} \tag{B.4}$$

The covariance matrix for the source is $\mathbf{R} = \sigma_S^2\mathbf{C}\mathbf{a}(\theta)\mathbf{a}^H(\theta)\mathbf{C}^H + \sigma_N^2\mathbf{I}_2$. Now arbitrarily let the noise power $\sigma_N^2 = 1$, then $\sigma_S^2$ is the SNR of the source. For convenience the subscript is dropped i.e. let $\sigma_S^2 = \sigma^2$. Substituting now the coupling matrix and array steering vector, into the expression for the covariance matrix,

$$\mathbf{R} = \sigma^2\begin{bmatrix} 1 & ce^{j\psi} \\ ce^{j\psi} & 1 \end{bmatrix}\begin{bmatrix} 1 \\ h \end{bmatrix}\begin{bmatrix} 1 & h^* \end{bmatrix}\begin{bmatrix} 1 & ce^{-j\psi} \\ ce^{-j\psi} & 1 \end{bmatrix} + \begin{bmatrix} 1 & 0 \\ 0 & 1 \end{bmatrix} \tag{B.5}$$

$$= \sigma^2\begin{bmatrix} 1 + hce^{j\psi} & h^* + ce^{j\psi} \\ ce^{j\psi} + h & h^*ce^{j\psi} + 1 \end{bmatrix}\begin{bmatrix} 1 & ce^{-j\psi} \\ ce^{-j\psi} & 1 \end{bmatrix} + \begin{bmatrix} 1 & 0 \\ 0 & 1 \end{bmatrix} \tag{B.6}$$

$$= \sigma^2\begin{bmatrix} (1+c^2) + hce^{j\psi} + h^*ce^{-j\psi} & h^* + hc^2 + ce^{-j\psi} + ce^{j\psi} \\ h + h^*c^2 + ce^{j\psi} + ce^{-j\psi} & (1+c^2) + hce^{-j\psi} + h^*ce^{j\psi} \end{bmatrix} + \begin{bmatrix} 1 & 0 \\ 0 & 1 \end{bmatrix} \tag{B.7}$$

An expression for $\mathbf{R}^{-1}$ is now obtained by first expressing $\mathbf{R}$ as follows

$$\mathbf{R} = \sigma^2\mathbf{v}(\theta)\mathbf{v}^H(\theta) + \mathbf{I}_2 \tag{B.8}$$

where $\mathbf{v}(\theta) = \mathbf{C}\mathbf{a}(\theta)$. Then

$$\mathbf{R}^{-1} = \frac{1}{\sigma^2}\left[\mathbf{v}(\theta)\mathbf{v}^H(\theta) + \frac{1}{\sigma^2}\mathbf{I}_2\right]^{-1} \tag{B.9}$$

$$= \frac{1}{\sigma^2}\left[\sigma^2\mathbf{I}_2 - \frac{\sigma^4\mathbf{v}(\theta)\mathbf{v}^H(\theta)}{1 + \sigma^2\mathbf{v}^H(\theta)\mathbf{v}(\theta)}\right] \tag{B.10}$$

$$= \mathbf{I}_2 - \frac{\sigma^2\mathbf{v}(\theta)\mathbf{v}^H(\theta)}{1 + \sigma^2\mathbf{v}^H(\theta)\mathbf{v}(\theta)} \tag{B.11}$$

$$= \mathbf{I}_2 - \frac{\sigma^2}{K(\theta)}\mathbf{C}\mathbf{a}(\theta)\mathbf{a}^H(\theta)\mathbf{C}^H \tag{B.12}$$

where the matrix inversion lemma has been used in equation (B.10), and $K(\theta) = 1 + \sigma^2 \mathbf{a}^H(\theta)\mathbf{C}^H\mathbf{C}\mathbf{a}(\theta)$. Now

$$K(\theta) = 1+\sigma^2\begin{bmatrix} 1 & h^* \end{bmatrix}\begin{bmatrix} 1 & ce^{-j\psi} \\ ce^{-j\psi} & 1 \end{bmatrix}\begin{bmatrix} 1 & ce^{j\psi} \\ ce^{j\psi} & 1 \end{bmatrix}\begin{bmatrix} 1 \\ h \end{bmatrix} \tag{B.13}$$

$$= 1+\sigma^2\begin{bmatrix} 1+h^*ce^{-j\psi} & ce^{-j\psi}+h^* \end{bmatrix}\begin{bmatrix} 1+hce^{j\psi} \\ ce^{j\psi}+h \end{bmatrix} \tag{B.14}$$

$$= 1+\sigma^2(2+2c^2+h^*ce^{-j\psi}+hce^{j\psi}+h^*ce^{j\psi}+hce^{-j\psi}) \tag{B.15}$$

From equation (B.12), $\mathbf{R}^{-1}$ is

$$\mathbf{R}^{-1} = \frac{\sigma^2}{K(\theta)}\left(\frac{K(\theta)}{\sigma^2}\mathbf{I}_2 - \mathbf{C}\mathbf{a}(\theta)\mathbf{a}^H(\theta)\mathbf{C}^H\right) \tag{B.16}$$

$$= \frac{\sigma^2}{K(\theta)}\begin{bmatrix} \frac{K(\theta)}{\sigma^2}-(1+c^2)-hce^{j\psi}-h^*ce^{-j\psi} & -h^*-hc^2-ce^{j\psi}-ce^{-j\psi} \\ -h-h^*c^2-ce^{j\psi}-ce^{-j\psi} & \frac{K(\theta)}{\sigma^2}-(1+c^2)-hce^{-j\psi}-h^*ce^{j\psi} \end{bmatrix} \tag{B.17}$$

$$= \frac{\sigma^2}{K(\theta)}\begin{bmatrix} \frac{1}{\sigma^2}+(1+c^2)+h^*ce^{j\psi}+hce^{-j\psi} & -h^*-hc^2-ce^{j\psi}-ce^{-j\psi} \\ -h-h^*c^2-ce^{j\psi}-ce^{-j\psi} & \frac{1}{\sigma^2}+(1+c^2)+hce^{j\psi}+h^*ce^{-j\psi} \end{bmatrix} \tag{B.18}$$

where $K(\theta)$ in equation (B.15) has been substituted in equation (B.18).

Consider now the partial derivatives,

$$\frac{\partial \mathbf{R}}{\partial \theta} = \sigma^2(j2\pi(x/\lambda)\cos(\theta))\begin{bmatrix} hce^{j\psi}-h^*ce^{-j\psi} & hc^2-h^* \\ h-h^*c^2 & hce^{-j\psi}-h^*ce^{j\psi} \end{bmatrix} \tag{B.19}$$

$$\frac{\partial \mathbf{R}}{\partial c} = \sigma^2\begin{bmatrix} 2c+he^{j\psi}+h^*e^{-j\psi} & 2hc+e^{-j\psi}+e^{j\psi} \\ 2h^*c+e^{j\psi}+e^{-j\psi} & 2c+he^{-j\psi}+h^*e^{j\psi} \end{bmatrix} \tag{B.20}$$

$$\frac{\partial \mathbf{R}}{\partial \psi} = j\sigma^2\begin{bmatrix} hce^{j\psi}-h^*ce^{-j\psi} & -ce^{-j\psi}+ce^{j\psi} \\ ce^{j\psi}-ce^{-j\psi} & -hce^{-j\psi}+h^*ce^{j\psi} \end{bmatrix} \tag{B.21}$$

Now consider

$$\mathbf{R}^{-1}\frac{\partial \mathbf{R}}{\partial \theta} = \left[\frac{j\sigma^4 2\pi(x/\lambda)\cos(\theta)}{K(\theta)}\right]\mathbf{L}_\theta \tag{B.22}$$

$$\mathbf{R}^{-1}\frac{\partial \mathbf{R}}{\partial c} = \frac{\sigma^4}{K(\theta)}\mathbf{L}_c \tag{B.23}$$

$$\mathbf{R}^{-1}\frac{\partial \mathbf{R}}{\partial \psi} = \frac{j\sigma^4}{K(\theta)}\mathbf{L}_\psi \tag{B.24}$$

where after some manipulation it can be shown that

$$[\mathbf{L}_\theta]_{11} = \frac{1}{\sigma^2}(hce^{j\psi} - h^*ce^{-j\psi}) + c^4 - 1 + c^3e^{j\psi}(h+h^*) + c^2(e^{j2\psi} - e^{-j2\psi}) \\ -ce^{-j\psi}(h+h^*) \tag{B.25}$$

$$[\mathbf{L}_\theta]_{12} = \frac{1}{\sigma^2}(hc^2 - h^*) + c^4h + 2c^3e^{j\psi} + c^2(h^*e^{j2\psi} - he^{-j2\psi}) - 2ce^{-j\psi} - h^* \tag{B.26}$$

$$[\mathbf{L}_\theta]_{21} = \frac{1}{\sigma^2}(h - c^2h^*) - c^4h^* - 2c^3e^{j\psi} - c^2(he^{j2\psi} - h^*e^{-j2\psi}) + 2ce^{-j\psi} + h \tag{B.27}$$

$$[\mathbf{L}_\theta]_{22} = \frac{1}{\sigma^2}(hce^{-j\psi} - h^*ce^{j\psi}) + 1 - c^4 - c^3e^{j\psi}(h+h^*) - c^2(e^{j2\psi} - e^{-j2\psi}) \\ +ce^{-j\psi}(h+h^*) \tag{B.28}$$

$$[\mathbf{L}_c]_{11} = \frac{1}{\sigma^2}(2c + he^{j\psi} + h^*e^{-j\psi}) + he^{j\psi} - h^*c^2e^{-j\psi} - (h^*)^2c + hc^2e^{-j\psi} + h^2c - h^*e^{j\psi} \tag{B.29}$$

$$[\mathbf{L}_c]_{12} = \frac{1}{\sigma^2}(2hc + e^{j\psi} + e^{-j\psi}) + e^{j\psi} + 2hc - 2h^*c + h^2c^2e^{-j\psi} - c^2e^{-j\psi} - (h^*)^2e^{j\psi} \tag{B.30}$$

$$[\mathbf{L}_c]_{21} = \frac{1}{\sigma^2}(2h^*c + e^{j\psi} + e^{-j\psi}) + e^{j\psi} - 2hc + 2h^*c + (h^*)^2c^2e^{-j\psi} - c^2e^{-j\psi} - h^2e^{j\psi} \tag{B.31}$$

$$[\mathbf{L}_c]_{22} = \frac{1}{\sigma^2}(2c + he^{-j\psi} + h^*e^{j\psi}) - he^{j\psi} + h^*c^2e^{-j\psi} + (h^*)^2c - hc^2e^{-j\psi} - h^2c + h^*e^{j\psi} \tag{B.32}$$

$$[\mathbf{L}_\psi]_{11} = \frac{1}{\sigma^2}(hce^{j\psi} - h^*ce^{-j\psi}) + h^2c^2 - (h^*)^2c^2 + hce^{j\psi} - h^*ce^{j\psi} + hc^3e^{-j\psi} \\ -h^*c^3e^{-j\psi} \tag{B.33}$$

$$[\mathbf{L}_\psi]_{12} = \frac{1}{\sigma^2}(-ce^{-j\psi} + ce^{j\psi}) - 2h^*c^2 + 2hc^2 - (h^*)^2ce^{j\psi} + h^2c^3e^{-j\psi} + ce^{j\psi} - c^3e^{-j\psi} \tag{B.34}$$

$$[\mathbf{L}_\psi]_{21} = \frac{1}{\sigma^2}(ce^{j\psi} - ce^{-j\psi}) + 2h^*c^2 - 2hc^2 + (h^*)^2c^3e^{-j\psi} - h^2ce^{j\psi} + ce^{j\psi} - c^3e^{-j\psi} \tag{B.35}$$

$$[\mathbf{L}_\psi]_{22} = \frac{1}{\sigma^2}(-hce^{-j\psi} + h^*ce^{j\psi}) - h^2c^2 + (h^*)^2c^2 - hce^{j\psi} + h^*ce^{j\psi} + h^*c^3e^{-j\psi} \\ -hc^3e^{-j\psi} \tag{B.36}$$

Due to the complexity of these expressions and the further algebra that has to be performed, specific coupling parameters were chosen. The coupling amplitude $c$ was chosen to be 0.5, and the coupling phase $\psi$ was chosen to be $\pi/2$, in order to simplify the above expressions. Since $\psi = \pi/2$, $e^{j\psi} = j$, $e^{-j\psi} = -j$, $e^{j2\psi} = -1$ and $e^{-j2\psi} = -1$. Note $K(\theta) = 1 + 2.5\sigma^2$, and $(x/\lambda)$ was chosen to be 0.4. Now

$$[\mathbf{L}_\theta]_{11} = \frac{0.5j}{\sigma^2}(h+h^*) + 0.625j(h+h^*) - 0.9375 \tag{B.37}$$

$$[\mathbf{L}_\theta]_{12} = \frac{1}{\sigma^2}(0.25h - h^*) + 0.3125h - 1.25h^* + 1.25j \tag{B.38}$$

$$[\mathbf{L}_\theta]_{21} = \frac{1}{\sigma^2}(h - 0.25h^*) - 0.3125h^* + 1.25h - 1.25j \tag{B.39}$$

$$[\mathbf{L}_\theta]_{22} = \frac{-0.5j}{\sigma^2}(h+h^*) - 0.625j(h+h^*) + 0.9375 \tag{B.40}$$

$$[\mathbf{L}_c]_{11} = \frac{1}{\sigma^2}(1 + jh - jh^*) + 0.75j(h - h^*) + 0.5(h^2 - (h^*)^2) \tag{B.41}$$

$$[\mathbf{L}_c]_{12} = \frac{h}{\sigma^2} + 1.25j + (h - h^*) - 0.25jh^2 - j(h^*)^2 \tag{B.42}$$

$$[\mathbf{L}_c]_{21} = \frac{h^*}{\sigma^2} + 1.25j - (h - h^*) - 0.25j(h^*)^2 - jh^2 \tag{B.43}$$

$$[\mathbf{L}_c]_{22} = \frac{1}{\sigma^2}(1 - jh + jh^*) - 0.75j(h - h^*) - 0.5(h^2 - (h^*)^2) \tag{B.44}$$

$$[\mathbf{L}_\psi]_{11} = \frac{0.5j}{\sigma^2}(h + h^*) + 0.25(h^2 - (h^*)^2) + 0.375j(h - h^*) \tag{B.45}$$

$$[\mathbf{L}_\psi]_{12} = \frac{j}{\sigma^2} + 0.5(h - h^*) - 0.5j(h^*)^2 - 0.125jh^2 + 0.625j \tag{B.46}$$

$$[\mathbf{L}_\psi]_{21} = \frac{j}{\sigma^2} - 0.5(h - h^*) - 0.5jh^2 - 0.125j(h^*)^2 + 0.625j \tag{B.47}$$

$$[\mathbf{L}_\psi]_{22} = \frac{0.5j}{\sigma^2}(h + h^*) - 0.25(h^2 - (h^*)^2) - 0.375j(h - h^*) \tag{B.48}$$

Substituting equations (B.22), (B.23) and (B.24) into equation (B.4) and inserting $K(\theta) = 1 + 2.5\sigma^2$, one can after some manipulation obtain the elements of the FIM as

$$J_{\theta\theta} = \frac{4\pi^2 T\sigma^4 (x/\lambda)^2 \cos^2(\theta)}{(1 + 2.5\sigma^2)^2}(3.125 + 7.8125\sigma^2) \tag{B.49}$$

$$J_{cc} = \frac{T\sigma^4}{(1 + 2.5\sigma^2)^2}(8 + 10\sigma^2 - 5\sigma^2 h^{-2} - 5\sigma^2 h^2 - 2h^{-2} - 2h^2) \tag{B.50}$$

$$J_{\psi\psi} = \frac{T\sigma^4}{(1 + 2.5\sigma^2)^2}(3 + 2.5\sigma^2 - 1.25\sigma^2 h^{-2} - 1.25\sigma^2 h^2 + 0.5h^{-2} + 0.5h^2) \tag{B.51}$$

$$J_{\theta c} = 0 \tag{B.52}$$

$$J_{\theta\psi} = \frac{j2\pi T\sigma^4 (x/\lambda)\cos(\theta)}{(1 + 2.5\sigma^2)^2}(1.25h^{-1} - 1.25h + 3.125\sigma^2 h^{-1} - 3.125\sigma^2 h) \tag{B.53}$$

$$J_{c\theta} = 0 \tag{B.54}$$

$$J_{c\psi} = \frac{-T\sigma^4}{(1 + 2.5\sigma^2)^2}(2h^{-1} + 2h) \tag{B.55}$$

$$J_{\psi\theta} = \frac{j2\pi T\sigma^4 (x/\lambda)\cos(\theta)}{(1 + 2.5\sigma^2)^2}(1.25h^{-1} - 1.25h + 3.125\sigma^2 h^{-1} - 3.125\sigma^2 h) \tag{B.56}$$

$$J_{\psi c} = \frac{-T\sigma^4}{(1 + 2.5\sigma^2)^2}(2h^{-1} + 2h) \tag{B.57}$$

Both the case where the source DOA is unknown (passive array calibration), and the case where the source DOA is known (active array calibration), are now considered separately. In each case the determinant of the FIM and the CRLB variances (diagonal elements of the inverse FIM), are obtained. Note the existence of the CRLB addresses the question of identifiability, and so the conditions under which the determinant of the FIM is zero, is of great importance.

## B.1 Passive Array Calibration

If the source DOA is unknown, then the FIM is a 3x3 matrix. Expressions are now obtained for the determinant of the FIM and the CRLB variances of the unknown parameters. Firstly consider the determinant of the passive array calibration FIM $\mathbf{J}$,

$$\begin{aligned}
\|\mathbf{J}\| &= \frac{-\pi^2 T^3 \sigma^{12} (x/\lambda)^2 \cos^2(\theta) h^4}{(1+2.5\sigma^2)^6} (125\sigma^2 - 50h^4 + 25 + 25h^8 + 156.25\sigma^4 - 250h^4\sigma^2 \\
&\quad -312.5h^4\sigma^4 + 156.25h^8\sigma^4 + 125h^8\sigma^2) && \text{(B.58)} \\
&= \frac{-\pi^2 T^3 \sigma^{12} (x/\lambda)^2 \cos^2(\theta) h^4}{(1+2.5\sigma^2)^6} \Big[156.25\sigma^4(h^8 - 2h^4 + 1) + 125\sigma^2(h^8 - 2h^4 + 1) \\
&\quad +25(h^8 - 2h^4 + 1)\Big] && \text{(B.59)} \\
&= \frac{-\pi^2 T^3 \sigma^{12} (x/\lambda)^2 \cos^2(\theta) h^4}{(1+2.5\sigma^2)^6} \Big[(156.25\sigma^4 + 125\sigma^2 + 25)(h^2+1)^2(h-1)^2(h+1)^2\Big] && \text{(B.60)}
\end{aligned}$$

The CRLB variance of the DOA is

$$\begin{aligned}
\sigma_\theta^2 &= \frac{-(1+2.5\sigma^2)^2}{T\sigma^4\pi^2\cos^2(\theta)\frac{x^2}{\lambda^2}} \left[\frac{6.25\sigma^2h^4 - 12.5\sigma^2h^2 + 6.25\sigma^2 - 2.5h^4 - 20h^2 - 2.5}{125h^2 + 312.5\sigma^2h^2 + 62.5 + 62.5h^4 + 156.25\sigma^2 + 156.25\sigma^2h^4}\right] && \text{(B.61)} \\
&= \frac{-(1+2.5\sigma^2)^2}{T\sigma^4\pi^2(x/\lambda)^2\cos^2(\theta)} \left[\frac{6.25\sigma^2(h^4 - 2h^2 + 1) - 2.5(h^4 + 8h^2 + 1)}{156.25\sigma^2(h^4 + 2h^2 + 1) + 62.5(h^4 + 2h^2 + 1)}\right] && \text{(B.62)} \\
&= \frac{-(1+2.5\sigma^2)^2}{T\sigma^4\pi^2(x/\lambda)^2\cos^2(\theta)} \left[\frac{6.25\sigma^2(h-1)^2(h+1)^2 - 2.5(h^4 + 8h^2 + 1)}{(156.25\sigma^2 + 62.5)(h^2+1)^2}\right] && \text{(B.63)} \\
&= \frac{-(1+2.5\sigma^2)}{T\sigma^4\pi^2(x/\lambda)^2\cos^2(\theta)} \left[\frac{6.25\sigma^2(h-1)^2(h+1)^2 - 2.5(h^4 + 8h^2 + 1)}{62.5(h^2+1)^2}\right] && \text{(B.64)}
\end{aligned}$$

where the last equation is obtained since $(156.25\sigma^2 + 62.5) = 62.5(1 + 2.5\sigma^2)$.

The CRLB variance of the coupling amplitude is

$$\begin{aligned}
\sigma_c^2 &= \frac{31.25(1+2.5\sigma^2)^2}{T\sigma^4} \left[\frac{-h^2}{156.25\sigma^2h^4 - 312.5\sigma^2h^2 + 156.25\sigma^2 + 62.5h^4 - 125h^2 + 62.5}\right] && \text{(B.65)} \\
&= \frac{31.25(1+2.5\sigma^2)^2}{T\sigma^4} \left[\frac{-h^2}{156.25\sigma^2(h^4 - 2h^2 + 1) + 62.5(h^4 - 2h^2 + 1)}\right] && \text{(B.66)} \\
&= \frac{31.25(1+2.5\sigma^2)^2}{T\sigma^4} \left[\frac{-h^2}{(156.25\sigma^2 + 62.5)(h-1)^2(h+1)^2}\right] && \text{(B.67)} \\
&= \frac{0.5(1+2.5\sigma^2)}{T\sigma^4} \left[\frac{-h^2}{(h-1)^2(h+1)^2}\right] && \text{(B.68)}
\end{aligned}$$

The CRLB variance of the coupling phase is

$$\sigma_\psi^2 = \frac{4(1+2.5\sigma^2)^2h^2}{T\sigma^4} *$$

$$
\begin{aligned}
& \left[\frac{-62.5h^2-78.125\sigma^2h^2+39.0625\sigma^2+39.0625\sigma^2h^4+15.625+15.625h^4}{156.25\sigma^2+156.25\sigma^2h^8-312.5\sigma^2h^4-125h^4+62.5+62.5h^8}\right] && \text{(B.69)}\\
&= \frac{4(1+2.5\sigma^2)^2h^2}{T\sigma^4}\left[\frac{39.0625\sigma^2(h^4-2h^2+1)+15.625(h^4-4h^2+1)}{156.25\sigma^2(h^8-2h^4+1)+62.5(h^8-2h^4+1)}\right] && \text{(B.70)}\\
&= \frac{4(1+2.5\sigma^2)^2h^2}{T\sigma^4}\left[\frac{39.0625\sigma^2(h-1)^2(h+1)^2+15.625(h^4-4h^2+1)}{(156.25\sigma^2+62.5)(h^2+1)^2(h+1)^2(h-1)^2}\right] && \text{(B.71)}\\
&= \frac{(1+2.5\sigma^2)h^2}{T\sigma^4}\left[\frac{39.0625\sigma^2(h-1)^2(h+1)^2+15.625(h^4-4h^2+1)}{15.625(h^2+1)^2(h+1)^2(h-1)^2}\right] && \text{(B.72)}
\end{aligned}
$$

When the determinant is zero the FIM is non-invertible, and hence the problem is non-identifiable for the case considered. Hence this gives the observability conditions. From equation (B.60) the determinant is zero when : (a) $\cos^2(\theta) = 0$; (b) $h^2 = -1$; (c) $h = 1$; and (d) $h = -1$. Condition (a) occurs when $\theta = \pm\pi/2$ (i.e. end-fire directions). Condition (b) occurs when

$$
\begin{aligned}
exp(j4\pi(x/\lambda)\sin(\theta)) &= -1 && \text{(B.73)}\\
4\pi(0.4)\sin(\theta) &= p\pi && \text{(B.74)}\\
\sin(\theta) &= \frac{p}{1.6} && \text{(B.75)}\\
\sin(\theta) &= 0.625p && \text{(B.76)}
\end{aligned}
$$

where $p = \pm1, \pm3, \pm5$, etc. Since sin() cannot be greater than one, the only solutions are when $p = \pm1$. These correspond to $\sin(\theta) = \pm0.625$, and hence occur when $\theta = \pm38.682^{\circ}$ (with respect to broadside). Condition (c) occurs when

$$
\begin{aligned}
exp(j2\pi(x/\lambda)\sin(\theta)) &= 1 && \text{(B.77)}\\
2\pi(0.4)\sin(\theta) &= q\pi && \text{(B.78)}\\
\sin(\theta) &= \frac{q}{0.8} && \text{(B.79)}\\
\sin(\theta) &= 1.25q && \text{(B.80)}
\end{aligned}
$$

where $q = 0, \pm2, \pm4$, etc. Since sin() cannot be greater than one, the only solution is when $q = 0$. This corresponds to $\sin(\theta) = 0$, which occurs when $\theta = 0$ (i.e. broadside direction). Condition (d) occurs when

$$
\begin{aligned}
exp(j2\pi(x/\lambda)\sin(\theta)) &= -1 && \text{(B.81)}\\
2\pi(0.4)\sin(\theta) &= p\pi && \text{(B.82)}
\end{aligned}
$$

$$\sin(\theta) = \frac{p}{0.8} \tag{B.83}$$

$$\sin(\theta) = 1.25p \tag{B.84}$$

where again $p = \pm 1, \pm 3, \pm 5$, etc. Since sin() cannot be greater than one, no solution exists. So this problem is non-identifiable when the source is either at broadside direction, end-fire directions, or ±38.682° from broadside. These are key observations, and the reason for these non-identifiable conditions will be given in section B.3.

High SNR approximations for the CRLB variances can be obtained, which illustrate how the variances vary with the source parameters. From equation (B.64) the CRLB variance for the DOA can be approximated as

$$(\sigma_\theta^2)_p \approx \frac{-2.5\sigma^2}{T\sigma^4\pi^2(0.4)^2\cos^2(\theta)}\left[\frac{6.25\sigma^2(h-1)^2(h+1)^2}{62.5(h^2+1)^2}\right] \tag{B.85}$$

$$= \frac{-0.15831(h+1)^2(h-1)^2}{T\cos^2(\theta)(h^2+1)^2} \tag{B.86}$$

$$= \frac{-0.15831(h^4-2h^2+1)}{T\cos^2(\theta)(h^4+2h^2+1)} \tag{B.87}$$

$$= \frac{-0.15831(h^2-2+h^{-2})}{T\cos^2(\theta)(h^2+2+h^{-2})} \tag{B.88}$$

$$= \frac{-0.15831}{T\cos^2(\theta)}\left[\frac{2\cos(1.6\pi\sin(\theta))-2}{2\cos(1.6\pi\sin(\theta))+2}\right] \tag{B.89}$$

$$= \frac{-0.15831}{T\cos^2(\theta)}\left[\frac{\cos(1.6\pi\sin(\theta))-1}{\cos(1.6\pi\sin(\theta))+1}\right] \tag{B.90}$$

The CRLB variance of the coupling amplitude in equation (B.68) can be approximated for high SNR as

$$(\sigma_c^2)_p \approx \frac{0.5(2.5\sigma^2)}{T\sigma^4}\left[\frac{-h^2}{(h-1)^2(h+1)^2}\right] \tag{B.91}$$

$$= \frac{-1.25h^2}{T\sigma^2(h^4-2h^2+1)} \tag{B.92}$$

$$= \frac{-1.25}{T\sigma^2(h^2-2+h^{-2})} \tag{B.93}$$

$$= \frac{-1.25}{T\sigma^2\left[2\cos(1.6\pi\sin(\theta))-2\right]} \tag{B.94}$$

$$= \frac{-0.625}{T\sigma^2\left[\cos(1.6\pi\sin(\theta))-1\right]} \tag{B.95}$$

The CRLB variance of the coupling phase in equation (B.72) is approximated for high SNR as

$$\begin{aligned}
(\sigma_{\psi}^{2})_{p} &\approx \frac{2.5\sigma^{2}h^{2}}{T\sigma^{4}}\left[\frac{39.0625\sigma^{2}(h-1)^{2}(h+1)^{2}}{15.625(h^{2}+1)^{2}(h+1)^{2}(h-1)^{2}}\right] && \text{(B.96)}\\
&= \frac{6.25h^{2}}{T(h^{2}+1)^{2}} && \text{(B.97)}\\
&= \frac{6.25h^{2}}{T(h^{4}+2h^{2}+1)} && \text{(B.98)}\\
&= \frac{6.25}{T(h^{2}+2+h^{-2})} && \text{(B.99)}\\
&= \frac{6.25}{T\left[2\cos(1.6\pi\sin(\theta))+2\right]} && \text{(B.100)}\\
&= \frac{3.125}{T\left[\cos(1.6\pi\sin(\theta))+1\right]} && \text{(B.101)}
\end{aligned}$$

## B.2 Active Array Calibration

When the DOA of the source is known, the FIM is a 2x2 matrix, with the first row and first column of $\mathbf{J}$ in equation (B.3) removed. Expressions are now determined for the determinant of the FIM and the CRLB variances of each of the unknown parameters. Consider first the determinant of the active array calibration FIM $\mathbf{J_a}$,

$$\begin{aligned}
\|\mathbf{J_a}\| &= \frac{T^{2}\sigma^{8}h^{4}}{(1+2.5\sigma^{2})^{4}}(-1-25\sigma^{2}h^{2}-25\sigma^{4}h^{2}+6.25\sigma^{4}-6h^{2}+50\sigma^{2}h^{4}+14h^{4}\\
&\qquad +37.5\sigma^{4}h^{4}-25\sigma^{4}h^{6}-25\sigma^{2}h^{6}+6.25\sigma^{4}h^{8}-h^{8}-6h^{6}) && \text{(B.102)}\\
&= \frac{T^{2}\sigma^{8}h^{4}}{(1+2.5\sigma^{2})^{4}}\left[-(h^{8}+6h^{6}-14h^{4}+6h^{2}+1)-25\sigma^{2}(h^{6}-2h^{4}+h^{2})\right.\\
&\qquad \left.+6.25\sigma^{4}(h^{8}-4h^{6}+6h^{4}-4h^{2}+1)\right] && \text{(B.103)}\\
&= \frac{T^{2}\sigma^{8}h^{4}}{(1+2.5\sigma^{2})^{4}}\left[-(h^{4}+8h^{2}+1)(h-1)^{2}(h+1)^{2}-25\sigma^{2}h^{2}(h-1)^{2}(h+1)^{2}\right.\\
&\qquad \left.+6.25\sigma^{4}(h-1)^{4}(h+1)^{4}\right] && \text{(B.104)}
\end{aligned}$$

The CRLB variance of the coupling amplitude is

$$\begin{aligned}
\sigma_{c}^{2} &= \frac{-(1+2.5\sigma^{2})^{2}h^{2}}{T\sigma^{4}}\left[\frac{-2.5\sigma^{2}h^{2}+1.25\sigma^{2}+1.25\sigma^{2}h^{4}-0.5-0.5h^{4}-3h^{2}}{D_{N}}\right] && \text{(B.105)}\\
&= \frac{-(1+2.5\sigma^{2})^{2}h^{2}}{T\sigma^{4}}\left[\frac{-0.5(h^{4}+6h^{2}+1)+1.25\sigma^{2}(h^{4}-2h^{2}+1)}{D_{N}}\right] && \text{(B.106)}\\
&= \frac{-(1+2.5\sigma^{2})^{2}h^{2}}{T\sigma^{4}}\left[\frac{-0.5(h^{4}+6h^{2}+1)+1.25\sigma^{2}(h-1)^{2}(h+1)^{2}}{D_{N}}\right] && \text{(B.107)}
\end{aligned}$$

where $D_N = -(h^4+8h^2+1)(h-1)^2(h+1)^2-25\sigma^2h^2(h-1)^2(h+1)^2+6.25\sigma^4(h-1)^4(h+1)^4$. The CRLB variance of the coupling phase is

$$\begin{aligned} \sigma_\psi^2 &= \frac{-(1+2.5\sigma^2)^2h^2}{T\sigma^4}\left[\frac{-10\sigma^2h^2+5\sigma^2+5\sigma^2h^4+2+2h^4-8h^2}{D_N}\right] && \text{(B.108)} \\ &= \frac{-(1+2.5\sigma^2)^2h^2}{T\sigma^4}\left[\frac{2(h^4-4h^2+1)+5\sigma^2(h^4-2h^2+1)}{D_N}\right] && \text{(B.109)} \\ &= \frac{-(1+2.5\sigma^2)^2h^2}{T\sigma^4}\left[\frac{2(h^4-4h^2+1)+5\sigma^2(h-1)^2(h+1)^2}{D_N}\right] && \text{(B.110)} \end{aligned}$$

From equation (B.104), the determinant is zero when $h = -1$, and when $h = 1$. As determined above, $h = 1$ when $\theta = 0$ (i.e. broadside direction), and $h = -1$ has no solution. Hence the problem is only non-identifiable when the source is at broadside direction. Note for passive array calibration the problem was non-identifiable when the source was at end-fire directions or from ±38.682°, in addition. These are key observations, and the reason for this non-identifiable condition will be given in section B.3.

High SNR approximations for the CRLB variances are now obtained. The CRLB variance of the coupling amplitude in equation (B.107), may be approximated as

$$\begin{aligned} (\sigma_c^2)_a &\approx \frac{-2.5^2\sigma^4h^2}{T\sigma^4}\left[\frac{1.25\sigma^2(h-1)^2(h+1)^2}{6.25\sigma^4(h-1)^4(h+1)^4}\right] && \text{(B.111)} \\ &= \frac{-1.25h^2}{T\sigma^2(h-1)^2(h+1)^2} && \text{(B.112)} \\ &= \frac{-0.625}{T\sigma^2\left[\cos(1.6\pi\sin(\theta))-1\right]} && \text{(B.113)} \end{aligned}$$

where equation (B.113) is obtained since equation (B.112) indicates that the CRLB variance of the coupling amplitude is the same as that in the passive array calibration case. The CRLB variance of the coupling phase in equation (B.110) is approximated as

$$\begin{aligned} (\sigma_\psi^2)_a &\approx \frac{-2.5^2\sigma^4h^2}{T\sigma^4}\left[\frac{5\sigma^2(h-1)^2(h+1)^2}{6.25\sigma^4(h-1)^4(h+1)^4}\right] && \text{(B.114)} \\ &= \frac{-5h^2}{T\sigma^2(h^4-2h^2+1)} && \text{(B.115)} \\ &= \frac{-5}{T\sigma^2(h^2-2+h^{-2})} && \text{(B.116)} \\ &= \frac{-5}{T\sigma^2\left[2\cos(1.6\pi\sin(\theta))-2\right]} && \text{(B.117)} \\ &= \frac{-2.5}{T\sigma^2\left[\cos(1.6\pi\sin(\theta))-1\right]} && \text{(B.118)} \end{aligned}$$

## B.3 Interpretation for Non-Identifiable Conditions

The non-identifiable conditions obtained in the previous sections are due to array ambiguities. Consider first the passive array calibration problem when the source is at end-fire directions or ±38.682°. When the source is at one of these directions, say $\theta_p$, the vector of sensor outputs (with mutual coupling) is the same as that for the case (without mutual coupling) where : (a) two coherent signals impinge the array, with one of the signals being a scaled and delayed replica of the other signal; (b) the DOA of the stronger signal is $\theta_p$; and (c) the DOA of the weaker signal is known. This is so, since it can be shown that the vector of sensor outputs

$$\begin{aligned} \mathbf{z}(t) &= \mathbf{C}\mathbf{a}(\theta_p)s(t) && \text{(B.119)} \\ &= \left(\mathbf{a}(\theta_p) + 0.5e^{j\delta}\mathbf{a}(\theta_q)\right) s(t) && \text{(B.120)} \end{aligned}$$

where $\delta$ is due to a time delay and $\theta_q$ is the DOA of the weaker signal. Like in equation (B.3), the unknowns are a single DOA ($\theta_p$), a scalar amplitude (0.5) and a phase ($\delta$) (note $\theta_q$ must be known). The combinations of parameters which satisfy equation (B.120) are given in Table B.1.

| $\theta_p$ | $\theta_q$ | $\delta$ |
|---|---|---|
| $-90^{\circ}$ | $+90^{\circ}$ | $-\frac{3\pi}{10}$ |
| $-38.682^{\circ}$ | $+38.682^{\circ}$ | $0$ |
| $+38.682^{\circ}$ | $-38.682^{\circ}$ | $\pi$ |
| $+90^{\circ}$ | $-90^{\circ}$ | $-\frac{7\pi}{10}$ |

Table B.1: Ambiguity Conditions

When the source is at broadside, both the passive and active array calibration problems are non-identifiable, since the vector of sensor outputs

$$\begin{aligned} \mathbf{z}(t) &= \mathbf{C}\mathbf{a}(90^{\circ})s(t) && \text{(B.121)} \\ &= \mathbf{a}(90^{\circ})s'(t) && \text{(B.122)} \end{aligned}$$

where $s'(t) = (1+0.5j)s(t)$. Thus the array cannot distinguish between the case where mutual coupling exists (as given by equation (B.1) with $c = 0.5$ and $\psi = \pi/2$) with a signal $s(t)$ impinging the array, and the case where no mutual coupling exists and a signal $(1 + 0.5j)s(t)$ impinges the array.

# APPENDIX C

# Analytic Expressions for Error Surfaces

Analytic expressions are derived here for studying the cost function / error surface in chapter 5, as a function of the unknown parameters. For each unknown parameter the error surface is analysed separately, with the other unknown parameters fixed at their true values. This simplifies the expressions derived, while still providing very useful insight.

The cost function, for the special case considered in chapter 5, was given in equation (5.44). When the number of snapshots and the SNRs of the sources, approach infinity, the estimated principal eigenvector equals the exact (true) principal eigenvector. Equation (5.44) then becomes

$$Q = \sum_{n=1}^{N} \left\| \mathbf{e}_n - \hat{\mathbf{C}}\hat{\mathbf{a}}(\hat{\theta}_n)\hat{s}_n \right\|^2 \tag{C.1}$$

where $\mathbf{e}_n = \mathbf{C}\mathbf{a}(\theta_n)s_n$ (true values), and the ˆ on top denotes that these parameters are to be estimated.

A 2-element array is considered, with the position of one sensor arbitrarily chosen to be at the origin, and the other sensor located at ($x$,0) i.e. along the $x$-axis. The first element of the symmetric coupling matrix is arbitrarily chosen to be unity. The coupling matrix is then

$$\mathbf{C} = \begin{bmatrix} 1 & c_1 e^{j\psi_1} \\ c_1 e^{j\psi_1} & c_2 e^{j\psi_2} \end{bmatrix} \tag{C.2}$$

The steering vector is

$$\mathbf{a}(\theta_n) = \begin{bmatrix} 1 \\ e^{j2\pi x \sin\theta_n/\lambda} \end{bmatrix} = \begin{bmatrix} 1 \\ h_n \end{bmatrix} \tag{C.3}$$

where $h_n = e^{j2\pi x \sin\theta_n/\lambda}$.

## C.1 Source DOA

Now consider the error surface when only one source's DOA is unknown and is to be estimated. All other parameters are assumed to be known and equal their true values. This error surface

$$Q_1(\hat{\theta}_n) = \left\|\mathbf{Ca}(\theta_n)s_n - \mathbf{Ca}(\hat{\theta}_n)s_n\right\|^2 \tag{C.4}$$

where the summation has been removed since the contribution to the cost function by all other disjoint clusters is zero. Now

$$\begin{aligned}
Q_1(\hat{\theta}_n) &= \left\|s_n\mathbf{C}(\mathbf{a}(\theta_n) - \mathbf{a}(\hat{\theta}_n))\right\|^2 && \text{(C.5)}\\
&= \left\|s_n\begin{bmatrix} 1 & c_1e^{j\psi_1}\\ c_1e^{j\psi_1} & c_2e^{j\psi_2}\end{bmatrix}\begin{bmatrix} 0\\ h_n-\hat{h}_n\end{bmatrix}\right\|^2 && \text{(C.6)}\\
&= \left\|s_n(h_n-\hat{h}_n)\begin{bmatrix} c_1e^{j\psi_1}\\ c_2e^{j\psi_2}\end{bmatrix}\right\|^2 && \text{(C.7)}\\
&= |s_n|^2(h_n^*h_n - h_n^*\hat{h}_n - \hat{h}_n^*h_n + \hat{h}_n^*\hat{h}_n)(c_1^2+c_2^2) && \text{(C.8)}\\
&= |s_n|^2(c_1^2+c_2^2)(1 - e^{-j2\pi x\sin\theta_n/\lambda}e^{j2\pi x\sin\hat{\theta}_n/\lambda}\\
&\qquad -e^{-j2\pi x\sin\hat{\theta}_n/\lambda}e^{j2\pi x\sin\theta_n/\lambda}+1) && \text{(C.9)}\\
&= |s_n|^2(c_1^2+c_2^2)\left(2-\exp\left(-\frac{j2\pi x}{\lambda}[\sin\theta_n-\sin\hat{\theta}_n]\right)\right.\\
&\qquad \left.-\exp\left(+\frac{j2\pi x}{\lambda}[\sin\theta_n-\sin\hat{\theta}_n]\right)\right) && \text{(C.10)}\\
&= |s_n|^2(c_1^2+c_2^2)\left(2-2\cos\left(\frac{2\pi x}{\lambda}[\sin\theta_n-\sin\hat{\theta}_n]\right)\right) && \text{(C.11)}\\
Q_1(\hat{\theta}_n) &= K_n\left(1-\cos\left(\frac{2\pi x}{\lambda}[\sin\theta_n-\sin\hat{\theta}_n]\right)\right) && \text{(C.12)}
\end{aligned}$$

where equation (C.11) is obtained since $e^{jk}+e^{-jk}=2\cos k$, and $K_n = 2|s_n|^2(c_1^2+c_2^2)$.

Now differentiating (C.12) with respect to $\hat{\theta}_n$,

$$\frac{dQ_1(\hat{\theta}_n)}{d\hat{\theta}_n} = -\frac{2\pi x}{\lambda}K_n\cos\hat{\theta}_n\sin\left(\frac{2\pi x}{\lambda}[\sin\theta_n-\sin\hat{\theta}_n]\right) \tag{C.13}$$

Differentiating again with respect to $\hat{\theta}_n$,

$$\frac{d^2Q_1(\hat{\theta}_n)}{d^2\hat{\theta}_n} = +\frac{2\pi x}{\lambda}K_n\left[\sin\hat{\theta}_n\sin\left(\frac{2\pi x}{\lambda}[\sin\theta_n-\sin\hat{\theta}_n]\right)\right.$$

$$+\frac{2\pi x}{\lambda}\cos^2\hat{\theta}_n\cos\left(\frac{2\pi x}{\lambda}[\sin\theta_n-\sin\hat{\theta}_n]\right)\Bigg] \tag{C.14}$$

## C.2 Sensor Position Error

Consider now the error surface when the position $x$ is unknown, while all other parameters are known and are equal to their true values. This error surface is

$$Q_2(\hat{x})=\sum_{n=1}^{N}\|\mathbf{C}\mathbf{a}(\theta_n)s_n-\mathbf{C}\hat{\mathbf{a}}(\theta_n)s_n\|^2 \tag{C.15}$$

where the summation is present since the contribution to the cost function by each disjoint cluster is non-zero.

The first few steps, up to equation (C.8), are the same (except for a summation) as those in the source DOA case, and hence are not repeated here. As in equation (C.8)

$$\begin{aligned}
Q_2(\hat{x}) &= \sum_{n=1}^{N}|s_n|^2(h_n^*h_n-h_n^*\hat{h}_n-\hat{h}_n^*h_n+\hat{h}_n^*\hat{h}_n)(c_1^2+c_2^2) && \text{(C.16)}\\
&= \sum_{n=1}^{N}|s_n|^2(c_1^2+c_2^2)(1-e^{-j2\pi x\sin\theta_n/\lambda}e^{j2\pi\hat{x}\sin\theta_n/\lambda} \\
&\qquad -e^{-j2\pi\hat{x}\sin\theta_n/\lambda}e^{j2\pi x\sin\theta_n/\lambda}+1) && \text{(C.17)}\\
&= \sum_{n=1}^{N}|s_n|^2(c_1^2+c_2^2)\left(2-\exp\left(+\frac{j2\pi[\hat{x}-x]}{\lambda}\sin\theta_n\right)\right.\\
&\qquad \left.-\exp\left(-\frac{j2\pi[\hat{x}-x]}{\lambda}\sin\theta_n\right)\right) && \text{(C.18)}\\
&= \sum_{n=1}^{N}|s_n|^2(c_1^2+c_2^2)\left(2-2\cos\left(\frac{2\pi[\hat{x}-x]}{\lambda}\sin\theta_n\right)\right) && \text{(C.19)}\\
&= \sum_{n=1}^{N}2|s_n|^2(c_1^2+c_2^2)\left(1-\cos\left(\frac{2\pi\Delta x}{\lambda}\sin\theta_n\right)\right) && \text{(C.20)}\\
Q_2(\Delta x) &= \sum_{n=1}^{N}K_n\left(1-\cos\left(\frac{2\pi\Delta x}{\lambda}\sin\theta_n\right)\right) && \text{(C.21)}
\end{aligned}$$

where the position error is $\Delta x=\hat{x}-x$.

Differentiating (C.21) with respect to $\Delta x$,

$$\frac{dQ_2(\Delta x)}{d\Delta x}=\sum_{n=1}^{N}\frac{2\pi}{\lambda}K_n\sin\theta_n\sin\left(\frac{2\pi\Delta x}{\lambda}\sin\theta_n\right) \tag{C.22}$$

Again differentiating with respect to $\Delta x$,

$$\frac{d^2 Q_2(\Delta x)}{d^2 \Delta x} = \sum_{n=1}^{N} \frac{4\pi^2}{\lambda^2} K_n \sin^2\theta_n \cos\left(\frac{2\pi\Delta x}{\lambda}\sin\theta_n\right) \tag{C.23}$$

## C.3 Coupling Amplitude

The error surface when $c_1$ is unknown and the other parameters are all known, is now considered. This error surface is

$$\begin{aligned}
Q_3(\hat{c}_1) &= \sum_{n=1}^{N} \left\| \mathbf{C}\mathbf{a}(\theta_n)s_n - \hat{\mathbf{C}}\mathbf{a}(\theta_n)s_n \right\|^2 && \text{(C.24)}\\
&= \sum_{n=1}^{N} \left\| (\mathbf{C} - \hat{\mathbf{C}})\mathbf{a}(\theta_n)s_n \right\|^2 && \text{(C.25)}\\
&= \sum_{n=1}^{N} \left\| s_n \left( \begin{bmatrix} 1 & c_1 e^{j\psi_1} \\ c_1 e^{j\psi_1} & c_2 e^{j\psi_2} \end{bmatrix} - \begin{bmatrix} 1 & \hat{c}_1 e^{j\psi_1} \\ \hat{c}_1 e^{j\psi_1} & c_2 e^{j\psi_2} \end{bmatrix} \right) \begin{bmatrix} 1 \\ h_n \end{bmatrix} \right\|^2 && \text{(C.26)}\\
&= \sum_{n=1}^{N} \left\| s_n \begin{bmatrix} 0 & e^{j\psi_1}(c_1 - \hat{c}_1) \\ e^{j\psi_1}(c_1 - \hat{c}_1) & 0 \end{bmatrix} \begin{bmatrix} 1 \\ h_n \end{bmatrix} \right\|^2 && \text{(C.27)}\\
&= \sum_{n=1}^{N} \left\| s_n e^{j\psi_1}(c_1 - \hat{c}_1) \begin{bmatrix} h_n \\ 1 \end{bmatrix} \right\|^2 && \text{(C.28)}\\
&= \sum_{n=1}^{N} |s_n|^2 (c_1 - \hat{c}_1)^2 \begin{bmatrix} h_n^* & 1 \end{bmatrix} \begin{bmatrix} h_n \\ 1 \end{bmatrix} && \text{(C.29)}\\
Q_3(\hat{c}_1) &= \sum_{n=1}^{N} 2|s_n|^2 (c_1^2 - 2c_1\hat{c}_1 + \hat{c}_1^2) && \text{(C.30)}
\end{aligned}$$

Now differentiating (C.30) with respect to $\hat{c}_1$,

$$\frac{dQ_3(\hat{c}_1)}{d\hat{c}_1} = \sum_{n=1}^{N} 4|s_n|^2 (\hat{c}_1 - c_1) \tag{C.31}$$

Differentiating again with respect to $\hat{c}_1$,

$$\frac{d^2 Q_3(\hat{c}_1)}{d^2 \hat{c}_1} = \sum_{n=1}^{N} 4|s_n|^2 \tag{C.32}$$

When $c_2$ is unknown and the other parameters are all known, the following expressions can be similarly obtained

$$\begin{aligned}
Q_4(\hat{c}_2) &= \sum_{n=1}^{N} |s_n|^2 (c_2^2 - 2c_2\hat{c}_2 + \hat{c}_2^2) && \text{(C.33)} \\
\frac{dQ_4(\hat{c}_2)}{d\hat{c}_2} &= \sum_{n=1}^{N} 2|s_n|^2 (\hat{c}_2 - c_2) && \text{(C.34)} \\
\frac{d^2Q_4(\hat{c}_2)}{d^2\hat{c}_2} &= \sum_{n=1}^{N} 2|s_n|^2 && \text{(C.35)}
\end{aligned}$$

## C.4 Coupling Phase

The error surface when $\psi_1$ is unknown and all the other parameters are known, is

$$\begin{aligned}
Q_5(\hat{\psi}_1) &= \sum_{n=1}^{N} \left\| s_n \left( \begin{bmatrix} 1 & c_1 e^{j\psi_1} \\ c_1 e^{j\psi_1} & c_2 e^{j\psi_2} \end{bmatrix} - \begin{bmatrix} 1 & c_1 e^{j\hat{\psi}_1} \\ c_1 e^{j\hat{\psi}_1} & c_2 e^{j\psi_2} \end{bmatrix} \right) \begin{bmatrix} 1 \\ h_n \end{bmatrix} \right\|^2 && \text{(C.36)} \\
&= \sum_{n=1}^{N} \left\| s_n \begin{bmatrix} 0 & c_1(e^{j\psi_1} - e^{j\hat{\psi}_1}) \\ c_1(e^{j\psi_1} - e^{j\hat{\psi}_1}) & 0 \end{bmatrix} \begin{bmatrix} 1 \\ h_n \end{bmatrix} \right\|^2 && \text{(C.37)} \\
&= \sum_{n=1}^{N} \left\| s_n c_1 (e^{j\psi_1} - e^{j\hat{\psi}_1}) \begin{bmatrix} h_n \\ 1 \end{bmatrix} \right\|^2 && \text{(C.38)} \\
&= \sum_{n=1}^{N} |s_n|^2 c_1^2 (e^{-j\psi_1} - e^{-j\hat{\psi}_1})(e^{j\psi_1} - e^{j\hat{\psi}_1})(h_n^* h_n + 1) && \text{(C.39)} \\
&= \sum_{n=1}^{N} |s_n|^2 c_1^2 (1 - e^{j\Delta\psi_1} - e^{-j\Delta\psi_1} + 1)(1 + 1) && \text{(C.40)} \\
Q_5(\Delta\psi_1) &= \sum_{n=1}^{N} 4|s_n|^2 c_1^2 (1 - \cos(\Delta\psi_1)) && \text{(C.41)}
\end{aligned}$$

where $\Delta\psi_1 = \hat{\psi}_1 - \psi_1$.

Differentiating with respect to $\Delta\psi_1$,

$$\begin{aligned}
\frac{dQ_5(\Delta\psi_1)}{d\Delta\psi_1} &= \sum_{n=1}^{N} 4|s_n|^2 c_1^2 \sin(\Delta\psi_1) && \text{(C.42)} \\
\frac{d^2Q_5(\Delta\psi_1)}{d^2\Delta\psi_1} &= \sum_{n=1}^{N} 4|s_n|^2 c_1^2 \cos(\Delta\psi_1) && \text{(C.43)}
\end{aligned}$$

For $\psi_2$ unknown with the other parameters all known, the following expressions may similarly be obtained :

$$\begin{aligned} Q_6(\Delta\psi_2) &= \sum_{n=1}^{N} 2|s_n|^2 c_2^2 (1-\cos(\Delta\psi_2)) && \text{(C.44)} \\ \frac{dQ_6(\Delta\psi_2)}{d\Delta\psi_2} &= \sum_{n=1}^{N} 2|s_n|^2 c_2^2 \sin(\Delta\psi_2) && \text{(C.45)} \\ \frac{d^2Q_6(\Delta\psi_2)}{d^2\Delta\psi_2} &= \sum_{n=1}^{N} 2|s_n|^2 c_2^2 \cos(\Delta\psi_2) && \text{(C.46)} \end{aligned}$$

where $\Delta\psi_2 = \hat{\psi}_2 - \psi_2$.

## C.5 Complex Scalar $s_n$

Expressions for both the amplitude $|s_n|$ and phase $\delta_n$ of the complex scalar $s_n$, can be similarly obtained, and are given below.

$$\begin{aligned} Q_7(|\hat{s}_n|) &= L_n(|s_n|^2 - 2|s_n||\hat{s}_n| + |\hat{s}_n|^2) && \text{(C.47)} \\ \frac{dQ_7(|\hat{s}_n|)}{d|\hat{s}_n|} &= 2L_n(|\hat{s}_n| - |s_n|) && \text{(C.48)} \\ \frac{d^2Q_7(|\hat{s}_n|)}{d^2|\hat{s}_n|} &= 2L_n && \text{(C.49)} \end{aligned}$$

where $L_n = 1 + 2c_1^2 + c_2^2 + c_1(h_n^* e^{-j\psi_1} + h_n e^{j\psi_1}) + c_1 c_2 (h_n e^{j(\psi_2-\psi_1)} + h_n^* e^{j(\psi_1-\psi_2)})$. Defining $\Delta\delta_n = \hat{\delta}_n - \delta_n$,

$$\begin{aligned} Q_8(\Delta\delta_n) &= 2|s_n|^2 L_n (1-\cos(\Delta\delta_n)) && \text{(C.50)} \\ \frac{dQ_8(\Delta\delta_n)}{d\Delta\delta_n} &= 2|s_n|^2 L_n \sin(\Delta\delta_n) && \text{(C.51)} \\ \frac{d^2Q_8(\Delta\delta_n)}{d^2\Delta\delta_n} &= 2|s_n|^2 L_n \cos(\Delta\delta_n) && \text{(C.52)} \end{aligned}$$

# Bibliography

[1] Yu. I. Abramovich, A. Yu. Gorokhov, V. N. Mikhaylyukov and I. P. Malyavin, "Exterior noise adaptive rejection for OTH radar implementations", ICASSP, April 1994, Adelaide, Australia, Vol. 6, pp. 105-107.

[2] Yu. I. Abramovich, A. Yu. Gorokhov and N. Spencer, "Convergence analysis of stochastically-constrained sample matrix inversion algorithms", ISCAS, 1996, Atlanta, U.S.A., pp. 449-452.

[3] Yu. I. Abramovich, S. J. Anderson and I. S. D. Solomon, "Adaptive ionospheric distortion correction techniques for HF skywave radar", IEEE National Radar Conference, 1996, Ann Arbor, Michigan (U.S.A.), pp. 267-272.

[4] R. S. Adve and T. K. Sarkar, "Elimination of the effects of mutual coupling in an adaptive nulling system with a look direction constraint", IEEE Antennas and Propagation Symposium, 1996, Maryland, U.S.A., Vol. 2, pp. 1164-1167.

[5] R. S. Adve, T. K. Sarkar and R. A. Schneible, "Accounting for the effects of mutual coupling in adaptive antennas", IEEE National Radar Conference, 1997, New York, U.S.A., pp. 361-366.

[6] H. Akaike, "Information theory and an extension of the maximum likelihood principle", International Symposium on Information Theory, 1973, pp. 267-281.

[7] M. Ali, J. Gotze and R. Pauli, "An algorithm for the calibration of sensor arrays with sensor gain and phase uncertainties", ICASSP, 1993, Minnesota, U.S.A., Vol. 4, pp. 121-124.

[8] S. J. Anderson, "Ionospheric Faraday rotation signatures in the space-time-frequency domain", International HF Radio Conference, July 1991, Edinburgh, Scotland, pp. 167-172.

[9] S. J. Anderson, G. S. Brimble, L. J. Durbridge, A. M. Forbes, P. M. Roberts and G. M. Warne, “HF surface-wave radar observations of waves and currents in Gulf St. Vincent”, Australian Physical Oceanography Conference, February 1995, Lorne, Australia (copies available from first author).

[10] S. J. Anderson and M. L. Lees, “High-resolution synoptic scale measurement of ionospheric motions with the Jindalee sky wave radar”, Radio Science, May-June 1988, Vol. 23, No. 3, pp. 265-272.

[11] E. H. Attia and B. D. Steinberg, “Self-cohering large antenna arrays using the spatial correlation properties of radar clutter”, IEEE Transactions on Antennas and Propagation, January 1989, Vol. 37, No. 1, pp. 30-38.

[12] H. M. Aumann and F. G. Willwerth, “Application of beamspace techniques to phased array calibration and fault compensation”, Antenna Measurement Techniques Association, 1991, Colorado, U.S.A., No. 10B, pp. 9-13.

[13] H. M. Aumann, “Eigenvalue analysis of phased array element patterns”, IEEE Antennas and Propagation Symposium, June 1994, Seattle, Washington (U.S.A.), Vol. 1, pp. 510-513.

[14] H. M. Aumann and F. G. Willwerth, “Phased array calibration using measured element patterns”, IEEE Antennas and Propagation Symposium, June 1995, California, U.S.A., Vol 2., pp. 918-921.

[15] E. C. Ballegooijen, G. W. M. Mierlo, C. Schooneveld, P. P. M. Zalm, A. T. Parsons and N. H. Field, “Measurement of towed array position, shape, and altitude”, IEEE Journal of Oceanic Engineering, October 1989, Vol. 14, No. 4, pp. 375-383.

[16] L. D. Bamford, P. S. Hall and A. Fray, “Calculation of antenna mutual coupling from radiated far fields”, International Conference on Computation in Electromagnetics, Second Conference, April 1994, University of Nottingham, England, pp. 263-266.

[17] A. J. Barabell, “Improving the resolution performance of eigenstructure-based direction-finding algorithms”, ICASSP, 1983, Boston, U.S.A., pp. 336-339.

[18] D. K. Barton and H. R. Ward “Handbook of radar measurement”, 1984, Artech House.

[19] G. Bienvenu and L. Kopp, "Adaptivity to background noise spatial coherence for high resolution passive methods", ICASSP, April 1980, Colorado, U.S.A, pp. 307-310.

[20] M. Bouvet, "Beamforming of a distorted line array in the presence of uncertainties on the sensor positions", Journal of the Acoustical Society of America, June 1987, Vol. 81, No. 6, pp. 1833-1840.

[21] Y. Bresler and A. Macovski, "Exact maximum likelihood parameter estimation of superimposed exponential signals in noise", IEEE Transactions on Acoustics, Speech, and Signal Processing, October 1986, Vol. 34, No. 5, pp. 1081-1089.

[22] G. C. Brown, J. H. McClellan and E. J. Holder, "A phased array calibration technique using eigenstructure methods", IEEE International Radar Conference, 1990, Arlington, Virginia (U.S.A.), pp. 304-308.

[23] G. C. Brown, J. H. McClellan and E. J. Holder, "Eigenstructure approach for array processing and calibration with general phase and gain perturbations", ICASSP, 1991, Toronta, Canada, Vol. 5, pp. 3037-3040.

[24] H. P. Bucker, "Beamforming a towed line array of unknown shape", Journal of the Acoustical Society of America, May 1978, Vol. 63, No. 5, pp. 1451-1454.

[25] J. Capon, "High-resolution frequency-wavenumber spectrum analysis", Proceedings of the IEEE, 1969, Vol. 57, pp. 1408-1418.

[26] M. A. Cervera, "Meteor observations with a narrow beam VHF radar", Ph.D. Dissertion, February 1996, University of Adelaide.

[27] Y. M. Chen, J. H. Lee, C. C. Yeh and J. Mar, "Bearing estimation without calibration for randomly perturbed arrays", IEEE Transactions on Signal Processing, 1991, Vol. 39, pp. 194-197.

[28] Y. M. Chen, J. H. Lee and C. C. Yeh, "Two-dimensional angle-of-arrival estimation for uniform planar arrays with sensor position errors", IEE Proceedings - part F, February 1993, Vol. 140, No. 1, pp. 37-42.

[29] S. Choi and T. K. Sarkar, "Statistical observations of position errors in two dimensional antenna arrays", IEEE Antennas and Propagations Symposium, 1989, San Jose, California (U.S.A.), pp. 408-411.

[30] H. Clergeot, S. Tressens and A. Ouamri, “Performance of high resolution frequencies estimation methods compared to the Cramer-Rao bounds”, IEEE Transactions on Acoustics, Speech, and Signal Processing, November 1989, Vol. 37, No. 11, pp. 1703-1720.

[31] P. Comon and L. Deruaz, “Array self calibration : identifiability issues”, EUSIPCO, September 1996, Italy, pp. 547-550.

[32] R. T. Compton, “The effect of random steering vector errors in the applebaum adaptive arrays”, IEEE Transactions on Aerospace and Electronics Systems, September 1982, Vol. AES-18, No. 5, pp. 392-400.

[33] T. J. Cornwell, “The applications of closure phase to astronomical imaging”, Science, July 1989, Vol. 245, pp. 263-269.

[34] H. Cox, “Resolving power and sensitivity mismatch of optimum array processors”, The Journal of the Acoustical Society of America, 1973, Vol. 54, No. 3, pp. 771-785.

[35] M. J. Daily, “Self-calibration of a multi-camera vision system”, Twenty Fourth Asilomar Conference, November 1990, California, U.S.A., Vol. 2, pp. 810-815.

[36] J. Dall, “A fast autofocus algorithm for synthetic aperture radar processing”, ICASSP, March 1992, California, U.S.A., Vol. 3, pp. 5-8.

[37] A. G. Derneryd, “Compensation of mutual coupling effects in array antennas”, IEEE Antennas and Propagation Symposium, 1996, Maryland, U.S.A., pp. 1122-1125.

[38] A. R. Djordjevic, M. B. Bazdar, G. M. Vitosevic, T. K. Sarkar and R. F. Harrington, “Analysis of Wire Antennas and Scatterers : Software and User Manual”, 1995, Artech House.

[39] M. C. Dogan and J. M. Mendel, “Applications of cumulants to array processing - part I : aperture extension and array calibration”, IEEE Transactions on Signal Processing, May 1995, Vol. 43, No. 5, pp. 1200-1216.

[40] C. N. Dorny, “A self-survey technique for self-cohering of antenna systems”, IEEE Transactions on Antennas and Propagation, November 1978, Vol. AP-26, No. 6, pp. 877-881.

[41] C. N. Dorny and B. S. Meagher Jr., "Cohering of an experimental nonrigid array by self-survey", IEEE Transactions on Antennas and Propagation, November 1980, Vol. AP-28, No. 6, pp. 902-904.

[42] B. L. Douglas, J. M. Silkaitis and H. Lee, "Single-reference calibration technique for multiple-element array sonar imaging systems", Journal of the Acoustical Society of America, July 1996, Vol. 100, No. 1, pp. 400-407.

[43] B. L. Douglas and H. Lee, "Synthetic-aperture sonar imaging with a multiple-element receiver array", ICASSP, April 1993, Minnesota, U.S.A., Vol. 5, pp. 445-448.

[44] W. Du and R. L. Kirlin, "Improved spatial smoothing techniques for DOA estimation of coherent signals", IEEE Transactions on Signal Processing, May 1991, Vol. 39, No. 5, pp. 1208-1210.

[45] G. F. Earl and B. D. Ward, "The frequency management system of the Jindalee over-the-horizon backscatter HF radar", Radio Science, March 1987, Vol. 22, No. 2, pp. 275-291.

[46] G. F. Earl and B. D. Ward, "Frequency management support for remote sea-state sensing using the Jindalee skywave radar", IEEE Journal of Oceanic Engineering, April 1986, Vol. OE-11, No. 2, pp. 164-173.

[47] P. H. Eichel, D. C. Ghiglia and C. V. Jakowatz Jr., "Speckle processing method for synthetic-aperture-radar phase correction", Optics Letters, January 1989, Vol. 14, No. 1, pp. 1-3.

[48] R. D. Ekers, "The almost serendipitous discovery of self-calibration", Workshop on Serendipity in Radio Astronomy, West Virginia, U.S.A., May 1993.

[49] M. H. Er and B. C. Ng, "Simple and effective approach to array beamforming in presence of steering error", Electronics Letters, February 1992, Vol. 28, No. 4, pp. 413-414.

[50] J. E. Evans, J. R. Johnson and D. F. Sun, "Application of advanced signal processing techniques to angle of arrival estimation in ATC navigation and surveillance systems", M.I.T. Lincoln Labs, Lexington, Massachusetts (U.S.A.), Technical Report No. 582, June 1982.

[51] R. L. Fante, "Effect of error correlations and systematic errors on average array sidelobes", IEEE Transactions on Antennas and Propagation, 1990, Vol. 38, No. 1, pp. 124-129.

[52] D. R. Farrier, "Gain of an array of sensors subjected to processor perturbations", IEE Proceedings - Part H, June 1983, Vol. 130, No. 4, pp. 251-254.

[53] D. R. Farrier, "Effect of processor perturbations on an adaptive beamformer", Electronics Letters, February 1984, Vol. 20, No. 3, pp. 133-134.

[54] M. Feder and E. Weinstein, "Parameter estimation of superimposed signals using the EM algorithm", IEEE Transactions on Acoustics, Speech, and Signal Processing, April 1988, Vol. 36, No. 4, pp. 477-489.

[55] B. G. Fejer and M. C. Kelly, "Ionospheric irregularities", Reviews of Geophysics and Space Physics, May 1980, Vol. 18, No. 2, pp. 401-454.

[56] D. D. Feldman and L. J. Griffiths, "A projection approach for robust adaptive beamforming", IEEE Transactions on Signal Processing, April 1994, Vol. 42, No. 4, pp. 867-876.

[57] P. Felisberto and S. M. Jesus, "Towed-array beamforming during ship's manoeuvering", IEE Proceedings - Radar, Sonar, and Navigation, June 1996, Vol. 143, No. 3, pp. 210-215.

[58] B. G. Ferguson, "Sharpness applied to the adaptive beamforming of acoustic data from a towed array of unknown shape", Journal of the Acoustical Society of America, December 1990, Vol. 88, No. 6, pp. 2695-2701.

[59] B. G. Ferguson, D. A. Gray and J. L. Riley, "Comparison of sharpness and eigenvector methods for towed array shape estimation", Journal of the Acoustical Society of America, March 1992, Vol. 91, No. 3, pp. 1565-1570.

[60] A. Flieller, A. Ferreol, P. Larzabal and H. Clergeot, "Robust bearing estimation in the presence of direction-dependent modelling errors : identifiability and treatment", ICASSP, May 1995, Michigan, U.S.A., pp. 1884-1887.

[61] F. Florin, "Calibration of high-frequency imaging deformable towed arrays", IEEE OCEANS, 1994, Vol. 1, pp. 247-252.

[62] C. S. Fraser, M. R. Shortis and G. Ganci, “Multi-sensor system self-calibration”, SPIE - Videometrics IV, October 1995, Vol. 2598, pp. 2-18.

[63] B. Friedlander and A. J. Weiss, “Eigenstructure methods for direction finding with sensor gain and phase uncertainties”, ICASSP, 1988, New York, U.S.A., pp. 2681-2684.

[64] B. Friedlander, “A sensitivity analysis of the MUSIC algorithm”, IEEE Transactions on Acoustics, Speech, and Signal Processing, October 1990, Vol. 38, No. 10, pp. 1740-1751.

[65] B. Friedlander, “Sensitivity analysis of the maximum likelihood direction-finding algorithm”, IEEE Transactions on Aerospace and Electronic Systems, November 1990, Vol. 26, No. 6, pp. 953-968.

[66] B. Friedlander and A. J. Weiss, “Direction finding in the presence of mutual coupling”, IEEE Transactions on Antennas and Propagation, March 1991, Vol. AP-39, pp. 273-284.

[67] B. Friedlander, “On the sensitivity of covariance based direction finding to gain and phase perturbations”, ICASSP, 1994, San Francisco, California (U.S.A.), Vol. 4, pp. 445-448.

[68] B. Friedlander and A. J. Weiss, “Effects of model errors on signal reconstruction using a sensor array”, ICASSP, 1993, Minnesota, U.S.A., Vol. IV, pp. 552-555.

[69] B. Friedlander and A. J. Weiss, “Effects of model errors on waveform estimation using the MUSIC algorithm”, IEEE Transactions on Signal Processing, January 1994, Vol. 42, No. 1, pp. 147-155.

[70] E. M. Friel and K. M. Pasala, “Wideband bearing estimation with compensation for mutual coupling effects”, IEEE Antennas and Propagation Symposium, 1994, Seattle, Washington U.S.A., pp. 1556-1559.

[71] J. J. Fuchs, “Shape calibration for a nominally linear equispaced array”, ICASSP, 1993, Minnesota, U.S.A., Vol. 4, pp. 300-303.

[72] J. J. Fuchs, “Array shape reconstruction for a nominally linear array”, ICASSP, 1994, Adelaide, Australia, Vol. 4, pp. 81-84.

[73] J. J. Fuchs, “Shape calibration for a nominally linear equispaced array”, IEEE Transactions on Signal Processing, October 1995, Vol. 43, No. 10, pp. 2241-2248.

[74] D. R. Fuhrmann, "Estimation of sensor gain and phase using known field covariance", ICASSP, 1991, Toronto, Canada, pp. 1369-1372.

[75] L. Fusillo and J. H. Satriano, "In-situ far-field calibration of multibeam sonar arrays for precise backscatter imagery", OCEANS - Supplementary Proceedings, September 1996, Florida, U.S.A., pp. 47-49.

[76] L. C. Godara, "The effect of phase-shifter errors on the performance of an antenna-array beamformer", IEEE Journal of Oceanic Engineering, July 1985, Vol. OE-10, No. 3, pp. 278-284.

[77] L. C. Godara, "Error analysis of the optimal antenna array processors", IEEE Transactions on Aerospace and Electronics Systems, July 1986, Vol. AES-22, No. 4, pp. 395-409.

[78] J. Goldberg, A. Perez-Neira and M. A. Lagunas, "Joint direction-of-arrival and array shape tracking for multiple moving targets", ICASSP, 1997, Munich, Germany, pp. 511-514.

[79] J. M. Goodman, "HF Communications : Science and Technology", Van Nostrand Reinhold, 1992.

[80] M. J. Goris, "Towed Array Calibration", Ph.D. Dissertion, December 1995, Australian National University.

[81] D. A. Gray, "Effect of time-delay errors on the beam pattern of a linear array", IEEE Journal of Oceanic Engineering, July 1985, Vol. OE-10, No. 3, pp. 269-277.

[82] D. A. Gray, W. O. Wolfe and J. L. Riley, "An eigenvector method for estimating the positions of the elements of an array of receivers", Australian Symposium on Signal Processing Applications, 1989, Gold Coast, Australia, Vol. 2., pp. 391-393.

[83] D. A. Gray and J. L. Riley, "Maximum likelihood estimate and Cramer-Rao bound for a complex signal vector", International Symposium on Signal Processing and its Applications, 1990, Gold Coast, Australia, pp. 352-355.

[84] D. A. Gray, B. D. O. Anderson and R. R. Bitmead, "Towed array shape estimation using Kalman filters - theoretical models", IEEE Journal of Oceanic Engineering, October 1993, Vol. 18, No. 4, pp. 543-556.

[85] J. S. Greenhow and J. E. Hall, "The variation of meteor heights with velocity and magnitude", Monthly Notices of the Royal Astronomical Society, 1960, Vol. 121, pp. 174-182.

[86] J. S. Greenhow and J. E. Hall, "The importance of initial trail radius on the apparent height and number distributions of meteor echoes", Monthly Notices of the Royal Astronomical Society, 1960, Vol. 121, pp. 183-196.

[87] I. J. Gupta and A. A. Ksienski, "Effect of mutual coupling on the performance of adaptive arrays", IEEE Transactions on Antennas and Propagation, September 1983, Vol. AP-31, No. 5, pp. 785-791.

[88] K. Gustafsson, F. McCarthy and A. Paulraj, "Mitigation of wing flexure induced errors for airborne direction-finding applications", IEEE Transactions on Signal Processing, February 1996, Vol. 44, No. 2, pp. 296-304.

[89] R. Hamza and K. Buckley, "An analysis of weighted eigenspace methods in the presence of sensor errors", IEEE Transactions on Signal Processing, May 1995, Vol. 43, No. 5, pp. 1140-1150.

[90] R. Hamza and K. Buckley, "Sensitivity analysis under model perturbations for weighted eigenspace methods", ICASSP, 1993, Minnesota, U.S.A., Vol. 4, pp. 332-335.

[91] S. D. Hayward, "Effects of motion on adaptive arrays", IEE Proceedings - Radar, Sonar and Navigation", February 1997, Vol. 144, No. 1, pp. 15-20.

[92] B. Himed and D. D. Weiner, "Compensation for mutual coupling effects in direction finding", ICASSP, 1990, New Mexico, U.S.A., pp. 2631-2634.

[93] M. J. Hinich, "Bearing estimation using a perturbed linear array", Journal of the Acoustical Society of America, June 1977, Vol. 61, No. 6, pp. 1540-1544.

[94] J. S. Hong, "Genetic approach to bearing estimation with sensor location uncertainties", Electronics Letters, November 1993, Vol. 29, No. 23, pp. 2013-2014.

[95] B. E. Howard and J. M. Syck, "Calculation of the shape of a towed underwater acoustic array", IEEE Journal of Oceanic Engineering, April 1992, Vol. 17, No. 2, pp. 193-203.

[96] J. K. Hsiao, "Normalized relationship among errors and sidelobe levels", Radio Science, January-February 1984, Vol. 19, No. 1, pp. 292-302.

[97] E. K. L. Hung, "Array element gain and phase estimation in the presence of interference", Defence Research Establishment Ottawa, December 1993, Report 1211.

[98] E. K. L. Hung, "Estimation of array element gains and phases in the presence of specular multipath", International Radar Conference, 1994, Paris, pp. 162-166.

[99] E. K. L. Hung, "Computation of the Coupling Matrix among the elements of an Array Antenna", International Radar Conference, 1994, Paris, pp. 703-706.

[100] B. D. Huxtable and E. M. Geyer, "Motion compensation feasibility for high resolution synthetic aperture sonar", IEEE OCEANS, 1993, Vol. 1, pp. 125-131.

[101] S. Hwang and D. B. Williams, "A constrained total least squares approach for sensor position calibration and direction finding", IEEE National Radar Conference, 1994, Atlanta, U.S.A, pp. 155-159.

[102] H. D. Jackson and A. Woode, "Development of the ERS-1 active radar calibration unit", IEEE Transactions on Microwave Theory and Techniques, June 1992, Vol. 40, No. 6, pp. 1063-1069.

[103] R. K. Jarrott, D. J. Netherway and S. J. Anderson, "Signal processing for ocean surveillance by HF skywave radar", ASSPA, 1989, Adelaide, Australia, pp. 293-297.

[104] D. J. Jeffries and D. R. Farrier, "Asymptotic results for eigenvector methods", IEE Proceedings - Part F, December 1985, Vol. 132, No. 7, pp. 589-594.

[105] S. Jiangda and G. Yanchang, "Peak sidelobe of linear array antennas with amplitude and phase errors", CIE International Conference on Radar, October 1991, Beijing, China, pp. 203-206.

[106] B. Kang, H. M. Subbaram and B. D. Steinberg, "Improved adaptive beamforming target for self-calibrating a distorted phased array", IEEE Transactions on Antennas and Propagation, February 1990, Vol. 38, No. 2, pp. 186-194.

[107] Y. W. Kang and D. M. Pozar, "Correction of error in reduced sidelobe synthesis due to mutual coupling", IEEE Transactions on Antennas and Propagation, September 1985, Vol. 33, No. 9, pp. 1025-1028.

[108] M. Kaveh and A. J. Barabell, "The statistical performance of the MUSIC and the Minimum-Norm algorithms in resolving plane waves in noise", IEEE Transactions on Acoustics, Speech, and Signal Processing, April 1986, Vol. ASSP-34, No. 2, pp. 331-341

[109] S. M. Kay, "Fundamentals of statistical signal processing : estimation theory", Prentice Hall Signal Processing Series.

[110] R. H. Khan, E. W. Gill, S. A. Saoudy, K. Hickey, B. J. Dawe and J. Walsh, "Experimental results from a long-range HF ground wave coastal surveillance radar", IEEE National Radar Conference, April 1993, Massachusetts, U.S.A., pp. 107-112.

[111] M. A. Koerber and D. R. Fuhrmann, "Array calibration by fourier series parameterization: scaled principal components method", ICASSP, 1993, Minnesota, U.S.A., Vol. 4, pp. 340-343.

[112] M. A. Koerber and D. R. Fuhrmann, "Radar antenna calibration using range-Doppler data", Seventh Workshop on Statistical Signal and Array Processing, 1994, pp. 441-444.

[113] H. Krim and M. Viberg, "Two decades of array signal processing research", IEEE Signal Processing Magazine, July 1996, pp. 67-94.

[114] R. Kumaresan and D. W. Tufts, "Estimating the angles of arrival of multiple plane waves", IEEE Transactions on Aerospace and Electronic Systems, January 1983, Vol. AES-19, No. 1, pp. 134-139.

[115] M. L. Lees, "An overview of signal processing for an over-the-horizon radar", ISSPA, 1987, Brisbane, Australia, pp. 491-494.

[116] M. L. Lees and R. M. Thomas, "Ionospheric probing with an HF radar", Electronics and Communication Engineering Journal, September-October 1989, pp. 233-240.

[117] C. C. Lee and J. H. Lee, "Eigenanalysis interference cancellers with robust capabilities", Signal Processing, 1997, Vol. 58, pp. 193-202.

[118] M. Levi and H. Messer, "Sufficient conditions for array calibration using sources of mixed types", ICASSP, April 1990, New Mexico, U.S.A., pp. 2943-2946.

[119] F. Li, R. J. Vaccaro and D. W. Tufts, "Unified performance analysis of subspace-based estimation algorithms", ICASSP, April 1990, New Mexico, U.S.A., pp. 2575-2578.

[120] J. T. Lo, "New Maximum Likelihood Approach to Multiple Signal Estimation", ICASSP, 1988, New York, pp. 2889-2892.

[121] J. T. Lo and S. L. Marple Jr., "Eigenstructure methods for array sensor localization", ICASSP, 1987, Texas, U.S.A., pp. 2260-2263.

[122] J. T. Lo and S. L. Marple Jr., "Observability conditions for multiple signal direction finding and array sensor localization", IEEE Transactions on Signal Processing, November 1992, Vol. 40, No. 11, pp. 2641-2650.

[123] E. Ludke, "A new polarisation calibration technique for a large phased array with maximum baseline approximately 220 Km", Eighth International Conference on Antennas and Propagation, April 1993, Heriot-Watt University, United Kingdom, Vol. 1, pp. 607-609.

[124] D. Maiwald and U. Nickel, "Multiple signal detection and parameter estimation using sensor arrays with phase uncertainties", EUSIPCO, September 1996, Italy, pp. 551-554.

[125] S. Marcos and O. Macchi, "Adaptive estimation of a time-varying array shape using the tracking properties of the LMS algorithm", ICASSP, April 1988, New York, U.S.A., pp. 1538-1541.

[126] A. Manikas and N. Fistas, "Modelling and estimation of mutual coupling between array elements", ICASSP, 1994, Adelaide, Australia, Vol. 4, pp. 553-556.

[127] S. J. Maybank and O. D. Faugeras, "A theory of self-calibration of a moving camera", International Journal of Computer Vision, 1992, Vol. 8, No. 2, pp. 123-151.

[128] D. McArthur and J. P. Reilly, "A computationally efficient self-calibrating direction-of-arrival estimator", ICASSP, 1994, Adelaide, Australia, Vol. 4, pp. 201-204.

[129] D. McArthur and J. P. Reilly, "An efficient self-calibrating direction-of-arrival estimator", 7th Workshop on Statistical Signal and Array Processing (SSAP), 1996, Greece, pp. 129-132.

[130] F. McCarthy, R. Ridgway and A. Paulraj, "Fast techniques for sensor array calibration", Twenty Eighth Asilomar Conference, October 1994, Pacific Grove, California (U.S.A.), Vol. 1, pp. 688-693.

[131] R. N. McDonough, "Degraded performance of nonlinear array processors in the presence of data modelling errors", The Journal of the Acoustical Society of America, 1972, Vol. 51, No. 4 (Part 1), pp. 1186-1193.

[132] D. W. R. McKinley, "Meteor Science and Engineering", McGraw-Hill Book Company, Inc., 1961.

[133] G. H. Millman and G. R. Nelson, "Surface wave HF radar for over-the-horizon detection", IEEE International Radar Conference, 1980, pp. 106-112.

[134] J. H. Mims and J. L. Farrell, "Synthetic aperture imaging with manoeuvers", IEEE Transactions on Aerospace and Electronics Systems, 1972, Vol. 8, pp. 410-418.

[135] R. A. Muller and A. Buffington, "Real-time correction of atmospherically degraded telescope images through image sharpening", Journal of the Optical Society of America, September 1974, Vol. 64, No. 9, pp. 1200-1210.

[136] D. J. Netherway and C. T. Carson, "Impedance and scattering matrices of a wideband HF phased array", Journal of Electrical and Electronics Engineering (Australia), 1986, Vol. 6, No. 1, pp. 29-39.

[137] A. P. C. Ng, "Direction-of-arrival estimates in the presence of wavelength, gain, and phase errors", IEEE Transactions on Signal Processing, January 1995, Vol. 43, No. 1, pp. 225-232.

[138] B. C. Ng and A. Nehorai, "Optimum active array shape calibration", 25th Asilomar Conference on Signals, Systems, and Computers, 1991, California, U.S.A, pp. 893-897.

[139] B. C. Ng and A. Nehorai, "Active array sensor localization", Signal Processing, 1995, Vol. 44, pp. 309-327.

[140] B. C. Ng and C. M. See, "Sensor-array calibration using a maximum-likelihood approach", IEEE Transactions on Antenna and Propagation, June 1996, Vol. 44, No. 6, pp 827-835.

[141] B. P. Ng, "Array shape self-calibration technique for direction finding problems", IEE Proceedings - Part H, December 1992, Vol. 139, No. 6, pp. 521-525.

[142] B. P. Ng, M. H. Er and C. Kot, "Array gain/phase calibration techniques for adaptive beamforming and direction finding", IEE Proceedings - Radar, Sonar, and Navigation, February 1994, Vol. 141, No. 1, pp. 25-29.

[143] R. Nitzberg, "Effect of errors in adaptive weights", IEEE Transactions on Aerospace and Electronic Systems, May 1976, Vol. AES-12, No. 3, pp. 369-373.

[144] M. O'Donnell and P. C. Li, "Aberration correction on a two-dimensional anisotropic phased array", Ultrasonics Symposium, December 1991, Florida, U.S.A., Vol. 2, pp. 1189-1193.

[145] C. J. Oliver, "High-frequency limits on SAR autofocus and phase correction", International Journal of Remote Sensing, 1993, Vol. 14, No. 3, pp. 495-519.

[146] D. Olsson-Steel and W. G. Elford, "The height distribution of radio meteors : observations at 2 MHz", Journal of Atmospheric and Terrestrial Physics, 1987, Vol. 49, No. 3, pp. 243-258.

[147] B. Ottersten, M. Viberg and B. Wahlberg, "Robust source localization based on local array response modelling", ICASSP, 1992, San Francisco, California (U.S.A.), Vol. 2, pp. 441-444.

[148] N. L. Owsley, "Joint source and sensor location estimation", ICASSP, April 1984, pp. 40.2.1-4.

[149] N. L. Owsley and G. R. Swope, "Array shape determination using time delay estimation procedures", IEEE EASCON, September 1980, Arlington, Virginia (U.S.A.), pp. 158-164.

[150] N. L. Owsley, "Shape estimation for a flexible underwater cable", IEEE EASCON, November 1981, Washington D.C., U.S.A., pp. 20-23.

[151] E. Painchault and A. Joisel, "Mutual coupling and phase control of large HF arrays", HF Radio Systems and Techniques, 1988, London, England, pp. 137-140.

[152] R. D. Palmer, S. Vangal, M. F. Larsen, S. Fukao, T. Nakamura and M. Yamamoto, "Phase calibration of VHF spatial interferometry radars", Radio Science, January-February 1996, Vol. 31, No. 1, pp. 147-156.

[153] A. Paulraj and T. Kailath, "Direction of arrival estimation by eigenstructure methods with unknown sensor gain and phase", ICASSP, 1985, Florida, U.S.A., pp. 640-643.

[154] A. Paulraj, R. Roy and T. Kailath, "Estimation of signal parameters via rotational invariance techniques - ESPRIT", 19th Asilomar Conference on Circuits, Systems and Computers, 1985, Pacific Grove, California U.S.A., pp. 83-89.

[155] T. H. Pearce, "Calibration of a large receiving array for HF radar", HF Radio Systems and Techniques Conference, July 1997, Nottingham, England, pp. 260-264.

[156] J. Pierre and M. Kaveh, "Experimental performance of calibration and direction finding algorithms", ICASSP, 1991, Toronto, Canada, pp. 1365-1368.

[157] S. U. Pillai and B. H. Kwon, "Forward/backward spatial smoothing techniques for coherent signal identification", IEEE Transactions on Acoustics, Speech, and Signal Processing, January 1989, Vol. ASSP-37, No. 1, pp. 8-15.

[158] V. F. Pisarenko, "The retrieval of harmonics from a covariance function", Geophysical J. Roy. Astron. Soc., 1973, Vol. 33, pp. 347-366.

[159] B. Porat and B. Friedlander, "Analysis of the asymptotic relative efficiency of the MUSIC algorithm", IEEE Transactions on Acoustics, Speech, and Signal Processing, April 1988, Vol. 36, No. 4, pp. 532-544.

[160] X. Qiu and Z. Zhu, "Mutual coupling calibration using a single source in near field", IEEE National Aerospace and Electronics Conference, 1994, Dayton, U.S.A., pp. 424-426.

[161] A. H. Quazi, "Array beam response in the presence of amplitude and phase fluctuations", Journal of the Acoustical Society of America, July 1982, Vol. 72, No. 1, pp. 171-180.

[162] B. G. Quinn, R. F. Barrett, P. J. Kootsookos and S. J. Searle, "The estimation of the shape of an array using a hidden markov model", IEEE Journal of Oceanic Engineering, October 1993, Vol. 18, No. 4, pp. 557-564.

[163] W. M. Radich and K. M. Buckley, "Robust high-resolution eigenspace DOA estimation", Asilomar Conference on Signals, Systems, and Computers, 1992, Pacific Grove, California (U.S.A.), pp. 204-208.

[164] S. S. Reddi, "Multiple source location - a digital approach", IEEE Transactions on Aerospace and Electronic Systems, 1979, Vol. AES-15, pp. 95-105.

[165] J. L. Riley, D. A. Gray and D. A. Holdsworth, "Estimating the positions of an array of receivers using Kalman filtering techniques", ISSPA, 1990, Gold Coast, Australia, Vol. 1, pp. 364-367.

[166] H. Rishbeth, "Basic physics of the ionosphere : a tutorial review", Journal of the Institution of Electronic and Radio Engineers, September 1988, Vol. 58, No. 6 (supplement), pp. 207-223.

[167] F. C. Robey, D. R. Fuhrmann and S. I. Krich, "Array calibration utilizing clutter scattering", Seventh Workshop on Statistical Signal and Array Processing, 1994, pp. 317-320.

[168] Y. Rockah, "Array processing in the presence of uncertainty", Ph.D. Dissertion, May 1986, Yale University.

[169] Y. Rockah, H. Messer and P. M. Schultheiss, "Localization performance of arrays subject to phase errors", IEEE Transactions on Aerospace and Electronics Systems, July 1988, Vol. 24, No. 4, pp. 402-410.

[170] Y. Rockah and P. M. Schultheiss, "Array shape calibration using sources in unknown locations - Part I : far-field Sources", IEEE Transactions on Acoustics, Speech, and Signal Processing, March 1987, Vol. ASSP-35, No. 3, pp. 286-299.

[171] Y. Rockah and P. M. Schulthesis, "Array shape calibration using sources in unknown locations - Part II : near-field sources and estimator implementation", IEEE Transactions on Acoustics, Speech, and Signal Processing, June 1987, Vol. ASSP-35, No. 6, pp. 724-735.

[172] M. C. Roggemann and J. A. Meinhardt, "Image reconstruction by means of wave-front sensor measurements in closed-loop adaptive optics systems", Journal of the Optical Society of America A, September 1993, Vol. 10, No. 9, pp. 1996-2007.

[173] C. Roller and W. Wasylkiwskyj, "Effects of mutual coupling on super-resolution DF in linear arrays", ICASSP, March 1992, San Fransico, California (U.S.A.), Vol 5, pp. 257-260.

[174] R. Roy and T. Kailath, "ESPRIT - estimation of signal parameters via rotational invariance techniques", IEEE Transactions on Acoustics, Speech, and Signal Processing, July 1989, Vol. 37, No. 7, pp. 984-995.

[175] J. Ruze, "The effect of aperture errors on the antenna radiation pattern", Nuovo Cimento Supplement, 1952, Vol. 9, pp. 364-380.

[176] K. Sarabandi and T. C. Chiu, "Optimum corner reflectors for calibration of imaging radars", IEEE Transactions on Antennas and Propagation, October 1996, Vol. 44, No. 10, pp. 1348-1361.

[177] R. O. Schmidt, "Multiple Emitter Location and Signal Parameter Estimation", RADC Spectral Estimation Workshop, Rome, New York (U.S.A.), 1979, pp 243-258.

[178] R. O. Schmidt, "A signal subspace approach to multiple emitter location and spectral estimation", Ph.D. Thesis, November 1981, Stanford University, California, U.S.A.

[179] R. O. Schmidt, "Multiple emitter location and signal parameter estimation", IEEE Transactions on Antennas and Propagation, March 1986, Vol. AP-34, No. 3, pp. 276-280.

[180] R. O. Schmidt, "Multilinear array manifold interpolation", IEEE Transactions on Signal Processing, April 1992, Vol. 40, No. 4, pp. 857-866.

[181] C. M. S. See, "Sensor array calibration in the presence of mutual coupling and unknown sensor gains and phases", Electronic Letters, 3rd March 1994, Vol. 30, No. 5, pp. 373-374.

[182] C. M. S. See, "Method for array calibration in high-resolution sensor array processing", IEE Proceedings - Radar, Sonar, and Navigation, June 1995, Vol. 142, No. 3, pp. 90-96.

[183] C. M. S. See, "A method for array calibration in parametric sensor array processing", ICCS, 1994, Singapore, pp. 915-919.

[184] C. M. S. See, B. K. Poh and C. F. N. Cowan, "Sensor array calibration using measured steering vectors of uncertain location", ICASSP, 1997, Munich, Germany, pp. 3749-3752.

[185] L. P. H. K. Seymour, C. F. N. Cowan and P. M. Grant, "Bearing estimation in the presence of sensor positioning errors", ICASSP, 1987, Texas, U.S.A., pp. 2264-2267.

[186] T. J. Shan, M. Wax and T. Kailath, "On spatial smoothing for direction-of-arrival estimation of coherent signals", IEEE Transactions on Acoustics, Speech, and Signal Processing, August 1985, Vol. ASSP-33, No.4, pp 806-811.

[187] K. C. Sharmann, "Maximum likelihood parameter estimation by simulated annealing", ICASSP, April 88, New York, U.S.A., pp. 2741-2744.

[188] R. M. Sharples, A. P. Doel and R. M. Myers, "Wavefront reconstruction algorithms for astronomical adaptive optics systems", SPIE - Adaptive Optics in Astronomy, 1994, Vol. 2201, pp. 658-665.

[189] Q. Shi and F. Haber, "Comparative performance of eigenvector rotation and MUSIC algorithms for angle-of-arrival estimation", ICASSP, April 1990, New Mexico, U.S.A., pp. 2839-2842.

[190] D. H. Sinnott, "Jindalee - DSTO's over-the-horizon radar project", IREECON, September 1987, Sydney, Australia, pp. 661-664.

[191] D. H. Sinnott, "The Jindalee over-the-horizon radar system", Air Power in Defence of Australia, 1986, Canberra, Australia.

[192] D. H. Sinnott, "Antenna requirements for over-the-horizon radar", IREECON, September 1987, Sydney, Australia, pp. 677-680.

[193] D. H. Sinnott and G. R. Haack, "The use of overlapped subarray techniques in simultaneous receive beam linear arrays", Antenna Applications Symposium, 1983, Illinois, U.S.A.

[194] J. J. Smith, "Line array shape estimation with a single source", Ph.D. Dissertion, February 1997, Curtin University of Technology.

[195] J. J. Smith, Y. H. Leung and A. Cantoni, "The partitioned eigenvector method for towed array shape estimation", ICASSP, May 1995, Atlanta, U.S.A., pp. 3103-3106.

[196] J. J. Smith, Y. H. Leung and A. Cantoni, "The partitioned eigenvector method for towed array shape estimation", IEEE Transactions on Signal Processing, September 1996, Vol. 44, No. 9, pp. 2273-2283.

[197] J. J. Smith, Y. H. Leung and A. Cantoni, "Broadband eigenvector methods for towed array shape estimation with a single source", ICASSP, 1996, Atlanta, U.S.A., pp. 3193-3196.

[198] I. S. D. Solomon, Yu. I. Abramovich, D. A. Gray and S. J. Anderson, "OTH radar antenna array calibration analysis", Fourth International Symposium on Signal Processing and its Applications, August 1996, Gold Coast, Australia, pp. 471-474.

[199] I. S. D. Solomon, D. A. Gray, Yu. I. Abramovich and S. J. Anderson, "Estimating of array mutual coupling and sensor positions for over-the-horizon radar", Digital Signal Processing Applications Conference (TENCON), November 1996, Perth, Australia, pp. 846-851.

[200] I. S. D. Solomon, D. A. Gray, Yu. I. Abramovich and S. J. Anderson, "Sources for OTH radar array calibration", IEEE Antennas and Propagation Symposium, July 1997, Montreal, Canada, pp. 306-309.

[201] I. S. D. Solomon, D. A. Gray, Yu. I. Abramovich and S. J. Anderson, "OTH radar array calibration using disparate sources", IEE Radar Conference, October 1997, Edinburgh, Scotland, pp. 176-180.

[202] I. S. D. Solomon, D. A. Gray, Yu. I. Abramovich and S. J. Anderson, "Over-the-horizon radar array calibration using echoes from ionised meteor trails", IEE Proceedings - Radar, Sonar and Navigation, June 1998, Vol. 145, No. 3 (to appear).

[203] I. S. D. Solomon, D. A. Gray, Yu. I. Abramovich and S. J. Anderson, "Array calibration of OTH radars using disparate sources", submitted to IEEE Transactions on Antennas and Propagation.

[204] I. S. D. Solomon, Yu. I. Abramovich, D. A. Gray and S. J. Anderson, "Performance of OTH radar array calibration", ICASSP, May 1998, Seattle, Washington, U.S.A., pp 2025-2028.

[205] I. S. D. Solomon, Yu. I. Abramovich, D. A. Gray and S. J. Anderson, "Mutual coupling estimation", International Radar Symposium, September 1998, Munich, Germany (to appear).

[206] K. R. Srinivas and V. U. Reddy, "Finite data performance of MUSIC and minimum-norm methods", IEEE Transactions on Aerospace and Electronic Systems, January 1994, Vol. 30, No. 1, pp. 161-174.

[207] J. P. Starski, "Calibration block for digital beam forming antenna", IEEE Antennas and Propagation Symposium, June 1995, California, U.S.A., Vol. 4, pp. 1978-1981.

[208] B. D. Steinberg, "Microwave Imaging of Aircraft", Proceedings of the IEEE, December 1988, Vol. 76, No. 12, pp. 1578-1592.

[209] B. D. Steinberg, "Principles of aperture and array system design", John Wiley and Sons, 1976.

[210] B. D. Steinberg, "Radar imaging from a distorted array : the radar camera algorithm and experiments", IEEE Transactions on Antennas and Propagation, September 1981, Vol. 29, No. 5, pp. 740-748.

[211] H. Steyskal and J. S. Herd, "Mutual coupling compensation in small array antennas", IEEE Transactions on Antennas and Propagation, December 1990, Vol. 38, No. 12, pp. 1971-1975.

[212] P. Stoica and A. Nehorai, "MUSIC, Maximum Likelihood, and Cramer-Rao bound", IEEE Transactions on Acoustics, Speech, and Signal Processing, May 1989, Vol. 37, No. 5, pp. 720-741.

[213] P. Stoica and A. Nehorai, "Performance study of conditional and unconditional direction-of-arrival estimation", IEEE Transactions on Acoustics, Speech, and Signal Processing, October 1990, Vol. 38, No. 10, pp. 1783-1795.

[214] P. Stoica and A. Nehorai, "MUSIC, Maximum Likelihood, and Cramer-Rao bound : further results and comparison", IEEE Transactions on Acoustics, Speech, and Signal Processing, December 1990, Vol. 38, No. 12, pp. 2140-2150.

[215] P. Stoica and K. C. Sharman, "A novel eigenanalysis method for direction estimation", IEE Proceedings - part F, February 1990, pp. 19-26.

[216] P. Stoica and K. C. Sharman, "Maximum likelihood methods for direction-of-arrival estimation", IEEE Transactions on Acoustics, Speech, and Signal Processing, July 1990, Vol. 38, No. 7, pp. 1132-1143.

[217] G. R. Sugar, "Radio propagation by reflection from meteor trails", Proceedings of the IEEE, February 1964, pp. 116-136.

[218] A. Swindlehurst, B. Ottersten and T. Kailath, "An analysis of MUSIC and root-MUSIC in the presence of sensor perturbations", ICASSP, 1989, Glascow, Scotland, pp. 930-934.

[219] A. L. Swindlehurst and T. Kailath, "A performance analysis of subspace-based methods in the presence of model errors, part I : the MUSIC algorithm", IEEE Transactions on Signal Processing, July 1992, Vol. 40, No. 7, pp. 1758-1774.

[220] R. M. Thomas and P. S. Whitham, "Frequency dependence of radar meteor echo rates", Astronomical Society of Australia, 1986, Vol. 6, No. 3, pp. 303-306.

[221] R. M. Thomas and D. J. Netherway, "Observation of meteors using an over-the-horizon Radar", Astronomical Society of Australia, 1989, Vol. 8, No. 1, pp. 88-93.

[222] R. M. Thomas, "Detection by HF radar of the Eta Aquarid meteor shower", Planet. Space Science, 1989, Vol. 37, No. 7, pp 837-346.

[223] R. M. Thomas, P. S. Whitham and W. G. Elford, "Response of high frequency radar to meteor backscatter", Journal of Atmospheric and Terrestrial Physics, 1988, Vol. 50, No. 8, pp. 703-724.

[224] T. Tollefsen and A. Nehorai, "Adaptive calibration of randomly perturbed sensor arrays", ICASSP, April 1988, New York, U.S.A., pp. 2646-2649.

[225] C. Y. Tseng, D. D. Feldman and L. J. Griffiths, "Steering vector estimation in uncalibrated arrays", IEEE Transactions on Signal Processing, June 1995, Vol. 43, No. 6, pp. 1397-1412.

[226] C. Vaidyanathan and K. M. Buckley, "Comparative studies of MUSIC and MVDR location estimators for model perturbations", ICASSP, 1995, Detroit, Michigan (U.S.A.), pp. 1665-1668.

[227] M. Viberg and B. Ottersten, "Sensor array processing based on subspace fitting", IEEE Transactions on Signal Processing, 1991, Vol. 39, No. 5, pp. 1110-1121.

[228] M. Viberg, B. Ottersten and T. Kailath, "Detection and estimation in sensor arrays using weighted subspace fitting", IEEE Transactions on Signal Processing, 1991, Vol. 39, No. 11, pp. 2436-2449.

[229] M. Viberg, "Subspace fitting concepts in sensor array processing", Ph.D Thesis, 1989, Linkoping University, Sweden.

[230] M. Viberg and A. L. Swindlehurst, "A Bayesian approach to direction finding with parametric array uncertainty", ICASSP, 1994, Adelaide, Australia, Vol. 4, pp. 85-88.

[231] M. Viberg and A. L. Swindlehurst, "A Bayesian approach to auto-calibration for parametric array signal processing", IEEE Transactions on Signal Processing, December 1994, Vol. 42, No. 12, pp. 3495-3507.

[232] W. R. Vincent and G. K. Lott, "Measurements of extensive HF industrial, scientific, and medical (ISM) interference far removed from the ITU allocated bands", HF Radio Systems and Techniques, July 1994, University of York, United Kingdom, pp. 155-158.

[233] A. M. Vural, "Effect of perturbations on the performance of optimum/adaptive arrays", IEEE Transactions on Aerospace and Electronic Systems, January 1979, Vol. AES-15, No. 1, pp. 76-87.

[234] D. E. Wahl, "A new method for array shape correction in towed linear arrays", Digital Signal Processing, January 1993, Vol. 3, No. 1, pp. 46-53.

[235] D. E. Wahl, "Towed array shape estimation using frequency-wavenumber data", IEEE Journal of Oceanic Engineering, October 1993, Vol. 18, No. 4, pp. 582-590.

[236] B. Wahlberg, B. Ottersten and M. Viberg, "Robust signal parameter estimation in the presence of array perturbations", ICASSP, 1991, Toronto, Canada, Vol. 5, pp. 3277-3280.

[237] A. Wang, K. Yao, R. E. Hudson, D. Korompis, F. Lorenzelli, S. D. Soli and S. Gao, "Modern microphone array for hearing aid and speech processing", SPIE - Advanced Signal Processing Algorithms, Architectures, and Implementations VI, August 1996, Colorado, U.S.A., Vol. 2846, pp. 112-121.

[238] C. Wang and J. A. Cadzow, "Direction-finding with sensor gain, phase and location uncertainty", ICASSP, 1991, Toronto, Canada, pp. 1429-1432.

[239] H. Wang and M. Kaveh, "On the performance of signal-subspace processing - Part I : narrow-band systems", IEEE Transactions on Acoustics, Speech, and Signal Processing, October 1986, Vol. ASSP-34, pp. 1201-1209.

[240] B. D. Ward, “Project Jindalee : the HF environment at Alice Springs, 1977-1978”, Technical Report, Jindalee Paper No. 134, 1983, Electronics Research Laboratory, Defence Science and Technology Organisation, Australia.

[241] M. Wax and T. Kailath, Determining the number of sources impinging on a passive array by Akaike’s information criterion, Inform. Syst. Lab., 1983, Stanford University.

[242] M. Wax, “Detection and localization of multiple sources via the stochastic signals model”, IEEE Transactions on Acoustics, Speech, and Signal Processing, 1991, Vol. 39, No. 11, pp. 2450-2456.

[243] M. Wax and Y. Anu, “Performance analysis of the minimum variance beamformer in the presence of steering vector errors”, IEEE Transactions on Signal Processing, April 1996, Vol. 44, No. 4, pp. 938-947.

[244] M. Wax and Y. Anu, “A new least squares approach to blind beamforming”, ICASSP, 1997, Munich, Germany, pp. 3477-3480.

[245] M. Wax and T. Kailath, “Detection of signals by information theoretic criteria”, IEEE Transactions on Acoustics, Speech, and Signal Processing, April 1985, Vol. ASSP-33, pp. 387-392.

[246] M. Wax and J. Sheinvald, “Direction finding of coherent signals via spatial smoothing for uniform circular arrays”, IEEE Transactions on Antennas and Propagation, May 1994, Vol. AP-42, No. 5, pp. 613-620.

[247] M. Wax and I. Ziskind, “Detection of the number of coherent signals by the MDL principle”, IEEE Transactions on Acoustics, Speech, and Signal Processing, 1989, Vol. 37, No. 8, pp. 1190-1196.

[248] Y. Wei and B. Zheng, “An effective autofocus algorithm for ISAR imaging”, CIE International Radar Conference, 1996, China, pp. 350-353.

[249] S. Weimin, N. Jinlin, L. Guosui and Z. Guangyi, “The effect of channel mismatch on the spatial spectrum and resolution ability of MUSIC algorithm”, CIE International Radar Conference, 1996, China, pp. 96-99.

[250] A. J. Weiss and B. Friedlander, "Array shape calibration using sources in unknown locations - a maximum likelihood approach", IEEE Transactions on Acoustics, Speech, and Signal Processing, December 1989, Vol. 37, No. 12, pp. 1958-1966.

[251] A. J. Weiss and B. Friedlander, "Array shape calibration using eigenstructure methods", 23rd Asilomar Conference on Signals, Systems, and Computers, 1989, Pacific Grove, California (U.S.A.), pp. 925-929.

[252] A. J. Weiss and B. Friedlander, "Direction finding in the presence of mutual coupling", Asilomar Conference on Signals, Systems, and Computers, November 1988, California, U.S.A., pp. 598-602.

[253] A. J. Weiss and B. Friedlander, "Manifold interpolation for diversely polarised arrays", IEE Proceedings - Radar, Sonar, and Navigations, February 1994, Vol. 141, No. 1, pp. 19-24.

[254] A. J. Weiss and B. Friedlander, "Effects of modelling errors on the resolution threshold of the MUSIC algorithm", IEEE Transactions on Signal Processing, June 1994, Vol. 42, No. 6, pp. 1519-1526.

[255] R. T. Williams, S. Prasad, A. K. Mahalanabis and L. H. Sibul, "An improved spatial smoothing technique for bearing estimation in a multipath environment", IEEE Transactions on Acoustics, Speech, and Signal Processing, April 1988, Vol. 36, No. 4, pp. 425-432.

[256] K. M. Wong, R. S. Walker and G. Niezgoda, "Effects of random sensor motion on bearing estimation by the MUSIC algorithm", IEE Proceedings - Part F, June 1988, Vol. 135, No. 3, pp. 233-250.

[257] S. Wu and Y. Li, "Adaptive channel equalization for space-time adaptive processing", IEEE International Radar Conference, May 1995, Virginia, U.S.A., pp. 624-628.

[258] H. Wu, Y. Jia and Z. Bao, "Direction finding and array calibration based on maximal set of nonredundant cumulants", ICASSP, 1996, Atlanta, U.S.A., Vol. 5, pp. 2626-2629.

[259] N. C. Wyeth, "Methods of array element localization for a towed underwater acoustic array", IEEE Journal of Oceanic Engineering, January 1994, Vol. 19, No. 1, pp. 128-133.

[260] M. P. Wylie, S. Roy and R. F. Schmitt, “Self-calibration of linear equispaced (LES) arrays”, ICASSP, 1993, Minnesota, U.S.A, Vol. 1, pp. 281-284.

[261] M. P. Wylie, S. Roy and H. Messer, “Joint DOA estimation and phase calibration of linear equispaced (LES) arrays”, IEEE Transactions on Signal Processing, December 1994, Vol. 42, No. 12, pp. 3449-3459.

[262] X. L. Xu and K. M. Buckley, “Bias analysis of the MUSIC location estimator”, IEEE Transactions on Signal Processing, October 1992, Vol. 40, No. 10, pp. 2559-2569.

[263] J. Yang and A. Swindlehurst, “Signal copy with array calibration errors”, 27th Asilomar Conference, November 1993, Pacific Grove, California (U.S.A.), pp. 1533-1537.

[264] J. Yang and A. Swindlehurst, “The effects of array calibration errors on DF-based signal copy performance”, IEEE Transactions on Signal Processing, November 1995, Vol. 43, No. 11, pp. 2724-2732.

[265] Y. Yardimci and J. A. Cadzow, “Direction-of-arrival estimation under sensor location uncertainty”, ICASSP, April 1993, Minnesota, U.S.A., Vol. 4, pp. 312-315.

[266] C. C. Yeh, M. L. Leou and D. R. Ucci, “Bearing estimation with mutual coupling present”, IEEE Transactions on Antennas and Propagation, October 1989, Vol. 37, No. 10, pp. 1332-1335.

[267] J. Yongkang, B. Zheng and W. Huan, “Array antenna errors calibration using signal sources in unknown directions”, CIE International Radar Conference, 1996, China, pp. 503-506.

[268] S. J. Yu and J. H. Lee, “Effect of random weight errors on the performance of partially adaptive array beamformers”, Signal Processing, 1994, Vol. 37, pp. 365-380.

[269] M. A. Zatman, H. J. Strangeways and E. M. Warrington, “Resolution of multimoded HF transmissions using the DOSE superresolution direction finding algorithm”, IEE International Conference on Antennas and Propagation, 1993, United Kingdom, pp. 415-418.

[270] M. Zhang and Z. Zhu, “Compensation for unknown mutual coupling in bearing estimation”, International Journal of Electronics, 1993, Vol. 75, No. 5, pp. 965-971.

[271] M. Zhang and Z. Zhu, "DOA estimation with sensor gain, phase and position perturbations", IEEE National Aerospace and Electronics Conference (NAECON), 1993, Dayton, U.S.A., Vol. 1, pp. 67-69.

[272] M. Zhang and Z. Zhu, "Array shape calibration using sources in known directions", IEEE National Aerospace and Electronics Conference (NAECON), 1993, Dayton, U.S.A., Vol. 1, pp. 70-73.

[273] M. Zhang and Z. Zhu, "A method for direction finding under sensor gain and phase uncertainties", IEEE Transactions on Antennas and Propagation, August 1995, Vol. 43, No. 8, pp. 880-883.

[274] M. Zhang and Z. Zhu, "Direction finding with unknown array sensor gains and phases", International Journal of Electronics, 1995, Vol. 78, No. 1, pp. 199-207.

[275] D. Zhao and G. E. Trahey, "A statistical analysis of phase aberration correction using image quality factors in coherent imaging system", IEEE Transactions on Medical Imaging, September 1992, Vol. 11, No. 3, pp. 446-452.

[276] Q. Zhu and B. D. Steinberg, "Wavefront amplitude distortion and image sidelobe levels: part I - theory and computer simulations", IEEE Transactions on Ultrasonics, Ferroelectrics, and Frequency Control, November 1993, Vol. 40, No. 6, pp. 747-753.

[277] Q. Zhu and B. D. Steinberg, "Wavefront amplitude distortion and image sidelobe levels: part II - in vivo experiments", IEEE Transactions on Ultrasonics, Ferroelectrics, and Frequency Control, November 1993, Vol. 40, No. 6, pp. 754-762.

[278] I. Ziskind and M. Wax, "Maximum likelihood localization of multiple sources by alternate projection", IEEE Transactions on Acoustics, Speech, and Signal Processing, October 1988, Vol. 36, No. 10, pp. 1553-1560.

[279] M. Zoltowski and F. Haber, "A vector space approach to direction finding in a coherent multipath environment", IEEE Transactions on Antennas and Propagation, September 1986, Vol. 34, No. 9, pp. 1069-1079.